UNIVERSITY OF MINNESOTA

This is to certify that I have examined this copy of a doctoral thesis by

AHREN WARD JASPER

and have found that it is complete and satisfactory in all respects,
and that any and all revisions required by the final
examining committee have been made.

Donald G. Truhlar

Name of Faculty Adviser

Signature of Faculty Adviser

Date

GRADUATE SCHOOL

NON-BORN–OPPENHEIMER CHEMISTRY: COUPLED POTENTIAL ENERGY SURFACES AND SEMICLASSICAL TRAJECTORIES

A THESIS
SUBMITTED TO THE FACULTY OF THE GRADUATE SCHOOL
OF THE UNIVERSITY OF MINNESOTA
BY

AHREN WARD JASPER

IN PARTIAL FULFILLMENT OF THE REQUIREMENTS
FOR THE DEGREE OF
DOCTOR OF PHILOSOPHY

DONALD G. TRUHLAR, ADVISER

JULY 2003

Acknowledgments

I thank Don Truhlar for providing the opportunity to contribute to this exciting field of research, for his indefatigable supply of stimulating conversation, for his example of excellence in scientific scholarship, and for his continuing thoughtful guidance. I thank my peers at the University of Minnesota for numerous rewarding personal and professional interactions. I especially thank Mike Hack (whose early attention was indispensable), Jay Srinivasan, and Yuri Volobuev for all of their assistance. I have greatly benefited from interactions with past and present group members and collaborators including Amos Anderson, Vanessa Audette, Arindam Chakraborty, Jill Leas, Ben Lynch, Tommy Miller, Hisao Nakamura, Shikha Nangia, Piotr Piecuch, Nate Schultz, Sam Stechmann, Jason Thompson, John Wei, and Chaoyuan Zhu. I thank my parents, Bruce and Sandy Jasper, and my family (including Chad Jasper, Barbara Rekela, Maxwell Jasper, Chris Jasper, Lesley Diamond, and Linda Cole) for a lifetime of loving encouragement. Finally, I thank my wife, Jessica, who deserves more than the kind of simple sentiment than can be recorded here.

This work was supported in part by the National Science Foundation under grant nos. CHE97–25965 and CHE00-92019.

Abstract

Non-Born–Oppenheimer processes (also called electronically nonadiabatic processes) are those in which nuclear motion induces a nonradiative change in the electronic state of the system. This thesis presents the results of theoretical and computational studies in three areas related to non-Born–Oppenheimer chemistry: (i) coupled potential energy matrices (PEMs), (ii) accurate quantum mechanical scattering calculations, and (iii) semiclassical trajectory methods for dynamics. Chapter 1 is an introduction. Chapter 2 presents PEMs, accurate quantum mechanical scattering calculations, and semiclassical trajectory calculations for a family of triatomic model systems with two weakly-coupled electronic states. The problem of energetically forbidden surface hops in the semiclassical trajectory surface hopping approach is discussed. Chapter 3 presents PEMs for the LiFH and NaFH systems and an application of the semiclassical trajectory approach to the photodissociation of LiFH and NaFH excited-state complexes. Trends in the lifetimes and reaction probabilities are related to features of the PEMs. Chapter 4 presents an improved semiclassical trajectory algorithm designed to lessen the errors that result from classically forbidden surface hops. The new method is shown to be the most accurate of several methods tested. Chapter 5 presents an analytic global PEM for the two lowest-energy electronic states of LiFH. The fit is based on high-level electronic structure calculations over a dense grid of nuclear geometries. Chapter 6 presents an improvement to the trajectory surface hopping method discussed in Chapter 4. Chapter 7 presents subthreshold and near-threshold quantum mechanical scattering calculations for the ground-state reaction Li + HF → LiF + H. Trends in the lifetimes of the series of resonances observed in the reaction profile are explained by associating the resonance features with quasibound states of the Li···FH van der Waals well.

Table of Contents

Chapter One

1

Introduction

This chapter introduces non-Born–Oppenheimer (non-BO) chemistry and summarizes the studies in Chapters 2–7. These chapters are arranged in the order in which the work was carried out and may be categorized as follows: (i) the development of potential energy matrices (PEMs) for model systems (Chapter 2) and for realistic chemical systems (Chapters 3 and 5), (ii) the calculation of accurate quantum mechanical scattering dynamics using the outgoing wave variational principle (Chapters 2 and 7), and (iii) the testing, application, and systematic improvement of the semiclassical trajectory method for simulating non-BO dynamics (Chapters 2, 3, 4, and 6).

Many chemical systems may be modeled adequately within the framework of the Born-Oppenheimer (BO) approximation.[1–3] This approximation recognizes the large mass disparity of nuclei and electrons and allows their different time-scale motions to be decoupled. Nuclear motion is then governed by a single BO (also called adiabatic) potential energy surface, which describes the variation of the ground-state electronic energy with changes in the nuclear geometry.

For some processes (called non-BO processes or electronically nonadiabatic processes), more than one electronic state is important in the overall dynamics, and the single-surface BO approximation is not accurate. Using a generalization of the BO approximation, one may obtain an adiabatic potential energy surface for each electronic state. In general, nuclear motion in each electronic state will be coupled to motion in the other electronic states by the action of the nuclear gradient operator ∇_N on the electronic part of the wave function, i.e., by the matrix elements

$$\mathbf{d}_{ij} = \langle i | \nabla_N | j \rangle, \quad (1)$$

where i and j label different electronic states, and $\mathbf{d}_{ij}$ is called the nonadiabatic coupling vector. It is usually possible to rotate the electronic states in electronic state space (via a unitary transformation) to obtain a diabatic representation[4,5] where the elements of the nonadiabatic coupling vector $\mathbf{d}_{ij}$ are small enough (for many purposes) to neglect. The resulting *diabatic* potential energy surfaces are coupled to one another by a scalar coupling term (sometimes called the potential coupling) that is a smooth function of geometry. If no approximations are made (e.g., in an accurate quantum mechanical calculation), the adiabatic and diabatic electronic representations yield identical results.

When characterizing non-BO systems using analytic functions to represent the potential surfaces and their couplings, it is often more convenient to work in the diabatic representation. For example, diabatic potential energy surfaces are usually smoother functions of geometry than adiabatic potential energy surfaces, and the nonadiabatic coupling vector may contain infinities, whereas the diabatic scalar coupling is well-behaved. The diabatic potential energy surfaces, together with the scalar potential energy coupling terms, are collectively referred to as a potential energy matrix (PEM). Chapters 2, 3, and 5 contain descriptions of PEMs for non-BO reactive chemical systems with three atoms and two electronic states.

With an analytic PEM in hand, one may proceed to modeling or calculating the non-BO dynamics. For chemical systems with three or four atoms and two electronic states, the dynamics may be calculated using accurate quantum mechanical techniques. The outgoing wave variational principle[6] (OWVP) has been applied to three-body, two-state systems and is a particularly efficient because it divides the scattering problem into two smaller problems. Specifically, the Hamiltonian is written as a distortion Hamiltonian plus a coupling potential. The distortion Hamiltonian is solved numerically to obtain a set of distorted wave functions. These wave functions are then used to solve variationally for the contribution to the scattering matrix that comes from the coupling potential. Chapters 2 and 7 contain applications of the OWVP method to the scattering dynamics of reactive non-BO chemical systems.

For systems larger than a few atoms, an accurate quantum mechanical dynamical treatment is not computationally affordable, and one employs approximate "semiclassical" methods where the full dynamics of the system is approximated in some way using classical ideas.[7] Semiclassical methods may be defined as the small-$\hbar$ (or large-mass, high-temperature, etc.) limit of quantum mechanics. It is often more useful, however, to develop semiclassical methods using the intuitive procedure of incorporating quantum effects *ad hoc* into classical theories. Although semiclassical algorithms presented in this way may be less rigorously justified, the methods are theoretically important because they often provide a physical picture (i.e., a language) with which one may interpret abstruse quantum mechanical phenomena.

The semiclassical methods considered here may be classified as trajectory ensemble (TE) methods, where a swarm of classical trajectories is used to simulate the nuclear motion of the system. A quantum mechanical nuclear wave packet has some inherent width in configuration and momentum space, whereas classical trajectories are delta functions in phase space. In addition, the coordinates and momenta of a quantal particle have some uncertainty, whereas these quantities are fully determined in a classical system. An *ensemble* of trajectories (as opposed to a single trajectory) is therefore required to approximate the quantal situation, where the initial conditions for each trajectory in the ensemble are distributed to mimic the accurate quantal wave packet.[8] In this sense, each trajectory may be thought of as a basis function, and taken together, the ensemble of trajectories approximates the full nuclear wave packet. Alternatively, each trajectory may be thought of as a single chemical event governed by the probability distribution inherent in the spread of the quantum mechanical wave packet.

A non-BO process modeled using the TE approach may be interpreted as follows: as the ensemble of nuclear trajectories evolves in time, the nuclear motion causes a change in the overall electronic state of the system (via the nonadiabatic or scalar coupling terms) which in turn results in a new effective potential energy felt by the trajectories, affecting the nuclear motion. This nuclear-electronic interaction is the source of nonadiabatic electronic state changes, and to properly treat these non-BO

effects a self-consistent treatment of the nuclear-electronic coupling is necessary (i.e., the electronic and nuclear degrees of freedom must be made to evolve simultaneously).[9] Several methods for incorporating this self-consistency into the TE approximation have been proposed, and before we discuss some of them specifically we will first consider the evolution of the nuclear and electronic degrees of freedom separately.

Each nuclear trajectory in the ensemble evolves classically according to Hamilton's equations of motion. The semiclassical effective potential energy function V that is used in the classical equations of motion must be carefully chosen such that the self-consistency discussed above is maintained. The electronic motion along each classical trajectory is obtained by propagating the solution to the electronic Schrödinger equation with the appropriate initial conditions. The solution takes the form of an electronic density matrix $\boldsymbol{\rho}$, where the diagonal elements ρ_{ii} are the electronic state probabilities, and ρ_{ij} for $i \neq j$ are the electronic state coherences.[10,11]

One may anticipate that a successful semiclassical effective potential energy function V will be some function of the potential surfaces, their couplings, and the electronic state density matrix $\boldsymbol{\rho}$. Several semiclassical algorithms have been proposed with differing prescriptions for V, and the approaches may be divided into two general categories: (i) time-dependent self-consistent field methods, and (ii) trajectory surface hopping methods. Each category will be discussed briefly.

The starting point for time-dependent self-consistent field (TDSCF) methods is the quantum Ehrenfest theorem[12,13] which states that the expectation values of the position and momentum operators evolve according to classical equations of motion with an effective potential energy function given by the expectation value of the potential energy operator. We define the semiclassical Ehrenfest (SE) TE method by taking V to be the expectation value of the electronic Hamiltonian.

The SE method has many disadvantages that result from the mean-field assumption.[14] Although at any instant along a SE trajectory it is physically meaningful for a system to be influenced by some average of the potential energies of all of the electronic states, it is not physically meaningful for the nuclear *motion* corresponding to each electronic state to be described by a single trajectory. If the potential energies of the

various electronic states are similar in topography and energy, then the nuclear motions in each state will be such that an average SE trajectory may provide a reasonable approximation. For many chemical systems, however, this is not the case, and it is not possible for a mean-field trajectory to approximate the motion in these different electronic states. An important consequence of this arises in the case of low-frequency events. A SE trajectory will be dominated by the character of the high-probability motions, and low-probability motions may not be properly explored. Furthermore, it is also not clear how to interpret the final state of a SE trajectory. In general, a SE trajectory will finish the simulation in a mixed electronic state, whereas physically we expect isolated products to be in pure electronic states (if there is no electronic state coupling in the product region of phase space). The internal energy distribution of products in a mixed electronic state is not reliable because it does not correspond directly to the internal energy distribution of any single physically meaningful product.

Several modifications of the SE method have been suggested to remedy these deficiencies. The NDM method[15] is representative of the modified SE methods, which vary in their details but in general attempt to force the system into a pure electronic state as the system leaves the strong coupling region. The NDM method adds terms to the electronic state density matrix ρ such that the system decoheres (dephases, demixes) to a pure electronic state in regions of vanishing coupling. At any instant along an NDM trajectory, the system is decohering from each state i towards state a single state K at a rate $\sim 1/\tau_{iK}$, where τ_{iK} is a physically motivated decoherence time (or demixing time) that may be calculated from the local properties of the system. A NDM trajectory behaves like a SE trajectory in strong coupling regions and collapses to a pure state asymptotically. The method retains the desirable feature of the SE method in that inter-state coherences are included when the electronic states are strongly coupled. Additionally, the NDM method is able to treat low-probability events and gives realistic product states.

Another approach to TE dynamics is the trajectory surface-hopping approach,[10] where the semiclassical potential V is taken to be the potential energy surface that corresponds to the currently occupied state. This single-surface propagation is

interrupted by instantaneous surface transitions (called surface hops) to some other state according to a time-dependent hopping probability that is integrated along the classical trajectory. The hopping probability may be defined in various ways, and we will discuss two of the prescriptions below.

The surface hopping method that has perhaps found the most use in physical applications is the molecular dynamics with quantum transitions method of Tully;[10,11] we will call this Tully's fewest-switches (TFS) method. Trajectories are propagated locally under the influence of a single-state potential energy function, and this propagation is interrupted at small time intervals with hopping decisions. A hopping decision consists of computing a probability for hopping from the currently occupied state to some other state such that hopping is minimized in the sense that hopping only occurs when there is a net flow (in an ensemble averaged sense) of electronic state probability density out of the currently occupied state. At each hopping decision, the hopping probability is computed and compared with a random number to determine if a surface hop occurs.

The accurate quantal picture is represented by a swarm of TFS trajectories, each hopping between the various electronic states at slightly different locations. In this way, the flow of probability density (which may occur over an extended region in phase space) is accurately modeled. One drawback of TFS method is the lack of the proper treatment of decoherence effects. In the SE method, a single trajectory is used to represent the motion in all of the electronic states and the different motions are thus allowed to interfere. In the TFS method, several trajectories are required to model the nonadiabatic dynamics *even for a single initial condition*. (In practice each trajectory has different initial conditions corresponding to initial vibrational and rotational phases, orientations of angular momentum states, and so forth, but the important point is that in contrast to the SE method where there is only one possible trajectory for each initial position and momentum, there are several possible trajectories for a single initial position and momentum in the TFS method which differ from each other in their hopping locations.) To properly treat coherence, the TFS trajectories would be required to interfere with each other,[16] but they do not do so in the standard TFS method. This lack of decoherence

effects can have a significant effect on the final results because the electronic state coherences show up in the expressions for electronic state populations, and these quantities are used to compute the TFS hopping probabilities. The trade-off for this lack of coherence is the ability to model chemical processes that involve divergent trajectories on different electronic states.

A significant problem that must be dealt with when using the TFS formulation is the existence of classically forbidden electronic transitions. The TFS algorithm may predict a nonzero hopping probability to a higher-energy electronic state in regions where the nuclear momentum is insufficient to allow for an energy adjustment that will conserve total energy. When these classically forbidden, or "frustrated" hops are encountered in the TFS method, they are either ignored or the momentum reversed in the direction of the nonadiabatic coupling vector $\mathbf{d}_{ij}$, and in both cases the trajectory does not change electronic states.

The existence of frustrated hopping may cause errors in the predicted nonadiabatic probabilities. For example, quantum mechanical particles have some probability density in regions of phase space that are classically forbidden due to tunneling. These tails of the nuclear wave function decrease exponentially, so we do not expect significant populations in "highly" classically forbidden regions, but these tails may be important for regions that are only "slightly" classically forbidden, i.e., regions that are somewhat close to classically accessible regions. These tails in the quantum mechanical wave function contribute to the existence of frustrated hopping, and these frustrated hops must be somehow allowed to switch electronic states in order to model the proper nonadiabatic dynamics.

The fewest-switches with time-uncertainty (FSTU) method has been developed to correct these deficiencies without explicitly including tunneling or coherence effects. The FSTU method is identical to the TFS method except when a frustrated hop is encountered. If a FSTU trajectory experiences a frustrated hop at time t_0, the system is allowed to hop at time t_h along the trajectory, where t_h is determined by selecting the closest time to t_0 (either forward or backward in time) such that: (1) a hop at that time is classically allowed, and (2) the difference between t_0 and t_h is small enough that

$$\left|t_0 - t_h\right|\Delta E \le \hbar/2\,, \qquad (2)$$

where ΔE is the amount of energy that the system would have to "borrow" to hop at time t_0. This treatment is clearly inspired by the time-energy uncertainty relations, and these nonlocal hops can be thought of as approximating those parts of the quantal system that borrow energy and tunnel into classically forbidden regions. If a suitable t_h cannot be found that meets the above criteria, then the frustrated hopping attempt is treated according to the ∇V prescription. Briefly, if the gradient of the target electronic state in the direction of the nuclear momentum is positive, the trajectory is reflected. Otherwise, no momentum adjustment is made. In both cases, the trajectory continues in the occupied electronic state and no surface hop occurs.

Semiclassical trajectory methods and results are presented and discussed in Chapters 2, 3, 4, and 6. Details of the studies presented in Chapters 2–7 will now be discussed briefly.

In Chapter 2, a family of four weakly coupled electronically nonadiabatic bimolecular model potential energy matrices is presented. Fully converged quantum mechanical calculations with up to 25 269 basis functions were performed for full-dimensional atom-diatom collisions to determine the accurate scattering dynamics for each of the four systems. The quantum mechanical probabilities for electronically nonadiabatic reaction and for nonreactive electronic de-excitation vary from 10^{-1} to 10^{-5}. Tully's fewest-switches (TFS) semiclassical trajectory surface-hopping method is tested against the accurate quantal results. The nonadiabatic reaction and nonreactive de-excitation events are found to be highly classically forbidden for these systems, which were specifically designed to model classically forbidden electronic transitions (also called frustrated hops). The TFS method is shown to systematically overestimate the nonadiabatic transition probabilities due to the high occurrence of frustrated hops. In order to better understand this problem and learn how to best minimize the errors, several variants of the TFS method are tested on the four model systems and also on a set of three more strongly coupled model systems. The methods tested here differ from one another in their treatment of the classical trajectory during and after a frustrated hopping event.

We find that ignoring frustrated hops instead of reversing the momentum along the nonadiabatic coupling vector results in the best agreement with the accurate quantum results for the final vibrational and rotational moments. We also test the use of symmetrized probabilities in the equations for the TFS hopping probabilities. These methods systematically lead to increased errors for systems with weakly coupled electronic states unless the hopping probabilities are symmetrized according to the electronic state populations. We will return to the problem of classically forbidden hops in Chapters 4 and 6.

In Chapter 3, the photodissociation of Li···FH and Na···FH van der Waals complexes[17,18] is studied using Tully's fewest-switches surface-hopping and the natural decay of mixing semiclassical trajectory methods for coupled-state dynamics. The lifetimes of the predissociated excited-state complex (exciplex), as well as the branching ratios into reactive and nonreactive arrangements and internal energy distribution of the products are reported at several excitation energies. The semiclassical trajectory methods agree with each other only qualitatively, and the results are even more strongly dependent on the choice of electronic representation. In general, the lifetime of the LiFH exciplex is shorter and less dependent on the excitation energy than the lifetime of the NaFH exciplex. The semiclassical dynamics of LiFH and NaFH are interpreted in terms of the features of their coupled potential energy surfaces.

In Chapter 4, a modification of Tully's fewest-switches (TFS) trajectory surface hopping is presented that is called the fewest-switches with time uncertainty (FSTU) method. The FSTU method improves the self-consistency of the fewest-switches algorithm by incorporating quantum uncertainty into the hopping times of classically forbidden hops. This uncertainty allows an electronic transition that is classically forbidden at some geometry to occur by hopping at a nearby classically allowed geometry if an allowed hopping point is reachable within the Heisenberg interval of time uncertainty. The increased accuracy of the FSTU method is verified using a challenging set of three-body, two-state test cases for which accurate quantum mechanical results are available. The FSTU method is shown to be more accurate than the TFS method in predicting total nonadiabatic quenching probabilities and product branching ratios.

In Chapter 5, high-level *ab initio* calculations for the global adiabatic potential energy surfaces of the ground state ($\tilde{X}\ ^2A'$) and several excited states ($\tilde{A}\ ^2A'$, $\tilde{B}\ ^2A''$, $\tilde{C}\ ^2A'$, $\tilde{D}\ ^2A'$, and $\tilde{E}\ ^2A''$) of LiFH including the valleys leading to Li + HF and LiF + H are presented. The *ab initio* calculations were carried out using the singles and doubles multireference configuration interaction method[19–21] with 99 reference configuration state functions (CSFs) for the $^2A'$ states and 39 reference CSFs for the $^2A''$ states. The basis set consisted of 140 contracted Gaussian functions, including specifically optimized diffuse functions, and calculations were performed on a dense grid of ~3500 nuclear geometries which allowed us to construct an accurate analytic representation of the two lowest-energy LiFH potential energy surfaces. An analytic 2 x 2 quasidiabatic potential energy matrix was obtained by fitting physically motivated functional forms to the *ab initio* data for the two lowest-energy adiabatic states and explicitly including long-range interactions. The newly presented LiFH fit is compared to several ground-state LiFH fits and one excited-state LiFH fit that have appeared in the literature.

In Chapter 6, a new prescription (called the ∇V prescription) for treating classically forbidden surface hops in semiclassical trajectory surface hopping simulations is presented. The new method uses gradient information about the target electronic surface to determine the nuclear dynamics at a frustrated hopping event. We have tested this prescription, along with previously suggested prescriptions, against accurate quantum dynamics for 21 cases. We find that the fewest switches with time uncertainty (FSTU) algorithm with the ∇V prescription for momentum changes at frustrated hops is the most accurate of the six variants of the surface hopping approach that we tested.

In Chapter 7, state-to-state, state-specific, and cumulative reaction probabilities are presented for the bimolecular scattering process Li + HF → H + LiF in the ground electronic state. Calculations were performed for zero total angular momentum at total energies from 0.26 to 0.50 eV (relative to HF at its classical equilibrium bond distance and infinitely far from Li). The energy dependence of the state-to-state, initial-state-selected, and cumulative reaction probabilities for LiFH in the low-energy regime displays a pronounced resonance structure due to quasibound states associated with a Li···FH van der Waals well in the entrance valley of the potential energy surface. The

lifetimes of the long-lived resonances are obtained by fitting the calculated eigenphase sum to the multichannel Breit-Wigner formula.[22–24] The final rotational state distributions of the LiF product fragment resulting from decay of the resonance state complexes are presented for two resonances. Quantum numbers are assigned to the resonances using bound-state and quasibound-state calculations in the Li···FH van der Waals well, and possible decay mechanisms are discussed. The lifetimes show a systematic dependence on the translational vibrational quantum number.

References

1 M. Born and R. Oppenheimer, *Ann. Phys.* **84**, 457 (1927).

2 M. Born, *Festschrift Gött. Nachr. Math. Phys.* K1, **1** (1951).

3 M. Born and K. Huang, *The Dynamical Theory of Crystal Lattices* (Oxford University Press, London, 1954).

4 A. D. McLachlan, *Mol. Phys.* **4**, 417 (1961).

5 C. A. Mead and D. G. Truhlar, *J. Chem. Phys.* **77,** 6090 (1982).

6 G. J. Tawa, S. L. Mielke, D. G. Truhlar, and D. W. Schwenke, in *Advances in Molecular Vibrations and Collisional Dynamics*, edited by J. M. Bowman (JAI, Greenwich, CT, 1994), Vol. 2B, pp. 45–116.

7 M. S. Child, in *Atom-Molecule Collision Theory*, edited by R. B. Bernstein (Plenum, New York, 1979), pp. 427–465.

8 D. G. Truhlar and J. T. Muckerman, in *Atom-Molecule Collision Theory*, edited by R. B. Bernstein (Plenum, New York, 1979), pp. 505–594.

9 D. A. Micha, J. Chem. Phys. **78**, 7138 (1983).

10 J. C. Tully, in *Dynamics of Molecular Collisions*, edited by W. H. Miller (Plenum, New York, 1976), Part B, pp. 217–267.

11 J. C. Tully J. Chem. Phys. **93**, 1061 (1990).

12 P. Ehrenfest, Z. Phys. **45**, 455 (1927).

13 L. I. Schiff, *Quantum Mechanics*, 3rd Edition (McGraw-Hill, New York, 1968), pp. 28–30.

14 M. D. Hack and D. G. Truhlar, *J. Phys. Chem. A* **104**, 7917 (2000).

15 M. D. Hack and D. G. Truhlar, *J. Chem. Phys.* **114**, 9305 (2001).

16 M. D. Hack, A. M. Wensmann, D. G. Truhlar, M. Ben-Nun, T. J. Martinez, *J. Chem. Phys.* **115**, 1172 (2001).

17 X.-Y. Chang, R. Ehrlich, A. J. Hudson, P. Piecuch, and J. C. Polanyi, *Faraday Discuss. Chem. Soc.* **108**, 411 (1997).

18 A. J. Hudson, H. B. Oh, J. C. Polanyi, and P. Piecuch, *J. Chem. Phys.* **113**, 9897 (2000).

19 R. J. Buenker and S. D. Peyerimhoff, *Theor. Chim. Acta* **35**, 33 (1974).

20 R. J. Buenker and S. D. Peyerimhoff, *Theor. Chim. Acta* **39**, 217 (1975).

21 P. J. Bruna and S. D. Peyerimhoff, *Adv. Chem. Phys.* **67**, 1 (1987).

22 R. K. Nesbet, *Adv. At. Mol. Phys.*, **13**, 315 (1997).

23 A. U. Hazi, *Phys. Rev. A*, **19**, 920 (1979).

24 R. S. Friedman and D. G. Truhlar, in *Multiparticle Quantum Scattering with Applications to Nuclear, Atomic, and Molecular Physics*, edited by D. G. Truhlar and B. Simon (Springer-Verlag, New York, 1997), pp. 243-281.

Chapter Two

2

The Treatment of Classically Forbidden Electronic Transitions in Semiclassical Trajectory Surface Hopping Calculations

I. Introduction

Semiclassical methods for calculating the probabilities of electronically nonadiabatic events have a long history,[1] and a variety of multistate approximations have been developed and reviewed.[2–6] An important recent development is the use of converged quantum mechanical dynamics calculations for full-dimensional atom-molecule collisions to test the semiclassical theories.[7–17]

One may classify electronically nonadiabatic systems in various ways, the simplest of which recognizes strongly coupled and weakly coupled systems. The former are epitomized by surface intersections and localized, narrowly avoided crossings, the so-called Landau-Zener-Teller case,[1,2,4,18] and the latter are epitomized by wide regions of coupling, often of weakly coupled but nearly parallel potential functions, the so-called Rosen-Zener-Demkov case.[1,2,4,19,20] The present article is primarily concerned with developing and testing semiclassical methods for atom-molecule collisions in the latter, less studied case. In particular we focus on the trajectory surface hopping[21–36] (TSH) method and specifically on Tully's fewest-switches (TFS) algorithm[6,30] for surface hopping. (TFS is also called molecular dynamics with quantum transitions or MDQT.) Surface hopping is an *ad hoc* addition to classical mechanics in which trajectories instantaneously switch electronic states, i.e., the potential energy function that determines the nuclear motion is discontinuous. The TFS algorithm is an affordable and often

accurate method[7–14] despite the apparent shortcoming of using sudden surface switches (hops) to describe the nonadiabatic flow of probability in electronic state space.

There are two important decisions that must be made when implementing surface hopping: 1) When a surface hop to a different electronic state is called for and is classically allowed, how should the kinetic energy be adjusted so as to conserve total energy? and 2) what is the best way to treat hopping attempts that are classically forbidden? The first question has a satisfactory answer. The direction along which the nuclear momentum is adjusted is represented by a unit vector called the hopping vector, and it has been shown[9,11] that using the direction of the nonadiabatic coupling vector (instead of the gradient of the electronic energy gap, for example) as the hopping vector and adjusting the nuclear momentum such that total energy is conserved results in the best agreement with quantum mechanical calculations. This procedure has also been justified theoretically.[22,28,37]

Our present study will concentrate on the second question. Hopping attempts that are classically forbidden are called frustrated hops, and their treatment has attracted some attention recently,[12,14,34–36,38,39] but a satisfactory procedure has not yet been obtained. It has been suggested that frustrated hops should be ignored, and this method has been applied with some success.[34] It has also been argued[23,25,38] that when a trajectory experiences a frustrated hop, the nuclear momentum should be reversed along the hopping vector, as if the trajectory experiences a repulsive wall normal to the hopping vector as it attempts and fails to hop to a higher-energy electronic state. In past work,[7,9–15,27] our group has generally followed the procedure used by Blais and Truhlar;[27] this involves a combination of these two approaches, i.e., energetically forbidden frustrated hops are ignored while energetically allowed, but momentum forbidden frustrated hops are reflected.

It has been noted[35] that one may distinguish two possible reasons for the occurrence of classically forbidden hopping attempts. The first possible reason is that the trajectory surface hopping algorithm is somehow inadequate and should not be predicting transitions where they cannot occur. This argument is strengthened by studies that show surface hopping methods to be more accurate when frustrated hops are ignored.[34]

Motivated by this reasoning, a variant of the TFS method called the MDQT* method has recently been proposed[35,36] that eliminates hopping attempts in classically forbidden regions by using a symmetrized velocity in the equations for the electronic state populations. The second possible reason for frustrated hops is that the trajectory *should* hop to the energetically forbidden state, but classical trajectories are limited by the conservation of total energy, whereas quantum mechanical particles can borrow energy for a finite time according to the uncertainty principle. This idea suggests that the method for adjusting the nuclear kinetic energy during a hopping attempt is somehow deficient. Our group has recently proposed a method for redistributing the nuclear kinetic energy in order to allow some classically forbidden hops,[12,14] although this method generally led to increased semiclassical errors for the cases to which it was applied.

In a recent work,[13] two semiclassical methods were tested against accurate quantum mechanical calculations for the weakly coupled BrH_2 system, which is a reactive Rosen-Zener-Demkov case. The results show that despite a difficulty in achieving numerical convergence, the TFS method is more accurate than the semiclassical Ehrenfest method[40,41] for this case. In the present work, we test semiclassical methods on a family of four weakly coupled three-atom systems called the YRH systems with features qualitatively similar to the BrH_2 system. The family of systems has members with quantum mechanical nonadiabatic transition probabilities varying from ~10^{-1} to ~10^{-5}, and it was specifically designed to provide a more systematic test of nonadiabatic semiclassical trajectory methods than the previously described BrH_2 system. Using the TFS algorithm, we find for the model systems studied here that hopping to the ground state is rare, but once the system is in the ground state, a large percentage (25 – 80%) of trajectories experience at least one frustrated hopping attempt. This results in a breakdown of the self-consistency of the TFS algorithm, i.e., the fraction of trajectories in each state does not correspond to the distribution demanded by the fewest-switches algorithm.

Due to the high percentage of trajectories affected by frustrated hops and the low probability of multiple hopping trajectories, the new YRH model systems presented here

provide good test cases for studying the treatment of frustrated hops. We use the family of YRH systems along with a previously described[15] set of more strongly coupled model systems, called MXH systems, to explore several variants of the TFS method which differ in their treatment of frustrated hopping. Section II presents the model YRH systems, and Section III presents the accurate quantum mechanical dynamics calculations for these systems. Section IV discusses the semiclassical algorithms, and Sections V and VI present and discuss the results of the semiclassical methods applied to the model YRH and MXH systems.

II. Model Potential Energy Matrices and Scattering Conditions

In order to design a simple and systematic set of test cases for studying the treatment of surface hops without interference from competing effects, a family of model three-body potential energy matrices (PEMs) with weakly coupled electronic states was created. Each PEM models the nonadiabatic scattering process of an electronically excited model Y atom interacting with a diatomic RH molecule initially in some discrete vibrational and rotational quantum state (v, j):

$$\mathrm{Y}^* + \mathrm{RH}(v, j) \rightarrow \begin{cases} \mathrm{Y} + \mathrm{RH}(v'', j'') & \text{(R1a)} \\ \mathrm{R} + \mathrm{YH}(v', j'), & \text{(R1b)} \end{cases}$$

where the asterisk indicates electronic excitation, and the primes on the quantum numbers indicate that these quantities are not conserved. There is some probability P_{R} that the system will react to form the YH diatomic product (R1b) and some probability P_{Q} that the system will quench, typically accompanied by vibrational and rotational excitation of the RH diatom (R1a). The sum of these probabilities is the total nonadiabatic probability P_{N} for the system to undergo an electronic transition to the ground state during the scattering event.

The electronic excitation energy of the Y atom is taken as 0.36 eV, and the equilibrium bond energies of the RH and YH molecules are 3.9 and 4.3 eV, respectively. The zero point energies of RH and YH are 0.18 eV and 0.19 eV, respectively. The mass combination for all calculations was chosen to be 10 amu and 6 amu for the Y and R atoms, respectively. The H atom has the mass of hydrogen, i.e., 1.00783 amu. This mass

combination provides an interesting and challenging test case for semiclassical methods. The system is modeled in the diabatic representation and has qualitative features of the Rosen-Zener-Demkov type,[1,2,19,20] i.e., the diagonal diabatic potential energy surfaces U_{11} and U_{22} never cross and are nearly parallel in the entrance valley. The diabatic coupling U_{12} is localized in the interaction region. The energy gap between the diabatic surfaces is roughly equal to 0.36 eV throughout the strong interaction region. Details of the functional forms and the parameters used in the analytic representation of the family of YRH surfaces are available as supporting information.[42]

Each member of the family of YRH matrices differs from the others only in the value of the maximum diabatic coupling $U_{12}^{\max}$. Four potential matrices with values of $U_{12}^{\max}$ = 0.20, 0.10, 0.03, and 0.01 eV are discussed in this paper. The PEMs in the series will be referred to individually as YRH($U_{12}^{\max}$/eV), where $U_{12}^{\max}$/eV is $U_{12}^{\max}$ in eV, e.g., YRH(0.20). A plot of the diabatic matrix elements U_{11}, U_{12} and U_{22} along an approximate reaction path of U_{11} in the internuclear bond distance coordinate system is given for YRH(0.10) in Figure 1. Also shown in Figure 1 are the two different total scattering energies (1.10 and 1.02 eV) used for the calculations reported in this paper and the energies of some asymptotic rovibrational states.

Adiabatic potential energy surfaces were obtained by diagonalizing the diabatic PEM. In the adiabatic representation the scalar product of the velocity and the nonadiabatic coupling vector **d** (due to the nuclear linear momentum) couples the nuclear and electronic degrees of freedom.[6,24] Using the Hellman-Feynman theorem, we can calculate **d** without approximation from the diabatic matrix elements and their gradients.[24] Figure 2 contains contour plots of the upper and lower adiabatic surfaces and the magnitude of **d**. Also shown are the magnitudes of the three components of **d**, expressed in the reactant-Jacobi coordinate system, where S is the magnitude of the vector **S** that points from Y to the center-of-mass of RH, s is the magnitude of the vector **s** that points from R to H, and χ is the angle between **S** and **s**.

Initial scattering conditions may be labeled by the shorthand (E/eV, j) where E/eV is the total energy in eV, and j is the initial rotational quantum number; in all cases the initial electronic quantum number is 2 (which corresponds to the excited electronic state), the initial vibrational quantum number is zero, and the total angular momentum is zero. We consider three cases for the YRH systems: (1.10, 0), (1.10, 6), and (1.02, 0). Note that the initial total internal energy for a collision of Y* with RH(v = 0, j = 0) is 0.94 eV and that for RH(v = 0, j = 6) is 1.02 eV.

Although this paper focuses on the model YRH systems, we also consider the previously described[15] set of MXH model PEMs. These systems are more strongly coupled than the YRH systems; the quantum mechanical nonadiabatic transition probabilities vary from 0.15 to 0.49. For these systems we consider the (m_M, m_X, m_H) = (6.04695 amu, 2.01565 amu, 1.00783 amu) mass combination and the (1.10, 0) set of initial conditions. We consider all three sets of MXH surfaces which were previously[15] labeled SB, SL, and WL. See Reference 15 for a complete description of the MXH surfaces.

III. Quantum Dynamics for the Model YRH Systems

Fully converged, six-dimensional (three vibrations and three rotations) quantum mechanical scattering calculations were performed on each of the four YRH potential energy matrices using the outgoing wave variational principle (OWVP),[43–46] as implemented in version 18.8 of the VP computer code.[47] The OWVP is a linear algebraic variational principle[48] employing both $\mathcal{L}^2$ and non-$\mathcal{L}^2$ basis functions. The calculations reported here employ a basis of asymptotic eigenstate functions multiplied by half-integrated Green's functions[49] for energetically open channels and by Gaussian functions for energetically closed channels. A channel is defined as a unique set of the asymptotic quantum numbers including: the molecular arrangement, the diabatic electronic quantum number, the vibrational quantum number of the diatomic molecule, and the rotational quantum number of the diatomic molecule. (For nonzero total angular momentum J one could also include the relative translational orbital angular momentum ℓ, but for J = 0, we

have ℓ equal to j, j', or j''.) All of the rotational-state channels for a given vibrational state, electronic state, and molecular arrangement were coupled to each other, whereas channels with different vibrational states, electronic states or molecular arrangements were uncoupled when solving the finite difference problem to obtain the basis functions for the variational step. The surfaces were fully coupled during the variational step in the calculations See Refs. 43–46 for details.

We define our potential energy matrices and perform our quantum mechanical calculations in the diabatic representation with zero nuclear momentum coupling. In such a model, there is a one-to-one transformation between diabatic and adiabatic representations, and the quantum mechanical results are independent of which one is chosen.

A list of the OWVP basis set parameters can be found in the supporting information.[42] Basis set I contains 18934 basis functions and was used to calculate all of the observables reported in this paper. The larger basis set, basis set II was used to check the convergence of basis set I for the YRH(0.20) and YRH(0.01) systems at several scattering energies. The number of basis functions in the convergence check is 25269. In these convergence checks, the state-to-state transition probabilities out of the Y* + RH($v = 0, j = 0$) (for $E = 1.10$ and 1.02 eV) and the Y* + RH($v = 0, j = 6$) (for $E = 1.10$ eV) initial states are converged to better than 1% for greater than 95% of the energetically accessible final channels, with the remaining state-to-state transition probabilities (high- j' or j'' channels) converged to better than 5%. For all of the state-to-state transition probabilities (including all initial states), 94% of the transition probabilities (with an average value of 0.013) are converged to better then 1%, 3% of the transition probabilities (with an average value of 4.5×10^{-5}) are converged to better than 5%, and the remaining 3% of transition probabilities have an average value of 2.1×10^{-8}. The first moments (i.e., averages) of the vibrational and rotational quantum numbers, and the reaction and quenching probabilities are converged to better than 1%.

Quantum mechanical observables often exhibit an oscillatory structure as functions of scattering energy. In contrast, semiclassical properties often do not show

these oscillations, and in such cases it is most appropriate to compare them to energy-averaged quantum results. In the present case we checked that the semiclassical results depend only slowly on energy. It is therefore desirable to compare the semiclassical results obtained at a single scattering energy to the average quantum mechanical value obtained over a range of energies. Quantum mechanical calculations were performed at seven energies at and around the nominal scattering energies[42] and averaged to obtain values that are used to compute the errors reported in Tables 2 and 3. In most cases, the values obtained by averaging are similar to the values obtained at the nominal scattering energy.

IV. Semiclassical Trajectory Calculations

Semiclassical trajectory surface hopping calculations were carried out using version 6.0 of the NAT computer code[50] (which is a generalized version of our previous TSH code). For all the calculations reported in this work, the hopping vector was taken to be a unit vector in the direction of the nonadiabatic coupling vector, i.e.,

$$\mathbf{h} = \frac{\mathbf{d}}{|\mathbf{d}|} \ . \tag{1}$$

The initial coordinates and momenta for each trajectory in the ensemble were selected as described previously.[11,25]

The final reaction and quenching probabilities (P_R and P_Q) were determined by counting trajectories, and the final rotational and vibrational moments ($< v' >$ and $< j' >$ for reactive trajectories, and $< v'' >$ and $< j'' >$ for quenching trajectories) were calculated according to the energy-nonconserving histogram (EN-H) analysis scheme.[11] Vibrational and rotational moments were also calculated using the energy-nonconserving quadratic smooth sampling[11,51] (EN-QSS), and the energy-nonconserving linear smooth sampling (EN-LSS) analysis schemes. We also tested an energy-conserving (EC) variant[11] of the three sampling schemes, i.e., EC-H, EC-QSS, and EC-LSS. The EC methods result in systematically slightly lower rotational and vibrational moments and lead to increased semiclassical errors. The results from the six analysis schemes typically

differ from each other by less than 2%. For this reason, we report only one set of results, and we chose the EN-H result, because it has a well defined statistical uncertainty estimate.[25]

IV.A. Treatment of the Nuclear Momentum at a Frustrated Hop

During a surface hopping event, a trajectory attempts to hop from the occupied electronic state to a target electronic state. A hopping attempt is classically forbidden if it is not possible to adjust the nuclear momenta along the hopping vector **h**, such that total energy is conserved. One may further divide classically forbidden hops into three categories,[12] namely: energy-, angular-momentum-, and linear-momentum-forbidden hops. Energy-forbidden hops occur when the target state has an energy greater than the total energy of the system. The distinction between the other two types of frustrated hops depends on dividing the energy into vibrational and rotational contributions. A hop is angular-momentum-forbidden when the hop is not energy-forbidden, but the vibrational energy is less than the energy of the target state, i.e., the nuclear momentum cannot be adjusted in any direction such that total angular momentum is conserved. A linear-momentum-forbidden hop occurs when there is sufficient energy in vibrational modes to exist on the target surface, but there is insufficient energy along the hopping vector **h** to allow for the energy adjustment. We note that for systems where the total angular momentum J is equal to zero, there is no energy in the rotation of the system and angular-momentum-forbidden hops cannot occur. For the calculations reported here, the orbital angular momentum ℓ_{class} is selected classically from $0 \leq \ell_{\text{class}} \leq \hbar$ for the $j = 0$ state and from $6\ \hbar \leq \ell_{\text{class}} \leq 7\ \hbar$ for the $j = 6$ state, and therefore the total angular momentum J is can have values that range from $-\frac{1}{2}\ \hbar < J < \frac{1}{2}\ \hbar$. The occurrence of angular-momentum-forbidden hops, however, is much less than 0.01% of the total number of attempted hops, and the treatment of angular-momentum-forbidden (but otherwise allowed) hops will not be considered in this paper.

Several variants of the TFS method which differ in their treatment of frustrated hops will be tested. We will refer to the TFS variants as TFS-(*Prot*-L, *Prot*-E), where

Prot-L denotes the protocol for linear-momentum-forbidden hops, and *Prot*-E denotes the protocol for energy-forbidden hops. The allowed values for *Prot*-L and *Prot*-E will be introduced and defined as needed.

In recent work,[7,9–15] following an older protocol,[27] our group has used an implementation of the TFS method in which momentum- and energy-forbidden hops are treated differently. When a trajectory experiences a linear-momentum-forbidden hop, the nuclear momentum along the hopping vector **h** is reversed, whereas when a trajectory experiences an energy-forbidden hop, the attempted hop is ignored. We will refer to this method as the TFS-(–,+) method, where the "–" indicates that the nuclear momentum is reversed along **h**, and the "+" indicates that the nuclear momentum is not reversed along **h**. In assessing whether this is the best procedure, we note that interstate coupling in the adiabatic representation is proportional to the scalar product of the velocity of the trajectory and **d**, and therefore it is independent of the components of the velocity orthogonal to **d**. We also note that it is the energy in the modes orthogonal to **d** that differentiates the two different types of forbidden hops. These considerations motivate a method that treats frustrated hops consistently. In particular, along with the TFS-(–,+) method, we test two alternate schemes, namely the TFS-(+,+) and the TFS-(–,–) methods. In the TFS-(–,–) method, all frustrated hops are reflected along **h**. The TFS-(–,–) method was the method used in the original implementation of the TFS method.[30,38] In the TFS-(+,+) method, all frustrated hops are ignored. The TFS-(+,+) method has also been suggested and tested in the literature.[34]

We have previously described a method for removing linear-momentum-frustrated hops by rotating the hopping vector **h** within the zero angular momentum region of configuration space by the smallest amount that allows for hopping.[12] In the present work, we call this the TFS-(R,+) method, where the "R" indicates that linear-momentum-forbidden hops are allowed using a rotated hopping vector. Rotating the hopping vector cannot be used to allow energy-forbidden hops, and when an energy-forbidden hop is attempted, it is ignored.

IV.B. Symmetrized-Speed and Symmetrized-Coupling Methods

The four variants of the TFS method discussed in the previous section, TFS-(−,+), TFS-(–,–), TFS-(+,+) and TFS-(R,+), differ in their treatment of the classical trajectory after a hopping attempt that is generated by the TFS algorithm turns out to be frustrated. An alternate approach is to modify the TFS algorithm to eliminate hopping attempts in regions where hops are classically forbidden. For a trajectory following the path $\mathbf{R}(t)$, we can write the electronic wavefunction for a two-state system as

$$\Psi(t) = c_1(t)\phi_1(\mathbf{R}(t)) + c_2(t)\phi_2(\mathbf{R}(t)), \tag{2}$$

where ϕ_1 and ϕ_2 are the adiabatic electronic basis functions for the ground-state and excited-state, respectively, and c_1 and c_2 are expansion coefficients that depend on the time t. The electronic state population of state χ at time t is given by

$$n_\chi(t) = \left|c_\chi(t)\right|^2. \tag{3}$$

The TFS probability of hopping from the occupied electronic state k to the target state l is given by[30]

$$g_{kl} = \max\left(0, \frac{b_{kl}\Delta t}{n_k}\right), \tag{4}$$

where

$$b_{kl} = -2\,\mathrm{Re}(a_{kl}^{*}\dot{\mathbf{R}}_k \cdot \mathbf{d}), \tag{5}$$

Δt is the change in time between hopping checks, a_{kl} is the electronic state coherence $c_k c_l^{*}$, and $\dot{\mathbf{R}}_k$ is the velocity of the system on the occupied surface k. When a hop occurs, the internal energy is adjusted along the $\mathbf{h}$ vector, such that energy is conserved, i.e., according to the following equation

$$T_{\mathbf{h}}(k) + E(k) = T_{\mathbf{h}}(l) + E(l), \tag{6}$$

where $T_{\mathbf{h}}(k)$ is the kinetic energy associated with the component of the nuclear linear momentum in the $\mathbf{h}$ direction when the trajectory is on surface k, and $E(k)$ is the potential energy of surface k. As mentioned previously, a hopping attempt is frustrated if the energy of the occupied state k is less than the energy of the target state l, and the kinetic

energy along **h** before the hopping attempt is less than the energy gap between the two potential energy surfaces, i.e., if

$$T_{\mathbf{h}}(k) < E(l) - E(k). \tag{7}$$

A method called the MDQT* method[35,36] has been proposed for the case where eq. (4) is used, such that one uses a geometrically symmetrized speed (GS) to eliminate hopping attempts in regions where eq. (7) is true. This method was justified[35] by noting that while a TFS classical trajectory exists on only one potential energy surface, a quantum mechanical wavefunction has some probability density on both electronic surfaces, and hence the magnitude of the velocity that appears in the electronic dynamics through eq. (5) is replaced by a speed more representative of the motion on both surfaces. We test this method along with seven variants. All eight methods eliminate frustrated hopping, by rewriting eq. (5) as

$$b'_{kl} = -2\,\mathrm{Re}(a^*_{kl} F(\dot{\mathbf{R}}_k, \dot{\mathbf{R}}_l, \mathbf{d})), \tag{8}$$

where the exact form of $F(\dot{\mathbf{R}}_k, \dot{\mathbf{R}}_l, \mathbf{d})$ depends on the method. (Note that a_{kl} is also a function of $\dot{\mathbf{R}}_k \cdot \mathbf{d}$, and $F(\dot{\mathbf{R}}_k, \dot{\mathbf{R}}_l, \mathbf{d})$ is used in place of $\dot{\mathbf{R}}_k \cdot \mathbf{d}$ when calculating a_{kl} for the eight new methods presented here.) In the MDQT* method, which we will also call the GS(½) method,

$$F^{\mathrm{GS}(½)}(\dot{\mathbf{R}}_k, \dot{\mathbf{R}}_l, \mathbf{d}) = \left|\dot{\mathbf{R}}_k\right|^{½} \left|\dot{\mathbf{R}}_l\right|^{½} \frac{\dot{\mathbf{R}}_k \cdot \mathbf{d}}{\left|\dot{\mathbf{R}}_k\right|}, \tag{9}$$

where the velocity of the trajectory in the currently occupied electronic state is $\dot{\mathbf{R}}_k$. The value of $\left|\dot{\mathbf{R}}_l\right|$ must be computed at each time step, where $\dot{\mathbf{R}}_l$ is the velocity that the trajectory would have if it were to hop to the other electronic surface. Whenever a hopping attempt would be frustrated, $\dot{\mathbf{R}}_l$ does not exist, and $F(\dot{\mathbf{R}}_k, \dot{\mathbf{R}}_l, \mathbf{d})$ is set to zero. All frustrated hops are eliminated in this method. The hopping probability does not go smoothly to zero as hopping becomes frustrated, because $\dot{\mathbf{R}}_l$ can have nonzero components orthogonal to **d** as hopping becomes frustrated.

We also note that in the GS(½) method,[35,36] the components of the velocity orthogonal to **d** contribute to the electronic dynamics. This might be considered

unphysical since, as previously mentioned, these components do not couple the adiabatic electronic states in the original equation for b_{kl} given in eq. (5). An alternate prescription that eliminates frustrated hopping with a smoothly vanishing hopping probability function is the geometrically symmetrized coupling scheme, GC(½). In this formulation,

$$F^{\mathrm{GC}(½)}(\dot{\mathbf{R}}_k, \dot{\mathbf{R}}_l, \mathbf{d}) = \left|\dot{\mathbf{R}}_k \cdot \mathbf{d}\right|^{½} \left|\dot{\mathbf{R}}_l \cdot \mathbf{d}\right|^{½} \frac{\dot{\mathbf{R}}_k \cdot \mathbf{d}}{\left|\dot{\mathbf{R}}_k \cdot \mathbf{d}\right|}. \tag{10}$$

Using eq. (10), the hopping probability goes smoothly to zero as hopping becomes frustrated. The GC(½) method symmetrizes only the component of the velocity which is along **d**; the components of the velocity orthogonal to **d** do not contribute to the electronic dynamics, which is consistent with eq. (5).

For completeness, we also test the AS(½) and AC(½) methods, in which the speed or the coupling is arithmetically symmetrized. Specifically,

$$F^{\mathrm{AS}(½)}(\dot{\mathbf{R}}_k, \dot{\mathbf{R}}_l, \mathbf{d}) = \left(½\left|\dot{\mathbf{R}}_k\right| + ½\left|\dot{\mathbf{R}}_l\right|\right) \frac{\dot{\mathbf{R}}_k \cdot \mathbf{d}}{\left|\dot{\mathbf{R}}_k\right|}, \tag{11}$$

$$F^{\mathrm{AC}(½)}(\dot{\mathbf{R}}_k, \dot{\mathbf{R}}_l, \mathbf{d}) = \left(½\left|\dot{\mathbf{R}}_k \cdot \mathbf{d}\right| + ½\left|\dot{\mathbf{R}}_l \cdot \mathbf{d}\right|\right) \frac{\dot{\mathbf{R}}_k \cdot \mathbf{d}}{\left|\dot{\mathbf{R}}_k \cdot \mathbf{d}\right|}. \tag{12}$$

The symmetrized coupling equations for the GS(½), GC(½), AS(½), and AC(½) methods defined in eqs. (9–12) weight the speed or coupling of both surfaces equally. In general, the wavepacket is not evenly distributed between the two electronic states. In order to incorporate this into the dynamics we define the method GC(n_χ) by rewriting eq. (10) as

$$F^{\mathrm{GC}(n_\chi)}(\dot{\mathbf{R}}_k, \dot{\mathbf{R}}_l, \mathbf{d}) = \left|\dot{\mathbf{R}}_k \cdot \mathbf{d}\right|^{n_k} \left|\dot{\mathbf{R}}_l \cdot \mathbf{d}\right|^{n_l} \frac{\dot{\mathbf{R}}_k \cdot \mathbf{d}}{\left|\dot{\mathbf{R}}_k \cdot \mathbf{d}\right|}, \tag{13}$$

where n_χ is the electronic state population of state χ. With this form of $F^{\mathrm{GC}(n_\chi)}$, the coupling terms that arise from each electronic surface are weighted according to their state populations n_χ instead of arbitrarily by ½. We also test the GS(n_χ), AS(n_χ), and AC(n_χ) methods which are defined by replacing the ½ weighting factors that appear in eq. (9), eq. (11) and eq. (12), respectively, by n_χ, specifically:

$$F^{\mathrm{GS}(n_\chi)}(\dot{\mathbf{R}}_k,\dot{\mathbf{R}}_l,\mathbf{d}) = \left|\dot{\mathbf{R}}_k\right|^{n_k}\ \left|\dot{\mathbf{R}}_l\right|^{n_l}\ \frac{\dot{\mathbf{R}}_k\cdot\mathbf{d}}{\left|\dot{\mathbf{R}}_k\right|}, \tag{14}$$

$$F^{\mathrm{AS}(n_\chi)}(\dot{\mathbf{R}}_k,\dot{\mathbf{R}}_l,\mathbf{d}) = \left(n_k\left|\dot{\mathbf{R}}_k\right| + n_l\left|\dot{\mathbf{R}}_l\right|\right)\frac{\dot{\mathbf{R}}_k\cdot\mathbf{d}}{\left|\dot{\mathbf{R}}_k\right|}, \tag{15}$$

$$F^{\mathrm{AC}(n_\chi)}(\dot{\mathbf{R}}_k,\dot{\mathbf{R}}_l,\mathbf{d}) = \left(n_k\left|\dot{\mathbf{R}}_k\cdot\mathbf{d}\right| + n_l\left|\dot{\mathbf{R}}_l\cdot\mathbf{d}\right|\right)\frac{\dot{\mathbf{R}}_k\cdot\mathbf{d}}{\left|\dot{\mathbf{R}}_k\cdot\mathbf{d}\right|}. \tag{16}$$

IV.C. Absorbing Frustrated Hops

It is interesting to calculate the reaction and quenching probabilities that would be obtained by the TFS method if somehow frustrated trajectories were provided with the necessary energy to hop. We can obtain a lower limit on the total nonadiabatic probability P_{N} by re-analyzing the data from a TFS calculation and using only those trajectories that do *not* experience a frustrated hop to calculate the final probabilities and moments. This method can be thought of as the result obtained by absorbing trajectories with frustrated hops to the upper electronic state and is called the AFH result. This result provides a lower limit on the TFS total nonadiabatic probability P_{N} because the possibility that some of the re-assigned trajectories may hop back down to the lower state is not included. Note that the TFS-AFH method cannot be used to compute the moments on the upper surface, but we do not consider such moments in the present paper.

IV.D. Semiclassical Ehrenfest Method

Although our main goal here is to determine the optimum procedure for trajectory surface hopping calculations when the surfaces are weakly coupled, we also carried out calculations using the semiclassical Ehrenfest version[39,40] of the time-dependent self-consistent-field method. The calculations show that the Ehrenfest method fails badly for these systems, and this finding further motivates the present study. The Ehrenfest results are discussed briefly in the appendix.

V. Results

We tested all of the methods mentioned in this paper on the YRH(0.2) PEM at the (1.10, 0) set of initial conditions, and the results are summarized in Table 1. We further tested the TFS-(–,+), TFS-(+,+), TFS-(–,–), TFS-(R,+), and GC(n_χ) methods on all four of the YRH PEMs at each of the three different sets of initial conditions (1.10, 0), (1.10, 6), and (1.02, 0) and on the set of three model MXH systems (SB, SL, and WL) for the (1.10, 0) set of initial conditions. The detailed results of all of the semiclassical trajectory calculations can be found in the supporting information.[42]

Unless one single semiclassical method is best for all observables for all cases, the choice of "best method" is not unique. Nevertheless, we will present some statistics that will help us to determine a reasonable (if not unique) answer to the question of which method is the most accurate and to quantitatively compare the overall accuracy of the several semiclassical methods. First, unsigned errors were computed for each vibrational and rotational moment. The quenching probabilities, reaction probabilities and total nonadiabatic probabilities vary by several orders of magnitude over the four YRH PEMs, and therefore the errors in these quantities were calculated using logarithms, in particular the unsigned logarithmic error in $\log_{10}P_X$ is given by

$$\mathrm{UE}(\log_{10} P_X) = \left| \log_{10} P_X^{\text{semiclassical}} - \log_{10} P_X^{\text{quantal}} \right|, \tag{17}$$

where X = "R", "Q" or "N". We also consider the error in the reactive branching ratio F_R which is defined as the ratio of the reaction probability P_R to the total nonadiabatic probability P_N. The unsigned errors for all of the semiclassical methods discussed in this paper for the YRH(0.20) PEM and the (1.10, 0) set of initial conditions are shown in Table 2. The method with the lowest unsigned error is listed in bold. If another semiclassical method has an uncertainty that overlaps that of the best method, that method is also listed in bold.

Mean unsigned errors (MUEs) were calculated for the TFS-(–,+), TFS-(+,+), TFS-(–,–), TFS-(R,+), and GC(n_χ) semiclassical methods for the YRH systems by averaging over the twelve cases studied here (four YRH PEMs and three sets of initial conditions) and are presented in Table 3. Table 4 shows the MUEs for five semiclassical

methods for the MXH systems, averaged over the three MXH PEMs. In each column, the method with the smallest MUE is indicated with bold font. By adding and subtracting the uncertainty of the observable from the nominal values, we obtain an upper and a lower bound on the value of the observables. We can then compute an upper bound on the MUEs by calculating the MUE using either the upper or lower value of each observable, whichever results in the greatest error. A lower bound on the MUE can be calculated in a similar way. Taken together, these values were used to determine if the method with the lowest MUE is statistically different from the other methods. If the method with the lowest MUE has an uncertainty in its MUE that overlaps with the uncertainty in the MUE of one or more the other methods, each method with overlapping MUEs is also listed in bold in Table 3.

Table 4 evaluates the semiclassical methods in a different way; in particular, it presents "scorecards" for the five semiclassical methods that we applied to all fifteen cases. For each of the observables, a point is given to the method with the lowest absolute error (or absolute error of the logarithms for the probabilities) for each PEM and set of initial conditions. If the best method has an error with an uncertainty that overlaps one or more of the other semiclassical methods, each of the winning methods receives a point. Table 5 summarizes the data in Tables 3 and 4.

VI. Discussion

The term "classically forbidden" can have a variety of meanings in a technical sense, but it is nevertheless useful and easily understood as a label for certain kinds of events. Consider, e.g., the expansion of the electronic wavefunction Ψ given in eq. (2). At the start of the simulation, the system is in a pure state, i.e., $c_\chi(t=0)$ is a Kronecker delta, $\delta_{\chi 2}$. It would be reasonable to say that a hop down is classically forbidden whenever $\left|c_1(t=\infty)\right|^2$ is less than ½. With this definition, electronic transitions are classically forbidden for nearly every one of the more than twelve million trajectories calculated for the YRH systems in the present study. In fact, less than 0.1% of trajectories for YRH(0.20) and YRH(0.10) have values of $\left|c_1(t=\infty)\right|^2 > ½$, and the

maximum value of $|c_1(t=\infty)|^2$ is 0.12 and 0.10 for YRH(0.03) and YRH(0.01), respectively. One may therefore expect semiclassical methods to fail for systems with weakly coupled electronic states. We find, however, that the semiclassical methods tested here provide reasonably accurate results, although the results are somewhat sensitive to the treatment of frustrated hops.

The weakly coupled nature of the electronic states of the YRH PEMs requires a large number of trajectories in order to generate good statistics. The number of trajectories computed for each simulation is included in the supporting information[42] and varies from five thousand to five hundred thousand. Each trajectory takes about 1.2 seconds of computer time on an IBM SP supercomputer with 375 MHz Power 3 WinterHawk+ processors, and it is worthwhile to note that for these weakly coupled systems, the fully converged quantum mechanical calculations (with our unique, highly optimized computer program) are less expensive than some of the well converged (with respect to the number of trajectories) semiclassical trajectory methods. Nevertheless, trajectory methods remain more easily programmable and affordable for large systems where accurate quantum dynamics become prohibitive, so it is important to test the reliability of the semiclassical methods.

The TFS-(–,+) method systematically overestimates the reaction and quenching probabilities for weakly coupled systems. (This is also true for the TFS-(–,–) and TFS-(+,+) methods. However, the choice of the "+" or "–" protocol is not important to the discussion in this and the next several paragraphs, and only the TFS-(–,+) method will be discussed.) We can explain the trend in P_R and P_Q by noting that in the twelve YRH cases studied here, 25 – 80% of the TFS-(–,+) trajectories that finish the simulation on the lower electronic surface experience at least one frustrated hopping attempt. Trajectories that experience frustrated hopping attempts are trapped in the ground electronic state, leading to values of P_R and P_Q that are greater than the value demanded by the fewest-switches algorithm. We can estimate a lower limit on the TFS transition probabilities by considering only those trajectories that do not experience any frustrated hops. This is accomplished by the TFS-AFH method. The TFS-(–,+) result, the

TFS-AFH result, and the quantum mechanical result for the reaction and quenching probabilities for the (1.10, 0) initial conditions are plotted in Figure 3. For all four of the PEMs, the quantum mechanical transition probabilities are bracketed by the TFS-(–,+) and TFS-AFH results. For (1.10, 6) and (1.02, 0), this trend is observed for three of the four PEMs. The total nonadiabatic probability P_N, which was defined above as $P_R + P_Q$, is bracketed by the TFS-(–,+) result and the TFS-AFH result for all four PEMs in the YRH family and all three sets of initial conditions.

For the YRH systems, the likelihood that a trajectory will hop to the ground-state twice is approximately equal to P_N^2, which is in most cases negligible compared to P_N. (Note that this is not true for the more strongly coupled MXH systems where multiple hopping trajectories are an important part of the nonadiabatic dynamics.) Therefore, for weakly coupled systems, the TFS-AFH result is not merely a lower limit on the TFS transition probabilities; the TFS-AFH result is approximately the result that would be obtained if every frustrated hopping attempt called for by the TFS algorithm were allowed to occur. The fact that neither the TFS-(–,+) method nor the TFS-AFH method is accurate for the weakly coupled YRH systems motivates the search reported in this paper for a modification to the TFS method that allows some frustrated hops and removes (or ignores) others.

We note that the model YRH systems provide a dramatic example of the role that frustrated hopping plays in the sensitivity of TSH calculations to the choice of electronic representation. As previously mentioned, all of the semiclassical calculations reported in this paper were carried out in the adiabatic representation, except when noted otherwise. The model YRH(0.20) system and the initial conditions (1.10, 0), TFS-(–,+) calculations carried out in the diabatic representation (called the TFS-(–,+)-di method) predict reaction probabilities ten times greater and quenching probabilities four times greater than those predicted by the adiabatic TFS-(–,+) calculations. We note that ~97% of trajectories that finish the simulation in the lower diabatic state experience at least one frustrated hopping attempt, and that the quantum mechanical reaction and quenching probabilities (which are invariant to the choice of electronic representation) are bracketed

by the TFS-(–,+)-di and the TFS-AFH-di methods, just as they are for the adiabatic results. We will not discuss the diabatic calculations further.

The symmetrized probability methods that weight the surfaces by ½ significantly over-estimate the reaction and quenching probabilities for the weakly coupled model YRH systems. We have previously discussed how frustrated hopping causes the TFS-(−,+) method to overestimate P_{N}. The symmetrized methods eliminate frustrated hopping, but do so in a way that increases the probability of transitions to lower-energy states and decreases the probability of transitions from lower-energy states to higher-energy states. This can be seen from eqs. (9–16). For any of the symmetrized methods, b'_{kl} will be greater than the value of b_{kl} for the TFS-(*Prot*-L, *Prot*-E) methods given by eq. (5) whenever the trajectory is in the higher-energy electronic state, and b'_{kl} will always be less than b_{kl} when the trajectory is in the lower-energy electronic state.

The more physical n_χ-weighted methods have much lower errors in the probabilities than the ½-weighted methods. For the YRH systems, $n_1 \approx 0$ and $n_2 \approx 1$, so the value of b'_{kl} is nearly equal to b_{kl} when the trajectory is in the higher-energy electronic state. The value of b'_{kl} is not equal to b_{kl} when the trajectory is in the lower-electronic state, but multiple hopping trajectories are not important in determining the dynamics of the YRH systems. Therefore, the value of b'_{kl} after a hop down to the lower-energy state is only important in determining whether or not the trajectory will experience a frustrated hop. In the n_χ-weighted methods, frustrated hops are eliminated, which has the same effect on the final observables as ignoring the frustrated hops, and the n_χ-weighted methods give similar results to the TFS-(+,+) method. The total nonadiabatic probability is systematically slightly higher than the TFS-(+,+) method due to the considerations discussed above for the ½-weighted methods. Table 3 shows that the GC(n_χ) method (which is, overall, the most accurate of the symmetrized methods tested here) predicts less accurate values for P_{N} than any of the TFS-(*Prot*-L, *Prot*-E) methods.

It should also be noted that the symmetrized methods cannot be used in the diabatic representation, because the diabatic coupling is not a function of the velocity of the classical trajectory. We also note that the functions presented in eqs. (9–16) are not smooth functions, i.e., they have discontinuous first derivatives. This arises from the fact that while the trajectory is traveling on a single electronic surface, eqs. (9–16) are functions of the velocity (or speed) of the trajectory on both electronic states. This speed for the unoccupied state does not correspond to a physical path of a trajectory travelling on the unoccupied electronic surface. For example, if on the occupied surface the trajectory experiences a turning point in one of its modes, the velocity in that mode will decrease, pass through zero, and increase from zero with a different sign. The velocity computed for the unoccupied surface will also switch signs, but it will not necessarily go through zero, resulting in discontinuities in the velocity in that mode and its derivative. These discontinuities can affect the efficiency of the trajectory calculation if the equations for a_{kl} are integrated with an algorithm that requires smooth derivatives.

We will now turn our attention to the TFS-(–,+), TFS-(+,+), TFS-(–,–), and TFS-(R,+) methods. The treatment of frustrated hops can have a significant effect the final observables. The effect is greater for the weakly coupled YRH systems than for the more strongly coupled MXH systems, where multiple hopping trajectories are important. In general, the TFS-(+,+) method predicts the most accurate moments, the TFS-(–,–) method predicts the most accurate values of F_{R}, and the TFS-(R,+) method predicts the most accurate values of P_{N}.

Reflecting the nuclear momentum along **d** during a frustrated hop leads to increased error in the final moments and decreased error in the product branching ratio. We can explain the trend in F_{R} by noting that for the (1.10, 0) and (1.02, 0) sets of initial conditions, the reaction probability P_{R} for the TFS-(–,–) method is usually less than P_{R} calculated by the TFS-(+,+) method, whereas the total nonadiabatic probability P_{N} is relatively unchanged. The upper electronic state in the reactive arrangement is energetically inaccessible, leading to a large number of trajectories that experience energy forbidden hops as they are exiting in this arrangement. In the TFS-(+,+) method,

these frustrated hops are ignored, and the trajectories finish in the reactive arrangement. In the TFS-(–,–) method, trajectories with frustrated hopping attempts in this region are reflected in the direction of **d**, which has a large component parallel to the reactive channel. This causes some trajectories to be reflected back into the interaction region, lowering the value of P_R for the TFS-(–,–) method. For the (1.10, 6) set of initial conditions, the increased energy in the rotational modes leads to an increased number of momentum-forbidden hops in the quenching product arrangement. These trajectories are reflected back into the interaction region in the TFS-(–,–) method, lowering the value of P_Q relative to the TFS-(+,+) method. For all three sets of initial conditions, reflection of trajectories with frustrated hops back into the interaction region improves the agreement of the semiclassical value of F_R with the quantum mechanical result. However, the reflection along **d** also leads to increased errors in the final moments.

It is reasonable, therefore, to consider methods that combine the "+" and the "–" protocols, such as the TFS-(–,+) method. We have previously mentioned, however, that energy-forbidden and momentum-forbidden hops should be treated consistently. Our results indicate that the TFS-(–,+) method is not the best strategy for combining the two reflection protocols, and it leads to less accurate final moments and the product branching ratios than either the TFS-(+,+) method or the TFS-(–,–) method. It should also be noted that the **d** direction may not be the best direction in which to reflect the nuclear momentum during a frustrated hopping attempt when applying the "–" protocol.

We can draw a similar conclusion about the TFS-(R,+) method. The TFS-(R,+) method predicts the best values for the total nonadiabatic probability P_N. We can explain this for the YRH systems, by observing that the quantum mechanical data lie between the TFS-(–,+) and the TFS-AFH data, as shown in Fig. 3. The TFS-(R,+) method allows a subset of frustrated trajectories (namely those trajectories with momentum-frustrated hops) to occur, improving the agreement of the semiclassical value of P_N with the quantum mechanical result. We note, however, that because the probability of hopping to the ground state twice is small, the trajectories that hop to the upper electronic state using the rotated **d** vector do not significantly affect the final reaction or quenching moments. In other systems where multiple hopping trajectories are important, the rotated hopping

vector has a larger effect on the final moments, as observed in a previous study[12] and in the present study for the rotational moments of the more strongly coupled MXH systems.

Although it would be desirable for Tables 3–5 to show a clearly superior method, it is evident that a semiclassical method that successfully solves the problem of classically forbidden hops must be more sophisticated than the simple methods tested in this paper. We can, however, use the results of the present systematic study to suggest several important features that a method likely must have in order to successfully treat frustrated hops: 1) Some, but not all, frustrated trajectories should be reflected. 2) Some, but not all, frustrated hops should somehow be allowed to hop to the upper electronic state. 3) The criterion for reflection and the criterion for allowing classically forbidden hops should not be based on the partition of energy in modes orthogonal to **d**, i.e., energy-forbidden and momentum-forbidden hops should be treated consistently. 4) The use of symmetrized speed or coupling functions in the expression for the hopping probability systematically leads to increased reaction and quenching probabilities and thereby to worse agreement with accurate calculations; hence these methods are not recommended.

The choice of "best method" depends on the observable of interest, specifically: the TFS-(+,+) method performs best when calculating the final vibrational and rotational moments, the TFS-(–,–) method gives the best value for the reactive/nonreactive branching ratio F_R, and the TFS-(R,+) method gives the best electronically nonadiabatic transition probabilities. Although there is no method that is the best method for all observables, we see from Table 5 that, averaged over all observables, the TFS-(+,+) method is the most accurate of the semiclassical methods for modeling weakly coupled systems, where classically forbidden hops are a serious problem.

VII. Conclusions

We have presented fully converged quantum mechanical scattering calculations for four weakly coupled three-atom, two-state systems. The systems are fully three-dimensional and realistic. The systems are specifically designed to be weakly coupled systems where the frustrated hopping problem is most serious; if one is to make a

recommendation about the best way to treat frustrated hopping, it is most appropriate to make that decision on the basis of studying systems where the various choices have the most significant impact on the results, i.e., systems where classically forbidden hops are an essential part of the problem.

We tested the TFS (Tully's fewest-switches) surface hopping method with three different sets of initial conditions for each of the four YRH PEMs, as well as with one set of initial conditions for a more strongly coupled set of three MXH PEMs. We have shown that for weakly coupled systems, the TFS method systematically over-estimates the reaction and quenching probabilities due to the frequent occurrence of classically forbidden hopping attempts. We have explored several variants of the TFS method which differ in their treatment of frustrated hopping and have shown that the treatment of frustrated hopping has a large effect on the final nonadiabatic transition probabilities and the final vibrational and rotational moments. The effect of frustrated hops was shown here to be critically important for the correct treatment of systems with weakly coupled electronic states, and we know from previous work[12,14] and additional studies presented here that the treatment of frustrated hops is also significant for more strongly coupled systems.

The TFS-(R,+) method is shown to predict the best total nonadiabatic probabilities. The TFS-(+,+) scheme, which ignores all types of frustrated hops, predicts the best final vibrational and rotational moments, and the TFS-(–,–) method predicts the best product branching ratios. Averaged over all observables, the TFS-(+,+) method is the best of the semiclassical methods tested here. Although there is no method that completely solves the problem of classically frustrated hops, we have motivated the search for a more sophisticated protocol for the treatment of frustrated hops, and we have inferred several features that a successful method is likely to have.

We also tested eight symmetrized velocity and coupling methods. These methods were shown to be extremely ill suited for modeling the dynamics of weakly coupled systems when the coupling contributions from both surfaces were weighted equally. Weighting using the electronic state populations significantly increased the accuracy of the method, and the results of the best symmetrized method are only slightly less

accurate, on the average, as those obtained using the best non-symmetrized coupling method. However, the symmetrized methods are specialized to the adiabatic representation, systematically increase the nonadiabatic transition probabilities, and can cause numerical difficulties in their implementation.

Although, a major goal of this work was the comparison of various strategies for dealing with the frustrated hopping problem, we should not lose sight (in considering *relative* accuracy of the methods) of an important conclusion about *absolute* accuracy of multidimensional semiclassical methods in general for weakly coupled systems. This is the most extensive test ever carried out (superceding Ref. 13) for weakly coupled multidimensional semiclassical nonadiabatic methods for three-body collisions in full three-dimensional space, featuring new quantum mechanical results and over twelve million trajectories. The accurate quantal values of the probability P_{N} of a nonadiabatic event (averaged over energy intervals of 0.06 eV) range from 3×10^{-5} to 1×10^{-1}, or, on a logarithmic scale, $\log_{10}P_N$ ranges from –4.5 to –1.0. And yet the five semiclassical methods that were applied to all twelve cases have mean unsigned errors in $\log_{10}P_N$ that range from 0.09 to 0.15 (corresponding to typical errors of only about 30%). Thus, semiclassical methods are remarkably accurate even in these highly nonclassical weakly coupled systems. This provides strong confirmation of the value of past detailed studies of these methods, and it also validates their use for applications. Furthermore it motivates the continuing search for further refining these methods so that other aspects of the results, for example, the probabilities of nonadiabatic reaction, may become equally accurate.

Acknowledgments

This work was supported in part by the National Science Foundation under grants nos. CHE97–25965 and CHE00-92019. Mike Hack contributed to this chapter.

Appendix: Ehrenfest Method

Although this paper is primarily concerned with studying the treatment of frustrated hopping in trajectory surface hopping calculations, we also tested the

semiclassical Ehrenfest method[39,40] for all four YRH systems and all three sets of initial conditions, for a total of twelve cases. In the semiclassical Ehrenfest method, trajectories are propagated on a mixed potential energy surface which is a linear combination of the adiabatic surfaces weighted by the quantum mechanical state populations. The semiclassical Ehrenfest method predicts no reaction because mixing in even a small amount of the upper surface prohibits the system from reaching the product. However, we can still test the method for P_{Q}, $< v'' >$, $< j'' >$, and P_{N}.

Semiclassical Ehrenfest (SE) trajectories finish the simulation in a mixed stated in the Y + RH arrangement. The final state electronic state populations n_1 and n_2 are used to assign electronic probability density to the upper and lower surfaces. Here we test three different methods for assigning the electronic probability. In the SE-H method, the trajectory is assigned to the closest electronic surface. For the YRH(0.20) system, a small set of trajectories finish with a $n_1 > 0.5$. For the other PEMs, the SE-H method predicts zero quenching probability. The SE-LSS method assigns a weight of n_1 to the quenching probability. This method has errors comparable to the TFS methods for the quenching and total nonadiabatic probabilities and the final moments. The SE-QSS method assigns a weight of n_1^2 to the quenching probability if $n_1 < n_2$ (which is usually the case) and a weight of $1-n_2^2$ if $n_1 > n_2$. The results of the SE-QSS method are intermediate of the SE-LSS and the SE-H methods. Table 6 gives MUEs of the semiclassical Ehrenfest methods.

References

1 E. E. Nikitin, Annu. Rev. Phys. Chem. **50**, 1 (1999).

2 E. E. Nikitin, and S. Ya. Umanski, *Theory of Slow Atomic Collisions* (Springer-Verlag, Berlin, 1984).

3 E. A. Gislason, G. Parlant, and M. Sizun, *Adv. Chem. Phys.* **82**, 321 (1992).

4 H. Nakamura, Adv. Chem. Phys. **82**, 243 (1992).

5 H. Nakamura, in *Dynamics of Molecules and Chemical Reactions*, edited by R. E. Wyatt and J. Z. H. Zhang (Marcel Dekker, New York, 1996), p. 473.

6 J. C. Tully, in *Modern Methods for Multidimensional Dynamics Computations in Chemistry*, edited by D. C. Thompson (World Scientific, Singapore, 1998), pp. 34, 72.

7 M. D. Hack, and D. G. Truhlar, J. Phys. Chem. A **104**, 7917 (2000).

8 S. L. Mielke, G. J. Tawa, D. G. Truhlar, and D. W. Schwenke, Chem. Phys. Lett. **234**, 57 (1995).

9 M. S. Topaler, M. D. Hack, T. C. Allison, Y.-P. Liu, S. L. Mielke, D. W. Schwenke, and D. G. Truhlar, J. Chem. Phys. **106**, 8699 (1997).

10 M. S. Topaler, T. C. Allison, D. W. Schwenke, and D. G. Truhlar, J. Phys. Chem. A **102**, 1666 (1998).

11 M. S. Topaler, T. C. Allison, D. W. Schwenke, and D. G. Truhlar, J. Chem. Phys. **109**, 3321 (1998).

12 M. D. Hack, A. W. Jasper, Y. L. Volobuev, D. W. Schwenke, and D. G. Truhlar, J. Phys. Chem. A **103**, 6309 (1999).

13 Y. L. Volobuev, M. D. Hack, and D. G. Truhlar, J. Phys. Chem. A **103**, 6225 (1999).

14 M. D. Hack, A. W. Jasper, Y. L. Volobuev, D. W. Schwenke, and D. G. Truhlar, J. Phys. Chem. A **104**, 217 (2000).

15 Y. L. Volobuev, M. D. Hack, M. S. Topaler, and D. G. Truhlar, J. Chem. Phys. **112**, 9716 (2000).

16 M. D. Hack and D. G. Truhlar, J. Chem. Phys. **114**, 2894 (2001).

17 M. D. Hack and D. G. Truhlar, J. Chem. Phys. **114**, 9305 (2001).

18 L. D. Landau, Phys. Z. Sowjet. **2**, 46 (1932). C. Zener, Proc. Roy. Soc. Lond. Ser. A **137**, 696 (1932). E. C. G. Stückelberg, Helv. Phys. Acta **5**, 369 (1932). E. Teller, J. Chem. Phys. **41**, 109 (1937).

19 N. Rosen, and C. Zener, Phys. Rev. **18**, 502 (1932).

20 Yu. N. Demkov, J. Exp. Theor. Phys. (USSR) **45**, 195 (1963) [English translation: Sov. Phys. JETP **18**, 138 (1964)]. Yu. N. Demkov, Dokl. Akad. Nauk SSSR **166**, 1076 (1966) [English translation: Sov. Phys. Dokl. **11**, 138 (1966)].

21 A. Bjerre, and E. E. Nikitin, Chem. Phys. Lett. **1**, 179 (1967).

22 R. K. Preston, and J. C. Tully, J. Chem. Phys. **54**, 4297 (1971). J. C. Tully and R. K. Preston, J. Chem. Phys. **55**, 562 (1971).

23 W. H. Miller, and T. F. George, J. Chem. Phys. **56**, 5637 (1972).

24 J. C. Tully, in *Dynamics of Molecular Collisions*, edited by W. H. Miller (Plenum, New York, 1976), Part B, pp. 217–267.

25 D. G. Truhlar, and J. T. Muckerman, in *Atom-Molecule Collision Theory*, edited by R. B. Bernstein (Plenum, New York, 1979), pp. 505–594.

26 P. J. Kuntz, J. Kendrick, and W. N. Whitton, Chem. Phys. **38**, 147 (1979). G. Parlant and E. A. Gislason, J. Chem. Phys. **91**, 4416 (1989).

27 N. C. Blais, and D. G. Truhlar, J. Chem. Phys. **79**, 1334 (1983).

28 M. F. Herman, J. Chem. Phys. **81**, 754 (1984).

29 N. C. Blais, D. G. Truhlar, and C. A. Mead, J. Chem. Phys. **89**, 6204 (1988).

30 J. C. Tully, J. Chem. Phys. **93**, 1061 (1990).

31 P. J. Kuntz, J. Chem. Phys. **95**, 141 (1991).

32 S. Chapman, Adv. Chem. Phys. **82**, 423 (1992).

33 M. F. Herman, Annu. Rev. Phys. Chem. **45**, 83 (1994).

34 U. Müller, and G. Stock, J. Chem. Phys. **107**, 6230 (1997).

35 J.-Y. Fang, and S. Hammes-Schiffer, J. Phys. Chem. A **103**, 9399 (1999).

36 J.-Y. Fang, and S. Hammes-Schiffer, J. Chem. Phys. **110**, 11166 (1999).

37 D. F. Coker, and L. Xiao, J. Chem. Phys. **102**, 496 (1995).

38 See endnote 39 in S. Hammes-Schiffer, and J. C. Tully, J. Chem. Phys. **101**, 4657 (1994).

39 C. Zhu, K. Nobusada, and H. Nakamura, J. Chem. Phys. **115**, 3031 (2001).

40 H.-D. Meyer, and W. H. Miller, J. Chem. Phys. **70**, 3214 (1979).

41 A. García-Vela, R. B. Gerber, and D. G. Imre, J. Chem. Phys. **97**, 7242 (1992).

42 See EPAPS Document No. E-JCPSA6-115-033125 for supporting information including: the functional form of the YRH model surfaces, the parameters of the quantum mechanical basis sets, the energy dependence of the quantum mechanical results, and the detailed results of the semiclassical trajectory calculations. This document may be retrieved via the EPAPS homepage (http://www.aip.org/pubservs/epaps.html) or from ftp.aip.org in the directory /epaps/. See the EPAPS homepage for more information.

43 Y. Sun, D. J. Kouri, D. G. Truhlar, and D. W. Schwenke, Phys. Rev. A **41**, 4857 (1990).

44 D. W. Schwenke, S. L. Mielke, and D. G. Truhlar, Theor. Chim. Acta **79**, 241 (1991).

45 G. J. Tawa, S. L. Mielke, D. G. Truhlar, and D. W. Schwenke, J. Chem. Phys. **100**, 5751 (1994).

46 G. J. Tawa, S. L. Mielke, D. G. Truhlar, and D. W. Schwenke, in *Advances in Molecular Vibrations and Collisional Dynamics*, edited by J. M. Bowman (JAI, Greenwich, CT, 1994), Vol. 2B, pp. 45–116.

47 D. W. Schwenke, Y. L. Volobuev, S. L. Mielke, G. J. Tawa, D. C. Chatfield, Y. Sun, K. Haug, T. C. Allison, R. S. Friedman, M. Zhao, P. Halvick, M. D. Hack, and D. G. Truhlar, VP–version 18.8, University of Minnesota, Minneapolis, 1999.

48 D. G. Truhlar, J. Abdallah Jr., and R. L. Smith, Adv. Chem. Phys. **25**, 211 (1974).

49 D. W. Schwenke, K. Haug, M. Zhao, D. G. Truhlar, Y. Sun, J. Z. H. Zhang, and D. J. Kouri, J. Phys. Chem. **92**, 3202 (1988).

50 M. S. Topaler, M. D. Hack, Y. L. Volobuev, A. W. Jasper, T. C. Allison, T. F. Miller III, Y.-P. Liu, N. C. Blais, and D. G. Truhlar, NAT–version 6.0, University of Minnesota, Minneapolis, 2000.

51 D. G. Truhlar, B. P. Reid, D. E. Zurawski, and J. C. Gray, J. Phys. Chem. **85**, 7861 (1981).

Table 1. Reaction, quenching and total nonadiabatic transition probabilities, final vibrational and rotational moments, and product branching ratios for the YRH(0.20) system and the (1.10, 0) initial conditions.

Method	P_R	$<v'>$	$<j'>$	P_Q	$<v''>$	$<j''>$	F_R	P_N
Quantum[a]	0.010	0.83	12.4	0.047	0.90	3.35	0.176	0.057
Average quantum[b]	0.012	0.93	12.1	0.045	0.90	3.30	0.213	0.057
TFS-(–,+)	0.034	0.77	13.1	0.068	0.47	5.57	0.333	0.102
TFS-AFH	0.007	0.81	13.9	0.020	0.35	7.92	0.256	0.027
TFS-(+,+)	0.035	0.90	12.7	0.066	0.65	5.12	0.349	0.101
TFS-(–,–)	0.027	0.81	12.7	0.073	0.45	5.77	0.272	0.101
TFS-(R,+)	0.020	0.84	13.5	0.035	0.56	5.95	0.361	0.055
GS(½)≡MDQT*	0.057	0.85	13.1	0.109	0.62	5.67	0.342	0.166
GC(½)	0.097	0.95	12.3	0.165	0.66	5.41	0.369	0.262
AS(½)	0.133	0.97	12.2	0.234	0.66	5.22	0.362	0.367
AC(½)	0.062	0.86	13.0	0.116	0.65	5.14	0.349	0.178
GS(n_χ)	0.038	0.87	12.8	0.067	0.62	5.74	0.359	0.105
GC(n_χ)	0.040	0.89	12.8	0.075	0.63	5.61	0.346	0.115
AS(n_χ)	0.040	0.86	12.9	0.070	0.59	6.03	0.364	0.110
AC(n_χ)	0.035	0.85	13.0	0.063	0.59	5.90	0.360	0.098
TFS-(–,+)-di	0.331	0.54	12.5	0.269	0.40	5.50	0.552	0.600
TFS-AFH-di	0.001	1.00	14.0	0.015	0.14	5.26	0.075	0.016

[a]Quantum mechanical result for the scattering energy 1.10 eV.

[b]Average of seven quantum mechanical calculations performed at the following scattering energies: 1.07, 1.08, 1.09, 1.10, 1.11, 1.12 and 1.13 eV.

Table 2. Unsigned errors in the semiclassical methods for the YRH(0.20) system and the (1.10,0) initial conditions.[a]

Method	$\log_{10}P_R$	$<v'>$	$<j'>$	$\log_{10}P_Q$	$<v''>$	$<j''>$	F_R	$\log_{10}P_N$	Overall[b]
TFS-(–,+)	0.45	0.16	0.99	0.18	0.43	2.27	0.12	0.25	0.62
TFS-(+,+)	0.46	**0.04**	0.66	0.16	**0.25**	**1.81**	0.14	0.24	**0.44**
TFS-(–,–)	0.35	0.12	0.61	0.21	0.45	2.47	**0.06**	0.24	0.52
TFS-(R,+)	**0.21**	0.10	1.44	**0.11**	0.34	2.64	0.15	**0.02**	0.54
GS(½)≡MDQT*	0.67	0.08	1.01	0.38	0.28	2.37	0.13	0.46	0.64
GC(½)	0.90	**0.01**	**0.22**	0.56	**0.24**	2.11	0.16	0.66	0.61
AS(½)	0.71	0.08	0.95	0.41	**0.25**	**1.84**	0.14	0.49	0.64
AC(½)	1.04	**0.03**	**0.07**	0.71	**0.24**	**1.91**	0.15	0.81	0.68
GS(n_χ)	0.49	0.06	0.71	0.17	0.28	2.44	0.15	0.26	0.50
GC(n_χ)	0.51	0.05	0.75	0.22	0.27	2.30	0.13	0.30	0.50
AS(n_χ)	0.46	0.08	0.87	0.14	0.31	2.60	0.15	0.23	0.53
AC(n_χ)	0.52	0.07	0.81	0.19	0.31	2.73	0.15	0.28	0.55
TFS-(–,+)-di	1.43	0.40	0.40	0.77	0.50	2.20	0.34	1.02	1.28

[a]Numbers in bold indicate the method with the lowest error for each column. See text for a complete discussion.

[b]To obtain the overall mean error, each column was normalized to have a mean value of 0.62, which is the average value of all unsigned errors in the table. Then the eight columns for a given method were averaged.

Table 3. Mean unsigned errors in the semiclassical methods averaged over 12 YRH cases and 3 MXH cases.[a]

System	Method	$\log_{10}P_R$	$<v'>$	$<j'>$	$\log_{10}P_Q$	$<v''>$	$<j''>$	F_R	$\log_{10}P_N$	Overall[b]
YRH[c]	TFS-(–,+)	0.36	0.25	**1.4**	**0.11**	0.36	2.2	0.11	0.13	0.59
	TFS-(+,+)	0.36	**0.15**	**1.3**	**0.10**	**0.22**	**1.9**	0.11	0.11	**0.47**
	TFS-(–,–)	**0.29**	0.25	**1.4**	**0.13**	0.38	2.2	**0.07**	0.13	**0.58**
	TFS-(R,+)	**0.30**	**0.15**	**1.5**	**0.13**	**0.25**	**2.1**	0.13	**0.09**	**0.51**
	GC(n_χ)	0.37	**0.18**	**1.5**	**0.13**	**0.23**	**2.1**	0.11	0.15	**0.54**
MXH[d]	TFS-(–,+)	0.37	**0.06**	**1.2**	0.09	**0.06**	0.43	0.23	0.16	**0.37**
	TFS-(+,+)	0.37	**0.07**	**1.1**	**0.06**	**0.06**	0.39	0.23	0.16	**0.35**
	TFS-(–,–)	**0.32**	**0.08**	**1.3**	0.10	**0.07**	0.50	**0.18**	0.15	**0.36**
	TFS-(R,+)	0.37	**0.06**	1.3	0.16	**0.05**	0.60	0.27	**0.12**	0.42
	GC(n_χ)	0.37	**0.07**	**1.2**	0.13	**0.06**	**0.27**	0.20	0.20	**0.40**

[a]Numbers in bold indicate the method with the lowest error for each column. See text for a complete discussion.

[b]To obtain the overall mean error, each column was normalized to have a mean value of 0.46, which is the average value of all unsigned errors in the table. Then the eight columns for a given method were averaged.

[c]Average of the 12 unsigned errors from all four YRH PEMs (0.20, 0.10, 0.03, and 0.01) at all three sets of initial conditions.

[d]Average unsigned error from the three MXH PEMs (SB, SL and WL) at the (1.10, 0) set of initial conditions.

Table 4. Scorecard for the semiclassical methods summed over twelve YRH cases (four potential energy matrices and three sets of initial conditions) and three MHX cases (three potential energy matrices and one set of initial conditions).

System	Method	$\log_{10}P_R$	$<v'>$	$<j'>$	$\log_{10}P_Q$	$<v''>$	$<j''>$	F_R	$\log_{10}P_N$	Probabilities[a]	Moments[b]
YRH[c]	TFS-(–,+)	3	4	7	6	1	2	2	4	15	14
	TFS-(+,+)	1	**9**	**11**	6	**8**	**8**	0	7	14	**36**
	TFS-(–,–)	5	4	8	2	0	3	**9**	6	22	15
	TFS-(R,+)	**9**	**9**	7	**8**	5	5	0	**8**	**25**	26
	GC(n_χ)	3	**9**	8	5	5	3	3	4	15	25
MXH[d]	TFS-(–,+)	0	**3**	**2**	0	1	1	0	0	0	**7**
	TFS-(+,+)	0	2	**2**	**2**	**2**	1	0	0	2	**7**
	TFS-(–,–)	**2**	2	1	0	1	0	**2**	0	**4**	4
	TFS-(R,+)	0	**3**	0	0	1	0	0	**3**	3	4
	GC(n_χ)	1	2	1	1	1	**3**	**2**	0	**4**	**7**

[a]Sum of the four probabilities columns.

[b]Sum of four moments columns.

[c]Twelve cases: four YRH PEMs (0.20, 0.10, 0.03, and 0.01) at three sets of initial conditions.

[d]Three cases: MXH PEMs (SB, SL and WL) at the (1.10, 0) set of initial conditions.

Table 5. Overall summary including both YRH and MXH systems

	Points[a]	Normalized mean unsigned error[b]
Probabilities		
TFS-(–,+)	3.8	0.46
TFS-(+,+)	5.5	0.43
TFS-(–,–)	9.5	0.42
TFS-(R,+)	9.2	0.48
GC(n_χ)	7.8	0.51
Moments		
TFS-(–,+)	10.5	0.50
TFS-(+,+)	16.0	0.39
TFS-(–,–)	7.8	0.52
TFS-(R,+)	10.5	0.45
GC(n_χ)	13.2	0.43
Probabilities and moments		
TFS-(–,+)	14.3	0.48
TFS-(+,+)	21.5	0.41
TFS-(–,–)	17.3	0.47
TFS-(R,+)	19.7	0.46
GC(n_χ)	21.0	0.47

[a]From Table 4 with YRH and MXH weighted equally, specifically: ¼ YRH points + MXH points.

[b]First, each column in Table 3 was normalized to have an average value of 0.46. Averages were then computed over the four probabilities, the four moments, or all eight observables with the YRH and MXH surfaces weighted equally.

Table 6. Mean unsigned errors in the semiclassical methods for quenching and nonadiabatic probabilities for the four YRH systems and three sets of initial conditions (12 cases).

Method	$\log_{10}P_Q$	$<v''>$	$<j''>$	$\log_{10}P_N$
TFS-(–,+)	0.11	0.36	2.20	0.13
TFS-(+,+)	0.10	0.22	1.92	0.11
TFS-(–,–)	0.13	0.38	2.19	0.13
TFS-(R,+)	0.13	0.25	2.14	0.09
SE-H[a]	1.12	0.03	1.79	1.21
SE-LSS	0.13	0.86	0.89	0.17
SE-QSS	1.67	0.88	1.29	1.75

[a]The Ehrenfest-Histogram method does not predict any quenching for YRH(0.10), YRH(0.03), or YRH(0.01) at any of the initial conditions. The errors presented here are the average of the three initial conditions for the YRH(0.20) system.

Figure Captions

Figure 1. Values of the diabatic potential energy matrix elements U_{11}, U_{12} and U_{12} plotted as a function of an approximate reaction coordinate for the ground state reaction Y + RH $\rightarrow$ R + YH at a fixed YRH bond angle of 120°. The U_{12} curve shown corresponds to the YRH(0.10) PEM. Also shown are the two scattering energies used in this study, as well as the energies of several asymptotic rovibrational states (χ,v,j), where χ is the electronic quantum number, v is the vibrational quantum number, and j is the rotational quantum number.

Figure 2. Contour plots of the adiabatic energies and the nonadiabatic coupling vector, plotted as functions of the translational Jacobi coordinate S, and the diatomic Jacobi coordinate s, with the Jacobi angle χ = 120°. (a) Lower-energy adiabatic potential energy surface. (b) Higher-energy adiabatic potential energy surface. (c) Magnitude of the nonadiabatic coupling vector |**d**|. (d) Magnitude of the component of **d** that lies in the direction of the diatomic Jacobi coordinate. (e) Magnitude of the component of **d** that lies in the direction of the translational Jacobi coordinate. (f) Magnitude of the component of **d** that lies in the direction of the Jacobi angle. For panels (a) and (b), the lowest energy contours are at 0.2 and 0.8 eV, respectively, and the contour spacing is 0.2 eV. For panels (c), (d), and (f) the contour spacing is 10^{-4} a_0^{-1}. For panel (e), the contour spacing is 10^{-5} a_0^{-1}.

Figure 3. Reaction and quenching probabilities for the four YRH PEMs and for the initial conditions (1.10, 0). The thick line represents the accurate quantum mechanical results. The solid line with symbols and error bars represents the TFS-(–,+) result. The dashed line with symbols and error bars represents the TFS-AFH result, i.e., the results for absorbing frustrated hops onto the upper surface. Note that both axes are logarithmic.

Figure 1

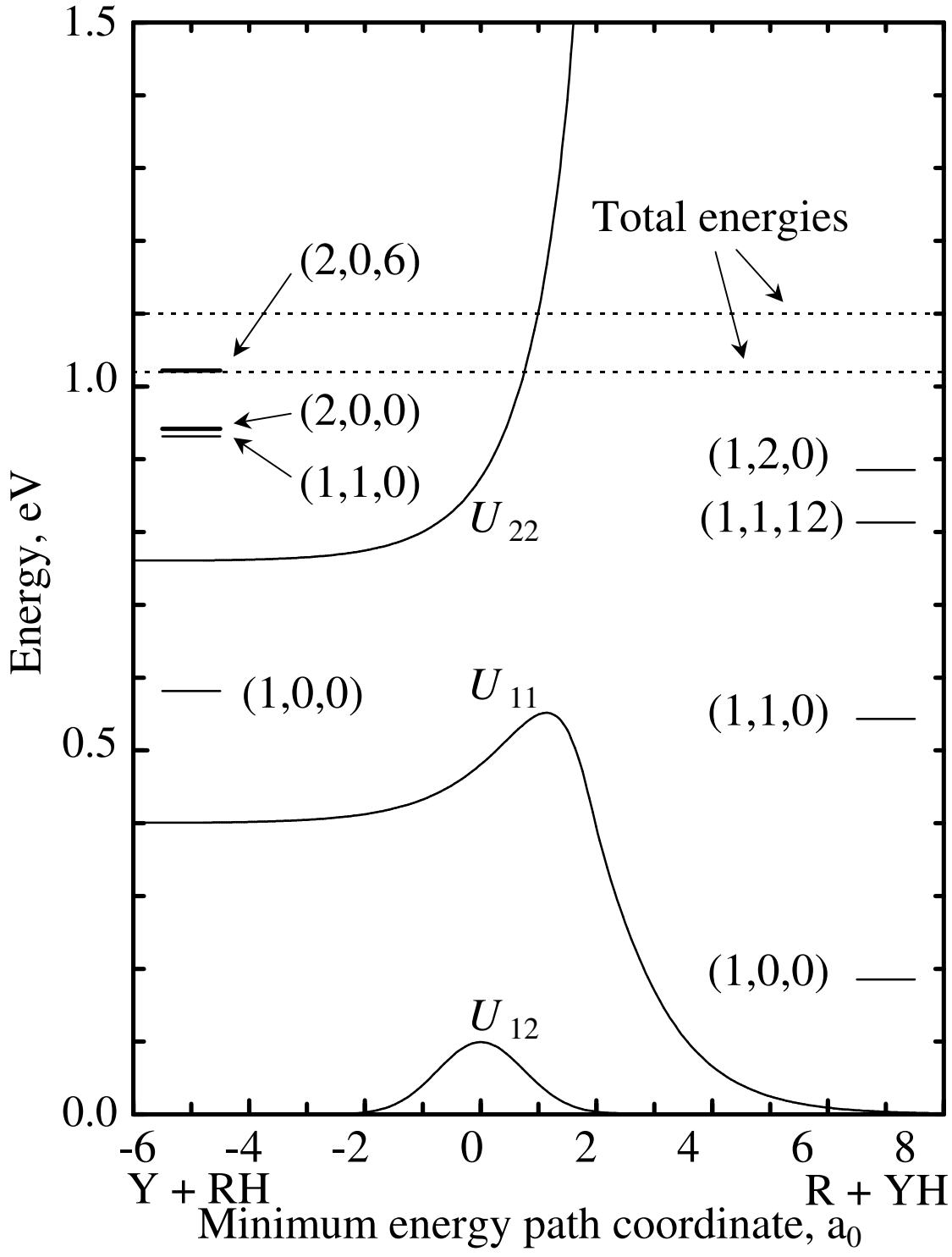
1.5
1.0
0.5
0.0
Energy, eV
Total energies
(2,0,6)
(2,0,0)
(1,1,0)
(1,0,0)
U_{22}
U_{11}
U_{12}
(1,2,0)
(1,1,12)
(1,1,0)
(1,0,0)
-6
-4
-2
0
2
4
6
8
Y + RH
R + YH
Minimum energy path coordinate, a_0

Figure 2

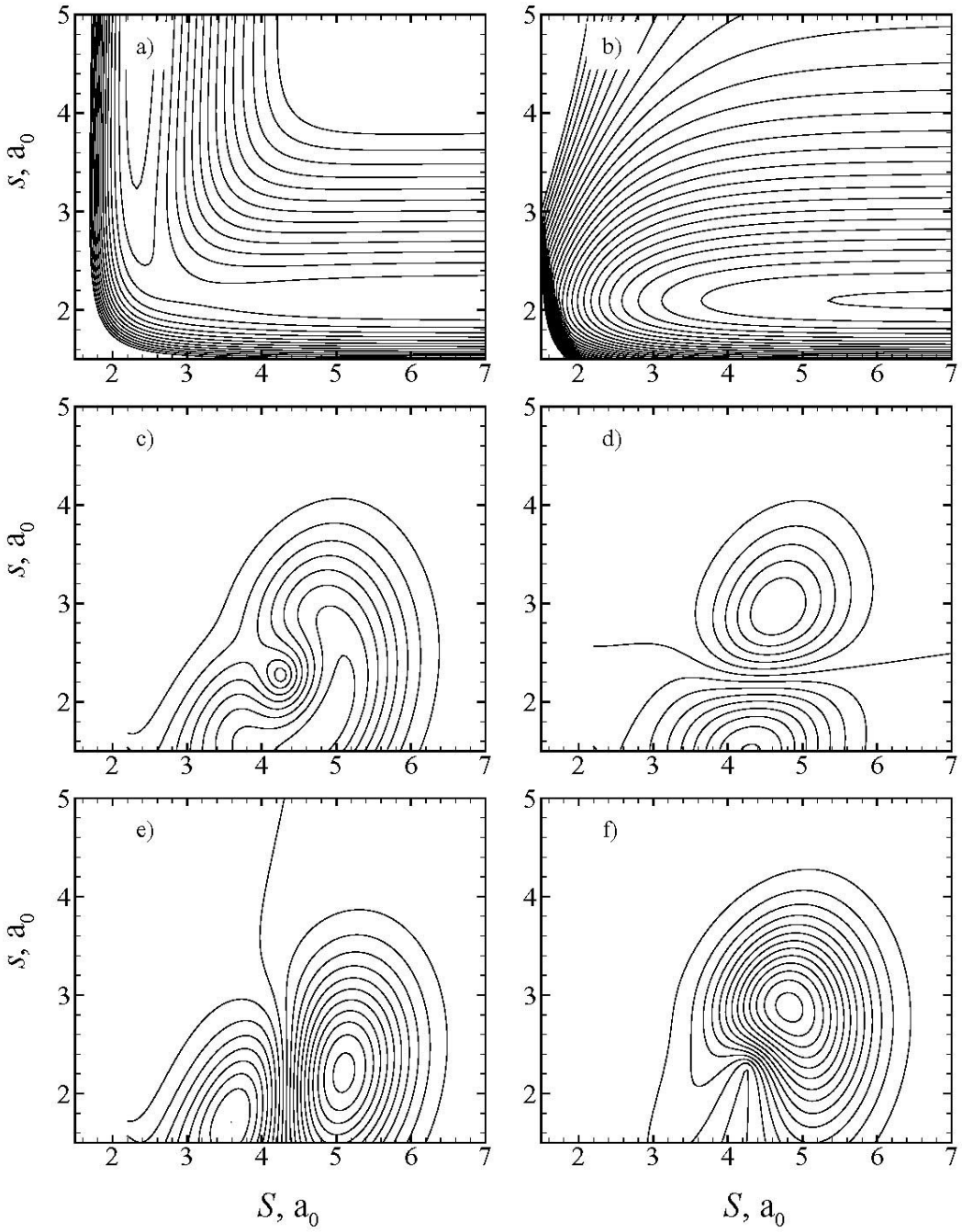

Figure 3

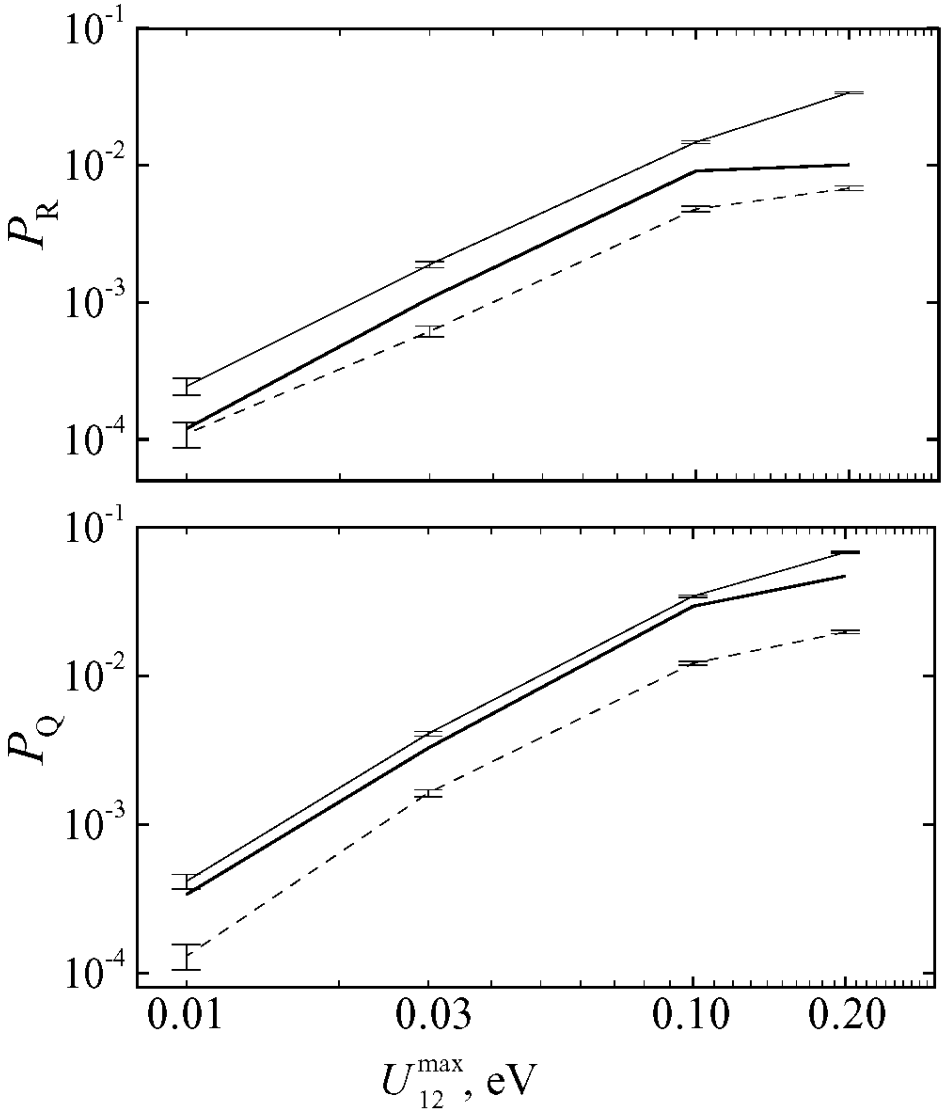

Supporting Information

S.1. Functional Form of the Model YRH Potential Energy Matrices

The model YRH matrices are formulated in the diabatic representation by defining the matrix elements U_{11}, U_{12} and U_{22}. The adiabatic potential energy surfaces and coupling terms can be obtained analytically from the diabatic matrix elements without approximation. The YRH systems are defined to have no electronic angular momentum.

S.1.1. U_{11} Potential Energy Surface

The functional form of $U_{11}(\mathbf{R})$ is an extended LEPS (London-Eyring-Polanyi-Sato) function of the form

$$U_{11}(\mathbf{R}) = Q_{\mathrm{RH}}(R_{\mathrm{RH}}) + Q_{\mathrm{YH}}(R_{\mathrm{YH}}) + Q_{\mathrm{YR}}(R_{\mathrm{YR}}) - \sqrt{\frac{1}{2}\left(W(\mathbf{R}) + c(\mathbf{R})^2\right)} + D_{\mathrm{YH}}, \tag{S-1}$$

where

$$c(\mathbf{R}) = c_a \exp[-c_b W(\mathbf{R}) - c_c (R_{\mathrm{RH}} + R_{\mathrm{YH}} + R_{\mathrm{RY}})], \tag{S-2}$$

$$W(\mathbf{R}) = (J_{\mathrm{RH}}(R_{\mathrm{RH}}) - J_{\mathrm{YH}}(R_{\mathrm{YH}}))^2 + (J_{\mathrm{YH}}(R_{\mathrm{YH}}) - J_{\mathrm{YR}}(R_{\mathrm{YR}}))^2 + (J_{\mathrm{RH}}(R_{\mathrm{RH}}) - J_{\mathrm{YR}}(R_{\mathrm{YR}}))^2, \tag{S-3}$$

and $\mathbf{R}$ is the vector of internuclear distances: R_{YH}, R_{RH}, R_{YR}. The exchange $J_\alpha(R_\alpha)$ and Coulomb $Q_\alpha(R_\alpha)$ integrals are given by

$$Q_\alpha(R_\alpha) = \frac{1}{2}\left(S_\alpha(R_\alpha) + w_\alpha T_\alpha(R_\alpha)\right), \tag{S-4}$$

$$J_\alpha(R_\alpha) = \frac{1}{2}\left(S_\alpha(R_\alpha) - w_\alpha T_\alpha(R_\alpha)\right), \tag{S-5}$$

where α = RH, YH, and YR. The parameters w_α were introduced to decrease the energy of the system in the interaction region. This treatment is identical to introducing Sato parameters directly into eq. (S-1). The singlets $S_\alpha(R_\alpha)$ and triplets $T_\alpha(R_\alpha)$ are Morse and anti-Morse curves, respectively, i.e.,

$$S_\alpha(R_\alpha) = D_\alpha\left[1-\exp\left(-(R_\alpha - R_\alpha^0)\beta_\alpha\right)\right]^2 - D_\alpha, \quad \text{(S-6)}$$

$$T_\alpha(R_\alpha) = \tfrac{1}{2}D_\alpha\left[1+\exp\left(-(R_\alpha - R_\alpha^0)\beta_\alpha\right)\right]^2 - \tfrac{1}{2}D_\alpha. \quad \text{(S-7)}$$

The values of the parameters used in the representation of $U_{11}(\mathbf{R})$ are listed in Table S-1.

S.1.2. U_{22} Potential Energy Surface

The $U_{22}(\mathbf{R})$ potential energy surface is a weighted sum of diatomic terms

$$U_{22}(\mathbf{R}) = S_{\mathrm{RH}}(R_{\mathrm{RH}}) + \left(T_{\mathrm{YR}}(R_{\mathrm{YR}}) + T_{\mathrm{RH}}(R_{\mathrm{RH}})\right)w_2 + E(\mathrm{Y}^*) + D_{\mathrm{YH}}, \quad \text{(S-8)}$$

where $E(\mathrm{Y}^*)$ can be thought of as the electronic excitation energy of the model Y atom and w_2 is a weighting factor that makes U_{22} more energetically accessible towards smaller R_{YR} and R_{RH}. $S_\alpha(R_\alpha)$ and $T_\alpha(R_\alpha)$ are the same singlets and triplets that appear in the definition of $U_{11}(\mathbf{R})$. The values of the parameters introduced for $U_{22}(\mathbf{R})$ are listed in Table S-1.

S.1.3. U_{12} Coupling Surface

The potential coupling surface is a rotated two-dimensional Gaussian in the YH and RH bond lengths

$$U_{12}(R_{\mathrm{YH}}, R_{\mathrm{RH}}) = U_{12}^{\max}\exp\left[-\alpha_x G_x(R_{\mathrm{YH}}, R_{\mathrm{RH}})^2 - \alpha_y G_y(R_{\mathrm{YH}}, R_{\mathrm{RH}})^2\right], \quad \text{(S-9)}$$

where $G_x(R_{\mathrm{YH}},R_{\mathrm{RH}})$ and $G_y(R_{\mathrm{YH}},R_{\mathrm{RH}})$ define the rotated coordinate system

$$G_x(R_{\mathrm{YH}}, R_{\mathrm{RH}}) = \left(R_{\mathrm{RH}} - R_{\mathrm{RH}}^*\right)\cos\theta + \left(R_{\mathrm{YH}} - R_{\mathrm{YH}}^*\right)\sin\theta \quad \text{(S-10)}$$

$$G_y(R_{\mathrm{YH}}, R_{\mathrm{RH}}) = \left(R_{\mathrm{RH}} - R_{\mathrm{RH}}^*\right)\sin\theta - \left(R_{\mathrm{YH}} - R_{\mathrm{YH}}^*\right)\cos\theta. \quad \text{(S-11)}$$

In the preceding set of equations, R_{RH}^* and R_{YH}^* define the location of maximum coupling, and θ is the angle of rotation of the Gaussian axes (G_x, G_y) with respect to the coordinates (R_{RH}, R_{YH}). The Gaussian width parameters are given by α_x and α_y. The values of the parameters used for $U_{12}(R_{\mathrm{YH}},R_{\mathrm{RH}})$ are listed in Table S-1. The parameter

$U_{12}^{\max}$ defines the maximum potential coupling; this parameter is varied to create the family of matrices used in this study.

Note that the electronic matrix elements of the nuclear momentum vector are assumed to be zero in the diabatic representation. Although the nuclear momentum coupling cannot be strictly vanishing everywhere, is can be neglected in the invariant-space approximation, and we use that approximation here.

Table S-1. Model YRH potential energy matrix parameters.

Surface	Parameter	Value		Surface	Parameter	Value	
U_{11}	D_{YH}	4.3	eV		w_{YH}	0.9	
	D_{RH}	3.9	eV		w_{RH}	0.9	
	D_{YR}	0.4	eV		w_{YR}	0.2	
	R^0_{YH}	2.1	a_0	U_{22}	$E(\mathrm{Y}^*)$	0.36	eV
	R^0_{RH}	2.1	a_0		w_2	0.2	
	R^0_{YR}	2.5	a_0	U_{12}	θ	$\pi/4$	rad
	β_{YH}	1.0	a_0^{-1}		α_x	0.8	a_0^{-2}
	β_{RH}	1.0	a_0^{-1}		α_y	1.0	a_0^{-2}
	β_{YR}	1.5	a_0^{-1}		R^*_{RH}	2.2	a_0
	C_a	1.5	eV		R^*_{YH}	4.2	a_0
	C_b	1.0	eV^{-2}		$U_{12}^{\max}$	Variable[a]	
	C_c	0.15	a_0^{-1}				

[a]The value of this parameter is varied to create the four different PEMs that are discussed in this paper. It has the values 0.20, 0.10, 0.03, and 0.01 eV.

Table S-2. OWVP basis set parameters.

Parameter	Set I	Set II	Parameter	Set I	Set II
N^{FD}	13	15	$S_{\mathrm{l}}^{\mathrm{G}}(\alpha=1,\chi=1)$	1.64	1.54
N^{asymp}	12	14	$S_{\mathrm{u}}^{\mathrm{G}}(\alpha=1,\chi=1)$	7.910	8.155
N_1^{QV}	10	12	$\Delta^{S}(\alpha=1,\chi=1)$	0.110	0.105
N_2^{QV}	15	17	$c(\alpha=1,\chi=1)$	0.90	0.95
N_{12}^{QA}	250	270	$m^{\mathrm{g,e}}(\alpha=1,\chi=1)$	58	64
N_1^{QA}	60	70	$N^{\mathrm{o}}(\alpha=1,\chi=1)$	27	27
N_2^{QA}	70	80	$N^{\mathrm{c}}(\alpha=1,\chi=1)$	80	105
N(HO)	80	90	$M^{\mathrm{e}}(\alpha=1,\chi=1)$	4640	6720
$J_{\max}(\alpha=1,\chi=1,v=0)$	28	31	$M^{\mathrm{g}}(\alpha=1,\chi=1)$	1566	1728
$J_{\max}(\alpha=1,\chi=1,v=1)$	25	27	$S_{\mathrm{l}}^{\mathrm{G}}(\alpha=1,\chi=2)$	1.58	1.50
$J_{\max}(\alpha=1,\chi=1,v=2)$	21	24	$S_{\mathrm{u}}^{\mathrm{G}}(\alpha=1,\chi=2)$	8.21	8.50
$J_{\max}(\alpha=1,\chi=1,v=3)$	17	20	$\Delta^{S}(\alpha=1,\chi=2)$	0.130	0.125
$J_{\max}(\alpha=1,\chi=1,v=4)$	11	15	$c(\alpha=1,\chi=2)$	0.90	0.95
$J_{\max}(\alpha=1,\chi=1,v=5)$		9	$m^{\mathrm{g,e}}(\alpha=1,\chi=2)$	52	57
$J_{\max}(\alpha=1,\chi=2,v=0)$	24	27	$N^{\mathrm{o}}(\alpha=1,\chi=2)$	9	9
$J_{\max}(\alpha=1,\chi=2,v=1)$	20	23	$N^{\mathrm{c}}(\alpha=1,\chi=2)$	64	84
$J_{\max}(\alpha=1,\chi=2,v=2)$	16	19	$M^{\mathrm{e}}(\alpha=1,\chi=2)$	3328	4788
$J_{\max}(\alpha=1,\chi=2,v=3)$	9	14	$M^{\mathrm{g}}(\alpha=1,\chi=2)$	468	513
$J_{\max}(\alpha=1,\chi=2,v=4)$		5	$S_{\mathrm{l}}^{\mathrm{G}}(\alpha=2,\chi=1)$	1.64	1.54
$J_{\max}(\alpha=2,\chi=1,v=0)$	33	35	$S_{\mathrm{u}}^{\mathrm{G}}(\alpha=2,\chi=1)$	7.91	8.155
$J_{\max}(\alpha=2,\chi=1,v=1)$	30	32	$\Delta^{S}(\alpha=2,\chi=1)$	0.110	0.105
$J_{\max}(\alpha=2,\chi=1,v=2)$	27	29	$c(\alpha=2,\chi=1)$	0.90	0.95
$J_{\max}(\alpha=2,\chi=1,v=3)$	23	26	$m^{\mathrm{g,e}}(\alpha=2,\chi=1)$	58	64
$J_{\max}(\alpha=2,\chi=1,v=4)$	19	22	$N^{\mathrm{o}}(\alpha=2,\chi=1)$	52	52
$J_{\max}(\alpha=2,\chi=1,v=5)$	13	17	$N^{\mathrm{c}}(\alpha=2,\chi=1)$	102	128
$J_{\max}(\alpha=2,\chi=1,v=6)$	2	12	$M^{\mathrm{e}}(\alpha=2,\chi=1)$	5916	8192

Table S-2(continued). OWVP basis set parameters.

Parameter	Set I	Set II	Parameter	Set I	Set II
S_0^{F}	1.0	0.9	M^{g} ($\alpha = 2$, $\chi = 1$)	3016	3328
$S_{N(\mathrm{F})+1}^{\mathrm{F}}$	20	22	M^{e}	13884	19700
f^{SD}	0.90	0.92	M^{g}	5050	5569
N^{SD}	40	42	M	18934	25269
$S_{\mathrm{l}}^{\mathrm{QR}}$	1.0	0.9	ε_{k}	12	14
$S_{\mathrm{u}}^{\mathrm{QR}}$	15	17	$\varepsilon_{\mathrm{rad}}$	100	120
N^{QS}	170	180	ε_{t}	12	14
N^{QGL}	7	9	ε_{W}	12	14
$N(\mathrm{F})$	1230	1662	ε_{B}	12	14

Table S-3. Quantum mechanical reaction probability, quenching probability and final vibrational and rotational moments as a function of scattering energy for the initial condition Y + RH($v = 0, j = 0$), and centered around 1.10 eV.

System	Energy	P_R	$<v'>$	$<j'>$	P_Q	$<v''>$	$<j''>$
YRH(0.20)	1.07	1.05E-02	1.17	10.9	5.56E-02	0.96	2.88
	1.08	1.27E-02	0.99	11.7	5.44E-02	0.95	2.84
	1.09	1.06E-02	0.86	12.1	5.39E-02	0.92	3.29
	1.10	1.01E-02	0.83	12.4	4.72E-02	0.90	3.35
	1.11	1.36E-02	0.97	12.2	3.82E-02	0.89	3.15
	1.12	1.37E-02	0.90	12.5	3.48E-02	0.84	3.68
	1.13	1.40E-02	0.83	12.9	3.25E-02	0.83	3.95
	Average	1.22E-02	0.93	12.1	4.52E-02	0.90	3.30
YRH(0.10)	1.07	6.98E-03	0.76	12.2	3.85E-02	0.96	1.91
	1.08	8.25E-03	0.81	11.9	3.43E-02	0.95	1.71
	1.09	8.97E-03	0.79	12.0	3.08E-02	0.93	1.60
	1.10	9.12E-03	0.76	12.4	2.95E-02	0.93	1.68
	1.11	9.76E-03	0.80	12.7	2.83E-02	0.93	1.55
	1.12	9.07E-03	0.76	13.1	2.86E-02	0.93	1.62
	1.13	7.67E-03	0.67	13.2	2.98E-02	0.93	1.95
	Average	8.55E-03	0.76	12.5	3.14E-02	0.94	1.72
YRH(0.03)	1.07	7.11E-04	0.93	11.7	2.85E-03	0.97	2.29
	1.08	7.44E-04	0.74	12.5	3.02E-03	0.95	2.62
	1.09	8.68E-04	0.81	12.1	3.24E-03	0.94	3.02
	1.10	1.07E-03	0.86	11.6	3.27E-03	0.93	3.24
	1.11	1.20E-03	0.82	11.9	3.17E-03	0.91	3.44
	1.12	1.20E-03	0.76	12.4	3.11E-03	0.90	3.52
	1.13	1.19E-03	0.76	12.4	3.04E-03	0.90	3.50
	Average	9.98E-04	0.81	12.1	3.10E-03	0.93	3.09
YRH(0.01)	1.07	8.54E-05	1.00	11.4	2.90E-04	0.97	2.24
	1.08	8.58E-05	0.79	12.5	3.04E-04	0.95	2.53
	1.09	9.75E-05	0.85	12.1	3.29E-04	0.93	3.00
	1.10	1.20E-04	0.89	11.6	3.38E-04	0.93	3.28
	1.11	1.32E-04	0.82	11.9	3.35E-04	0.91	3.53
	1.12	1.32E-04	0.77	12.3	3.31E-04	0.90	3.60
	1.13	1.33E-04	0.78	12.4	3.29E-04	0.90	3.59
	Average	1.12E-04	0.84	12.0	3.22E-04	0.93	3.11

Table S-4. Quantum mechanical reaction probability, quenching probability and final vibrational and rotational moments as a function of scattering energy for the initial condition Y + RH($v = 0$, $j = 6$), and centered around 1.10 eV.

System	Energy	P_R	$\langle v' \rangle$	$\langle j' \rangle$	P_Q	$\langle v'' \rangle$	$\langle j'' \rangle$
YRH(0.20)	1.07	2.71E-02	1.06	11.6	7.71E-02	0.96	4.06
	1.08	2.83E-02	1.06	12.3	1.22E-01	0.97	5.35
	1.09	2.73E-02	1.23	11.3	1.32E-01	0.95	5.01
	1.10	2.43E-02	1.20	11.6	1.39E-01	0.96	4.95
	1.11	2.59E-02	1.11	12.4	1.91E-01	0.96	5.83
	1.12	2.27E-02	0.92	12.8	1.74E-01	0.94	5.61
	1.13	2.45E-02	0.91	12.8	1.20E-01	0.95	4.49
	Average	2.57E-02	1.07	12.1	1.37E-01	0.95	5.04
YRH(0.10)	1.07	2.24E-02	1.42	10.0	4.96E-02	0.94	5.04
	1.08	2.47E-02	1.27	10.9	3.48E-02	0.89	6.13
	1.09	2.63E-02	1.15	11.9	4.07E-02	0.84	5.82
	1.10	2.54E-02	1.06	12.5	6.24E-02	0.89	5.19
	1.11	2.44E-02	0.95	13.4	7.99E-02	0.95	5.15
	1.12	2.69E-02	0.91	13.8	9.49E-02	0.95	5.45
	1.13	2.61E-02	0.77	14.2	9.66E-02	0.96	5.01
	Average	2.52E-02	1.08	12.4	6.56E-02	0.92	5.40
YRH(0.03)	1.07	2.20E-03	1.46	10.1	1.61E-02	0.96	4.56
	1.08	2.81E-03	1.41	10.3	1.01E-02	0.92	4.34
	1.09	3.11E-03	1.27	11.4	8.68E-03	0.89	5.26
	1.10	3.41E-03	1.10	12.6	1.16E-02	0.91	5.51
	1.11	3.29E-03	1.02	13.2	1.31E-02	0.94	5.61
	1.12	3.60E-03	0.99	13.5	1.39E-02	0.97	5.85
	1.13	3.98E-03	0.92	13.8	1.51E-02	0.97	5.98
	Average	3.20E-03	1.17	12.1	1.27E-02	0.94	5.30
YRH(0.01)	1.07	2.55E-04	1.46	10.1	1.67E-03	0.95	4.49
	1.08	3.20E-04	1.43	10.2	1.18E-03	0.92	4.45
	1.09	3.55E-04	1.29	11.3	9.74E-04	0.88	5.27
	1.10	3.92E-04	1.11	12.5	1.38E-03	0.91	5.53
	1.11	3.81E-04	1.04	13.1	1.57E-03	0.94	5.60
	1.12	4.15E-04	1.00	13.5	1.66E-03	0.98	5.90
	1.13	4.62E-04	0.93	13.8	1.78E-03	0.97	6.02
	Average	3.69E-04	1.18	12.1	1.46E-03	0.94	5.32

Table S-5. Quantum mechanical reaction probability, quenching probability and final vibrational and rotational moments as a function of scattering energy for the initial condition Y + RH($v = 0, j = 0$), and centered around 1.02 eV.

System	Energy	P_R	$<v'>$	$<j'>$	P_Q	$<v''>$	$<j''>$
YRH(0.20)	0.99	1.19E-02	1.28	8.92	5.85E-02	0.96	2.23
	1.00	4.89E-03	1.52	7.59	3.79E-02	0.98	2.10
	1.01	8.28E-03	1.36	8.60	3.31E-02	0.95	2.91
	1.02	1.18E-02	1.51	8.52	4.23E-02	0.97	3.12
	1.03	1.13E-02	1.28	9.42	3.60E-02	0.93	2.84
	1.04	7.98E-03	1.31	10.0	3.33E-02	0.95	2.53
	1.05	6.28E-03	1.19	11.2	4.43E-02	0.94	3.04
	Average	8.92E-03	1.35	9.18	4.08E-02	0.95	2.68
YRH(0.10)	0.99	3.59E-04	1.59	7.31	2.64E-02	1.00	2.00
	1.00	3.73E-04	1.63	6.45	2.49E-02	1.00	1.86
	1.01	1.09E-03	1.59	6.97	2.70E-02	0.99	1.45
	1.02	1.20E-03	1.38	8.72	2.98E-02	0.99	1.49
	1.03	1.72E-03	1.03	10.7	3.64E-02	0.99	1.79
	1.04	3.12E-03	0.89	11.5	4.17E-02	0.99	1.93
	1.05	4.55E-03	0.84	12.0	4.20E-02	0.98	2.10
	Average	1.77E-03	1.28	9.10	3.26E-02	0.99	1.80
YRH(0.03)	0.99	1.25E-05	1.51	7.67	3.83E-03	1.00	2.55
	1.00	1.90E-05	1.54	7.35	3.93E-03	1.00	2.47
	1.01	7.48E-05	1.60	7.22	4.24E-03	1.00	2.67
	1.02	2.15E-04	1.55	7.88	3.83E-03	0.99	2.78
	1.03	2.94E-04	1.47	8.69	3.67E-03	0.99	2.29
	1.04	5.42E-04	1.44	9.20	2.49E-03	0.98	1.66
	1.05	5.77E-04	1.25	10.5	2.22E-03	0.98	1.77
	Average	2.48E-04	1.48	8.37	3.46E-03	0.99	2.31
YRH(0.01)	0.99	1.23E-06	1.51	7.68	4.31E-04	1.00	2.58
	1.00	1.93E-06	1.52	7.47	4.30E-04	1.00	2.55
	1.01	7.46E-06	1.59	7.32	4.78E-04	1.00	2.72
	1.02	2.37E-05	1.55	7.89	4.42E-04	0.99	2.88
	1.03	3.39E-05	1.47	8.69	4.36E-04	0.99	2.43
	1.04	6.54E-05	1.45	9.13	2.97E-04	0.98	1.76
	1.05	7.12E-05	1.29	10.4	2.30E-04	0.98	1.77
	Average	2.92E-05	1.48	8.37	3.92E-04	0.99	2.38

Table S-6. Reaction and quenching probabilities and vibrational and rotational moments for Y* + RH(0,0), 1.10 eV.[a]

PEM	Method	N_{traj} (thousands)	P_R	$<v'>$	$<j'>$	P_Q	$<v''>$	$<j''>$
YRH(0.20)	Quantum		1.22×10^{-2}	0.93	12.1	4.52×10^{-2}	0.90	3.30
	TFS-(–,+)	100	$(3.40 \pm 0.01) \times 10^{-2}$	0.77 ± 0.01	13.1 ± 0.1	$(6.82 \pm 0.08) \times 10^{-2}$	0.47 ± 0.01	5.57 ± 0.05
	TFS-AFH	100	$(6.81 \pm 0.01) \times 10^{-3}$	0.81 ± 0.03	13.9 ± 0.2	$(1.98 \pm 0.04) \times 10^{-2}$	0.35 ± 0.01	7.92 ± 0.10
	TFS-(+,+)	100	$(3.52 \pm 0.06) \times 10^{-2}$	0.90 ± 0.01	12.7 ± 0.1	$(6.56 \pm 0.08) \times 10^{-2}$	0.65 ± 0.01	5.12 ± 0.06
	TFS-(–,–)	100	$(2.73 \pm 0.05) \times 10^{-2}$	0.81 ± 0.01	12.7 ± 0.1	$(7.32 \pm 0.08) \times 10^{-2}$	0.45 ± 0.01	5.77 ± 0.05
	TFS-(R,+)	100	$(2.00 \pm 0.04) \times 10^{-2}$	0.84 ± 0.02	13.5 ± 0.1	$(3.54 \pm 0.06) \times 10^{-2}$	0.56 ± 0.01	5.95 ± 0.08
	GS(½) ≡ MDQT*	10	$(5.67 \pm 0.23) \times 10^{-2}$	0.85 ± 0.03	13.1 ± 0.2	$(1.09 \pm 0.03) \times 10^{-1}$	0.62 ± 0.01	5.67 ± 0.15
	GC(½)	10	$(9.65 \pm 0.30) \times 10^{-2}$	0.95 ± 0.03	12.3 ± 0.1	$(1.65 \pm 0.04) \times 10^{-1}$	0.66 ± 0.01	5.41 ± 0.12
	AS(½)	10	$(1.33 \pm 0.03) \times 10^{-1}$	0.97 ± 0.02	12.2 ± 0.1	$(2.34 \pm 0.04) \times 10^{-1}$	0.66 ± 0.01	5.22 ± 0.10
	AC(½)	10	$(6.21 \pm 0.24) \times 10^{-2}$	0.86 ± 0.03	13.0 ± 0.2	$(1.16 \pm 0.03) \times 10^{-1}$	0.65 ± 0.01	5.14 ± 0.14
	GS(n_χ)	100	$(3.76 \pm 0.06) \times 10^{-2}$	0.87 ± 0.01	12.8 ± 0.1	$(6.71 \pm 0.08) \times 10^{-2}$	0.62 ± 0.01	5.74 ± 0.06
	GC(n_χ)	100	$(3.97 \pm 0.07) \times 10^{-2}$	0.89 ± 0.01	12.8 ± 0.1	$(7.52 \pm 0.08) \times 10^{-2}$	0.63 ± 0.01	5.61 ± 0.06
	AS(n_χ)	100	$(4.00 \pm 0.06) \times 10^{-2}$	0.86 ± 0.01	12.9 ± 0.1	$(6.98 \pm 0.08) \times 10^{-2}$	0.59 ± 0.01	6.03 ± 0.06
	AC(n_χ)	100	$(3.53 \pm 0.06) \times 10^{-2}$	0.85 ± 0.01	13.0 ± 0.1	$(6.28 \pm 0.08) \times 10^{-2}$	0.59 ± 0.01	5.90 ± 0.06
	TFS-(–,+)-di	5	$(3.31 \pm 0.07) \times 10^{-1}$	0.54 ± 0.02	12.5 ± 0.1	$(2.69 \pm 0.06) \times 10^{-1}$	0.40 ± 0.01	5.50 ± 0.12
	TFS-AFH-di	5	$(1.20 \pm 0.49) \times 10^{-3}$	1.00 ± 0.33	14.0 ± 1.3	$(1.48 \pm 0.17) \times 10^{-2}$	0.14 ± 0.04	5.26 ± 0.44
YRH(0.10)	Quantum		8.55×10^{-3}	0.76	12.5	3.14×10^{-3}	0.94	1.72
	TFS-(–,+)	100	$(1.48 \pm 0.04) \times 10^{-2}$	0.79 ± 0.02	13.0 ± 0.1	$(3.45 \pm 0.06) \times 10^{-2}$	0.47 ± 0.01	5.51 ± 0.07
	TFS-AFH	100	$(4.81 \pm 0.22) \times 10^{-3}$	0.88 ± 0.03	13.2 ± 0.2	$(1.22 \pm 0.03) \times 10^{-2}$	0.38 ± 0.01	7.50 ± 0.12
	TFS-(+,+)	100	$(1.49 \pm 0.04) \times 10^{-2}$	0.89 ± 0.02	12.9 ± 0.1	$(3.22 \pm 0.06) \times 10^{-2}$	0.66 ± 0.01	5.04 ± 0.08
	TFS-(–,–)	100	$(1.27 \pm 0.04) \times 10^{-2}$	0.87 ± 0.02	12.7 ± 0.1	$(3.46 \pm 0.06) \times 10^{-2}$	0.46 ± 0.01	5.71 ± 0.07
	TFS-(R,+)	100	$(1.01 \pm 0.03) \times 10^{-2}$	0.81 ± 0.02	13.5 ± 0.1	$(1.92 \pm 0.04) \times 10^{-2}$	0.53 ± 0.01	6.24 ± 0.11
	GC(n_χ)	100	$(1.62 \pm 0.04) \times 10^{-2}$	0.91 ± 0.02	12.7 ± 0.1	$(3.61 \pm 0.06) \times 10^{-2}$	0.62 ± 0.01	5.51 ± 0.08

Table S-6(continued). Reaction and quenching probabilities and vibrational and rotational moments for Y* + RH(0,0), 1.10 eV.[a]

PEM	Method	N_{traj} (thousands)	P_R	$<v'>$	$<j'>$	P_Q	$<v''>$	$<j''>$
YRH(0.03)	Quantum		9.98×10^{-4}	0.81	12.1	3.10×10^{-3}	0.93	3.09
	TFS-(–,+)	200	$(1.89 \pm 0.10) \times 10^{-3}$	0.82 ± 0.04	13.0 ± 0.2	$(4.09 \pm 0.14) \times 10^{-3}$	0.50 ± 0.02	5.39 ± 0.14
	TFS-AFH	200	$(6.70 \pm 0.58) \times 10^{-4}$	0.97 ± 0.06	12.4 ± 0.3	$(1.60 \pm 0.09) \times 10^{-3}$	0.51 ± 0.03	6.28 ± 0.26
	TFS-(+,+)	200	$(1.95 \pm 0.10) \times 10^{-3}$	0.84 ± 0.04	12.8 ± 0.2	$(4.15 \pm 0.14) \times 10^{-3}$	0.64 ± 0.02	4.98 ± 0.16
	TFS-(–,–)	200	$(1.44 \pm 0.08) \times 10^{-3}$	0.89 ± 0.04	12.6 ± 0.3	$(4.45 \pm 0.15) \times 10^{-3}$	0.49 ± 0.02	5.53 ± 0.14
	TFS-(R,+)	200	$(1.36 \pm 0.08) \times 10^{-3}$	0.84 ± 0.05	13.3 ± 0.3	$(2.38 \pm 0.11) \times 10^{-3}$	0.60 ± 0.02	5.45 ± 0.21
	GC(n_χ)	200	$(2.02 \pm 0.10) \times 10^{-3}$	0.86 ± 0.04	13.2 ± 0.2	$(4.29 \pm 0.15) \times 10^{-3}$	0.67 ± 0.04	4.99 ± 0.15
YRH(0.01)	Quantum		1.12×10^{-4}	0.84	12.0	3.22×10^{-4}	0.93	3.11
	TFS-(–,+)	300	$(2.57 \pm 0.29) \times 10^{-4}$	0.83 ± 0.09	12.6 ± 0.5	$(4.50 \pm 0.39) \times 10^{-4}$	0.56 ± 0.04	4.90 ± 0.35
	TFS-AFH	300	$(1.00 \pm 0.18) \times 10^{-4}$	0.97 ± 0.13	12.4 ± 0.7	$(1.70 \pm 0.24) \times 10^{-4}$	0.51 ± 0.07	5.76 ± 0.65
	TFS-(+,+)	300	$(1.83 \pm 0.25) \times 10^{-4}$	0.87 ± 0.10	12.3 ± 0.6	$(4.40 \pm 0.38) \times 10^{-4}$	0.64 ± 0.04	4.97 ± 0.39
	TFS-(–,–)	300	$(1.73 \pm 0.24) \times 10^{-4}$	0.90 ± 0.11	12.6 ± 0.6	$(5.67 \pm 0.43) \times 10^{-4}$	0.48 ± 0.04	5.49 ± 0.33
	TFS-(R,+)	300	$(1.23 \pm 0.20) \times 10^{-4}$	0.73 ± 0.13	13.1 ± 0.8	$(2.33 \pm 0.28) \times 10^{-4}$	0.66 ± 0.05	4.27 ± 0.45
	GC(n_χ)	300	$(2.43 \pm 0.28) \times 10^{-4}$	0.81 ± 0.08	13.0 ± 0.6	$(5.47 \pm 0.43) \times 10^{-4}$	0.62 ± 0.04	5.15 ± 0.36

[a]The values after the ± sign are the 1σ statistical uncertainties due to the finite number of trajectories.

Table S-7. Reaction and quenching probabilities and vibrational and rotational moments for Y* + RH(0,6), 1.10 eV.

PEM	Method	N_{traj} (thousands)	P_R	$\langle v' \rangle$	$\langle j' \rangle$	P_Q	$\langle v'' \rangle$	$\langle j'' \rangle$
YRH(0.20)	Quantum		2.57×10^{-2}	1.07	12.1	1.37×10^{-1}	0.95	5.04
	TFS-(–,+)	50	$(2.57 \pm 0.07) \times 10^{-2}$	0.81 ± 0.02	12.0 ± 0.1	$(1.74 \pm 0.02) \times 10^{-1}$	0.71 ± 0.00	5.90 ± 0.04
	TFS-AFH	50	$(2.14 \pm 0.21) \times 10^{-3}$	1.33 ± 0.07	11.9 ± 0.4	$(1.20 \pm 0.01) \times 10^{-1}$	0.79 ± 0.01	5.62 ± 0.05
	TFS-(+,+)	50	$(1.58 \pm 0.06) \times 10^{-2}$	0.99 ± 0.03	12.6 ± 0.0	$(1.71 \pm 0.02) \times 10^{-1}$	0.78 ± 0.00	6.03 ± 0.05
	TFS-(–,–)	50	$(2.51 \pm 0.07) \times 10^{-2}$	0.90 ± 0.02	11.7 ± 0.1	$(1.76 \pm 0.02) \times 10^{-1}$	0.70 ± 0.00	5.89 ± 0.04
	TFS-(R,+)	50	$(7.42 \pm 0.38) \times 10^{-3}$	1.13 ± 0.04	12.2 ± 0.3	$(1.37 \pm 0.02) \times 10^{-1}$	0.79 ± 0.00	5.77 ± 0.05
	GC(n_χ)	50	$(1.85 \pm 0.06) \times 10^{-2}$	0.97 ± 0.03	12.8 ± 0.1	$(2.08 \pm 0.02) \times 10^{-1}$	0.78 ± 0.00	6.03 ± 0.04
YRH(0.10)	Quantum		2.52×10^{-2}	1.08	12.4	6.56×10^{-2}	0.92	5.40
	TFS-(–,+)	75	$(1.40 \pm 0.04) \times 10^{-2}$	0.98 ± 0.02	11.8 ± 0.1	$(1.15 \pm 0.01) \times 10^{-1}$	0.77 ± 0.00	6.14 ± 0.04
	TFS-AFH	75	$(2.65 \pm 0.19) \times 10^{-3}$	1.25 ± 0.05	11.9 ± 0.3	$(8.87 \pm 0.10) \times 10^{-2}$	0.82 ± 0.00	5.91 ± 0.05
	TFS-(+,+)	75	$(1.37 \pm 0.04) \times 10^{-2}$	0.98 ± 0.03	12.8 ± 0.1	$(1.14 \pm 0.01) \times 10^{-1}$	0.80 ± 0.00	6.45 ± 0.04
	TFS-(–,–)	75	$(1.44 \pm 0.04) \times 10^{-2}$	0.97 ± 0.02	11.9 ± 0.1	$(1.17 \pm 0.01) \times 10^{-1}$	0.76 ± 0.00	6.02 ± 0.04
	TFS-(R,+)	75	$(6.48 \pm 0.29) \times 10^{-3}$	1.15 ± 0.04	11.9 ± 0.2	$(1.03 \pm 0.01) \times 10^{-1}$	0.82 ± 0.00	6.09 ± 0.04
	GC(n_χ)	75	$(1.56 \pm 0.05) \times 10^{-2}$	1.04 ± 0.02	12.6 ± 0.1	$(1.29 \pm 0.01) \times 10^{-1}$	0.79 ± 0.00	6.57 ± 0.04
YRH(0.03)	Quantum		3.20×10^{-3}	1.17	12.1	12.7×10^{-2}	0.94	5.30
	TFS-(–,+)	100	$(2.33 \pm 0.15) \times 10^{-3}$	1.00 ± 0.05	12.4 ± 0.3	$(1.41 \pm 0.04) \times 10^{-2}$	0.76 ± 0.01	6.72 ± 0.10
	TFS-AFH	100	$(6.30 \pm 0.79) \times 10^{-4}$	1.32 ± 0.09	12.1 ± 0.5	$(1.09 \pm 0.03) \times 10^{-2}$	0.82 ± 0.01	6.64 ± 0.11
	TFS-(+,+)	100	$(2.04 \pm 0.14) \times 10^{-3}$	1.09 ± 0.06	12.9 ± 0.3	$(1.46 \pm 0.04) \times 10^{-2}$	0.78 ± 0.01	7.17 ± 0.10
	TFS-(–,–)	100	$(1.83 \pm 0.14) \times 10^{-3}$	1.08 ± 0.06	12.2 ± 0.4	$(1.44 \pm 0.04) \times 10^{-2}$	0.75 ± 0.01	6.56 ± 0.10
	TFS-(R,+)	100	$(1.44 \pm 0.12) \times 10^{-3}$	1.15 ± 0.06	12.4 ± 0.4	$(1.22 \pm 0.03) \times 10^{-2}$	0.81 ± 0.01	6.65 ± 0.10
	GC(n_χ)	100	$(2.35 \pm 0.15) \times 10^{-3}$	1.12 ± 0.05	12.4 ± 0.3	$(1.40 \pm 0.04) \times 10^{-2}$	0.74 ± 0.01	7.62 ± 0.10
YRH(0.01)	Quantum		3.69×10^{-4}	1.18	12.1	1.46×10^{-3}	0.94	5.32
	TFS-(–,+)	200	$(1.90 \pm 0.31) \times 10^{-4}$	1.03 ± 0.14	12.0 ± 0.9	$(1.75 \pm 0.09) \times 10^{-3}$	0.73 ± 0.02	7.11 ± 0.20
	TFS-AFH	200	$(6.00 \pm 1.73) \times 10^{-5}$	1.17 ± 0.23	12.7 ± 1.4	$(1.40 \pm 0.08) \times 10^{-3}$	0.78 ± 0.02	7.07 ± 0.21
	TFS-(+,+)	200	$(2.30 \pm 0.34) \times 10^{-4}$	1.04 ± 0.12	13.2 ± 0.8	$(1.70 \pm 0.09) \times 10^{-3}$	0.79 ± 0.02	7.29 ± 0.20
	TFS-(–,–)	200	$(2.05 \pm 0.32) \times 10^{-4}$	1.22 ± 0.13	11.2 ± 0.8	$(1.79 \pm 0.09) \times 10^{-3}$	0.73 ± 0.02	6.96 ± 0.20
	TFS-(R,+)	200	$(1.85 \pm 0.30) \times 10^{-4}$	1.14 ± 0.12	11.9 ± 0.7	$(1.33 \pm 0.08) \times 10^{-3}$	0.85 ± 0.02	6.72 ± 0.20
	GC(n_χ)	200	$(2.45 \pm 0.35) \times 10^{-4}$	0.96 ± 0.11	13.9 ± 0.5	$(1.72 \pm 0.09) \times 10^{-3}$	0.74 ± 0.02	7.79 ± 0.21

Table S-8. Reaction and quenching probabilities and vibrational and rotational moments for Y* + RH(0,0), 1.02 eV.

PEM	Method	N_{traj} (thousands)	P_R	$\langle v' \rangle$	$\langle j' \rangle$	P_Q	$\langle v'' \rangle$	$\langle j'' \rangle$
YRH(0.20)	Quantum		8.92×10^{-3}	1.35	9.18	4.08×10^{-2}	0.95	2.68
	TFS-(–,+)	100	$(2.29 \pm 0.05) \times 10^{-2}$	0.87 ± 0.02	11.9 ± 0.1	$(7.60 \pm 0.08) \times 10^{-2}$	0.54 ± 0.01	4.73 ± 0.04
	TFS-AFH	100	$(3.28 \pm 0.18) \times 10^{-3}$	1.05 ± 0.04	11.7 ± 0.2	$(3.11 \pm 0.05) \times 10^{-2}$	0.72 ± 0.01	4.54 ± 0.06
	TFS-(+,+)	100	$(2.24 \pm 0.05) \times 10^{-2}$	1.09 ± 0.02	11.3 ± 0.1	$(7.24 \pm 0.08) \times 10^{-2}$	0.80 ± 0.00	3.82 ± 0.04
	TFS-(–,–)	100	$(1.74 \pm 0.04) \times 10^{-2}$	0.80 ± 0.02	11.8 ± 0.1	$(8.19 \pm 0.09) \times 10^{-2}$	0.53 ± 0.01	4.60 ± 0.04
	TFS-(R,+)	100	$(1.48 \pm 0.04) \times 10^{-2}$	1.02 ± 0.02	11.7 ± 0.1	$(4.53 \pm 0.07) \times 10^{-2}$	0.74 ± 0.01	4.38 ± 0.05
	GC(n_χ)	100	$(2.51 \pm 0.05) \times 10^{-2}$	1.04 ± 0.02	11.5 ± 0.1	$(8.08 \pm 0.09) \times 10^{-2}$	0.80 ± 0.00	4.05 ± 0.04
YRH(0.10)	Quantum		1.77×10^{-3}	1.28	9.10	3.26×10^{-2}	0.99	1.80
	TFS-(–,+)	100	$(8.35 \pm 0.29) \times 10^{-3}$	0.87 ± 0.03	12.0 ± 0.2	$(3.08 \pm 0.05) \times 10^{-2}$	0.51 ± 0.01	4.97 ± 0.06
	TFS-AFH	100	$(2.03 \pm 0.14) \times 10^{-3}$	1.02 ± 0.05	11.8 ± 0.3	$(1.37 \pm 0.04) \times 10^{-2}$	0.63 ± 0.01	5.19 ± 0.09
	TFS-(+,+)	100	$(8.28 \pm 0.29) \times 10^{-3}$	1.03 ± 0.03	11.7 ± 0.2	$(2.97 \pm 0.05) \times 10^{-2}$	0.76 ± 0.01	4.20 ± 0.07
	TFS-(–,–)	100	$(6.70 \pm 0.26) \times 10^{-3}$	0.84 ± 0.03	11.8 ± 0.2	$(3.04 \pm 0.05) \times 10^{-2}$	0.51 ± 0.01	4.76 ± 0.06
	TFS-(R,+)	100	$(5.39 \pm 0.23) \times 10^{-3}$	0.98 ± 0.03	12.0 ± 0.2	$(1.88 \pm 0.04) \times 10^{-2}$	0.68 ± 0.01	4.86 ± 0.08
	GC(n_χ)	100	$(8.96 \pm 0.30) \times 10^{-3}$	1.08 ± 0.03	11.5 ± 0.1	$(3.16 \pm 0.06) \times 10^{-2}$	0.73 ± 0.01	4.53 ± 0.07
YRH(0.03)	Quantum		2.48×10^{-4}	1.48	8.37	3.46×10^{-3}	0.99	2.31
	TFS-(–,+)	200	$(1.05 \pm 0.07) \times 10^{-3}$	0.89 ± 0.05	12.0 ± 0.3	$(3.41 \pm 0.13) \times 10^{-3}$	0.53 ± 0.02	5.17 ± 0.13
	TFS-AFH	200	$(3.05 \pm 0.39) \times 10^{-4}$	0.93 ± 0.09	11.9 ± 0.5	$(1.62 \pm 0.09) \times 10^{-3}$	0.62 ± 0.03	5.28 ± 0.20
	TFS-(+,+)	200	$(8.80 \pm 0.66) \times 10^{-4}$	1.06 ± 0.06	11.7 ± 0.3	$(3.62 \pm 0.13) \times 10^{-3}$	0.70 ± 0.02	4.93 ± 0.14
	TFS-(–,–)	200	$(7.40 \pm 0.61) \times 10^{-4}$	0.85 ± 0.07	12.0 ± 0.3	$(3.84 \pm 0.14) \times 10^{-3}$	0.51 ± 0.02	5.13 ± 0.13
	TFS-(R,+)	200	$(7.25 \pm 0.60) \times 10^{-4}$	1.05 ± 0.06	11.6 ± 0.3	$(2.29 \pm 0.11) \times 10^{-3}$	0.58 ± 0.02	5.57 ± 0.17
	GC(n_χ)	200	$(1.05 \pm 0.07) \times 10^{-3}$	1.01 ± 0.05	11.8 ± 0.3	$(3.61 \pm 0.13) \times 10^{-3}$	0.69 ± 0.02	4.79 ± 0.14
YRH(0.01)	Quantum		2.92×10^{-5}	1.48	8.37	3.92×10^{-4}	0.99	2.38
	TFS-(–,+)	500	$(1.16 \pm 0.15) \times 10^{-4}$	0.83 ± 0.10	12.0 ± 0.5	$(4.16 \pm 0.29) \times 10^{-4}$	0.47 ± 0.03	5.64 ± 0.24
	TFS-AFH	500	$(4.00 \pm 0.89) \times 10^{-5}$	1.25 ± 0.15	10.9 ± 0.9	$(1.96 \pm 0.20) \times 10^{-4}$	0.51 ± 0.05	6.39 ± 0.35
	TFS-(+,+)	500	$(9.00 \pm 2.12) \times 10^{-5}$	1.56 ± 0.14	8.9 ± 0.9	$(4.05 \pm 0.45) \times 10^{-4}$	0.75 ± 0.05	4.41 ± 0.40
	TFS-(–,–)	500	$(8.50 \pm 2.06) \times 10^{-5}$	0.82 ± 0.13	12.7 ± 0.6	$(4.60 \pm 0.48) \times 10^{-4}$	0.39 ± 0.05	5.30 ± 0.36
	TFS-(R,+)	500	$(4.50 \pm 1.50) \times 10^{-5}$	1.22 ± 0.21	11.8 ± 0.9	$(2.25 \pm 0.34) \times 10^{-4}$	0.71 ± 0.07	5.20 ± 0.53
	GC(n_χ)	500	$(1.14 \pm 0.15) \times 10^{-4}$	0.96 ± 0.10	12.3 ± 0.6	$(4.10 \pm 0.29) \times 10^{-4}$	0.75 ± 0.03	4.48 ± 0.26

Table S-9. Reaction and quenching probabilities and vibrational and rotational moments for the MXH systems with the (1.10, 0) initial conditions.[a]

PEM	Method	P_R	$<v'>$	$<j'>$	P_Q	$<v''>$	$<j''>$
MXH(SB)	Quantum[b]	0.15	0.26	7.76	0.32	0.82	3.64
	TFS-(–,+)[b]	0.45	0.26	6.49	0.35	0.73	3.42
	TFS-AFH	0.21	0.25	6.60	0.14	0.97	3.69
	TFS-(+,+)	0.47	0.23	6.74	0.32	0.82	3.36
	TFS-(–,–)	0.35	0.25	6.72	0.42	0.70	3.22
	TFS-(R,+)	0.45	0.24	6.42	0.27	0.88	3.18
	GC(n_χ)	0.53	0.23	6.52	0.37	0.84	3.53
MXH(SL)	Quantum[b]	0.20	0.23	8.11	0.49	0.57	3.56
	TFS-(–,+)[b]	0.53	0.33	6.89	0.35	0.60	3.07
	TFS-AFH	0.37	0.32	7.15	0.13	0.65	2.82
	TFS-(+,+)	0.54	0.32	7.14	0.34	0.56	3.00
	TFS-(–,–)	0.49	0.34	6.77	0.37	0.61	2.98
	TFS-(R,+)	0.53	0.33	6.79	0.38	0.66	2.93
	GC(n_χ)	0.52	0.33	6.69	0.40	0.52	3.23
MXH(WL)	Quantum[b]	0.37	0.28	8.34	0.17	0.49	3.19
	TFS-(–,+)[b]	0.61	0.35	7.21	0.14	0.58	2.68
	TFS-AFH	0.53	0.35	7.33	0.07	0.50	2.80
	TFS-(+,+)	0.57	0.39	6.98	0.17	0.34	2.87
	TFS-(–,–)	0.60	0.39	6.90	0.15	0.53	2.67
	TFS-(R,+)	0.59	0.36	7.01	0.12	0.49	2.47
	GC(n_χ)	0.51	0.38	7.32	0.30	0.37	2.82

[a]The Monte Carlo errors for P_R, P_Q, and $<v'>$ are no greater than 0.01, for $<v''>$ are no greater than 0.02, and for $<j'>$ and $<j''>$ are no greater than 0.2.

[b]The quantum and TFS-(–,+) results are taken from Ref. 15.

Chapter Three

3

Photodissociation of LiFH and NaFH van der Waals Complexes: A Semiclassical Trajectory Study

I. Introduction

There has been recent interest in the transition-state spectroscopy[1,2] of metal-halide "harpooning"[3–8] reactions:

$$\mathrm{M}\cdots\mathrm{HX} \xrightarrow{h\upsilon} \mathrm{MXH}^* \rightarrow \begin{cases} \mathrm{MX} + \mathrm{H} & \text{(R1)} \\ \mathrm{M} + \mathrm{HX}\,, & \text{(R2)} \end{cases}$$

where X is a halogen, M is a metal atom, "⋯" indicates a weak van der Waals interaction, and "*" indicates electronic excitation. These processes provide a means of probing the transition-state of the M* + HX reaction. The excited-state complex (exciplex) that is formed by vertically exciting the system from the van der Waals well is characterized by a relatively deep well in the excited-state (e.g., ~0.5 eV for Na⋯FH[9,10]). The long-lived exciplex may decay by one of two pathways. In the "harpooning" process (R1), the change in the electronic state of the system weakens the HX bond and leads to the formation of MX product. In the competing process (R2), the system relaxes to the ground electronic state by exciting the internal vibrational and rotational modes of HX. In addition, when the excitation energy is high enough, the system may also decay into excited M* and HX.

Here we consider the (R1) and (R2) processes for the cases where M = Li or Na and X = F. Both the potential energy surfaces[9–25] and dynamics[18,22–37] of the ground electronic states of the LiFH and NaFH systems have been widely studied. The coupled potential energy surfaces and coupled-state dynamics of LiFH[19] and NaFH[7,9,10,38] have

also been studied in a more limited sense. The NaFH and LiFH systems are similar in many respects to the coupled-state problem in the well studied LiH_2[39–42] and NaH_2[39,43–50] systems, which may be interpreted to first approximation by the ionic-covalent intersection model of Magee et al.[51] A critical difference though is that LiH_2 and NaH_2 have conical intersections of their adiabatic ground- and excited-state surfaces, whereas LiFH and NaFH have appreciable energy gaps at all geometries.

We have previously presented[38] collinear quantum mechanical wave packet and semiclassical trajectory results for the NaFH system. These results show qualitative disagreement between the semiclassical and quantum calculations, presumably due to the deep quantum nature of the electronic transitions in systems with large adiabatic energy gaps. Our group has recently developed several improved methods[52–54] for simulating processes involving electronic state changes that may be more applicable to large-gap systems. These methods are based on the semiclassical Ehrenfest[55] method and have the desirable feature that trajectories decohere to a single electronic state in the absence of electronic-state coupling. One of these new methods, namely the natural decay of mixing[54] (NDM) algorithm, is general enough to treat photodissociation, and we will apply this method to the photodissociation of Li···FH and Na···FH in the present paper. For comparison we also consider the fewest-switches[56] surface-hopping[56–70] scheme suggested by Tully.

In this article we report fully three-dimensional semiclassical dynamics calculations in which we modeled the photodissociation of the LiFH and NaFH systems using the NDM self-consistent potential method and Tully's fewest-switches (TFS) surface-hopping method. Both methods may be formulated in terms of the adiabatic or the diabatic representations. It has been suggested[70] that the adiabatic representation should always be preferred, although we have found that in some cases more accurate results are obtained using the diabatic electronic states.[71] In the present work, we find that surface-hopping is more sensitive to the choice of electronic representation than the NDM method. The results of the NDM and TFS methods agree with each other only qualitatively, and we discuss the differences in terms of the problem of frustrated

hopping[69,72] that plagues most TFS calculations. The dynamics of LiFH is also compared to that of NaFH and interpreted in terms of the features of the LiFH and NaFH coupled potential energy surfaces.

The calculations on NaFH employ an improved version of a set of coupled potential energy surfaces presented previously,[10] and the calculations on LiFH employ a new set of coupled potential energy surfaces described briefly in Sec. II.A. Section II.B presents the improved potential energy surfaces for NaFH. Section III presents the dynamics calculations. Sections IV and V contain the results and discussion, and Sec. V gives a brief summary.

II. LiFH and NaFH Potential Energy Surfaces

II.A. LiFH Potential Energy Surfaces

We have performed high-level *ab initio* calculations for the two lowest-energy adiabatic states of LiFH. The electronic structure calculations used in the present work are a subset of the calculations that will be presented in more detail in a future publication.[73] For the present work, more than 4000 calculations were performed over a dense grid of nuclear geometries using the MRDCI variant of the multireference configuration interaction method.[74–76] Specifically, the HF internuclear distance was varied from 1.2 – 7.0 bohr, and the LiF internuclear distance was varied from 2.0 to 15 bohr. This two-dimensional grid was repeated at five Li-F-H bond angles: 45, 70, 90, 110, and 179.99°. Additional points were calculated for other Li-F-H angles including 0.01, 130 and 150° The resulting dense grid of adiabatic energies was used to develop a coupled set of analytic potential energy surfaces for the two lowest-energy electronic states, as discussed next.

Coupled potential energy surfaces may be expressed in either the adiabatic or the diabatic representation. We fit the LiFH surfaces in the diabatic (more precisely, quasidiabatic[77–89]) representation, because the coupling between quasidiabatic states is scalar, whereas the coupling between adiabatic states is a vector quantity and hence requires more analytic functions to represent. The quasidiabatic surfaces have the additional advantage that they are typically smoother functions of geometry than the

adiabatic surfaces, and therefore require less complicated functional forms. The quasidiabatic potential energy matrix **U** consists of the potential energy surfaces U_{11} and U_{22} and their scalar coupling $U_{12} = U_{21}$. The matrix **U** can be diagonalized to recover the adiabatic surfaces V_1 and V_2, and we can also obtain the nonadiabatic coupling (i.e., the nuclear-momentum coupling that couples motion on the adiabatic surfaces) analytically from the quasidiabatic energies and their gradients.[90]

The analytic matrix **U** was obtained by developing physically-motivated functional forms for the individual matrix elements, and flexibility in the fit was achieved by introducing more than 80 adjustable parameters. These parameters were optimized using a genetic algorithm[91] such that the RMS deviation of the adiabatic energies V_1 and V_2 from the *ab initio* data was minimized and such that U_{12} vanishes in all asymptotic regions (i.e., in regions where one atom is infinitely far from the other two). Critical regions of the surface (e.g., the van der Waals well) were weighted more than less important regions (e.g., high-energy regions) to obtain the final values of the parameters. Details of the functional forms and parameters of the analytic LiFH fit are given in the supporting information.[92] The geometries and energies of the stationary points of the analytic LiFH surfaces are shown in Table 1. The potential energy surfaces along the minimum energy path of the ground-state reaction are plotted in Fig. 1.

II.B. NaFH Potential Energy Surfaces

We have previously presented an analytic fit[10] for the two lowest-energy electronic states of NaFH (which we will call surface set NaFH-A) based on high level *ab initio* (MRDCI) calculations. The surface set was shown to be quantitatively accurate in the interaction region and was successfully used to reproduce the experimental photodepletion spectrum of the NaFH van der Waals system.[7] In the current work we use an improved version of the previous fit which we will call surface set NaFH-B. The new fit includes better representations of the experimental diatomic curves for HF and NaF in the asymptotic regions and features a localized diabatic coupling that vanishes in all asymptotic regions. The NaFH-B fit was obtained by adding a correction function to

the diagonal quasidiabatic surfaces U_{11} and U_{22} and cutting off the scalar coupling U_{12}. Details of the functional forms of the new fit are given in the supporting information.[92] The geometries and energies of the stationary points are shown in Table 1. The potential energy surfaces along the minimum energy path of the ground-state reaction for the surface set NaFH-B are shown in Fig. 2.

III. Semiclassical Trajectory Calculations

We performed a series of semiclassical trajectory calculations simulating the photodissociation processes (R1) and (R2) using the LiFH and NaFH-B quasidiabatic potential energy matrices. The semiclassical trajectory calculations were carried out using version 6.4 of the NAT computer code.[93] Each simulation included an ensemble of 3000 trajectories.

The initial conditions for a given trajectory in each ensemble were selected according to the following prescription: (1) The initial position and momentum of the trajectory were selected from a distribution that is similar to the non-rotating ground vibrational state in the electronically adiabatic ground-state van der Waals well. Specifically, the three Jacobi coordinates of the system (the HF stretch *r*, the M-[HF] stretch *R*, and the M-[HF] bend χ, where [HF] indicates the center of mass of HF) at the minimum of the van der Waals complex were assumed to be separable, and each trajectory was given the appropriate zero point energy (obtained from one-dimensional Morse fits to the potential energy along *r* and *R*) in the *r* and *R* stretching modes and a random phase. The angle χ was selected randomly from 0 to 2π. (2) After assigning the initial geometry $\mathbf{R}_0$ and momentum as described, the trajectories were immediately excited into the excited adiabatic state with an energy $h\upsilon$. If the difference between adiabatic energy gap of the electronic states at $\mathbf{R}_0$ and the excitation energy $h\upsilon$ was not within some specified tolerance ε, the excitation was rejected, and step (1) was repeated. The tolerance ε used for all of the runs reported here was 0.01 eV. Calculations were performed with excitation energies $h\upsilon$ equal to 1.5, 1.6, 1.7, 1.8, and 1.9 eV.

The energy of the ground vibrational state in the separable Jacobi approximation is 0.065 and 0.19 eV for Li···FH and Na···FH, respectively. (These values were obtained by adding the zero point energies of 0.28 and 0.27 eV to well energies of –0.21 and –0.074 eV, respectively.) Note that these energies differ from those reported in Table 1, because the values in Table 1 are estimated using separable normal modes (and are therefore our best estimate), whereas our semiclassical trajectory code requires the zero-point energy expressed in terms of separable r, R, and χ motions. The total energy of the semiclassical trajectories ranges from approximately 1.6 to 2.0 eV for LiFH and from approximately 1.7 to 2.1 eV for NaFH. The zero of energy is defined as Li or Na infinitely far from HF at its equilibrium internuclear bond distance.

We used two different semiclassical trajectory methods for coupled-states dynamics: Tully's fewest-switches[56] (TFS) method and the natural decay of mixing[54] (NDM) method. The TFS method belongs to the general class of surface-hopping methods where each trajectory in the ensemble is propagated under the influence of a single potential energy surface and propagation is interrupted by instantaneous surface transitions according to a fewest-switches algorithm. A corresponding kinetic energy adjustment is made along the nonadiabatic coupling vector such that the total energy is conserved. For the calculations reported here, classically forbidden electronic transitions were ignored. We performed TFS calculations in both the adiabatic (TFSa) and quasidiabatic representations (TFSd).

The NDM method[54] is a modification of the Ehrenfest self-consistent potential method that incorporates decoherence into the equations for the electronic motion and thereby produces trajectories that finish the simulation in a pure electronic state. When the surfaces are strongly coupled, NDM trajectories evolve on an average potential energy surface similar to the Ehrenfest potential energy surface. As the coupling between the electronic surfaces decreases to zero, the electronic density matrix gradually collapses to the diagonal form that corresponds to propagation in a single electronic state. We performed calculations in both the adiabatic (NDMa) and quasidiabatic (NDMd) representations. The NDM method has previously only been discussed in terms of the diabatic representation; we discuss the NDMa method in the appendix.

As discussed above, the initial conditions were selected using the adiabatic potential energy surfaces, independent of the representation used for propagation. For NDMd runs, the initial electronic state was transformed from the adiabatic to the quasidiabatic representation before propagation as discussed previously.[54] For the TFSd runs, the electronic representation transformation was performed as follows. The excited adiabatic state may be expressed as a linear combination of the two quasidiabatic electronic states. The initial quasidiabatic state for a TFSd run was selected randomly with a probability given by the square of the corresponding expansion coefficient. In general, the state that is selected as the initial quasidiabatic state will not have the same potential energy as the initial adiabatic state. In order to compensate for the change in the potential energy, the nuclear momentum was scaled such that the total energy was conserved and the direction of the nuclear momentum was unchanged.

Trajectories were propagated until the resulting products were dissociated by at least 15 bohr. The product branching ratios were computed by counting the trajectories that finish in each of the two final product arrangements. We refer to the M + FH product arrangement as the "quenching" process and the MF + H arrangement as the "reactive" process, although they may be more accurately described as nonreactive de-excitation and reactive de-excitation, respectively. These nonadiabatic probabilities are labeled P_{Q} and P_{R}, respectively. Trajectories may also dissociate into reactants in an excited electronic state (M* + HF) at excitation energies $h\upsilon$ of 1.78 eV for the LiFH system and 1.91 eV for the NaFH system. (These excitation energies correspond to 1.85 and 2.10 eV for the Li → Li* and Na → Na* excitations, respectively. Note that classical trajectories may dissociate without the required zero-point energy in HF.) Even when energetically allowed, the probability of this process is small (much less than 0.01), and we will not consider unquenched trajectories in the present work.

For both quenching and reactive trajectories, we computed the final vibrational ($\langle v' \rangle$ and $\langle v'' \rangle$) and rotational ($\langle j' \rangle$ and $\langle j'' \rangle$) moments (i.e., averages), where the single and double primes refer to reactive and quenching trajectories, respectively. The moments were calculated using the energy-nonconserving histogram (ENH) method, as described elsewhere.[94] We verified that using the energy-nonconserving quadratic- and

linear-smooth sampling schemes and the energy-conserving variants of all three sampling schemes give results that are within the uncertainties reported for the ENH results.

The lifetime of the exciplex was computed as follows: The delay time T_d for each trajectory in the ensemble was calculated from the total simulation time T, the final relative velocity $v_R(T)$, and the final translational Jacobi atom-diatom distance $R(T)$:

$$T_d = T - v_R(T)/R(T). \quad (1)$$

The second term in eq. (1) makes the result be independent of the arbitrary stopping time T. Trajectories with the delay times greater than T_d^{max} or less than T_d^{min} were excluded, and the remaining delay times were binned. The resulting curve, which represents the probability that the system has not dissociated from the exciplex as a function time, was fit to the exponential

$$P(T_d) = A\exp(-T_d/\tau), \quad (2)$$

where τ is the lifetime of the exciplex and A is a fitting parameter. The parameters T_d^{max} and T_d^{min} were chosen such that ~20% of trajectories were excluded by each cut-off parameter, i.e., the middle 60% of delay times were considered. The number of bins was typically 80–100. The calculated lifetimes were found to vary only slightly with small changes in the number of bins and the cut-off parameters T_d^{max} and T_d^{min}.

Note that one could also define the delay time for a photodissociation process as

$$T_d = T - v_R(T)/[R(T) - R(0)], \quad (3)$$

where $R(0)$ is the initial translational Jacobi distance. We verified that the differences in the lifetimes obtained by using eqs. (1) and (3) were smaller than the estimated uncertainties, and we report only the lifetimes calculated with eq. (1).

IV. Results

Tables 2 and 3 present the lifetimes, product branching probabilities, and final vibrational and rotational moments for the NaFH and LiFH systems. The observables are reported as a function of the excitation energy $h\upsilon$ for the both TFS and NDM semiclassical trajectory methods in both the adiabatic and quasidiabatic electronic representations. The relative uncertainties in the reactive and quenching moments are typically 2% and 4%, respectively, and the uncertainty in the probabilities is typically 0.01. The dominant uncertainty in the lifetimes is due to the choice of the cut-off parameters $T_{\mathrm{d}}^{\max}$ and $T_{\mathrm{d}}^{\min}$, and we estimate the relative uncertainty in the lifetimes to be between 5% and 10%.

The four semiclassical trajectory methods predict the same trends in the lifetimes, as shown in Fig. 3. Specifically, the lifetime of the LiFH exciplex is shorter and less dependent on energy than that of the NaFH exciplex. The lifetime of LiFH increases as a function of the excitation energy by a factor of 1.2 to 2.5 over the range of energies studied, whereas the lifetime of NaFH decreases. The relative decrease in the lifetime of NaFH is greater for the adiabatic methods (factors of 34 and 13) than for the quasidiabatic methods (factors of 9.8 and 2.4). The lifetimes of the LiFH exciplex calculated by the NDM method are relatively independent of the choice of electronic representation, whereas the TFSa method predicts lifetimes slightly greater than those of the NDM methods, and the TFSd method predicts shorter lifetimes by a factor of 2 to 4. The agreement between the adiabatic and diabatic methods is worse for the NaFH system, where the results vary, on average, by a factor of 16 for the NDM methods and 21 for the TFS methods. In all cases except one, the diabatic methods predict shorter lifetimes, and the agreement between the two electronic representations usually improves as the excitation energy decreases.

Although the magnitudes vary significantly among the methods, the reactive quenching process is usually preferred, and the probability of reaction P_{R} is usually greater for the LiFH system than for the NaFH system. For the adiabatic methods, P_{R} is generally constant as a function of energy for both the NaFH and LiFH systems. There is

a greater variation of P_R with energy in the diabatic results, especially for the NaFH system. The magnitude of P_R is usually in the range of 0.70 to 0.90 except for the diabatic results for the NaFH system, where P_R is as low as 0.22 for TFSd and does not exceed 0.56 for NDMd.

The final vibrational and rotational moments show no clear trend as a function of energy, and the magnitudes vary significantly between the semiclassical trajectory methods. The NDMa and TFSa methods qualitatively agree with each other, whereas the NDMd and TFSd method exhibit a larger discrepancy.

V. Discussion

The excitation energy of Li (1.85 eV) is lower than that of Na (2.10 eV) by 0.25 eV. This, combined with the fact that the product LiF + H valley is lower in energy than the NaF + H product valley, results in an adiabatic energy gap that is typically smaller in the LiFH system. In Fig. 4, we show contour plots of the adiabatic energy gap ($V_2 - V_1$) for the collinear LiFH and NaFH systems. Also shown is the exciplex well, the line of avoided crossings, and the location of the saddle point on the ground electronic surface at collinear geometries. For LiFH, the smallest energetically accessible adiabatic energy gap for the excitation energies studied here is approximately 0.8 eV, and the line of smallest energy gap passes near to the minimum of the exciplex well. Electronic transitions are promoted near the line of minimum energy gaps, and we therefore observe LiFH lifetimes that are short and relatively independent of the total energy of the system. The energetically accessible minimum energy gap for NaFH, on the other hand, varies from about 0.9 to 1.2 eV as a function of the excitation energy, and the line of avoided crossing is farther from the minimum of the exciplex well in the NaFH system than in the LiFH system. We therefore observe NaFH complexes with long lifetimes that are strongly dependent on the excitation energy.

We have previously introduced and discussed several criteria for estimating the most accurate electronic representation for surface-hopping.[71] We concluded that the representation that minimizes the number of attempted hops (and is therefore the representation in which the states of the system are the least coupled) is the preferred

electronic representation for surface-hopping, and we call this the Calaveras Co. (CC) representation. For both the LiFH and NaFH systems, the CC representation is the adiabatic representation. The rationale for preferring the CC representation is closely related to the problem of frustrated hops.[71] For the LiFH and NaFH systems, frustrated hopping occurs in nearly every one of the TFSd trajectories, whereas only 60% of TFSa trajectories experience a frustrated hop. The breakdown of the TFS algorithm leads to a decrease in the lifetimes, and we observe that the TFSd method predicts smaller lifetimes than the TFSa method. We can also assume that the TFSa method is predicting lifetimes that are too short due to the presence of frustrated hops in the adiabatic calculations.

Frustrated hops destroy the self-consistency of the trajectories and the electronic density matrix, but these remain fully self-consistent in the NDM method. It is encouraging that the NDM results are less sensitive to the choice of electronic representation than the TFS results are. The lifetimes predicted by the NDM method are largely independent of electronic representation for the LiFH system, but there is some dependence for the NaFH system. We note that when the decoherence time is infinitely large, the nuclear and electronic motion is independent of electronic representation, and that the NDM decoherence time is inversely proportional to the adiabatic energy gap for NDMa and the diabatic energy gap for NDMd. As discussed above, the LiFH system has a smaller energy gap than the NaFH system, and we therefore expect the results for the LiFH system to be less dependent on the choice of electronic representation. We also note that the definition of the decoherence time in the NDM method is somewhat arbitrary. More sophisticated forms of the decoherence time could be introduced (perhaps the simplest of which would be to introduce a multiplicative prefactor that is greater than one) such that the dependence of the NDM results on the choice of electronic representation is reduced for large-gap systems.

Physically, the line of avoided crossings (where $U_{11} = U_{22}$) corresponds to a change in the valence-bond character of the adiabatic state and is in the center of the region where electronic transitions are most likely to occur. From Fig. 4 we see that in the energetically accessible regions of the excited electronic state, the LiFH exciplex is more readily able to access the seam than is the NaFH exciplex. We also note that in the

LiFH system, electronic transitions are likely to occur closer to the saddle point than for the NaFH system. In fact, the well on the upper surface of the LiFH system stretches to a region of the saddle point on the ground-state surface. This is not the case for NaFH. In addition, the height of the reaction barrier for LiFH is much smaller than for NaFH. Therefore, we expect LiF to form more readily than NaF for a given total energy, and this trend is observed in the results of the semiclassical trajectory calculations.

VI. Summary

We have performed a set of semiclassical trajectory calculations for the photodissociation of LiFH and NaFH. The calculations were performed with two different methods for nonadiabatic dynamics and in both the adiabatic and diabatic representations. Although the results are not in quantitative agreement with each other, several clear trends emerge. Specifically, the lifetime of the NaFH complex decreases with increasing excitation energy and is strongly dependent on the excitation energy. The lifetime of the LiFH complex, on the other hand, is shorter than the lifetime of the NaFH complex and is less dependent on the excitation energy. The LiFH system is also found to be more reactive than the NaFH system at similar excitation energies. We have explained these results by considering the features of the coupled potential energy surfaces of the LiFH and NaFH systems.

Experiments on these systems are underway in the laboratory of Professor John Polanyi, and our calculations are stimulated by the hope that calculations such as those reported here can eventually be compared to experiment.

Acknowledgments

This work was supported in part by the National Science Foundation under grant no. CHE00-92019 and by the Michigan State University Intramural Research Grant Program. The authors are grateful to Rudolph Burcl, Xaio Yan Chang, Andrew Hudson, Gil Katz, Ronnie Kosloff, Han-Bin Oh, John Polanyi, Vladimir Špirko, and Yehuda Zeiri for many helpful interactions. Mike Hack, Arindam Chakraborty, and Piotr Piecuch contributed to this chapter.

Appendix: Natural Decay of Mixing in the Adiabatic Representation

The NDM method was initially presented[54] in the diabatic representation, and here we present the details of the NDMa method. We will consider a two-state system where the electronic wave function is given by

$$\Psi = c_1\phi_1 + c_2\phi_2\,, \tag{4}$$

ϕ_k are the adiabatic electronic basis functions, and c_k are the complex expansion coefficients

$$c_k = \frac{1}{\sqrt{2}}\left(x_k + ip_k\right). \tag{5}$$

The NDMa expressions for the rate of change of the real and imaginary parts of c_k are

$$\dot{x}_k = \dot{x}_k^{\mathrm{E}} + \dot{x}_k^{\mathrm{D}} \tag{6}$$

$$\dot{p}_k = \dot{p}_k^{\mathrm{E}} + \dot{p}_k^{\mathrm{D}}\,, \tag{7}$$

where the superscript 'E' denotes the usual Ehrenfest[55] electronic dynamics. The additional decoherence terms are given by

$$\dot{x}_k^{\mathrm{D}} = \left(1-\delta_{kK}\right)\left(-\frac{1}{2}\frac{x_k}{\tau_{kK}}\right) + \delta_{kK}\,\frac{1}{2}\frac{x_k}{\left|c_k\right|^2}\sum_{k'\neq k}\frac{\left|c_{k'}\right|^2}{\tau_{kk'}} \tag{8}$$

$$\dot{p}_k^{\mathrm{D}} = \left(1-\delta_{kK}\right)\left(-\frac{1}{2}\frac{p_k}{\tau_{kK}}\right) + \delta_{kK}\,\frac{1}{2}\frac{p_k}{\left|c_k\right|^2}\sum_{k'\neq k}\frac{\left|c_{k'}\right|^2}{\tau_{kk'}}\,, \tag{9}$$

where *K* is the state towards which the system is decohering,

$$\tau_{ik} = \frac{\hbar}{\left|V_i - V_k\right|}\frac{E}{T_{\mathrm{vib}}}\,, \tag{10}$$

E is the total energy of the system, V_k is the adiabatic energy of state *k*, and T_{vib} is the vibrational energy, as described elsewhere.[54] The decoherent state *K*, is selected using the fewest-switches criterion and the adiabatic electronic states. See Ref. 54 for details.

We note that the Ehrenfest expressions that appear in eqs. (6) and (7) can in principle be integrated in either representation for the NDMa method, but the expressions are much easier to integrate in the diabatic representation. In our implementation of the

NDMa method, the decoherence terms are calculated from eqs. (8) and (9) and transformed to the diabatic representation before being added to the diabatic Ehrenfest terms for propagation.

References

1 P. R. Brooks, Chem. Rev. **88**, 407 (1988).

2 J. C. Polanyi and A. H. Zewail, Acc. Chem. Res. **29**, 119 (1995).

3 M. Polanyi, *Atomic Reactions* (Williams and Norgate, London, 1932).

4 D. R. Herschbach, *Adv. Chem. Phys.*, vol. 10, edited by J. Ross (Interscience, New York, 1966), p.319.

5 R. D. Levine and R. B. Bernstein, *Molecular Reaction Dynamics and Chemical Reactivity* (Oxford University Press, New York, 1987), pp. 134ff.

6 X.-Y. Chang, R. Ehrlich, A. J. Hudson, P. Piecuch, and J. C. Polanyi, Faraday Discuss. Chem. Soc. **108**, 411 (1997).

7 M. S. Topaler, D. G. Truhlar, X. Y. Chang, P. Piecuch, and J. C. Polanyi, J. Chem. Phys. **108**, 5378 (1998).

8 A. J. Hudson, H. B. Oh, J. C. Polanyi, and P. Piecuch, J. Chem. Phys. **113**, 9897 (2000). A. J. Hudson and J. C. Polanyi, personal communication.

9 A. Sevin, P. C. Hilberty, and J.-M. Lefour, J. Am. Chem. Soc. **109**, 1845 (1987).

10 M. S. Topaler, D. G. Truhlar, X. Y. Chang, P. Piecuch, and J. C. Polanyi, J. Chem. Phys. **108**, 5349 (1998).

11 W. A. Lester, Jr. and M. Krauss, J. Chem. Phys. **52**, 4775 (1970).

12 G. G. Balint-Kurti and R. N. Yardley, Faraday Discuss. Chem. Soc. **62** 77 (1977).

13 Y. Zeiri and M. Shapiro, Chem. Phys. **31**, 217 (1978); M. Shapiro and Y. Zeiri, J. Chem. Phys. **70**, 5264 (1979).

14 M. M. L. Chen and H. F. Schaefer III, J. Chem. Phys. **72**, 4376 (1980).

15 S. Carter and J. N. Murrell, Mol. Phys. **41**, 567 (1980).

16 A. Laganà and E. Garcia, Theochem **16**, 91 (1984); E. Garcia and A. Laganà, Mol. Phys. **52**, 1115 (1984); V. Aquilanti, A. Laganà, and R. D. Levine, Chem. Phys. Lett. **158**, 87 (1989); A. Laganà, G. O. d. Aspuru, and E. Garcia, J. Chem. Phys. **108**, 3886 (1998).

17 M. Paniagua, J. M. Garcia de la Vega, J. R. Alvarez Collado, J. C. Sanz, J. M. Alvariño, and A. Laganà, J. Mol. Struct. **142**, 525 (1986).

18 A. Laganà, O. Gervasi, and E. García, Chem. Phys. Lett. **143**, 174 (1988).

19 M. Paniagua and A. Aguado, Chem. Phys. **134**, 287 (1989); A. Aguado and M. Paniagua, J. Chem. Phys. **96**, 1265 (1992); C. Suárez, A. Aguado, and M. Paniagua, Chem. Phys. **178**, 357 (1993); C. Suárez, A. Aguado, C. Tablero, and M. Paniagua, Int. J. Quantum Chem. **52**, 935 (1994); A. Aguado, C. Suárez, and M. Paniagua, Chem. Phys. **201**, 107 (1995).

20 A. Laganà, M. L. Hernandez, J. M. Alvariño, L. Castro, and P. Palmieri, Chem. Phys. Lett. **202**, 284 (1993).

21 O. N. Ventura, Mol. Phys. **89**, 1851 (1996).

22 G. A. Parker, A. Laganà, S. Crocchianti, and R. T Pack, J. Chem. Phys. **102**, 1238 (1995).

23 A. Aguado, M. Paniagua, M. Lara, and O. Roncero, J. Chem. Phys. **106**, 1013 (1997), **107**, 10085 (1997).

24 A. Laganà, J. M. Alvariño, M. L. Hernandez, P. Palmieri, E. Garcia, and T. Martinez, J. Chem. Phys. **106**, 10222 (1997).

25 R. Burcl, P. Piecuch, V. Špirko, and O. Bludský, Int. J. Quantum Chem. **80**, 916 (2001); V. Špirko, P. Piecuch, and O. Bludský, J. Chem. Phys. **112**, 189 (2000); F. Mrugała, P. Piecuch, V. Špirko and O. Bludský, J. Mol. Struct. **555**, 43 (2000).

26 C. H. Becker, P. Casauecchia, P. W. Tiedeman, J. J. Valentini, and Y. T. Lee, J. Chem. Phys. **73**, 2833 (1980).

27 R. B. Walker, Y. Zeiri, and M. Shapiro, J. Chem. Phys. **74**, 1763 (1981).

28 J. M. Alvariño, M. L. Hernández, E. Garcia, and A. Laganà, J. Chem. Phys. **84**, 3059 (1986); A. Laganà, E. Garcia, and O. Gervasi, J. Chem. Phys. **89**, 7238 (1988); A. Laganà, X. Giménez, E. Garcia, and O. Gervasi, Chem. Phys. Lett. **176**, 280 (1991); A. Laganà, G. O. d. Aspuru, A. Aguilar, X. Giménez, and J. M. Lucas, J. Phys. Chem. **99**, 11696 (1995); J. M. Alvariño, V. Aquilanti, S. Cavalli, S. Crocchianti, A. Laganà, and T. Martinez, J. Chem. Phys. **107**, 3339 (1997); A. Laganà, A. Bologna, and S. Crocchianti, Phys. Chem. Chem. Phys. **2**, 535 (2000).

29 M. Hoffmeister, R. Schleysing, F. Steinkemeier, and H. J. Loesch, J. Chem. Phys. **90**, 3528 (1989); H. J. Loesch, E. Stenzel, and B. Wüstenbecker, J. Chem. Phys. **95**, 3841 (1991); H. J. Loesch and F. Steinkemeier, J. Chem. Phys. **98**, 9570

(1993), **99**, 9598 (1993); H. J. Loesch, A. Ramscheid, E. Stenzel, F. Struckmayer, and B. Wuestenbecker, in *Physics of Electronic and Atomic Collisions*, edited by W. R. MacGilliuray, I. E. McCarthy, and M. C. Staudagi (Adam Hilyer, Bristol, 1992), p. 579.

30 G. G. Balint-Kurti, F. Gögtas, S. P. Mort, A. R. Offer, A. Laganà, and O. Gervasi, J. Chem. Phys. **99**, 9567 (1993); F. Gögtas, G. G. Balint-Kurti, and A. R. Offer, J. Chem. Phys. **104**, 7927 (1996).

31 M. Baer, H. J. Loesch, H.-J. Werner, and I. Last, Chem. Phys. Lett. **291**, 372 (1994); M. Baer, I. Last, and H. J. Loesch, J. Chem. Phys. **101**, 9648 (1994).

32 G. Villani and R. Wallace, Acta Chim. Hung. **131**, 167 (1994), ACH- Models Chem. **131**, 167 (1994).

33 W. Zhu, D. Wang, and J. Z. Zhang, Theor. Chem. Acc. **96** 31 (1997).

34 M. Paniagua, A. Aguado, M. Lara, and O. Roncero, J. Chem. Phys. **109**, 2971 (1998), **111**, 6712 (1999).

35 M. Lara, A. Aguado, O. Roncero, and M. Paniagua, J. Chem. Phys. **109**, 9391 (1998).

36 F. J. Aoiz, M. T. Martinez, M. Menéndez, V. S. Rábanos, and E. Verdasco, Chem. Phys. Lett. **299**, 25 (1999).

37 F. J. Aoiz, E. Verdasco, V. S. Rábanos, H. J. Loesch, M. Menéndez, and F. Steinkemeier, Phys. Chem. Chem. Phys. **2**, 541 (2000).

38 Y. Zeiri, G. Katz, R. Kosloff, M. S. Topaler, D. G. Truhlar, and J. C. Polanyi, Chem. Phys. Lett. **300**, 523 (1999).

39 D. R. Jenkins, Proc. Roy. Soc. Lond. Ser. A **306**, 413 (1968).

40 M. Krauss, J. Res. Natl. Bur. Stand. **72A**, 553 (1968); K. Mizutani, T. Yano, A. Sekiguchi, K. Nayahi, and S. Muksumoto, Bull. Chem. Soc. Japan **57**, 3368 (1984); F. Rossi and J. Pascale, Phys. Rev. A **32**, 2657 (1985).

41 J. C. Tully, J. Chem. Phys. **59**, 5122 (1993).

42 T. J. Martinez, Chem. Phys. Lett. **272**, 139 (1997); H. S. Lee, Y. S. Lee, and G.-H. Jeung, J. Phys. Chem. A **103**, 11080 (1999).

43 I. V. Hertel, H. Hofmann, and K. A. Rost, J. Chem. Phys. **71**, 674 (1979).

44 P. Botschwina, W. Meyer, I. V. Hertel, and W. Reiland, J. Chem. Phys. **75**, 5438 (1981); W. Reiland, H.-V. Tiltes, and I. V. Hertel, Phys. Rev. Lett. **48**, 1389 (1982); P. McGuire and J. C. Bellum, J. Chem. Phys. **77**, 764 (1982); N. C. Blais and D. G. Truhlar, J. Chem. Phys. **79**, 1334 (1983).

45 B. C. Garrett and D. G. Truhlar, in *Theory of Scattering: Papers in Honor of Henry Eyring* (*Theoretical Chemistry*, Vol. 6), edited by D. Henderson (Academic, New York, 1981), Part A, p. 216.

46 D. G. Truhlar, J. W. Duff, N. C. Blais, J. C. Tully, and B. C. Garrett, J. Chem. Phys. **77**, 764 (1982); N. C. Blais, D. G. Truhlar, and B. C. Garrett, J .Chem. Phys., **78**, 2956 (1983).

47 P. Halvick and D. G. Truhlar, J. Chem. Phys. **96**, 2895 (1992).

48 M. D. Hack and D. G. Truhlar, J. Chem. Phys. **110**, 4315 (1999).

49 D. W. Schwenke, S. L. Mielke, G. J. Tawa, R. S. Friedman, P. Halvick, and D. G. Truhlar, Chem. Phys. Lett. **203**, 565 (1993); S. L. Mielke, G. J. Tawa, D. G. Truhlar, and D. W. Schwenke, J. Am. Chem. Soc. **115**, 6436 (1993), Int. J. Quantum Chem. Symp. **27**, 621 (1993); G. J. Tawa, S. L. Mielke, D. G. Truhlar, and D. W. Schwenke, J. Chem. Phys. **100**, 5751 (1994); M. D. Hack, A. W. Jasper, Y. L. Volobuev, D. W. Schwenke, and D. G. Truhlar, J. Phys. Chem. A **103**, 6309 (1999).

50 D. R. Yarkony, J. Chem. Phys. **84**, 3206 (1976); C. W. Eaker, J. Chem. Phys. **87**, 4532 (1987); P. Hering, S. L. Cunha, and K. L. Kompa, J. Phys. Chem. **91**, 5459 (1987); R. d. Vivie-Reidle, P. Hering, K. L. Kompa, R. R. B. Correira, S. L. Cunha, and G. Pichler, A.I.P. conf. Proc. **216**, 415 (1990); R. d. Vivie-Reidle, P. Hering, and K. L. Kompa, Z. Phys. D. **17**, 299 (1990); R. R. B. Correia, S. L. Cunha, R. d. Vivie-Reidle, G. Pichler, K. L. Kompa, and P. Hering, Chem. Phys. Lett. **186**, 531 (1991); G. Pichler, R. R. B. Correira, S. L. Cunha, K. L. Kompa, and P. Hering, Opr. Commun. **92**, 346 (1992).

51 J. L. Magee and T. Ri, J. Chem. Phys. **9**, 639 (1941), K. J. Laidler, J. Chem. Phys. **10**, 34 (1942).

52 Y. L. Volobuev, M. D. Hack, M. S. Topaler, and D. G. Truhlar, J. Chem. Phys. **112**, 9716 (2000).

53 M. D. Hack and D. G. Truhlar, J. Chem. Phys. **114**, 2894 (2001).

54 M. D. Hack and D. G. Truhlar, J. Chem. Phys. **114**, 9305 (2001).

55 H.-D. Meyer and W. H. Miller, J. Chem. Phys. **70**, 3214 (1979).

56 J. C. Tully, J. Chem. Phys. **93**, 1061 (1990).

57 A. Bjerre, and E. E. Nikitin, Chem. Phys. Lett. **1**, 179 (1967).

58 R. K. Preston, and J. C. Tully, J. Chem. Phys. **54**, 4297 (1971). J. C. Tully and R. K. Preston, J. Chem. Phys. **55**, 562 (1971).

59 W. H. Miller, and T. F. George, J. Chem. Phys. **56**, 5637 (1972).

60 J. C. Tully, in *Dynamics of Molecular Collisions*, edited by W. H. Miller (Plenum, New York, 1976), Part B, pp. 217–267.

61 D. G. Truhlar, and J. T. Muckerman, in *Atom-Molecule Collision Theory*, edited by R. B. Bernstein (Plenum, New York, 1979), pp. 505–594.

62 P. J. Kuntz, J. Kendrick, and W. N. Whitton, Chem. Phys. **38**, 147 (1979). G. Parlant and E. A. Gislason, J. Chem. Phys. **91**, 4416 (1989).

63 N. C. Blais, and D. G. Truhlar, J. Chem. Phys. **79**, 1334 (1983).

64 M. F. Herman, J. Chem. Phys. **81**, 754 (1984).

65 N. C. Blais, D. G. Truhlar, and C. A. Mead, J. Chem. Phys. **89**, 6204 (1988).

66 P. J. Kuntz, J. Chem. Phys. **95**, 141 (1991).

67 S. Chapman, Adv. Chem. Phys. **82**, 423 (1992).

68 M. F. Herman, Annu. Rev. Phys. Chem. **45**, 83 (1994).

69 U. Müller, and G. Stock, J. Chem. Phys. **107**, 6230 (1997).

70 J. C. Tully, in *Modern Methods for Multidimensional Dynamics Computations in Chemistry*, edited by D. L. Thompson (World Scientific, Singapore, 1998), p. 34.

71 M. D. Hack and D. G. Truhlar, J. Phys. Chem. A **104**, 7917 (2000).

72 A. W. Jasper, M. D. Hack, and D. G. Truhlar, J. Chem. Phys., J. Chem. Phys. **115**, 1804 (2001).

73 A. W. Jasper, M. D. Hack, D. G. Truhlar, and P. Piecuch, J. Chem. Phys. **116**, 8353 (2002).

74 R. J. Buenker and S. D. Peyerimhoff, Theor. Chim. Acta **35**, 33 (1974).

75 R. J. Buenker and S. D. Peyerimhoff, Theor. Chim. Acta **39**, 217 (1975).

76 P. J. Bruna and S. D. Peyerimhoff, Adv. Chem. Phys. **67**, 1 (1987).

77 A. D. McLachlan, Mol. Phys. **4**, 417 (1961).

78 T. F. O'Malley, Adv. At. Mol. Phys. **7**, 223 (1971).

79 V. Sidis and H. Lefebvre-Brion, J. Phys. B **4**, 1040 (1971).

80 S. A. Evans, J. S. Cohen, and N. F. Lane, Phys. Rev. A **4**, 2235 (1971).

81 R. W. Numrich and D. G. Truhlar, J. Phys. Chem. **79**, 2745 (1975).

82 A. Macias and A. Riera, J. Phys. B **11**, L489 (1978).

83 C. A. Mead and D. G. Truhlar, J. Chem. Phys. **77**, 6090 (1982).

84 C. A. Mead, J. Chem. Phys. **78**, 807 (1983).

85 T. C. Thompson, D. G. Truhlar, and C. A. Mead, J. Chem. Phys. **82**, 2392 (1985).

86 V. Sidis, Adv. Chem. Phys. **82**, 73 (1992).

87 T. Pacher, L. S. Cederbaum, and H. Köppel, Adv. Chem. Phys. **84**, 293 (1993).

88 V. M. García, M. Reguero, R. Caballol, and J. P. Malrieu, Chem. Phys. Lett. **281**, 161 (1997).

89 G. J. Atchity and K. Ruedenberg, Theor. Chem. Acc. **97**, 47 (1997).

90 M. D. Hack, A. W. Jasper, Y. L. Volobuev, D. W. Schwenke, and D. G. Truhlar, J. Phys. Chem. A **103**, 6309 (1999).

91 Genetic algorithm calculations were carried out using the program FORTRAN GA, version 1.6.4 as described in D. L. Carroll, AIAA J. **34**, 338 (1996).

92 See EPAPS Document No. E-JCPSA6-115-008141 for supporting information including the functional forms and parameters of the analytic LiFH and NaFH-B surface sets. This document may be retrieved via the EPAPS homepage (http://www.aip.org/pubservs/epaps.html) or from ftp.aip.org in the directory /epaps/. See the EPAPS homepage for more information.

93 M. S. Topaler, M. D. Hack, Y. L. Volobuev, A. W. Jasper, T. C. Allison, T. F. Miller III, Y.-P. Liu, N. C. Blais, and D. G. Truhlar, NAT-version 6.4 (University of Minnesota, Minneapolis, 2001).

94 M. S. Topaler, T. C. Allison, D. W. Schwenke, and D. G. Truhlar, J. Chem. Phys. **109**, 3321 (1998).

95 E. B. Wilson, J. C. Decius, and P. C. Cross, *Molecular Vibrations* (McGraw-Hill, New York, 1955).

96 J. C. Corchado, Y.-Y. Chuang, P. L. Fast, J. Villà, W.-P. Hu, Y.-P. Liu, G. C. Lynch, K. A. Nguyen, C. F. Jackels, V. S. Melissas, B. J. Lynch, I. Rossi, E. L. Coitiño, A. Fernandez-Ramos, R. Steckler, B. C. Garrett, A. D. Isaacson, and D. G. Truhlar, POLYRATE-version 8.5.1, University of Minnesota, Minneapolis, 2000.

97 A. D. Isaacson and D. G. Truhlar, J. Chem. Phys. **76**, 1380 (1982).

Table 1. Geometries and energies of the adiabatic stationary points of LiFH and NaFH. All bond lengths are in bohr, the M–F–H angle θ is in degrees, and the energies are in eV.

LiFH features	r_{LiF}	r_{HF}	r_{LiH}	θ_{LiFH}	V_1	V_1 + ZPE[a]	V_2	V_2 + ZPE[a]
Reactants	–	1.73	–	–	0.000	0.251 (0.249)	1.848	2.099 (2.097)
Reactant vdW well of V_1	3.56	1.75	4.48	110.	–0.211	0.096 (0.094)	1.204	–
Saddle point[b] of V_1	3.16	2.43	3.37	72.3	0.352	0.402 (0.402)	2.798	–
Product vdW well of V_1	2.99	3.33	4.67	69.7	0.214	0.287 (0.287)	5.441	–
Products	2.96	–	–	–	0.213	0.260 (0.260)	c	–
Exciplex of V_2	3.33	1.82	4.70	129.	–0.143	–	1.165	1.396 (1.394)
NaFH features[d]	r_{NaF}	r_{HF}	r_{NaH}	θ_{NaFH}	V_1	V_1 + ZPE[a]	V_2	V_2 + ZPE[a]
Reactants	–	1.73	–	–	0.000	0.251 (0.249)	2.097	2.342 (2.346)
Reactant vdW well of V_1	4.68	1.74	5.71	118.	–0.074	0.351 (0.352)	2.031	–
Saddle point[e] of V_1	3.66	3.49	5.09	90.8	1.270	1.299 (1.299)	5.622	–
Products	3.64	–	–	–	1.182	1.218 (1.220)	c	–
Exciplex of V_2	4.17	1.83	5.26	117.	0.020	–	1.600	1.911 (1.909)

[a]The zero point energy (ZPE) was calculated treating the normal modes as separable harmonic oscillators[95] using the POLYRATE v. 8.5.1 software package.[96] Values in parentheses were obtained by using the Morse I approximation[97] to include anharmonicity in the stretches. Zero point energy is included in one mode for reactants and products, in the two bound modes for the saddle points, and in three modes for the three-body local minima.

[b]Imaginary frequency: 1480i cm^{-1}.

[c]The product arrangement is not bound on the excited-state surface V_2.

[d]The NaFH surface does not support a product van der Waals well.

[e]Imaginary frequency: 1650i cm^{-1}.

Table 2. Lifetimes, branching ratios, and final vibrational and rotational moments for NaFH.

Method	$h\upsilon$ (eV)	τ (ps)	P_R	$\langle v' \rangle$	$\langle j' \rangle$	P_Q	$\langle v'' \rangle$	$\langle j'' \rangle$
NDMa	1.5	21.	0.81	2.76	10.6	0.19	1.79	6.2
	1.6	7.8	0.80	3.19	12.8	0.20	1.49	8.0
	1.7	3.3	0.76	3.11	14.2	0.24	1.56	7.6
	1.8	1.6	0.83	3.07	13.8	0.17	1.58	8.4
	1.9	0.68	0.82	3.04	15.6	0.18	1.70	8.6
TFSa	1.5	11.	0.96	2.74	11.9	0.04	1.63	8.6
	1.6	4.8	0.90	2.93	11.5	0.11	1.61	9.5
	1.7	3.0	0.88	3.50	12.5	0.12	1.47	10.6
	1.8	1.6	0.90	3.79	13.3	0.10	1.59	11.8
	1.9	0.88	0.88	4.67	14.0	0.11	1.67	12.0
NDMd	1.5	0.57	0.37	1.93	10.3	0.63	1.17	5.2
	1.6	0.40	0.33	2.39	12.9	0.67	0.91	8.7
	1.7	0.32	0.34	2.99	15.0	0.66	0.88	8.6
	1.8	0.26	0.55	3.75	14.5	0.45	0.92	9.1
	1.9	0.24	0.56	4.11	18.3	0.44	1.25	9.2
TFSd	1.5	0.26	0.22	0.63	13.4	0.79	2.34	2.5
	1.6	0.19	0.51	0.80	13.7	0.49	2.04	4.3
	1.7	0.17	0.63	1.54	14.1	0.38	1.84	5.6
	1.8	0.10	0.81	3.09	14.7	0.19	1.86	5.9
	1.9	0.027	0.87	4.93	14.6	0.12	1.81	8.5

Table 3. Lifetimes, branching ratios, and final vibrational and rotational moments for LiFH.

Method	$h\upsilon$ (eV)	τ (ps)	P_R	$\langle v' \rangle$	$\langle j' \rangle$	P_Q	$\langle v'' \rangle$	$\langle j'' \rangle$
NDMa	1.5	0.094	0.90	2.87	11.3	0.10	1.51	5.9
	1.6	0.13	0.89	3.25	14.5	0.11	1.31	8.6
	1.7	0.13	0.87	3.89	13.0	0.13	1.61	7.3
	1.8	0.14	0.89	4.10	14.6	0.11	1.55	7.9
	1.9	0.11	0.94	3.65	17.4	0.06	1.37	14.1
TFSa	1.5	0.15	0.98	2.56	9.0	0.02	1.76	8.7
	1.6	0.21	0.95	3.31	12.2	0.05	1.94	7.9
	1.7	0.26	0.91	3.86	13.8	0.09	2.02	9.2
	1.8	0.28	0.90	4.16	16.6	0.10	1.93	10.7
	1.9	0.28	0.82	4.15	18.1	0.09	1.85	12.1
NDMd	1.5	0.061	0.88	3.19	13.1	0.12	0.94	7.5
	1.6	0.095	0.81	3.12	19.6	0.19	0.88	10.1
	1.7	0.13	0.69	3.17	20.3	0.31	0.98	10.7
	1.8	0.14	0.64	3.42	19.1	0.36	0.87	13.3
	1.9	0.15	0.65	3.33	19.9	0.34	0.74	17.0
TFSd	1.5	0.015	0.93	4.58	7.8	0.07	1.32	6.0
	1.6	0.026	0.90	4.80	8.4	0.10	1.45	6.9
	1.7	0.029	0.89	5.10	7.7	0.11	1.32	7.8
	1.8	0.030	0.89	6.14	6.5	0.11	1.36	7.8
	1.9	0.036	0.89	6.26	6.7	0.10	1.51	8.8

Figure captions

Figure 1. Adiabatic (thick solid lines) and quasidiabatic (thin dashed lines) energies along the ground-state reaction coordinate s for Li + HF → LiF + H at a fixed bond angle of 72°.

Figure 2. Adiabatic (thick solid lines) and quasidiabatic (thin dashed lines) energies along the ground-state reaction coordinate s for Na + HF → NaF + H at a fixed bond angle of 91°.

Figure 3. Lifetime τ of the LiFH exciplex (dashed lines) and NaFH exciplex (solid line) as a function of excitation energy $h\upsilon$. Solid squares represent the TFSa method, open squares represent the TFSd method, solid triangles represent the NDMa method, and open triangles represent the NDMd method. Note that the ordinate axis is logarithmic.

Figure 4. Adiabatic energy gap for a) the LiFH system and b) the NaFH system. The bond angle is fixed at 180°. The solid contours represent the adiabatic energy gap ($V_2 - V_1$), where the minimum contour is 0.6 eV for LiFH and 0.8 eV for NaFH, and the contour spacing is 0.2 eV. The 1.0 eV contours are labeled in both cases. The dashed contours show the exciplex wells, where the highest energy contour is 2.1 eV and the contour spacing is 0.1 eV. The line of avoided crossings of V_1 and V_2 (where U_{11} and U_{22} cross) is shown as a thick solid line, and the saddle point on the ground electronic surface is indicated by the square.

Figure 1

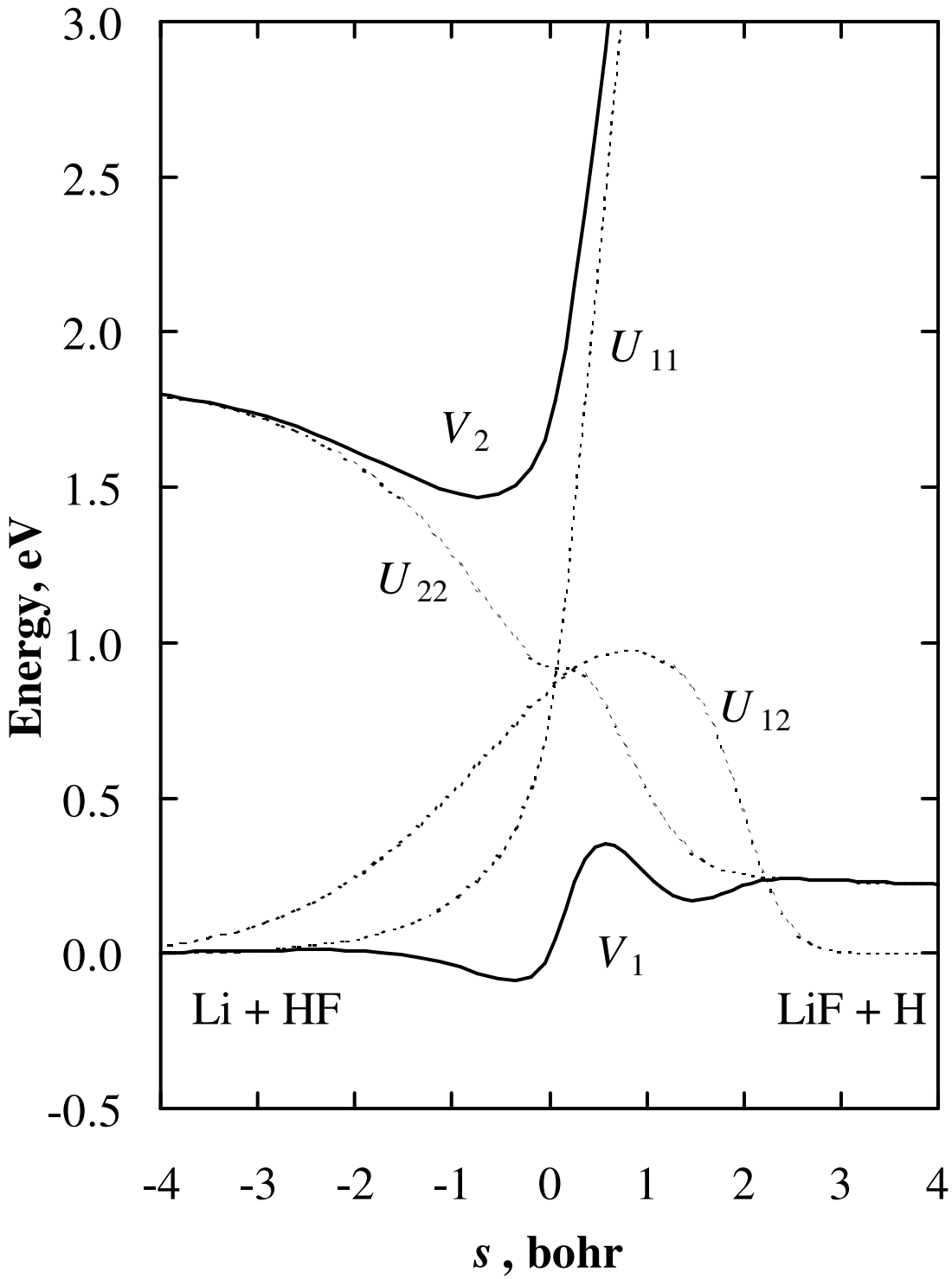
3.0
2.5
2.0
1.5
1.0
0.5
0.0
-0.5
Energy, eV
U_{11}
V_2
U_{22}
U_{12}
V_1
Li + HF
LiF + H
-4
-3
-2
-1
0
1
2
3
4
s , bohr

Figure 2

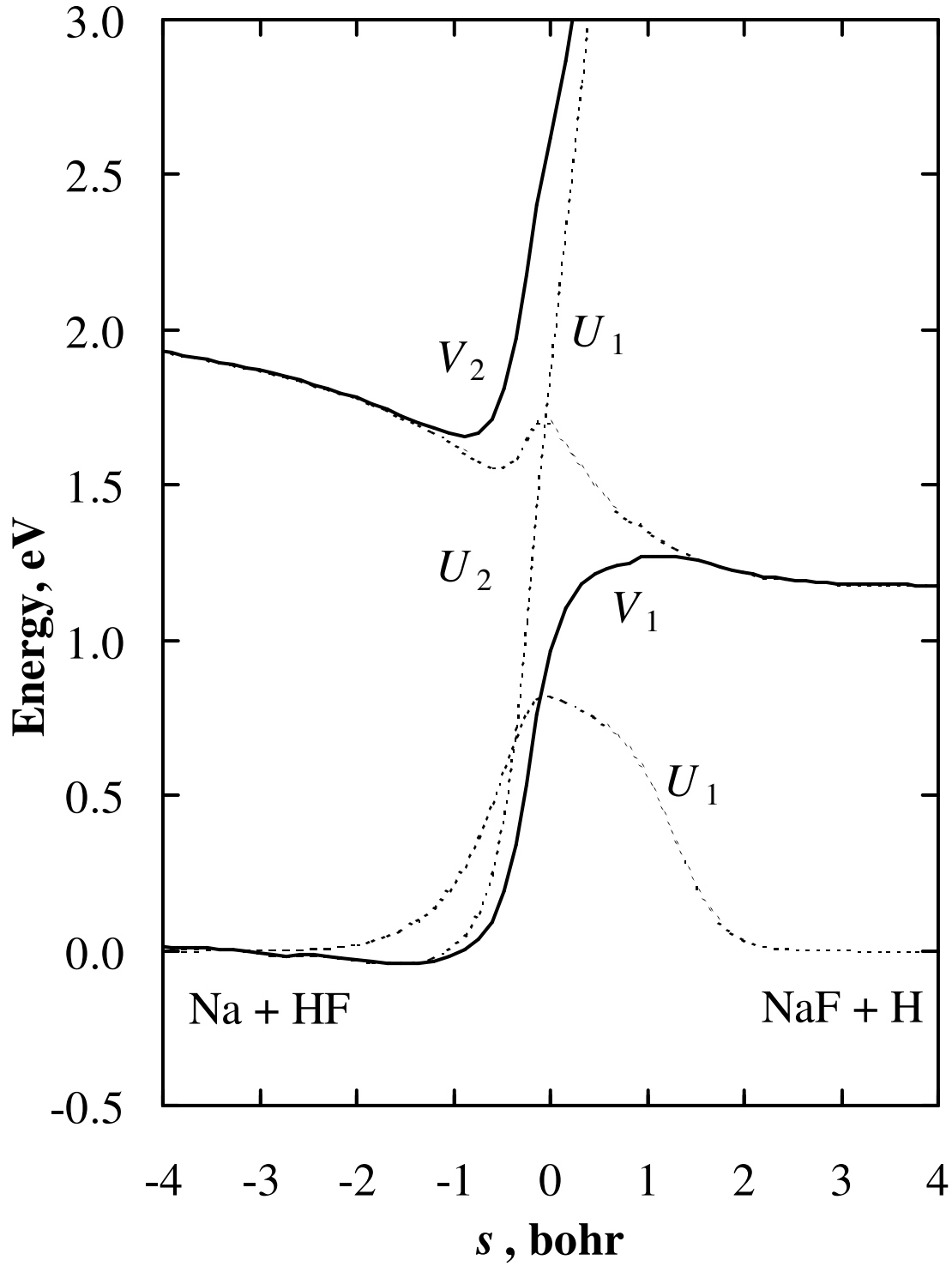
3.0
2.5
2.0
1.5
1.0
0.5
0.0
-0.5
Energy, eV
-4
-3
-2
-1
0
1
2
3
4
s , bohr
V2
U1
U2
V1
U1
Na + HF
NaF + H

Figure 3

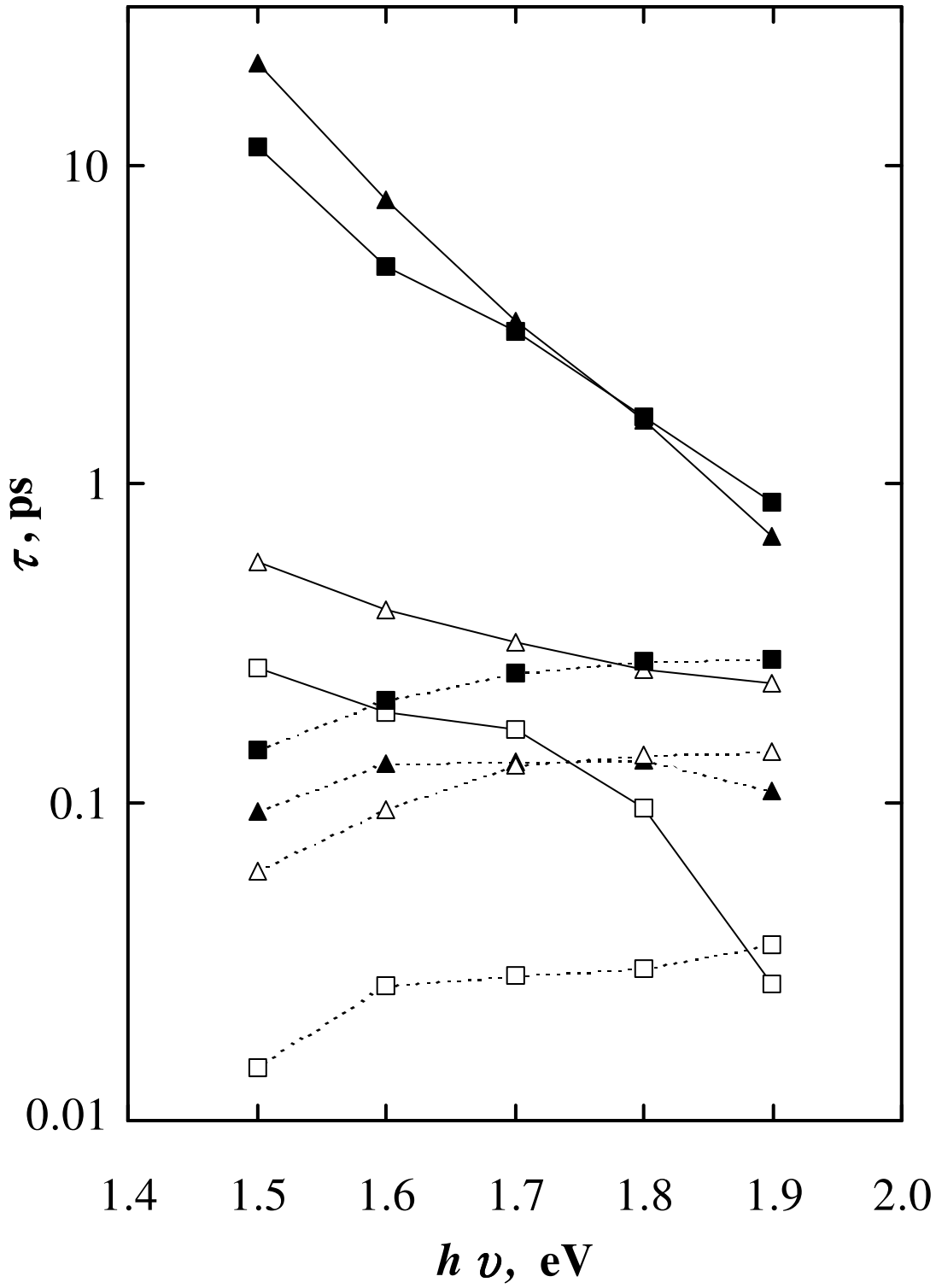

Figure 4

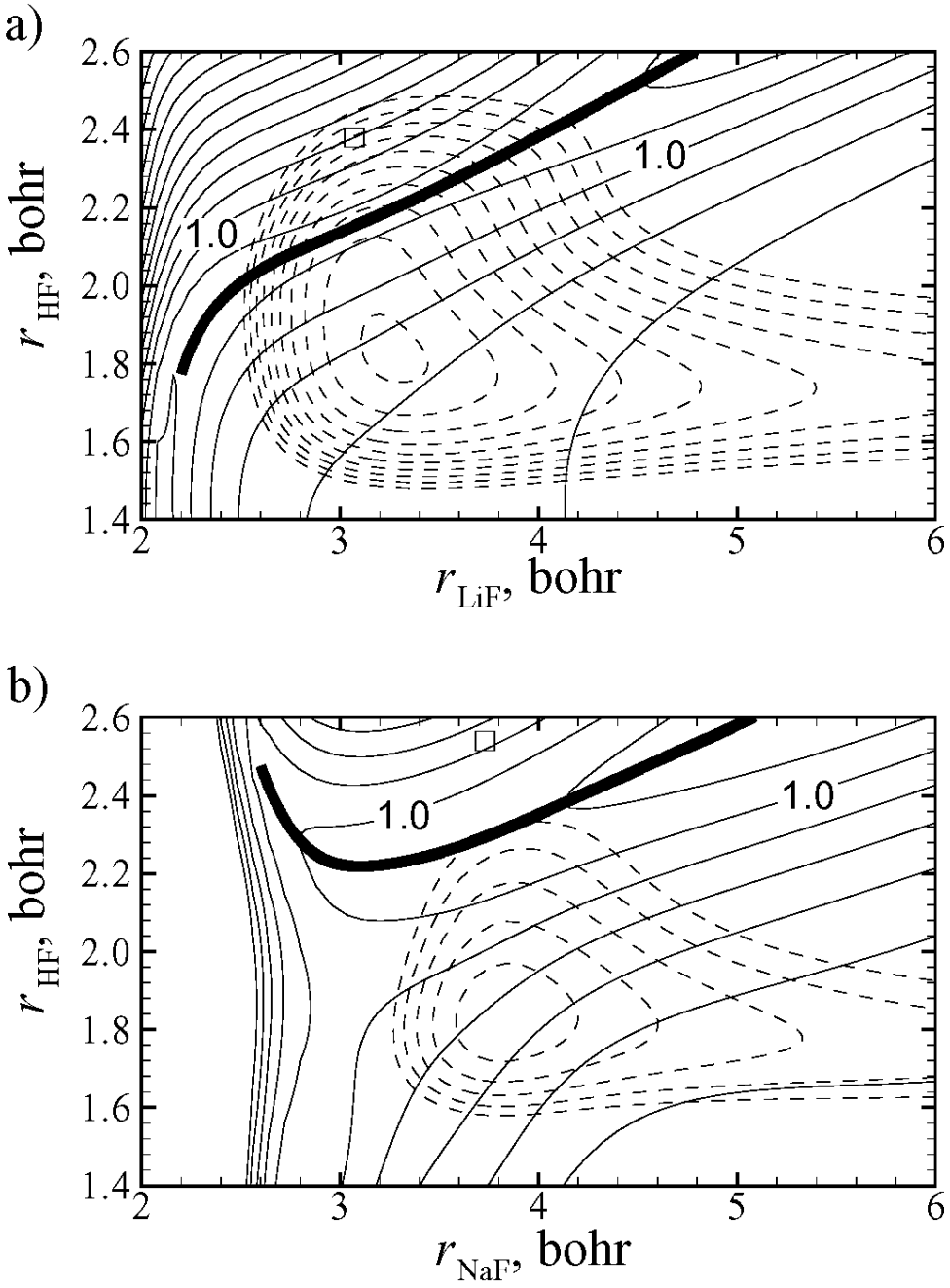
a)
2.6
2.4
2.2
2.0
1.8
1.6
1.4
2
3
4
5
6
r_{HF}, bohr
r_{LiF}, bohr
1.0
1.0
b)
2.6
2.4
2.2
2.0
1.8
1.6
1.4
2
3
4
5
6
r_{HF}, bohr
r_{NaF}, bohr
1.0
1.0

Supporting Information

S.1. Functional Form of the Model LiFH Potential Energy Matrix

S.1.1. LiFH U_{11} Surface

The lowest-energy quasidiabatic surface in the Li + FH arrangement is labeled U_{11} and is described by the sum of three diatomic terms,

$$U_{11}(\mathbf{R}) = S_1(\mathbf{R}) + S_2(r_{\mathrm{HF}}) + S_3(\mathbf{R}) + D_{\mathrm{HF}}^{\mathrm{e}}, \tag{S-1}$$

where the LiH diatomic $S_1(\mathbf{R})$ is a dressed state (i.e., it represents Li–H interactions in the close presence of F, not in isolation) that is taken as purely repulsive, the HF diatomic $S_2(r_{\mathrm{HF}})$ is an attractive Morse-like curve, and the LiF diatomic $S_3(\mathbf{R})$ is another dressed state and is taken to be a shallow Morse curve. This simple functional form is appropriate to describe U_{11} which is relatively devoid of features, having only a small van der Waals well and otherwise being repulsive along the Li + HF coordinate. The use of dressed states for the Li–H and Li–F interactions is necessary because the LiH and LiF diatomic limits are energetically inaccessible for this quasidiabatic surface at the energies we are interested in studying.

The LiH diatomic curve for the U_{11} matrix element is a combination of two repulsive curves and is given by

$$S_1(\mathbf{R}) = S_1^{\mathrm{a}}(r_{\mathrm{LiH}}) + [S_1^{\mathrm{c}}(r_{\mathrm{LiH}}) - S_1^{\mathrm{a}}(r_{\mathrm{LiH}})]\Phi_1(\mathbf{R}), \tag{S-2}$$

$$S_1^{\mathrm{a}}(r_{\mathrm{LiH}}) = D_1^{\mathrm{a}} \exp[-\beta_1^{\mathrm{a}}(r_{\mathrm{LiH}} - r_{\mathrm{LiH}}^0)], \tag{S-3}$$

$$S_1^{\mathrm{c}}(r_{\mathrm{LiH}}) = D_1^{\mathrm{c}} \exp[-\beta_1^{\mathrm{c}}(r_{\mathrm{LiH}} - r_{\mathrm{LiH}}^0)], \tag{S-4}$$

where $\Phi_1(\mathbf{R})$ is a switching function given by

$$\Phi_1(\mathbf{R}) = \frac{1}{2} - \frac{1}{2}\tanh\left(\frac{r_1 - \rho_1}{\Delta_1}\right), \tag{S-5}$$

$$r_1 = r_{\mathrm{LiH}} - r_{\mathrm{LiF}} + \alpha_1 r_{\mathrm{HF}}. \tag{S-6}$$

The HF potential curve S_2 was fit to experimental Rydberg-Klein-Rees (RKR) data for the HF molecule;[1] the functional form is a Morse curve with a range parameter that depends on the HF bond length,

$$S_2(r_{\mathrm{HF}}) = D_{\mathrm{HF}}^{\mathrm{e}} X_2(r_{\mathrm{HF}})[X_2(r_{\mathrm{HF}}) - 2], \tag{S-7}$$

where

$$X_2(r_{\mathrm{HF}}) = \exp[-\beta_2(r_{\mathrm{HF}})(r_{\mathrm{HF}} - r_{\mathrm{HF}}^{\mathrm{e}})], \tag{S-8}$$

and

$$\beta_2(r_{\mathrm{HF}}) = b_1 + b_2(r_{\mathrm{HF}} - r_{\mathrm{HF}}^{0}) + b_3(r_{\mathrm{HF}} - r_{\mathrm{HF}}^{0})^2. \tag{S-9}$$

The LiF diatomic curve for the U_{11} matrix element is a combination of two shallow Morse curves and is given by

$$S_3(\mathbf{R}) = S_3^{\mathrm{a}} + (S_3^{\mathrm{c}} - S_3^{\mathrm{a}})\Phi_3(\mathbf{R}), \tag{S-10}$$

$$S_3^{\mathrm{a}}(r_{\mathrm{LiF}}) = D_3^{\mathrm{a}} X_3^{\mathrm{a}}(r_{\mathrm{LiF}})[X_3^{\mathrm{a}}(r_{\mathrm{LiF}}) - 2], \tag{S-11}$$

$$S_3^{\mathrm{c}}(r_{\mathrm{LiF}}) = D_3^{\mathrm{c}} X_3^{\mathrm{c}}(r_{\mathrm{LiF}})[X_3^{\mathrm{c}}(r_{\mathrm{LiF}}) - 2], \tag{S-12}$$

$$X_3^{\mathrm{a}}(r_{\mathrm{LiF}}) = \exp[-\beta_3^{\mathrm{a}}(r_{\mathrm{LiF}} - r_{\mathrm{LiF}}^{\mathrm{a}})], \tag{S-13}$$

$$X_3^{\mathrm{c}}(r_{\mathrm{LiF}}) = \exp[-\beta_3^{\mathrm{c}}(r_{\mathrm{LiF}} - r_{\mathrm{LiF}}^{\mathrm{c}})], \tag{S-14}$$

$$\Phi_3(\mathbf{R}) = \frac{1}{2} - \frac{1}{2}\tanh\left(\frac{r_3 - \rho_3}{\Delta_3}\right), \tag{S-15}$$

$$r_3 = r_{\mathrm{LiH}} - r_{\mathrm{LiF}} + \alpha_3 r_{\mathrm{HF}}. \tag{S-16}$$

The values of the parameters used in the U_{11} potential matrix element are given in Table S-1.

S.1.2. LiFH U_{22} Surface

The U_{22} potential energy matrix element was fit to a modified[2] London-Eyring-Polanyi-Sato (LEPS)[3,4] form,

$$U_{22}(\mathbf{R}) = J_1(\mathbf{R}) + J_2(\mathbf{R}) + J_3(\mathbf{R}) - \frac{1}{\sqrt{2}}\sqrt{W(\mathbf{R}) + Z(\mathbf{R})^2} + D_{\mathrm{HF}}^{\mathrm{e}} + E_{\mathrm{Li}}^{*}, \tag{S-17}$$

where

$$W(\mathbf{R}) = (K_2(\mathbf{R}) - K_1(\mathbf{R}))^2 + (K_1(\mathbf{R}) - K_3(\mathbf{R}))^2 + (K_3(\mathbf{R}) - K_2(\mathbf{R}))^2. \tag{S-18}$$

The functions J_α and K_α (α = 1, 2, and 3) are given by

$$J_\alpha(\mathbf{R}) = \frac{1}{2}(S_\alpha(\mathbf{R}) + T_\alpha(\mathbf{R})), \tag{S-19}$$

$$K_\alpha(\mathbf{R}) = \frac{1}{2}(S_\alpha(\mathbf{R}) - T_\alpha(\mathbf{R})), \tag{S-20}$$

and

$$Z(\mathbf{R}) = c_{2\mathrm{a}} \exp[-c_{2\mathrm{b}} W(\mathbf{R}) - c_{2\mathrm{c}}(r_{\mathrm{HF}} + r_{\mathrm{LiH}} + r_{\mathrm{LiF}})]. \tag{S-21}$$

is a necessary to remove a cusp that would otherwise occur in eq. (S-17) when $W(\mathbf{R})$ goes through zero. The LEPS function eq. (S-17) allows the global potential energy surface for the triatomic system to be expressible as a function of diatomic terms, specifically, three singlet terms (S_1, S_2, and S_3) and three triplet terms (T_1, T_2, and T_3).

The LiH singlet curve is a combination of two different curves, one of which is present at all geometries and one of which is turned on when the LiH diatom is interacting with the F atom,

$$S_1(\mathbf{R}) = S_1^{\mathrm{a}}(r_{\mathrm{LiF}}) + S_1^{\mathrm{c}}(r_{\mathrm{LiF}})\Phi_1(\mathbf{R}), \tag{S-22}$$

$$S_1^{\mathrm{a}}(r_{\mathrm{LiH}}) = c_{S1,1} X_{S1}(r_{\mathrm{LiH}})^2 + c_{S1,2} X_{S1}(r_{\mathrm{LiH}}), \tag{S-23}$$

$$X_{S1}(r_{\mathrm{LiH}}) = \exp[-\beta_{S1}^{\mathrm{a}}(r_{\mathrm{LiH}} - r_{\mathrm{LiH}}^{\mathrm{e}})], \tag{S-24}$$

$$S_1^{\mathrm{c}}(r_{\mathrm{LiH}}) = \exp[-\beta_{S1}^{\mathrm{c}}(r_{\mathrm{LiH}} - r_{\mathrm{LiH}}^{\mathrm{e}})], \tag{S-25}$$

$$\Phi_1(\mathbf{R}) = \frac{1}{2} - \frac{1}{2}\tanh(\frac{r_1 - \rho_1}{\Delta_1}), \tag{S-26}$$

$$r_1 = r_{\mathrm{LiH}} - r_{\mathrm{LiF}} + \alpha_1 r_{\mathrm{HF}}. \tag{S-27}$$

The LiH triplet is a modified anti-Morse curve,

$$T_1(\mathbf{R}) = c_{T1,1} X_{T1}(r_{\mathrm{LiH}})^2 + c_{T1,2} X_{T1}(r_{\mathrm{LiH}}), \tag{S-28}$$

$$X_{T1}(r_{\mathrm{LiH}}) = \exp[-\beta_{T1}(r_{\mathrm{LiH}} - r_{\mathrm{LiH}}^{\mathrm{e}})]. \tag{S-29}$$

The HF singlet S_2, is similar to the form used for the U_{11} potential matrix element,

$$S_2(\mathbf{R}) = D_{S2}^{\mathrm{mod}}(\mathbf{R}) X_2(r_{\mathrm{HF}})[X_2(r_{\mathrm{HF}}) - 2], \tag{S-30}$$

where

$$D_{S2}^{\mathrm{mod}}(\mathbf{R}) = D_{\mathrm{HF}}^{\mathrm{e}} - D_{S2}^{\mathrm{c}} \frac{1}{2}(1 - \cos\chi)\left(\frac{1}{2} - \frac{1}{2}\tanh\frac{r_{\mathrm{LiF}} - \rho_{S2}}{\Delta_{S2}}\right). \tag{S-31}$$

which allows the depth of the Morse curve to vary as a function of χ for short LiF distances. The function $X_2(r_{\mathrm{HF}})$ is defined by eq. (S-8).

The HF triplet potential is a linear combination of two repulsive curves,

$$T_2(\mathbf{R}) = T_2^0(r_{\mathrm{HF}}) + T_2^{180}(r_{\mathrm{HF}}) \frac{1}{2}(1 - \cos\chi), \tag{S-32}$$

$$T_2^0(r_{\mathrm{HF}}) = c_{T2,1} X_{T2}^0(r_{\mathrm{HF}})^2 + c_{T2,2} X_{T2}^0(r_{\mathrm{HF}}), \tag{S-33}$$

$$T_2^{180}(r_{\mathrm{HF}}) = c_{T2,3} X_{T2}^{180}(r_{\mathrm{HF}})^2 + c_{T2,4} X_{T2}^{180}(r_{\mathrm{HF}}), \tag{S-34}$$

$$X_{T2}^0(r_{\mathrm{HF}}) = \exp[-\beta_{T2}^0(r_{\mathrm{HF}})(r_{\mathrm{HF}} - r_{T2}^0)], \tag{S-35}$$

$$X_{T2}^{180}(r_{\mathrm{HF}}) = \exp[-\beta_{T2}^{180}(r_{\mathrm{HF}})(r_{\mathrm{HF}} - r_{T2}^0)]. \tag{S-36}$$

The LiF potential curve has a long-range tail arising from the contribution of the $Li^+ + F^-$ state. This long range character is not present in other parts of the potential surface, for example, in the Li + HF entrance channel. Therefore, it is necessary to allow the singlet describing the LiF interaction to change as a function of the other two internuclear distances. This is accomplished by defining the LiF singlet as

$$S_3(\mathbf{R}) = S_3^{\mathrm{c}}(\mathbf{R}) + [S_3^{\mathrm{a}}(\mathbf{R}) - S_3^{\mathrm{c}}(\mathbf{R})]\Phi_{S3}(\mathbf{R}). \tag{S-37}$$

The asymptotic term, $S_3^{\mathrm{a}}(\mathbf{R})$, is given by

$$S_3^{\mathrm{a}}(\mathbf{R}) = (D_{\mathrm{LiF}}^e + E_{\mathrm{Li}}^*) X_{S3}^{\mathrm{a}}(\mathbf{R})[X_{S3}^{\mathrm{a}}(\mathbf{R}) - 2], \tag{S-38}$$

where

$$X_{S3}^{\mathrm{a}}(\mathbf{R}) = \exp[-\beta_{\mathrm{S3}}(\mathbf{R})(r_{\mathrm{LiF}} - r_{\mathrm{LiF}}^e)], \tag{S-39}$$

and

$$\beta_{S3}(\mathbf{R}) = \beta_f(\mathbf{R}) \frac{\beta_i(r_{\mathrm{LiF}}) + \left(r_{\mathrm{LiF}} \big/ \gamma \right)^n}{\beta_f(\mathbf{R}) + \left(r_{\mathrm{LiF}} \big/ \gamma \right)^n}, \tag{S-40}$$

$$\beta_f(\mathbf{R}) = \beta_i(r_{\mathrm{LiF}}) + G(\mathbf{R})(\beta_{ff} - \beta_i(r_{\mathrm{LiF}})), \tag{S-41}$$

$$G(\mathbf{R}) = \left(\frac{1}{2} - \frac{1}{2} \tanh \frac{r_{\mathrm{HF}} - \rho_G}{\Delta_G} \right) \frac{1}{2} (1 + \cos \chi), \tag{S-42}$$

$$\beta_i(r_{\mathrm{LiF}}) = b_1 + \frac{b_2 r_{\mathrm{LiF}}}{b_3 + b_4 r_{\mathrm{LiF}}^2}. \tag{S-43}$$

The somewhat complicated definition of the Morse range parameter defined by eqs. (S-40)–(S-42) stems from practical considerations. We wish to use the LiFH surface in quantum mechanical calculations; these calculations are much easier to carry out when the diabatic coupling vanishes at all three dissociation limits. It was found, however, that

when we caused the diabatic coupling to decay in the LiF + H channel, the analytical fit no longer qualitatively agreed with the *ab initio* data, owing to the diabatic coupling being involved in defining the shape of the excited adiabatic surface. In order to somewhat alleviate this shortcoming, the adjustments defined in eqs. (S-37)–(S-43) above were introduced.

The form of the LiF diatomic used in the Li + HF channel is given by

$$S_3^{\mathrm{c}}(\mathbf{R}) = [D_{S3}^{\mathrm{c}}(\mathbf{R}) + E_{\mathrm{Li}}^{*}]X_{S3}^{\mathrm{c}}(\mathbf{R})[X_{S3}^{\mathrm{c}}(\mathbf{R}) - 2], \tag{S-44}$$

$$D_{S3}^{\mathrm{c}} = D_{S3}^{\mathrm{c},0}(r_{\mathrm{HF}}) + D_{S3}^{\mathrm{c},180}(r_{\mathrm{HF}})\frac{1}{2}(1-\cos\chi), \tag{S-45}$$

$$X_{S3}^{\mathrm{c}}(\mathbf{R}) = \exp[-\beta_{S3}^{\mathrm{c}}(r_{\mathrm{LiF}} - r_{\mathrm{LiF}}^{e})], \tag{S-46}$$

$$\beta_{S3}^{\mathrm{c}} = \beta_{S3}^{\mathrm{c},0}(r_{\mathrm{HF}}) + \beta_{S3}^{\mathrm{c},180}(r_{\mathrm{HF}})\frac{1}{2}(1-\cos\chi). \tag{S-47}$$

The asymptotic and close forms of the LiF singlet are joined together with a switching function,

$$\Phi_{S3}(\mathbf{R}) = \frac{1}{2} - \frac{1}{2}\tanh\frac{g(\mathbf{R})}{\Delta_{\mathrm{S3}}(\mathbf{R})}, \tag{S-48}$$

$$g(\mathbf{R}) = (r_{\mathrm{HF}}^{e} - r_{\mathrm{HF}})\cos\theta_{S3}(\mathbf{R}) - (\rho_{\mathrm{S3}}(\mathbf{R}) - r_{\mathrm{LiF}})\sin\theta_{S3}(\mathbf{R}), \tag{S-49}$$

$$\rho_{\mathrm{S3}}(\mathbf{R}) = \rho_{\mathrm{S3}}^{0} + \rho_{\mathrm{S3}}^{180}(r_{\mathrm{HF}})\frac{1}{2}(1-\cos\chi), \tag{S-50}$$

$$\theta_{\mathrm{S3}}(\mathbf{R}) = \theta_{\mathrm{S3}}^{0} + \theta_{\mathrm{S3}}^{180}(r_{\mathrm{HF}})\frac{1}{2}(1-\cos\chi), \tag{S-51}$$

$$\Delta_{\mathrm{S3}}(\mathbf{R}) = \Delta_{\mathrm{S3}}^{0} + \Delta_{\mathrm{S3}}^{180}(r_{\mathrm{HF}})\frac{1}{2}(1-\cos\chi). \tag{S-52}$$

The LiF triplet potential is a modified anti-Morse curve,

$$T_3(\mathbf{R}) = T_3^{0}(r_{\mathrm{HF}}) + T_3^{180}(r_{\mathrm{HF}})\frac{1}{2}(1-\cos\chi), \tag{S-53}$$

$$T_3^0(r_{\mathrm{LiF}}) = c_{T3,1}(r_{\mathrm{LiF}})X_{T3}^0(r_{\mathrm{LiF}})^2 + c_{T3,2}(r_{\mathrm{LiF}})X_{T3}^0(r_{\mathrm{LiF}}), \quad \text{(S-54)}$$

$$T_3^{180}(r_{\mathrm{LiF}}) = c_{T3,3}(r_{\mathrm{LiF}})X_{T3}^{180}(r_{\mathrm{LiF}})^2 + c_{T3,4}(r_{\mathrm{LiF}})X_{T3}^{180}(r_{\mathrm{LiF}}), \quad \text{(S-55)}$$

$$X_{T3}^0(r_{\mathrm{LiF}}) = \exp[-\beta_{T3}^0(r_{\mathrm{LiF}})(r_{\mathrm{LiF}} - r_{\mathrm{LiF}}^e)], \quad \text{(S-56)}$$

$$X_{T3}^{180}(r_{\mathrm{HF}}) = \exp[-\beta_{T3}^{180}(r_{\mathrm{HF}})(r_{\mathrm{HF}} - r_{\mathrm{LiF}}^e)]. \quad \text{(S-57)}$$

The values of the parameters used in the U_{22} potential matrix element are given in Table S-2.

S.1.3. LiFH U_{12} Coupling Surface

The off-diagonal electronic potential energy surface is described by

$$U_{12}(\mathbf{R}) = U_{12}^0(\mathbf{R})\left(\frac{1}{2} - \frac{1}{2}\tanh\frac{r_{\mathrm{HF}} - \rho_{12}}{\Delta_{12}}\right), \quad \text{(S-58)}$$

where $U_{12}^0(\mathbf{R})$ is a physically motivated functional form that is caused to approach zero for large values of r_{HF} where the excited-state potential energy surface becomes energetically inaccessible. Nonadiabatic transitions in this regions are unimportant and eliminating the off-diagonal coupling in these regions greatly reduces the expense of accurate quantum mechanical dynamics calculations.

Of the three diatomic asymptotes, there is only electronic coupling in the LiH and LiF arrangements. The two electronic states that we treat arise from the Li(2*s*) and Li(2*p*) atomic orbitals, and the coupling between these vanishes as Li is separated from the HF diatom. It is therefore natural to treat the diabatic coupling in the full system as arising from diatomic terms in the LiF and LiH bond distances,

$$U_{\mathrm{LiH}}(r_{\mathrm{LiH}}) = g_1\left(\frac{r_{\mathrm{LiH}}}{r_{\mathrm{LiH}}^0}\right)^6 \exp\left[-6\left(\frac{r_{\mathrm{LiH}}}{r_{\mathrm{LiH}}^0} - 1\right)\right], \quad \text{(S-59)}$$

$$U_{\mathrm{LiF}}(r_{\mathrm{LiF}}) = g_3\left(\frac{r_{\mathrm{LiF}}}{r^0_{\mathrm{LiF}}}\right)^8 \exp\left[-8\left(\frac{r_{\mathrm{LiF}}}{r^0_{\mathrm{LiF}}}-1\right)\right]. \tag{S-60}$$

These are functions which are zero when the diatomic distances are zero, increase in magnitude to a maximum of g_i at $r_{\mathrm{LiX}} = r^0_{\mathrm{LiX}}$ (X = H, F), and then decrease in magnitude at a rate determined by the power on the pre-exponential factor.

We expect the magnitude of each of these terms to be reduced by the approach of the remaining atom to the diatom, and we use the following form to accomplish this:

$$\begin{aligned} U^0_{12}(\mathbf{R}) = {} & U_{\mathrm{LiH}}(r_{\mathrm{LiH}})\Phi_{\mathrm{HF},1}(r_{\mathrm{HF}})\Phi_{\mathrm{LiF}}(r_{\mathrm{LiF}}) \\ & + U_{\mathrm{LiF}}(r_{\mathrm{LiF}})\Phi_{\mathrm{HF},2}(r_{\mathrm{HF}})\Phi_{\mathrm{LiH}}(r_{\mathrm{LiH}}). \end{aligned} \tag{S-61}$$

The reduction functions $\Phi_{\mathrm{HF},1}$, Φ_{LiF}, $\Phi_{\mathrm{HF},2}$, and Φ_{LiH} are given by

$$\Phi_{\mathrm{HF},1}(r_{\mathrm{HF}}) = \frac{1}{2} + \frac{1}{2}\tanh\frac{r_{\mathrm{HF}} - \rho_{\mathrm{HF},1}}{\Delta_{\mathrm{HF},1}}, \tag{S-62}$$

$$\Phi_{\mathrm{LiF}}(r_{\mathrm{LiF}}) = \frac{1}{2} + \frac{1}{2}\tanh\frac{r_{\mathrm{LiF}} - \rho_{\mathrm{LiF}}}{\Delta_{\mathrm{LiF}}}, \tag{S-63}$$

$$\Phi_{\mathrm{HF},2}(r_{\mathrm{HF}}) = \frac{1}{2} + \frac{1}{2}\tanh\frac{r_{\mathrm{HF}} - \rho_{\mathrm{HF},2}}{\Delta_{\mathrm{HF},2}}, \tag{S-64}$$

$$\Phi_{\mathrm{LiH}}(r_{\mathrm{LiH}}) = \frac{1}{2} + \frac{1}{2}\tanh\frac{r_{\mathrm{LiH}} - \rho_{\mathrm{LiH}}}{\Delta_{\mathrm{LiH}}}. \tag{S-65}$$

The values of the parameters used in the U_{22} potential matrix element are given in Table S-3.

S.2. NaFH-B Potential Energy Surface

We have recently presented the details of an analytic two-state NaFH quasidiabatic energy matrix.[5] The fit was successfully used to reproduce the experimentally observed photoabsorption spectrum of the Na...FH van der Waals complex,[6] indicating that the fit is very accurate in the interaction region. The NaFH fit

has two undesirable asymptotic features that we correct here: 1) the diabatic coupling U_{12} does not vanish in the NaF + H asymptote, and 2) the dissociation energy of the HF diatomic in the Na + HF asymptote is 0.35 eV below the experimental value. In this Appendix, we present an improved NaFH fit (called NaFH-B) which has the desired asymptotic forms and is obtained by modifying the original NaFH fit (called NaFH-A). Specifically, the diabatic coupling is cut off for large HF internuclear bond distances, and an asymptotic correction function is added to each of the diagonal diabats.

S.2.1. NaFH U_{12} Coupling Surface

The coupling between the two lowest energy states of the NaFH system does not vanish in the NaF + H asymptote. Asymptotic coupling complicates several aspects of our semiclassical and quantum mechanical simulations. We note that this coupling is not important in determining the dynamics of the NaFH system at reasonable energies due to the high energy of the upper electronic state in this asymptote. The functional form of the diabatic coupling surface for the improved NaFH-B fit, is given by

$$U_{12}^{\mathrm{B}}(\mathbf{R}) = U_{12}^{\mathrm{A}}(\mathbf{R})\,\Phi_{12}(r_{\mathrm{HF}}), \tag{S-66}$$

where U_{12}^{A} is the diabatic coupling function presented previously[5] for the NaFH-A fit. $\Phi_{12}(R_{\mathrm{HF}})$ is a cutoff function in the HF bond direction and has the form

$$\Phi_{12}(r_{\mathrm{HF}}) = \frac{1}{2} - \frac{1}{2}\tanh\left(\frac{r_{\mathrm{HF}} - r_{12}}{\Delta_{12}}\right), \tag{S-67}$$

where r_{12} = 3.5 a_0 and Δ_{12} = 0.5 a_0. The cutoff function does not significantly change the value of the diabatic coupling near the line of avoided crossings.

S.2.2. NaFH U_{11} and U_{22} Surfaces

The diagonal diabats U_{11}^{B} and U_{22}^{B} for NaFH-B are obtained by adding correction functions to the original NaFH diabats,

$$U_{jj}^{\mathrm{B}}(\mathbf{R}) = U_{jj}^{\mathrm{A}}(\mathbf{R}) + F_j(\mathbf{R}), \tag{S-68}$$

where j = 1 or 2 and U_{jj}^{A} are the surfaces presented previously.[5] We require that the functions F_j correct the asymptotic diatomic energy curves, minimize the change to the interaction region, and smoothly introduce the correction into the surfaces. A simple choice for F_j that satisfies these three requirements is the difference of two LEPS[3] functions

$$F_j(\mathbf{R}) = L_j^{\mathrm{B}}(\mathbf{R}) - L_j^{\mathrm{A}}(\mathbf{R}), \tag{S-69}$$

where L_j^{A} is a LEPS function with asymptotic forms that are exactly equal to the asymptotic forms of the NaFH-A fit, and L_j^{B} is a LEPS function with the desired (i.e., experimental) asymptotic forms. The LEPS function can be written

$$\begin{aligned} L_j^x(\mathbf{R}) = & \sum_\alpha Q_{\alpha,j}^x(r_\alpha) \\ & - \left(\sum_\alpha \left(J_{\alpha,j}^x(r_\alpha) \right)^2 - \frac{1}{2} \sum_\alpha \sum_{\alpha' \neq \alpha} J_{\alpha,j}^x(r_\alpha) J_{\alpha',j}^x(r_\alpha) \right)^{1/2} + D_{e,\mathrm{HF}}^x, \end{aligned} \tag{S-70}$$

where

$$Q_{\alpha,j}^x(r_\alpha) = \tfrac{1}{2}[S_{\alpha,j}^x(r_\alpha) + T_{\alpha,j}^x(r_\alpha)], \tag{S-71}$$

$$J_{\alpha,j}^x(r_\alpha) = \tfrac{1}{2}[S_{\alpha,j}^x(r_\alpha) - T_{\alpha,j}^x(r_\alpha)], \tag{S-72}$$

x = 'A' or 'B', the summations run over α = HF, NaF, or NaH, and $D_{e,\mathrm{HF}}^x$ sets the zero of energy.

The functional forms and parameters used for the singlets $S_{\alpha,i}^{\mathrm{A}}$ are equal to the singlets that appear in the NaFH-A fit.[5] The U_{11} diabat in the NaF + H and NaH + F asymptotes and the U_{22} diabat in the NaH + F asymptote are not corrected, i.e., $S_{\alpha,i}^{\mathrm{B}} = S_{\alpha,i}^{\mathrm{A}}$ for (α,i) = (NaH,1), (NaH,2), and (NaF,1). (Note that because the diabatic coupling is cut off in the HF bond direction, the lower diabatic surface in the NaF + H asymptote

(U_{22}) must be re-fit, such that the lower adiabat is left unchanged asymptotically.)

The remaining singlets required for L_i^{B} are $S_{\mathrm{HF},1}^{\mathrm{B}}$, $S_{\mathrm{HF},2}^{\mathrm{B}}$, and $S_{\mathrm{NaF},2}^{\mathrm{B}}$. These singlets have the following functional forms:

$$S_{\mathrm{HF},1}^{\mathrm{B}}(r_{\mathrm{HF}}) = D_{e,\mathrm{HF}}^{\mathrm{B}}\left(1-\exp[-\beta_{\mathrm{HF}}^{\mathrm{B}}(r_{\mathrm{HF}})(r_{\mathrm{HF}}-r_{e,\mathrm{HF}}^{\mathrm{B}})]\right)^2 - D_{e,\mathrm{HF}}^{\mathrm{B}}, \qquad \text{(S-73)}$$

$$S_{\mathrm{HF},2}^{\mathrm{B}}(r_{\mathrm{HF}}) = \frac{1}{2}\left(1-\Theta_{\mathrm{HF},2}^{\mathrm{B}}(r_{\mathrm{HF}})\right)\left(S_{\mathrm{HF},1}^{\mathrm{B}}(r_{\mathrm{HF}}) + E_{s\to p}^{\mathrm{B}}\right), \qquad \text{(S-74)}$$

$$S_{\mathrm{NaF},2}^{\mathrm{B}}(r_{\mathrm{NaF}}) = D_{e,\mathrm{NaF}}^{\mathrm{B}}\left(1-\exp[-\beta_{\mathrm{NaF}}^{\mathrm{B}}(r_{\mathrm{NaF}})(r_{\mathrm{NaF}}-r_{e,\mathrm{N}a\mathrm{F}}^{\mathrm{B}})]\right)^2 - D_{e,\mathrm{NaF}}^{\mathrm{B}}, \qquad \text{(S-75)}$$

where

$$\beta_{\mathrm{HF}}^{\mathrm{B}}(r_{\mathrm{HF}}) = c_{1,\mathrm{HF}}^{\mathrm{B}} + c_{2,\mathrm{HF}}^{\mathrm{B}}(r_{\mathrm{HF}}-c_{4,\mathrm{HF}}^{\mathrm{B}}) + c_{3,\mathrm{HF}}^{\mathrm{B}}(r_{\mathrm{HF}}-c_{4,\mathrm{HF}}^{\mathrm{B}})^2, \qquad \text{(S-76)}$$

$$\beta_{\mathrm{NaF}}^{\mathrm{B}}(r_{\mathrm{NaF}}) = c_{1,\mathrm{NaF}}^{\mathrm{B}}\frac{c_{2,\mathrm{NaF}}^{\mathrm{B}} + \left(\frac{r_{\mathrm{NaF}}}{c_{3,\mathrm{NaF}}^{\mathrm{B}}}\right)^{c_{4,\mathrm{NaF}}^{\mathrm{B}}}}{c_{1,\mathrm{NaF}}^{\mathrm{B}} + \left(\frac{r_{\mathrm{NaF}}}{c_{3,\mathrm{NaF}}^{\mathrm{B}}}\right)^{c_{4,\mathrm{NaF}}^{\mathrm{B}}}}, \qquad \text{(S-77)}$$

$$\Theta_{\mathrm{HF},2}^{\mathrm{B}}(r_{\mathrm{HF}}) = \tanh\left(\kappa_{\mathrm{HF}}^{\mathrm{B}}[S_{\mathrm{HF},1}^{\mathrm{B}}(r_{\mathrm{HF}}) - E_{s\to p}^{\mathrm{B}}]\right). \qquad \text{(S-78)}$$

The parameters for these functions are given in Table S-4. The HF singlet fit is based on experimental RKR data.[1] Experimental data for the NaF curve[7] is available up to ~0.5 eV. During the fitting procedure for the NaF curve, the dissociation energy was not allowed to vary, and the electronic structure data used in the original fit were included above 0.5 eV to make sure that the corrected NaF curve was qualitatively correct above 0.5 eV.

The triplet functions in eqs. (S-71) and (S-72) do not affect the asymptotic forms of the LEPS equations, but they are important in determining the character of the interaction region. In order to provide the correction functions F_j with flexibility, we introduced adjustable parameters into the triplet functions. For F_1, one adjustable parameter $w_{\alpha,1}^{x}$ was introduced which weights the entire triplet by a constant, i.e.,

$$T^{x}_{\alpha,1}(r_\alpha) = w^{x}_{\alpha,1} t_{\alpha,1}(r_\alpha), \tag{S-79}$$

where the set of $w^{x}_{\alpha,1}$ are listed in Table S-5. (Note that weighting the triplet functions by a single parameter is exactly equivalent to introducing Sato parameters[2] in the LEPS equation.) The form of $t^{x}_{\mathrm{HF},1}$ is an anti-Morse curve with a constant range parameter,

$$t_{\mathrm{HF},1}(r_{\mathrm{HF}}) = \tfrac{1}{2} D^{\mathrm{t}}_{\mathrm{e,HF}} \left(2\exp[-\beta^{\mathrm{t}}_{\mathrm{e,HF}}(r_{\mathrm{HF}} - r^{\mathrm{t}}_{\mathrm{e,HF}})] - \exp[-2\beta^{\mathrm{t}}_{\mathrm{e,HF}}(r_{\mathrm{HF}} - r^{\mathrm{t}}_{\mathrm{e,HF}})] \right), \tag{S-80}$$

where $D^{\mathrm{t}}_{\mathrm{e,HF}}$, $r^{\mathrm{t}}_{\mathrm{e,HF}}$, and $\beta^{\mathrm{t}}_{\mathrm{e,HF}}$ are listed in Table S-5. The functional forms of the collinear geometry triplets that appear in the previous fit[5] were used for $t_{\mathrm{NaF},1}$ and $t_{\mathrm{NaH},1}$.

For F_2, the $T^{x}_{\mathrm{NaH},2}$ triplets were not parameterized and were set equal to the collinear triplets that appear previously.[5] The functional forms of the $T^{x}_{\mathrm{HF},2}$ and $T^{x}_{\mathrm{NaF},2}$ triplets are anti-Morse curves with two adjustable parameters, i.e.,

$$T^{x}_{\alpha,2}(r_\alpha) = \tfrac{1}{2} D^{\mathrm{t}}_{\mathrm{e},\alpha} \left(2\, w^{1,x}_{\alpha,2} \exp[-\beta^{\mathrm{t}}_{\alpha}(r_\alpha - r^{\mathrm{t}}_{\mathrm{e},\alpha})] - w^{2,x}_{\alpha,2} \exp[-2\beta^{\mathrm{t}}_{\alpha}(r_\alpha - r^{\mathrm{t}}_{\mathrm{e},\alpha})] \right) \tag{S-81}$$

where the set of $w^{k,x}_{\alpha,2}$ (k = 1,2) and the anti-Morse curve parameters are given in Table S-5.

The values of the adjustable parameters $w^{x}_{\alpha,1}$, $w^{1,x}_{\alpha,2}$, and $w^{2,x}_{\alpha,2}$ were obtained using a genetic algorithm[8] such that the magnitudes of F_1 and F_2 were minimized in the interaction region. From Table S-6, we see that the correction functions do not significantly change the properties of the NaFH surface at the minima of the van der Waals and exciplex wells. Note that the mean unsigned deviation from the electronic structure data for the original fit is 0.02–0.03 eV.

Table S-1. Values of the parameters used in the LiFH U_{11} potential energy function.

Parameter	Value	Parameter	Value
D_1^a	12.90323 eV	r_{HF}^0	2.1042 a_0
D_1^c	7.09677 eV	D_3^a	0.14286 eV
β_1^a	1.73333 a_0^{-1}	D_3^c	0.25 eV
β_1^c	1.36 a_0^{-1}	β_3^a	1.22667 a_0^{-1}
r_{LiH}^0	1.53333 a_0	β_3^c	1.92857 a_0^{-1}
ρ_1	1.07143 a_0	r_{LiF}^a	3.66667 a_0
Δ_1	0.6 a_0	r_{LiF}^c	2.48571 a_0
α_1	0.4	ρ_3	0.4 a_0
b_1	1.1622 a_0^{-1}	Δ_3	0.89333 a_0
b_2	–0.025647 a_0^{-2}	α_3	0.7333
b_3	0.059062 a_0^{-3}	r_{HF}^e	1.733 a_0
D_{HF}^e	6.122 eV		

Table S-2. Values of the parameters used in the LiFH U_{22} potential energy function.

Parameter	Value	Parameter	Value
c_{2a}	3.5 eV	r^e_{LiF}	2.9553 a_0
c_{2b}	0.27362 eV^{-2}	β_{ff}	0.25333 a_0^{-1}
c_{2c}	0.15 a_0^{-1}	γ	3.87097 $a_0^{1+1/n}$
$c_{S1,1}$	4.32258 eV	n	8
$c_{S1,2}$	7.06452 eV	ρ_G	1.41935 a_0
β^a_{S1}	1.36 a_0^{-1}	Δ_G	3.77419 a_0
β^c_{S1}	0.90667 a_0^{-1}	b_1	0.064076 a_0^{-1}
r^e_{LiH}	1.2 a_0	b_2	103.57
ρ_1	0.72 a_0	b_3	4.6498 a_0^{-2}
Δ_1	0.5 a_0	b_4	7.0489
α_1	1.0	r^e_{HF}	1.733 a_0
$c_{T1,1}$	1.64516 eV	$D^{c,0}_{S3}$	5.25806 eV
$c_{T1,2}$	10.38710 eV	$D^{c,180}_{S3}$	2.58065 eV
β_{T1}	2.10667 a_0^{-1}	$\beta^{c,0}_{S3}$	0.91613 a_0^{-1}
D^e_{HF}	6.122 eV	$\beta^{c,180}_{S3}$	0.95484 a_0^{-1}
D^c_{S2}	0.26 eV	ρ^0_{S3}	0.51613 a_0
ρ_{S2}	2.38095 a_0	ρ^{180}_{S3}	1.33333 a_0
Δ_{S2}	0.5 a_0	θ^0_{S3}	0.09333 rad.
$c_{T2,1}$	1.26667 eV	θ^{180}_{S3}	0.18 rad.
$c_{T2,2}$	16.06667 eV	Δ^0_{S3}	0.49032 a_0
$c_{T2,3}$	11.61290 eV	Δ^{180}_{S3}	0.31613 a_0
$c_{T2,4}$	15.51613 eV	$c_{T3,1}$	0.38710 eV
β^0_{T2}	2.10667 a_0^{-1}	$c_{T3,2}$	1.80645 eV
β^{180}_{T2}	1.73333 a_0^{-1}	$c_{T3,3}$	0.51613 eV
D^e_{LiF}	5.909 eV	$c_{T3,4}$	0.51613 eV
E_{Li}*	1.848 eV	β^0_{T3}	0.89333 a_0^{-1}
		β^{180}_{T3}	0.80 a_0^{-1}

Table S-3. Values of the parameters used in the LiFH U_{12} potential energy function.

Parameter	Value	Parameter	Value
ρ_{12}	3.87097 a_0	$\rho_{HF,2}$	1.45161 a_0
Δ_{12}	0.45806 a_0	$\Delta_{HF,1}$	1.75806 a_0
g_1	1.27742 eV	$\Delta_{HF,2}$	0.98387 a_0
g_3	0.48 eV	ρ_{LiF}	2.17742 a_0
r_{LiH}^0	2.5873 a_0	Δ_{LiF}	0.56452 a_0
r_{LiF}^0	3.47619 a_0	ρ_{LiH}	4.27097 a_0
$\rho_{HF,1}$	1.15484 a_0	Δ_{LiH}	2.5 a_0

Table S-4. Singlet correction function parameters for NaFH-B.

Parameter	Value	Parameter	Value
$D_{e,\mathrm{HF}}^{\mathrm{B}}$	6.122 eV	$D_{e,\mathrm{NaF}}^{\mathrm{B}}$	4.94 eV
$r_{e,\mathrm{HF}}^{\mathrm{B}}$	1.733 a_0	$r_{e,\mathrm{NaF}}^{\mathrm{B}}$	3.6395 a_0
$c_{1,\mathrm{HF}}^{\mathrm{B}}$	1.1622 a_0^{-1}	$c_{1,\mathrm{NaF}}^{\mathrm{B}}$	0.32453 a_0^{-1}
$c_{2,\mathrm{HF}}^{\mathrm{B}}$	–0.025647 a_0^{-2}	$c_{2,\mathrm{NaF}}^{\mathrm{B}}$	1.5102
$c_{3,\mathrm{HF}}^{\mathrm{B}}$	0.059062 a_0^{-3}	$c_{3,\mathrm{NaF}}^{\mathrm{B}}$	3.0938 a_0
$c_{4,\mathrm{HF}}^{\mathrm{B}}$	2.1042 a_0	$c_{4,\mathrm{NaF}}^{\mathrm{B}}$	1.7107
$E_{s\to p}^{\mathrm{B}}$	2.097338 eV	κ_{HF}	15. a_0^{-1}

Table S-5. Triplet correction function parameters for NaFH-B.

Parameter	Value	Parameter	Value
$D_{e,HF}^{t}$	5.77096 eV	$w_{NaH,1}^{B}$	3.5875
$r_{e,HF}^{t}$	1.733 a_0	$w_{NaH,1}^{A}$	3.5875
$\beta_{e,HF}^{t}$	1.2669 a_0^{-1}	$w_{HF,2}^{1,B}$	5.54
$D_{e,NaF}^{t}$	4.49 eV	$w_{HF,2}^{2,B}$	4.15
$r_{e,NaF}^{t}$	3.6395 a_0	$w_{HF,2}^{1,A}$	5.125
$\beta_{e,NaF}^{t}$	0.696141 a_0^{-1}	$w_{HF,2}^{2,A}$	5.125
$w_{HF,1}^{B}$	2.913	$w_{NaF,2}^{1,B}$	9.01
$w_{HF,1}^{A}$	3.1183	$w_{NaF,2}^{2,B}$	1.92
$w_{NaF,1}^{B}$	2.0626	$w_{NaF,2}^{1,A}$	8.8
$w_{NaF,1}^{A}$	2.0528	$w_{NaF,2}^{2,A}$	1.62

Table S-6. Location and energy of the van der Waals and exciplex wells for the previous (A) and improved (B) NaFH fits.

	vdW well		exciplex	
	NaFH-A	NaFH-B	NaFH-A	NaFH-B
r_{HF} (a_0)	1.738	1.739	1.795	1.827
R_{NaF} (a_0)	4.671	4.684	4.304	4.167
χ (deg)	117.8	117.8	115.1	116.9
V_1 (eV)	-0.0761	-0.0737	-0.0312	0.0172
V_2 (eV)	1.624	1.684	1.571	1.600
V_2-V_1 (eV)	1.700	1.758	1.602	1.583

References for the Supporting Information

1 G. Di Lonardo and A. E. Douglas, Can. J. Phys. **51**, 434 (1973); J. A. Coxon, and P. G. Hajigeorgiou, J. Molec. Spec. **142**, 254 (1990).

2 J. Sato, J. Chem. Phys. **23**, 2465 (1955).

3 K. J. Laidler and J. C. Polanyi, Prog. Reaction Kinetics **3**, 1 (1965).

4 J. K. Cashion and D. R. Hershbach, J. Chem. Phys. **40**, 2358 (1964).

5 M. S. Topaler, D. G. Truhlar, X. Y. Chang, P. Piecuch, and J. C. Polanyi, J. Chem. Phys. **108**, 5349 (1998).

6 M. S. Topaler, D. G. Truhlar, X. Y. Chang, P. Piecuch, and J. C. Polanyi, J. Chem. Phys. **108**, 5378 (1998).

7 M. C. Douay, A. M. R. P. Bopegedra, C. R. Brazier, and P. F. Bernath, Chem. Phys. Lett. **148**, 1 (1988).

8 D. L. Carroll, FORTRAN GA (1996) as described in D. L. Carroll, AIAA J. **34**, 338 (1996).

Chapter Four

4

Fewest-Switches with Time Uncertainty: A Modified Trajectory Surface Hopping Algorithm with Better Accuracy for Classically Forbidden Electronic Transitions

I. Introduction

Semiclassical trajectory simulations[1–11] have proven useful for modeling electronically nonadiabatic dynamics for a wide variety of chemical systems,[11–23] and we have recently engaged in a systematic set of studies designed to test and improve these methods.[11–23] Semiclassical trajectory methods are especially interesting because they are readily applicable to large systems (e.g., bacteriorhodopsin) for which a full quantum dynamical treatment is likely to remain prohibitively computationally expensive for some time. Before applying semiclassical methods to large systems, it is advisable to validate them by studying smaller systems where benchmarks are available or can be calculated. Fortunately, the increased availability of converged quantum mechanical calculations for fully three-dimensional atom-diatom systems[12–14,16–19,23,24] has provided a useful set of benchmark test cases for judging the accuracy of several semiclassical trajectory methods[11–14,16,17,19–23,25–31] that have been proposed. The set of test cases, if carefully designed, also provides a means of systematically improving the semiclassical trajectory approach by identifying the dominant errors and developing methods that reduce these errors.

Although many of the existing and newly designed semiclassical trajectory methods show promise, the fewest-switches[8,27,32] surface hopping[1,2,5,6,8,9,11,12,14,16–18,23,26,27,30–41] algorithm of Tully (called here TFS and

elsewhere molecular dynamics with quantum transitions or MDQT) has proved to be surprisingly robust despite its simple formulation.[11–14,16–23] Trajectory surface hopping methods assume that the nuclear dynamics of the system may be approximately described by an ensemble of noninteracting trajectories, and that each trajectory evolves classically under the influence of a potential energy surface that corresponds locally to a single electronic state. Electronic transitions are incorporated into the classical nuclear dynamics by interrupting the single electronic surface propagation with a series of hopping decisions. At a hopping decision, a surface switch (or hop) from the occupied electronic state *i* to some target electronic state *j* occurs with a probability P_{h}^{ij}, where P_{h}^{ij} is usually some function of the quantum mechanical electronic state probability density integrated along the classical trajectory. The TFS algorithm defines P_{h}^{ij} such that hopping is minimized in the sense that trajectories hop only when there is a net flow of electronic state probability density out of the occupied state during the time interval between hopping decisions. In general, the target state and the occupied state may have different potential energies at a surface hop, and when a trajectory hops successfully the nuclear momentum is adjusted along some hopping vector **h** (usually the nonadiabatic coupling vector[1,8]) such that total energy is conserved.

As mentioned above, the TFS method has been applied with success to a wide variety of chemical systems. However, some limitations and ambiguities in the TFS method (and surface hopping methods in general) were pointed out in the original formulation[27] and have also been discussed more recently.[23,31,41] Here we focus attention on the problem of frustrated hopping.[16–18,23,30,31,41–44] The TFS algorithm may give a nonzero value of P_{h}^{ij} (and therefore may call for a surface hop) at a geometry along the trajectory where the energy gap between the occupied and the target electronic state is greater than the maximum classically allowed nuclear energy adjustment that is achievable by adjusting the momentum in the direction of **h**, i.e., a hop may be called for when the nuclear momentum cannot be adjusted along **h** such that total energy is conserved. Hopping attempts of this type are said to be “classically forbidden” or “frustrated”. The presence of frustrated hopping ruins the self-consistency built into the

TFS method and can therefore lead to an incorrect final electronic state distribution of trajectories.

Recently, we have systematically tested[23] several variants of the TFS method that have been proposed to deal with the problem of frustrated hopping. Unfortunately, none of the methods tested were completely satisfactory. In general, we found that the loss of self-consistency that results from frustrated hopping causes the TFS method to significantly overestimate the total probability of nonadiabatic quenching for weakly coupled systems. Conversely, by artificially allowing *all* trajectories that experience classically forbidden hopping attempts to switch electronic surfaces (simulating a fully self-consistent result), the total probability of nonadiabatic quenching is significantly underestimated. This numerical result motivates the search for a modification of the TFS method that allows some but not all hops that are frustrated to somehow switch electronic states, and in the present paper we describe such a method.

One can identify two limitations of the TFS semiclassical trajectory approach that lead to frustrated hopping: (1) The TFS semiclassical trajectory approach algorithm does not allow tunneling into a new electronic state, and (2) the TFS hopping probability does not properly treat electronic state decoherence (also called dephasing). The first consideration (1) is a consequence of the classical trajectory approach. The quantum mechanical nuclear wavefunction of a dynamical system may have a finite probability amplitude in a region where classical trajectories are forbidden by energy conservation. These quantum mechanical “tails” may induce physically meaningful electronic transitions in regions where surface hops are classically energetically forbidden, and this is a manifestation of tunneling. Within the classical trajectory approach these meaningful electronic state tunneling transitions result in frustrated hops. The second consideration (2) is a result of the formulation of the TFS hopping probability. Specifically, the TFS method gives the fully self-consistent electronic state populations at all times only for systems with degenerate electronic states, i.e., only when the ensembles of trajectories that occupy different electronic states do not separate in phase space. Of course, realistic chemical systems feature nondegenerate electronic states, often with greatly disparate potential energy topographies. Nondegenerate potential energy surfaces lead to

decoherent ensembles of trajectories in each electronic state,[20,21,45] and this decoherence results in a decreased probability of electronic transition. The TFS formulation does not properly treat electronic state decoherence, and therefore the TFS method over-predicts electronic transitions, especially in classically forbidden regions where classical trajectories cannot exist in the target electronic state.

The frustrated hops associated with (1) above are considered physically meaningful in the fewest-switches surface hopping context and should be allowed to switch electronic states. The frustrated hops resulting from (2) above are not physically meaningful and should be ignored. These two considerations provide a reasonable means of interpreting the numerical result obtained in our previous study[23] that was discussed above. The present paper describes a modification of the TFS algorithm that first identifies if a frustrated hop is physically meaningful and is a result of electronic state tunneling (consideration 1) or if a frustrated hop is not physically meaningful and is a result of the improper treatment of electronic state decoherence (consideration 2). The method then allows trajectories that experience a physically meaningful frustrated hops to tunnel to a nearby classically allowed geometry and switch electronic states. The new semiclassical trajectory method is called the fewest-switches with time uncertainty (FSTU) method and is identical to the TFS method for classically allowed surface hops.

We tested the FSTU method against the TFS method on a family of weakly coupled systems[23] that were designed to be very sensitive to the treatment of classically forbidden hops. The results of these tests show that the nonlocal hopping (as in the FSTU method) is necessary for properly modeling electronic transitions and accurately predicting the total nonadiabatic quenching probability and the product branching ratio.

The modification of the TFS method proposed here is similar in its aims to a recent attempt to modify the surface hopping method that was proposed by Zhu et al.,[43,44] although we each arrived at our starting point and out modifications independently by separate routes. Both methods remove frustrated hopping by allowing nonlocal surface hops, and the two methods will be compared in more detail in the Discussion section.

This paper is organized as follows: Section II summarizes the important features of the model surfaces. The semiclassical calculations, including the details of the FSTU method, are described in Sec. III, and the results are presented in Sec. IV. The results are discussed and summarized in Secs. V and VI, respectively.

II. Model Potential Energy Matrices

The YRH family[23] of three-body potential energy matrices (PEMs) used to test the FSTU method models the nonadiabatic scattering process of an electronically excited model Y atom and a diatomic molecule RH:

$$\mathrm{Y}^* + \mathrm{RH}(v, j) \rightarrow \begin{cases} \mathrm{Y} + \mathrm{RH}(v'', j'') & \text{(R1a)} \\ \mathrm{R} + \mathrm{YH}(v', j')\,, & \text{(R1b)} \end{cases}$$

where the asterisk indicates electronic excitation, and the primes on the vibrational v and rotational j quantum numbers indicate that these quantities are not necessarily conserved. The mass combination for the model atoms was chosen to be 10 and 6 amu for the Y and R atoms, respectively. The H atom has the mass of hydrogen, i.e., 1.00783 amu. Details of the family of YRH surfaces are presented in an earlier work.[23] Briefly, the family of YRH surfaces is made up of four members, and each member differs from the others only in the magnitude of the diabatic coupling. The maximum diabatic coupling for the four potential matrices discussed in the present work are $U_{12}^{\max} = 0.20$, 0.10, 0.03, and 0.01 eV.

As discussed below, the semiclassical trajectory calculations were carried out in the adiabatic representation. The adiabatic potential energy surfaces were obtained by diagonalizing the diabatic PEM. The adiabatic surfaces are coupled by the scalar product of the velocity and the nonadiabatic coupling vector **d**.[1,8] As discussed elsewhere,[18] one can calculate **d** without approximation from the diabatic matrix elements and their gradients.

The initial scattering conditions will be labeled by the shorthand (E/eV, j) where E/eV is the total energy in eV, and j is the initial rotational quantum number of the RH diatom. The initial vibrational quantum number of the RH diatom is zero, and the total

angular momentum is also zero. We consider a total of twelve test cases; for each of the four PEMs discussed above, we consider three sets of initial conditions: (1.10, 0), (1.10, 6), and (1.02, 0).

III. Semiclassical Trajectory Calculations and Time-Uncertainty Switching Algorithm

Semiclassical trajectory surface hopping calculations were carried out using version 6.6 of the NAT computer code.[46] Details of our implementation of the semiclassical trajectory algorithm including the selection of the initial conditions, the propagation of the classical trajectories, the implementation of the fewest-switches algorithm, and the final-state analysis may be found elsewhere.[2,14,23] Briefly, all of the calculations reported here were carried out in the adiabatic representation, and the hopping vector **h** was taken to be a unit vector in the direction of the nonadiabatic coupling vector **d**.[1,8] This choice for **h** has been justified theoretically[34,37,47] and numerically.[12,14]

The fewest-switches with time uncertainty (FSTU) method is a modification of the TFS method that incorporates nonlocal hopping such that some (but not all) frustrated hops are allowed to switch electronic states. The FSTU method is identical to the TFS method except when a trajectory experiences a frustrated hop. Specifically, the quantum mechanical electronic state population density $P_i(t)$ is obtained by integrating the solution of the time-dependent Schrödinger equation along the classical trajectory $\mathbf{R}(t)$ and is given by (in the adiabatic representation for a two-state system)[1,8,27]

$$\dot{P}_i(t) = -2\,\mathrm{Re}[a_{ij}^*(t)\,\dot{\mathbf{R}}(t)\cdot\mathbf{d}], \qquad (1)$$

where the overdot indicates a time derivative, $i \neq j$, a_{ij} is the cross term of the electronic state density matrix (e.g., $P_i = a_{ii}$), $\dot{\mathbf{R}}$ is the velocity of the classical trajectory, **d** is the nonadiabatic coupling vector between states i and j, and $i = 1$ for the ground electronic state and $i = 2$ for the excited electronic state. The fewest-switches[8,27] hopping probability P_{h}^{ij} is computed from $P_i(t)$

$$P_{\mathrm{h}}^{ij}(t) = \max\left(0, \frac{-\dot{P}_i(t)\,\delta t}{P_i(t)}\right), \tag{2}$$

where the system is currently occupying state i, and δt is the time interval between hopping decisions. If the fraction of trajectories in each electronic state $F_i(t)$ is equal to the quantum mechanical electronic state density $P_i(t)$ (for all i) at the start of the simulation, trajectories switch surfaces according to eq. (2), and *all* surface hops are allowed then $F_i(t)$ and $P_i(t)$ will be equal for all t. (Of course, $F_i(t)$ and $P_i(t)$ will not be *exactly* equal due to the finite number of trajectories in the computational ensemble.) If a surface hop is called for by eq. (2) and the hop is frustrated, this self-consistency will no longer be maintained. We note that the presence of frustrated hops results in a "fewer-than-fewest-switches" method, and we will comment on this at the end of Section V.

The FSTU treatment of a frustrated hop is discussed next. The time-energy version of the uncertainty principle[48]

$$\Delta E \Delta t \approx \hbar\,. \tag{3}$$

may be interpreted as the system borrowing some energy ΔE for some time Δt. We incorporate this feature in the semiclassical theory by allowing a trajectory $\mathbf{R}(t)$ that experiences a frustrated hop to tunnel and hop successfully at some nearby geometry along $\mathbf{R}(t)$ that it is classically allowed and where the time that the trajectory tunnels is within the time interval Δt given by eq. (3). Specifically, if a hop at time t_0 is classically forbidden, the trajectory is assumed to hop at some time t_{h} (if any such time exists) that minimizes $|t_0 - t_{\mathrm{h}}|$ subject to the following two criteria: (1) a hop is classically allowed at $\mathbf{R}(t_{\mathrm{h}})$, and (2) the difference between t_0 and t_{h} satisfies

$$\left|t_0 - t_{\mathrm{h}}\right| \le \hbar / 2\Delta E\,, \tag{4}$$

where the factor of ½ introduced into eq. (4) ensures that the distribution of nonlocal hops around t_0 will have a maximum width of Δt given by eq. (3). In eq. (4), ΔE is the difference between the potential energy gap at $\mathbf{R}(t_0)$ and the available kinetic energy along the hopping vector at time t_0, i.e., ΔE is the energy that the trajectory would need to "borrow" in order to hop at t_0. Notice that the trajectory may hop nonlocally both

forward and backward in time. For some frustrated hops these criteria cannot be satisfied, and these frustrated hops are thought to be caused by the improper treatment of decoherence effects (as discussed in Secs. I and V) and are ignored.

Our development of the FSTU method is a culmination of a series of studies[11–23] in which we have systematically examined and tested several possible options and variations in the surface hopping approach. This includes comparing the original fewest-switches criterion for invoking a surface hopping decision to the Blais-Truhlar[12–16] and generalized Blais-Truhlar[16] criteria, comparing diabatic and adiabatic representations for the electronic probability amplitude and trajectory propagation,[11,18–22] testing the effect of symmetrizing the speed or coupling in computing the hopping probability,[11,23] comparing various choices for the hopping vector,[13,15,17] and testing the effect of rotating the hopping vector when the momentum component along the hopping vector is too small to allow a hop,[11,17,18,23] testing various combinations of reflecting or ignoring hops when they are frustrated,[23] comparing energy conserving to energy non-conserving methods for assigning final discrete quantum numbers on the basis of the continuous final trajectory variables,[11,14,16,23] and comparing histogram methods to smooth sampling for assigning final discrete quantum numbers.[11,14,16,17,23] Consideration of what we learned in those studies[11–23] and from related work[30,49,50] not only motivated the present suggestion of an improved fewest-switches algorithm but also—very significantly—gives us confidence that the improved performance (see below) of the FSTU scheme is not simply the result of an unphysical cancellation of errors resulting from poor methodological decisions for the other aspects of the surface hopping scheme. Our final recommendations for the best way to carry out surface hopping calculations can be summarized as follows: (1) Choose hopping decision locations on the basis of the fewest-switches with time uncertainty algorithm. (2) Choose the electronic state representation (adiabatic or diabatic) by the Calaveras County[11] criterion. (3) Do not employ symmetrization schemes. (4) Choose the hopping vector along the nonadiabatic coupling vector without rotation. (5) If hops are frustrated, ignore them. (6) Assign electronic states according to the surface that a trajectory finishes on, and assign final

vibrational and rotational quantum numbers by either the energy non-conserving histogram (ENH) method,[14,16,17] which gives a well defined error estimate,[2] or the energy non-conserving quadratic smooth sampling (ENQSS) method,[14,17,48] which may be significantly more accurate or give better statistics (but without a well-defined error estimate), with the possibility in reserve that a more sophisticated final-state algorithm may be needed when one is near an energy threshold for a final state of interest. The combination of all these choices defines the standard FSTU algorithm. In the present paper, all reported results were obtained by the ENH scheme, but the ENQSS results are very similar.

All calculations in the present paper were carried out using the adaptive integration algorithm that we designed for fewest-switches surface hopping calculations in a previous paper.[17] This algorithm uses a Bulirsch-Stoer integrator with polynomial extrapolation,[12,51] and is specifically modified to prohibit the integrator from stepping over peaks and local minima in the electronic probabilities.[17] For the present calculations the parameters[17] were given the following values: $\varepsilon_{BS} = 10^{-12}\ E_h$ ($1\ E_h = 27.211$ eV) and $h_{min} = 10^{-4}$ a.u. (1 a.u. = 2.4189×10^{-2} fs), which gives convergence for the TFS results. For the FSTU results, another consideration arises. In particular, we found that in typical cases $\hbar / 2\Delta E$ is only a few times larger than the step size required to converge the integration of the coupled differential equations. Thus one may require smaller a step size for the integration to the final value of t_h than for the rest of the propagation. In the present application we selected t_h from a set of discrete times obtained by integrating the classical trajectories numerically, and we checked that the FSTU results are well converged with respect to step size.

IV. Results

We tested the FSTU method on the four YRH systems using the three sets of initial conditions described in Sec. II, for a total of twelve test cases. Table 1 shows the mean unsigned relative error (MURE) of the vibrational v and rotational j moments for the reactive (single primes) and non-reactive electronically quenched (double primes)

products, the probability of reaction P_R, the probability of nonreactive electronic quenching P_Q, the total nonadiabatic quenching probability $P_N = P_R + P_Q$, and the product branching ratio $F_R = P_R/P_N$, obtained by averaging the unsigned relative errors (UREs) for the twelve test cases. Also shown is the MURE for the TFS method. The TFS semiclassical trajectory results and the fully-converged quantum mechanical results used to compute the UREs were taken from Ref. 23. Note that of the several variants of the TFS method discussed in Ref. 23, we used the data for the TFS variant where all frustrated hopping attempts were ignored [called TFS-(+,+) in Ref. 23]. Table 1 shows that nonlocal hopping (as in the FSTU method) reduces the error in the reaction probability by a factor of 1.9, the error in the quenching probability by a factor of 1.5, the error in the product branching ratio by a factor of 1.4, and the error in the total nonadiabatic probability by a factor of 2, where all errors are MUREs. The MUREs in the reactive moments are similar for the FSTU and TFS methods, whereas the FSTU method is less accurate by a factor of 1.5 for the quenching moments.

Table 2 shows the UREs for the total nonadiabatic probability P_N and the product branching ratio F_R for each of the twelve test cases. For P_N, the FSTU method is less accurate than the TFS method for only two of the twelve test cases, and in these two cases both the FSTU and the TFS method have small UREs. For the other ten test cases, the FSTU method is more accurate than the TFS method for P_N; the URE for the FSTU method is smaller than the URE for the TFS method by a factor of ~2 for six cases, a factor of ~4 for two cases, and factors of 5.8 and 9.3 for the remaining two cases. For the product branching ratio F_R, the FSTU method is slightly less accurate than the TFS method for four of the twelve cases (by an average factor in the UREs of 1.1). For the remaining eight cases, the FSTU method is more accurate than the TFS method in predicting F_R; the URE in F_R is smaller for the FSTU method by factors of 1.4 – 2.0 for six cases, and factors of 3.0 and 4.9 for the remaining two cases.

Shown in Table 3 is the average final value of the quantum mechanical ground electronic-state probability density [i.e., $P_1(t = \infty)$ averaged over all the trajectories in the ensemble] for each of the twelve test cases and for both the FSTU and TFS methods.

Also shown is the fraction of trajectories that finished the simulation in the ground electronic state [note that $P_N \equiv F_1(t = \infty)$]. The FSTU method retains more self-consistency in the fewest-switches algorithm than the TFS method (i.e., P_N is closer to $<P_1(t = \infty)>$ for the FSTU method). Also shown in Table 3 is the probability (f) that a trajectory experienced a frustrated hop and finished the simulation in the ground electronic state. The FSTU method (by design) has less frustrated hopping than the TFS method by an average factor of 1.5.

The product of P_N and $(1 - f)$ (where $1 - f$ is the probability that a trajectory finished the simulation in the ground electronic state and did *not* experience a frustrated hop) is tabulated in Table 3 and gives a rough estimate of the fully self-consistent fewest-switches result. These values agree very well with $<P_1(t = \infty)>$, but do not agree with the accurate quantum mechanical values of the total nonadiabatic quenching probability P_N^{QM}, also shown in Table 3.

V. Discussion

The TFS method is formulated such that surface hops are minimized, and this "fewest-switches" formulation is accomplished by allowing surface hops only when there is a net flow of electronic state probability density out of the currently occupied electronic state during the interval between hopping decisions. The presence of classically forbidden electronic transitions destroys the self-consistency built into the TFS method, and results in a "fewer-than-fewest-switches" method. We note, however, that a fully self-consistent fewest-switches algorithm [i.e., $P_N \approx <P_1(t = \infty)>$ in Table 3] would greatly underestimate the accurate total nonadiabatic quenching probability P_N^{QM}. The fact that $P_N^{QM} \not\approx <P_1(t = \infty)>$ points out the serious problem in the semiclassical trajectory formalism that was mentioned earlier. Namely, the electronic state population density $P_i(t)$ given by eq. (1) does not properly include electronic state decoherence effects. A proper treatment of decoherence within the semiclassical trajectory approach would require that the electronic state density coherence a_{ij} depend on all of the

trajectories in the ensemble, and thus would require simultaneous propagation of the entire ensemble of trajectories.[22,52] This would increase the computational complexity and cost of the surface hopping algorithm, and we therefore restrict our attention to the independent trajectory approach.

One effect of the lack of proper treatment of the electronic state decoherence in the semiclassical trajectory approach is that the electronic state coherence term a_{ij} computed for each independent trajectory does not properly go to zero when the ensembles of trajectories in the two electronic states *i* and *j* separate in phase space. If for some fully decoherent trajectory a_{ij} is nonzero, there will be a flow of electronic state density (hopping) between electronic states, whereas an accurate treatment of a_{ij} would give $a_{ij} = 0$ and would damp out these (often frustrated) electronic transitions, as can be seen from eqs. (1) and (2). The improper treatment of decoherence can have serious effects anywhere along the classical trajectory, but we note that a dramatic example of this problem occurs when the unoccupied electronic state is too high in energy to be occupied by any classical trajectories. When this is the case, there will be no trajectories directly "above" the ensemble of ground-state trajectories, and a_{ij} should therefore be nearly zero. As mentioned above, the independent semiclassical trajectory value of a_{ij} may not be zero, and a trajectory on the lower potential energy surface may therefore experience a frustrated hop in this region where a proper treatment of the decoherence would have predicted no hops at all.

From these considerations alone, one may be motivated to ignore all frustrated hopping as being caused by the lack of the proper treatment of the decoherence of divergent trajectories. We have shown, however, that ignoring all frustrated hopping (as in the TFS method) leads to systematic errors in the total nonadiabatic quenching probability.[23] The FSTU method, by allowing some frustrated hopping attempts to become successful nonlocal hops, greatly reduces these errors, as shown in Sec. IV. The FSTU method may be justified by noting that a quantum mechanical nuclear wavefunction will have tails that extend into regions that are inaccessible to classical trajectories. These tails lead to electronic state population transfer in classically

forbidden regions and therefore may induce frustrated hopping in the TFS algorithm, whereas this kind of hop is allowed by the FSTU method by incorporating nonlocal hopping into the fewest-switches formalism. The maximum "nonlocality" of a hop in the FSTU method corresponds to the approximate extension of the quantum mechanical tails into the classically forbidden regions as estimated by eq. (4).

Ideally, one would develop a method that incorporates the proper treatment of decoherence into the independent semiclassical trajectory scheme by modifying the equations for calculating a_{ij} along the classical trajectory. Such a scheme, however, would still feature classically frustrated hopping as a result of the electronic state tunneling discussed above. The FSTU is a desirable practical alternative to an explicit treatment of decoherence effects because it is a simple extension of the TFS method. Its usefulness is further justified numerically in the present study, as it is shown to greatly improve the accuracy of the fewest-switches method.

The present formulation of the FSTU method is simple and straightforward, but it is not unique. For example, the uncertainty relation in eq. (3) is strictly an inequality, and we can therefore write the FSTU nonlocal hopping criterion in eq. (4) as

$$\left|t_0 - t_\mathrm{h}\right| \le x\hbar / 2\Delta E \,, \tag{5}$$

where x is some number greater than or equal to one. It is natural to take $x = 1$ (as in the FSTU method), but we also tested several variants of the FSTU method with different values of x, namely $x = 2$, 4, 10, and ∞ (where $x = 0$ is, of course, the TFS method). We found that the value of $x = 1$ gives the best agreement with the accurate quantum mechanical results.

For some systems, it may be necessary to devise more complicated schemes for introducing nonlocal hopping into the fewest-switches algorithm such as alternate definitions of ΔE or allowing trajectories to tunnel in some direction other than along the classical trajectory (say, along the nonadiabatic coupling vector). The FSTU method performs well without greatly increasing the complexity of the surface hopping algorithm, and we did not test the more complicated schemes mentioned above. We did consider allowing trajectories to hop at any time (not just the closest time to t_0) that satisfies the FSTU nonlocal hopping criteria in Sec. III by choosing between each time

that satisfies these criteria with some probability. We found, however, that this modification had no significant effect on the values of the observables, and we can explain this by noting that the average value of $\hbar/2\Delta E$ is much less than the characteristic time scales of the system. Therefore, resolving the hopping time within the $\hbar/2\Delta E$ interval has little effect on the overall dynamics.

It is interesting to note that the problem of frustrated hopping has been addressed recently[43,44] using nonlocal hopping within the Landau-Zener trajectory surface hopping scheme. The Landau-Zener trajectory surface hopping scheme allows electronic transitions whenever a classical trajectory crosses some predefined hopping seam, and the hopping probability is computed from the electronic-state energies at the seam and the component of the nuclear momentum perpendicular to the hopping seam. Zhu et al. have proposed an elegant method[43,44] (which we will call the ZNN method) that incorporates nonlocal hopping into the Landau-Zener surface hopping formalism. Specifically, frustrated hops are removed by allowing trajectories to tunnel perpendicular to the hopping seam. The ZNN method was shown to greatly improve the semiclassical trajectory results for the cases to which is was applied.

We note that the ZNN method differs from the FSTU method in several important ways. First, a FSTU trajectory, like a TFS trajectory, may experience a hopping attempt anywhere along the classical trajectory and not only at a predefined hopping seam. We consider this to be essential for modeling many kinds of nonadiabatic systems, and hence we are only interested in the further development of methods with this generality. Second, the FSTU hopping probabilities are determined by integrating the time-dependent Schrödinger equation along the classical trajectory, whereas the ZNN hopping probabilities are based on information at the hopping seam. The ZNN hopping probabilities therefore do not suffer from the decoherence problem discussed here for the TFS method, at least when the assumptions underlying the Landau-Zener-type treatment are satisfied. Third, FSTU trajectories tunnel along the classical trajectory *in time* for some time that is no greater than that allowed by the uncertainty principle, whereas the ZNN trajectories tunnel *in space* perpendicular to the hopping seam and are not limited in their tunneling distance.

Other methods that delocalize the intersurface transitions are the full multiple spawning method,[22,29] which is based on the semiclassical propagation of Gaussian wave packets,[53,54] and methods based on a self-consistent or mean-field potential,[11,14,16,19–21,25,28] such as the semiclassical Ehrenfest method,[11,14,16,25,28] continuous surface-switching,[11,19,20] and natural decay of mixing.[21] Our view is that there are three kinds of semiclassical molecular dynamics methods for non-Born-Oppenheimer systems, namely, trajectory surface hopping methods, self-consistent potential methods, and wave packet propagation methods, and it is useful to find the best general method in each category as well as to compare different kinds of methods. We have previously presented arguments that the natural decay of mixing[21] is the best method of the self-consistent potential type, and the present paper indicates that the FSTU method appears to be a culmination of our efforts to find a best general method of the trajectory surface hopping type. The systematic testing of standardized semiclassical wave packet methods is more in its infancy, but the FMS-M method has been proposed as a standardized validated method.[22] Comparing method between categories, we can summarize our previous studies[11,14–16,18–23] without repeating all the details by saying that the natural decay of mixing algorithm has the strong advantages that it avoids discontinuities (hops) and is independent of choosing an adiabatic of diabatic representation in strong interaction regions, whereas surface hopping methods have an important advantage of simplicity of computer coding, and the Calaveras County criterion[11,20–22] provides a general prescription for choosing a representation. Both of these kinds of methods have the advantage over wave packet propagation methods that they are less expensive (at least with currently available computer programs[45,55]), and hence they facilitate a more thorough sampling of the space of the initial conditions, making realistic simulations more feasible.

It has been noted above that the FSTU method has more surface switches than the TFS method. This should not be seen as a violation of the "fewest-switches" formulation. As discussed above the presence of frustrated hops in the TFS method results in a "fewer-than-fewest-switches" method. Only in the limit of a fully self-consistent surface hopping method does the number of hops *increase* such that the

method becomes the “fewest-switches” method as it was originally formulated. The FSTU method is, in fact, closer than the TFS method to the “fewest-switches” fully-self consistent result.

VI. Conclusions

We have described a new method for treating classically forbidden electronic transitions in trajectory surface hopping calculations called the fewest-switches with time uncertainty (FSTU) algorithm. The FSTU method improves the self-consistency of the fewest-switches algorithm. We tested the FSTU method using a set of twelve three-body, two-state test cases that were designed to provide sensitive tests of methods for treating weakly coupled highly quantal systems, and hence the provide a challenging test of methods for correcting the problem of frustrated hopping. We found that the new formalism greatly increases the accuracy of the total nonadiabatic quenching probability and the product branching ratio.

Acknowledgments

This work was supported in part by the National Science Foundation under grant no. CHE00-92019. Sam Stechmann contributed to this chapter.

References

1 J. C. Tully, in *Dynamics of Molecular Collisions*, edited by W. H. Miller (Plenum, New York, 1976), Part B, pp. 217–267.

2 D. G. Truhlar and J. T. Muckerman, in *Atom-Molecule Collision Theory*, edited by R. B. Bernstein (Plenum, New York, 1979), pp. 505–566.

3 H. Nakamura, Adv. Chem. Phys. **82**, 243 (1992).

4 E. A. Gislason, G. Parlant, and M. Sizun, Adv. Chem. Phys. **82**, 321 (1992).

5 S. Chapman, Adv. Chem. Phys. **82**, 423 (1992).

6 M. F. Herman, Annu. Rev. Phys. Chem. **45**, 83 (1994).

7 H. Nakamura, in *Dynamics of Molecules and Chemical Reactions*, edited by R. E. Wyatt and J. Z. H. Zhang (Marcel Dekker, New York, 1996), p. 473–529.

8 J. C. Tully, in *Modern Methods for Multidimensional Dynamics Computations in Chemistry*, edited by D. C. Thompson (World Scientific, Singapore, 1998), pp. 34–72.

9 J. C. Tully, Faraday Discuss. Chem. Soc. **110**, 407 (1998).

10 E. E. Nikitin, Annu. Rev. Phys. Chem. **50**, 1 (1999).

11 M. D. Hack and D. G. Truhlar, J. Phys. Chem. A **104**, 7917 (2000).

12 M. S. Topaler, M. D. Hack, T. C. Allison, Y.-P. Liu, S. L. Mielke, D. W. Schwenke, and D. G. Truhlar, J. Chem. Phys. **106**, 8699 (1997).

13 M. S. Topaler, T. C. Allison, D. W. Schwenke, and D. G. Truhlar, J. Phys. Chem. A **102**, 1666 (1998).

14 M. S. Topaler, T. C. Allison, D. W. Schwenke, and D. G. Truhlar, J. Chem. Phys. **109**, 3321 (1998), **110**, 687(E) (1999), **113**, 3928(E) (2000).

15 Y. Zeiri, G. Katz, R. Kosloff, M. S. Topaler, D. G. Truhlar, and J. C. Polanyi, Chem. Phys. Lett. **300**, 523 (1999).

16 Y. L. Volobuev, M. D. Hack, and D. G. Truhlar, J. Phys. Chem. A **103**, 6225 (1999).

17 M. D. Hack, A. W. Jasper, Y. L. Volobuev, D. W. Schwenke, and D. G. Truhlar, J. Phys. Chem. A **103**, 6309 (1999).

18 M. D. Hack, A. W. Jasper, Y. L. Volobuev, D. W. Schwenke, and D. G. Truhlar, J. Phys. Chem. A **104**, 217 (2000).

19 Y. L. Volobuev, M. D. Hack, M. S. Topaler, and D. G. Truhlar, J. Chem. Phys. **112**, 9716 (2000).

20 M. D. Hack and D. G. Truhlar, J. Chem. Phys. **114**, 2894 (2001).

21 M. D. Hack and D. G. Truhlar, J. Chem. Phys. **114**, 9305 (2001).

22 M. D. Hack, A. M. Wensmann, D. G. Truhlar, M. Ben-Nun, and T. J. Martinez, J. Chem. Phys. **115**, 1172 (2001).

23 A. W. Jasper, M. D. Hack, and D. G. Truhlar, J. Chem. Phys. **115**, 1804 (2001).

24 S. L. Mielke, G. J. Tawa, D. G. Truhlar, and D. W. Schwenke, Chem. Phys. Lett. **234**, 57 (1995).

25 H.-D. Meyer and W. H. Miller, J. Chem. Phys. **70**, 3214 (1979).

26 N. C. Blais and D. G. Truhlar, J. Chem. Phys. **79**, 1334 (1983).

27 J. C. Tully, J. Chem. Phys. **93**, 1061 (1990).

28 A. Garcìa-Vela, R. B. Gerber, and D. G. Imre, J. Chem. Phys. **97**, 7242 (1992).

29 T. J. Martinez, M. Ben-Nun, and R. D. Levine, J. Phys. Chem. **100**, 7884 (1996), **101**, 6839 (1997).

30 U. Müller and G. Stock, J. Chem. Phys. **107**, 6230 (1997).

31 J.-Y. Fang and S. Hammes-Schiffer, J. Phys. Chem. A **103**, 9399 (1999).

32 J. C. Tully, Int. J. Quantum Chem. Symp. **25**, 299 (1991).

33 A. Bjerre and E. E. Nikitin, Chem. Phys. Lett. **1**, 179 (1967).

34 R. K. Preston and J. C. Tully, J. Chem. Phys. **54**, 4297 (1971). J. C. Tully and R. K. Preston, *ibid*. **55**, 562 (1971).

35 W. H. Miller and T. F. George, J. Chem. Phys. **56**, 5637 (1972).

36 P. J. Kuntz, J. Kendrick, and W. N. Whitton, Chem. Phys. **38**, 147 (1979).

37 M. F. Herman, J. Chem. Phys. **81**, 754 (1984).

38 N. C. Blais, D. G. Truhlar, and C. A. Mead, J. Chem. Phys. **89**, 6204 (1988).

39 G. Parlant and E. A. Gislason, J. Chem. Phys. **91**, 4416 (1989).

40 P. J. Kuntz, J. Chem. Phys. **95**, 141 (1991).

41 J.-Y. Fang and S. Hammes-Schiffer, J. Chem. Phys. **110**, 11166 (1999).

42 See endnote 39 in S. Hammes-Schiffer and J. C. Tully, J. Chem. Phys. **101**, 4657 (1994).

43 C. Zhu, K. Nobusada, and H. Nakamura, J. Chem. Phys. **115**, 3031 (2001).

44 C. Zhu, H. Kamisaka, and H. Nakamura, J. Chem. Phys. **116**, 3234 (2002).

45 E. Neria, A. Nitzan, R. N. Barnett, and U. Landman, Phys. Rev. Lett. **67**, 1011 (1991). O. V. Prezhdo and P. J. Rossky, J. Chem. Phys. **107**, 5863 (1997).

46 A. W. Jasper, Y. L. Volobuev, M. S. Topaler, T. C. Allison, M. D. Hack, Y.-P. Liu, S. N. Stechmann, T. F. Miller III, N. C. Blais, and D. G. Truhlar, NAT–version 6.6 (University of Minnesota, Minneapolis, 2000).

47 D. F. Coker and L. Xiao, J. Chem. Phys. **102**, 496 (1995).

48 J. J. Sakurai, *Modern Quantum Mechanics* (Addison-Wesley, Redwood City, 1985), pp. 78–80.

49 D. G. Truhlar, B. P. Reid, D. E. Zurawski, and J. C. Gray, J. Chem. Phys. **85**, 786 (1981).

50 M. S. Topaler and D. G. Truhlar, J. Chem. Phys. **107**, 392 (1997).

51 W. H. Press, S. A. Teukolsky, W. T. Vetterling, and B. P. Flannery, *Numerical Recipes in FORTRAN*, 2nd ed. (Cambridge University Press, Cambridge, UK, 1994); pp. 716–725.

52 R. B. Gerber, V. Buch, and M. A. Ratner, J. Chem. Phys. **77**, 3022 (1982). C. C. Martens and J.-Y. Fang, J. Chem. Phys. **106**, 4918 (1997). A. Donoso, D. Kohen, and C. C. Martens, J. Chem. Phys. **112**, 7345 (2000).

53 E. J. Heller, J. Chem. Phys. **75**, 2923 (1981).

54 R. T. Skodje and D. G. Truhlar, J. Chem. Phys. **80**, 3123 (1984).

55 M. D. Hack, D. G. Truhlar, M. Ben-Nun, T. J. Martinez, and R. D. Levine, FMS90–version 2.1 (University of Minnesota, Minneapolis and University of Illinois, Urbana, 2000).

Table 1. Mean unsigned relative errors (MUREs) for the TFS and FSTU methods averaged over twelve test cases.

Method	P_R	$\langle v' \rangle$	$\langle j' \rangle$	P_Q	$\langle v'' \rangle$	$\langle j'' \rangle$	P_N	F_R	Prob.[a]	Mom.[b]	All[c]
TFS[d]	1.36	0.12	0.14	0.29	0.23	0.67	0.32	0.93	0.73	0.29	0.51
FSTU	1.25	0.14	0.15	0.21	0.27	0.79	0.19	1.12	0.69	0.34	0.51

[a]Average MURE for the probabilities P_R, P_Q, F_R, and P_N.

[a]Average MURE for the moments $\langle v' \rangle$, $\langle j' \rangle$, $\langle v'' \rangle$, and $\langle j'' \rangle$.

[c]Average MURE for all eight observables.

[d]The MUREs for the TFS method were computed from the TFS-(+,+) data in Ref. 23.

Table 2. Unsigned relative errors (UREs) for the TFS and FSTU methods for the twelve test cases.

I. C.[a]	$U_{12}^{\max}$ / eV	P_N		F_R	
		TFS	FSTU	TFS	FSTU
(1.10, 0)	0.20	0.75	0.31	0.64	0.33
	0.10	0.18	0.05	0.48	0.28
	0.03	0.49	0.08	0.31	0.10
	0.01	0.43	0.24	0.14	0.15
(1.10, 6)	0.20	0.15	0.06	0.47	0.33
	0.10	0.41	0.26	0.61	0.66
	0.03	0.05	0.10	0.39	0.49
	0.01	0.05	0.09	0.41	0.49
(1.02, 0)	0.20	0.91	0.58	0.32	0.07
	0.10	0.11	0.06	3.23	2.32
	0.03	0.21	0.06	1.93	1.30
	0.01	0.16	0.02	2.25	1.51
Mean[b]		0.32	0.16	0.93	0.67

[a]Initial conditions are specified in Sec. II.

[b]Average of twelve cases.

Table 3. The quantum mechanical total nonadiabatic quenching probability P_N^{QM}, final ground electronic state probability density averaged over the ensemble of classical trajectories $\langle P_1\ (t = \infty)\rangle$, and the total nonadiabatic quenching probability P_N and frustrated hopping probability f for the TFS and FSTU methods.

I. C.[a]	U_{12}^{max} / eV	P_N^{QM} [b]	$\langle P_1\ (t = \infty)\rangle$[c]	TFS			FSTU		
				P_N	f	$(1-f)\,P_N$	P_N	f	$(1-f)\,P_N$
(1.10, 0)	0.20	5.74(2)[d]	3.48(2)	9.87(2)	0.73	2.67(2)	7.51(2)	0.64	2.67(2)
	0.10	3.99(2)	1.80(2)	4.87(2)	0.65	1.72(2)	3.80(2)	0.55	1.72(2)
	0.03	4.10(3)	1.21(3)	5.71(3)	0.60	2.26(3)	4.44(3)	0.49	2.26(3)
	0.01	4.34(4)	2.79(4)	6.93(4)	0.59	2.87(4)	5.40(4)	0.47	2.87(4)
(1.10, 6)	0.20	1.62(1)	1.59(1)	1.97(1)	0.39	1.20(1)	1.73(1)	0.31	1.20(1)
	0.10	9.07(2)	1.11(1)	1.27(1)	0.29	9.05(2)	1.15(1)	0.21	9.05(2)
	0.03	1.59(2)	1.32(2)	1.57(2)	0.28	1.14(2)	1.42(2)	0.20	1.14(2)
	0.01	1.83(3)	1.48(3)	1.87(3)	0.27	1.37(3)	1.66(3)	0.18	1.37(3)
(1.02, 0)	0.20	4.97(2)	5.08(2)	9.66(2)	0.64	3.51(2)	7.84(2)	0.55	3.51(2)
	0.10	3.44(2)	1.99(2)	3.98(2)	0.60	1.61(2)	3.24(2)	0.50	1.61(2)
	0.03	3.71(3)	2.93(3)	4.21(3)	0.56	1.86(3)	3.49(3)	0.47	1.86(3)
	0.01	4.21(4)	2.79(4)	5.04(4)	0.55	2.26(4)	4.14(4)	0.45	2.26(4)

[a]Initial conditions are specified in Sec. II.

[b]Accurate quantum mechanical P_N; these values are taken from Ref. 23.

[c]Average value of the ground-state electronic probability density, averaged over all the trajectories in the ensemble. This value is found to be the same for the TFS and FSTU methods to the number of figures presented.

[d]Note that $5.74(2) \equiv 5.74 \times 10^{-2}$.

Chapter Five

5

Coupled Quasidiabatic Potential Energy Surfaces for LiFH

I. Introduction

The LiFH system is ideal for detailed theoretical study because it is relatively simple yet features an interesting potential energy surface topography. The ground-state LiFH potential energy surface[1–13] and the dynamics of the electronically adiabatic Li + HF → LiF + H reaction[10–25] have been widely studied. The excited states[8,26,27] and electronically nonadiabatic dynamics[26,28] of LiFH have attracted attention only recently. The ground-state potential energy surface has a relatively deep van der Waals well in the Li(2*s*) + HF entrance valley and a barrier in the LiF + H exit valley. A strongly bound excited-state complex (exciplex) is present in the first excited-state at a geometry similar to (but tighter than) the geometry of the ground-state van der Waals well. The ground and first-excited states of the LiFH system are coupled nonadiabatically, forming a seam of avoided crossing at larger Li–F and H–F separations.

The features of the coupled LiFH potential energy surfaces allow for interesting dynamical processes. For example, the ground-state van der Waals molecules (Li···FH) may be excited into the exciplex [(Li···FH)*]. These excited-state complexes are relatively long-lived and may undergo electronically nonadiabatic dissociation[26,28] which can proceed either reactively to form LiF + H or non-reactively to form electronically quenched Li(2*s*) + HF:

$$\mathrm{Li}\cdots\mathrm{FH} \xrightarrow{h\nu} (\mathrm{Li}\cdots\mathrm{FH})^* \rightarrow \begin{cases} \mathrm{LiF} + \mathrm{H} & \text{(R1a)} \\ \mathrm{Li}(2s) + \mathrm{HF}. & \text{(R1b)} \end{cases}$$

This type of reaction is of particular importance as a means of probing the transition state region of the excited-state Li($2p$) + HF reaction. For sufficiently large excitation energies $h\upsilon$, another dissociation pathway is accessible where the (Li···FH)* exciplexes dissociate in an electronically excited state and form the Li($2p$) + HF product.

In order to facilitate the detailed theoretical study of the LiFH system, we present high-level *ab initio* calculations for a dense grid of nuclear geometries for the ground state and first five excited states of LiFH. Some of the features on the ground- and excited-state adiabatic potential surfaces are the result of the interaction of covalent and ionic valence bond configurations, and a multiconfigurational treatment is necessary to accurately describe these features. *Ab initio* calculations were performed with the multi-reference configuration interaction (MRCI) method employing relatively large reference spaces and a large one-electron basis set. Although in this work we focus mainly on the potential energy surfaces of the ground and first-excited states of the LiFH system, we also present less extensive results for other low-lying states of LiFH, including all states that correlate with the Li($2s\ ^2S$) + HF($X\ ^1\Sigma^+$) and Li($2p\ ^2P$) + HF($X\ ^1\Sigma^+$) limits.

The energies obtained from the *ab initio* calculations were used to construct a three-dimensional analytic fit for the two lowest-energy quasidiabatic[29–44] states of LiFH and their electronic coupling. In a previous work,[26] we have presented semiclassical trajectory photodissociation calculations using analytic fits for the NaFH and LiFH systems. The LiFH fit used in the previous study (which may be called surface fit H) was based on a limited set of *ab initio* data. In the current work, we described an improved LiFH fit called surface fit J that is based on the larger set of *ab initio* data presented here. Care has also been taken to explicitly include accurate long-range interactions, which were not included in the preliminary fit. The newly presented LiFH quasidiabatic potential energy matrix is global and can be used to describe ground-state or nonadiabatic bimolecular scattering processes as well as the photodissociation processes shown in eqs. (R1a) and (R1b) for both quantum mechanical and semiclassical dynamics simulations.

In Section II we present the details of the *ab initio* calculations for the LiFH system. Section III describes the procedure we used to obtain an analytic fit of the *ab*

initio data. Section IV discusses the fit and compares it to several ground-state LiFH fits and one excited-state LiFH fit that have appeared previously in the literature.[4,5,8,11–13]

II. *Ab Initio* Electronic Structure Calculations

Ab initio calculations were performed using the MRDCI variant[45] of the multi-reference configuration interaction (MRCI) method. In this approach, a series of variational CI calculations is carried out using sets of spin- and symmetry-adapted configuration state functions (CSFs) that are selected from all possible CSFs generated by single and double substitutions in reference configurations. For multi-reference calculations, the reference space contains those CSFs that are believed to be essential for the description of the nondynamical correlation in the electronic states of interest as well as some of the leading configurations needed for dynamical correlation. In each CI calculation, the selection of excited CSFs is made based on their importance in the CI wave function expansions, as determined by a selection threshold T (usually, a few μE_h or a fraction of one μE_h). The selection of excited CSFs is based on the estimated energy lowering effect of each added CSF on the desired eigenvalues of the Hamiltonian matrix involving reference CSFs, as explained elsewhere.[45] The CI eigenvalue problem then is solved several times for different values of selection threshold T, and the resulting energies are extrapolated to the $T = 0$ limit. This limit corresponds to the complete MRCISD (MRCI singles and doubles) eigenvalue problem.[45] The final MRDCI energy of a given electronic state is obtained by adding the simplified quasidegenerate Davidson correction[46] to the extrapolated MRCISD energy. In each of the three types of the MRDCI calculations reported in this work (referred to as Strategies A–C and fully described below), the extrapolated energies were obtained using three threshold values T, as described below.

Although in this study we were mainly interested in the two lowest states of $^2A'$ symmetry, we also wanted to understand the topography of the potential energy surfaces characterizing other low-lying states of the LiFH system. Thus, along with the ground

state ($\tilde{X}\ ^2A'$) and the first excited state ($\tilde{A}\ ^2A'$), we calculated the potential energy surfaces of four other states, including two more states of the $^2A'$ symmetry (the $\tilde{C}\ ^2A'$ and $\tilde{D}\ ^2A'$ states) and the two lowest states of $^2A''$ symmetry (the $\tilde{B}\ ^2A''$ and $\tilde{E}\ ^2A''$ states). The calculated states correlate with the six doublet states corresponding to the lowest-energy noninteracting-atom limit [i.e., the Li($2s\ ^2S$) + F($2p^5\ ^2P$) + H($1s\ ^2S$) asymptote]. These states include the Li($2s\ ^2S$, $2p\ ^2P$, $3s\ ^2S$) + HF($X\ ^1\Sigma^+$) states of the reactants and the LiF($X\ ^1\Sigma^+$, $A\ ^1\Pi$, $B\ ^3\Pi$, $C\ ^3\Sigma^+$, $D\ ^1\Sigma^+$) + H($1s\ ^2S$) states of products. In choosing the reference spaces and basis sets for our MRDCI calculations, we obtain a balanced description of the four lowest $^2A'$ and two lowest $^2A''$ states. We also obtain a very accurate description of the lowest two $^2A'$ states, and this was used to construct a 2 x 2 quasidiabatic fit described in Sections III and IV.

The basis set used in the MRDCI calculations consisted of the standard 6-311G(3d2f,3p2d) basis set,[47] augmented by several diffuse functions whose exponents were optimized to accurately reproduce selected properties of the Li, H, and F atoms (excitation energies of Li, ionization potential of Li, and electron affinities of H and F) and basic properties of the HF, LiF, and LiH diatomic fragments (the equilibrium bond lengths, vibrational term values, dissociation energies, dipole moments, and low-lying excited states). The following diffuse functions were used to augment the 6-311G(3d2f,3p2d) basis set (exponents in parentheses): s(0.0052) and p(0.0097) functions centered on Li, s(0.089), s(0.00001), and p(0.083) functions centered on F, and s(0.037), s(0.012), and p(0.055) functions centered on H. Cartesian representations of the d and f functions were employed throughout, so that the total number of contracted Gaussian functions in the basis set was 140. The high accuracy of our basis set can be judged by the results of the MRDCI calculations for the Li, H, and F atoms and HF, LiF, and LiH molecules, as shown in Tables 1-6. The total absolute energies for the diatomic calculations at the minimum energy bond length are −100.353263, −107.298414, and −8.043992 E_h, for the HF, LiF, and LiH diatomics, respectively.

The MRDCI calculations reported in this work were performed using ground-state restricted open-shell Hartree-Fock (ROHF) orbitals, and the lowest $1a'$ molecular

orbital was kept frozen. All ROHF and correlated calculations were performed using the C_S symmetry common to all LiFH nuclear configurations. The use of C_S symmetry in our calculations prompts a few remarks. When collinear arrangements of the Li, F, and H atoms are approached (i.e., at Li-F-H angles of 180° or 0°), the symmetry of the LiFH electronic Hamiltonian increases from C_S to $C_{\infty v}$, so that the A' and A'' states classify as Σ, Π, etc. states (similarly, the ROHF orbitals that for the bent configurations classify as a' and a'' orbitals become σ, π, etc. orbitals for the collinear arrangements of the Li, F, and H atoms). The incomplete reference spaces and the CSF selection procedures that are used in MRDCI calculations give results that are not unitarily invariant with respect to general orbital rotations within the core, active, and virtual blocks. In particular, the results for the collinear geometries may depend on whether we use C_S or $C_{\infty v}$ symmetry-adapted orbitals and CSFs. For this reason, we never used the $C_{\infty v}$ symmetry (or its C_{2v} Abelian subgroup) in our calculations, as this would result in a nonsmooth behavior of our calculated potential energy surfaces for Li–F–H angles approaching 180° and 0°. To mimic the collinear arrangements of the Li, F, and H atoms, while retaining the C_S symmetry for all geometries, we included Li–F–H angles of 179.99° and 0.01° in our grids.

The MRDCI calculations for the $^2A'$ states are based on 62 symmetry-adapted reference configurations (as defined by the orbital occupation numbers) or, equivalently, 99 spin- and symmetry-adapted CSFs. The $^2A''$ states were described by 24 reference configurations or 39 CSFs. These configurations were chosen so as to provide an accurate and well balanced zero-order description of the four lowest $^2A'$ and two lowest $^2A''$ states in the 6-root calculations with thresholds T = 4, 6, and 8 μE_h referred to as Strategy A (see the discussion below for further details), over a wide range of nuclear geometries, including: the Li + HF and LiF + H dissociation channels, the vdW well on the ground-state potential energy surface, the excited-state well, the region of the avoided crossing between ground and excited-state potential energy surfaces, and the transition-state region for the ground-state Li + HF → LiF + H reaction.

In the language appropriate for the Li + HF limit, the reference CSFs defining the $^2A'$ CI subproblem included the ground-state ROHF determinant, the $2s \rightarrow 2p$, $3s$, $3p$, $3d$, $4s$, $4p$, etc. single excitations in Li (important to describe excited states of the Li···FH complex), the valence $\sigma \rightarrow \sigma^*$ single and double excitations in HF (important to describe the bond breaking in HF), the valence $\pi \rightarrow \sigma^*$ as well as the Rydberg $\sigma, \pi \rightarrow \sigma$, π mono- and biexcitations in HF, the $2s$(Li) $\rightarrow \sigma^*$(HF), σ(HF) $\rightarrow 2s$, $2p$, $3s$, $3p$, $3d$, $4s$, $4p$(Li), etc. and π(HF) $\rightarrow 2s$, $2p$, $3s$, $3p$, $3d$, $4s$, $4p$(Li), etc. monoexcitations between Li and HF, and various "product" double excitations, such as σ^2(HF) $\rightarrow 2s^1 2p^1, 2s^1 3s^1$(Li), σ^2(HF) $\rightarrow 2s^1$(Li)$(\sigma^*)^1$(HF), π^2(HF) $\rightarrow 2s^1 2p^1, 2s^1 3s^1$(Li), and π^2(HF) $\rightarrow 2s^1$(Li)$(\sigma^*)^1$(HF). Thus, along with the ground-state ROHF determinant

$$\Phi^{(0)} = \left| \{\text{core}\} (4a')^2 (5a')^2 (1a'')^2 (6a')^1 \right|, \tag{1}$$

where $\{\text{core}\} = (1a')^2 (2a')^2 (3a')^2$, in which the lowest $1a'$ molecular orbital (~ $1s$ orbital on fluorine) was kept frozen, the CSFs of the following types were chosen as reference configurations:

$$\Phi_n^{(1)} = \left| \{\text{core}\} (4a')^2 (5a')^2 (1a'')^2 (na')^1 \right|, \tag{2}$$

$$\Phi_n^{(2)} = \left| \{\text{core}\} (4a')^1 (5a')^2 (1a'')^2 (6a')^1 (na')^1 \right|, \tag{3}$$

$$\Phi_n^{(3)} = \left| \{\text{core}\} (4a')^2 (5a')^1 (1a'')^2 (6a')^1 (na')^1 \right|, \tag{4}$$

where $7 \le n \le 20$,

$$\Phi^{(4)} = \left| \{\text{core}\} (4a')^1 (5a')^2 (1a'')^2 (6a')^2 \right|, \tag{5}$$

$$\Phi^{(5)} = \left| \{\text{core}\} (4a')^2 (5a')^1 (1a'')^2 (6a')^2 \right|, \tag{6}$$

$$\Phi_n^{(6)} = \left| \{\text{core}\} (5a')^2 (1a'')^2 (6a')^1 (na')^2 \right|, \tag{7}$$

$$\Phi_n^{(7)} = \left| \{\text{core}\} (5a')^2 (1a'')^2 (6a')^2 (na')^1 \right|, \tag{8}$$

$$\Phi_n^{(8)} = \left| \{\text{core}\} (4a')^2 (1a'')^2 (6a')^1 (na')^2 \right|, \tag{9}$$

$$\Phi_n^{(9)} = \left|\{\text{core}\}(4a')^2(1a'')^2(6a')^2(na')^1\right|, \quad (10)$$

where $7 \le n \le 9$, and

$$\Phi^{(10)} = \left|\{\text{core}\}(4a')^2(5a')^2(1a'')^1(6a')^1(2a'')^1\right|, \quad (11)$$

$$\Phi_n^{(11)} = \left|\{\text{core}\}(4a')^1(5a')^1(1a'')^2(6a')^1(7a')^1(na')^1\right|, \quad (n = 31, 32), \quad (12)$$

$$\Phi^{(12)} = \left|\{\text{core}\}(4a')^1(5a')^2(1a'')^1(6a')^1(7a')^1(12a'')^1\right|, \quad (13)$$

$$\Phi^{(13)} = \left|\{\text{core}\}(4a')^2(5a')^1(1a'')^1(6a')^1(7a')^1(12a'')^1\right|. \quad (14)$$

Two CSFs were particularly important for the description of the two lowest $^2A'$ states, namely, the ROHF configuration $\Phi^{(0)}$, eq. (1), and the monoexcited configuration $\Phi_7^{(1)}$, eq. (2). These two configurations correlate with the Li($2s\ ^2S$) + HF($X\ ^1\Sigma^+$) and the Li($2p\ ^2P$) + HF($X\ ^1\Sigma^+$) limits of reactants. In this case, the $6a'$ and $7a'$ orbitals represent, respectively, the $2s$ and $2p$ orbitals of Li. As the Li–F distance decreases and the H–F distance increases, the $7a'$ orbital evolves into an antibonding orbital of HF having a significant admixture of diffuse atomic orbitals centered on Li, allowing us to describe an ionic intermediate Li^+–$(F–H)^-$, which plays an important role in the electron transfer between the excited lithium atom and the HF fragment in (LiFH)*, ultimately allowing for nonadiabatic dissociation of (LiFH)* into the reaction products, eq. (R1a). At the same time, the $6a'$ orbital becomes a $1s$ orbital of hydrogen, so that when the H-F bond finally breaks, the ROHF configuration $\Phi^{(0)}$, eq. (1), describes the ionic product channel, i.e., LiF($X\ ^1\Sigma^+$) + H($1s\ ^2S$). The presence of the carefully optimized diffuse functions in the basis set was essential for obtaining an accurate description of the $\tilde{X}\ ^2A'$ and $\tilde{A}\ ^2A'$ potential energy surfaces in the region of nuclear geometries where the nonadiabatic transitions and a significant rearrangement in the electronic structure of the excited Li···FH complex (from the covalent to largely ionic Li^+–$(F–H)^-$ intermediate), which are responsible for the photoinduced charge transfer in Li···FH, take place.

A similar set of references, including the $2s \rightarrow 2p$, $3p$, $3d$, $4p$, etc. single excitations in Li, the $\sigma \rightarrow \pi$ and $\pi \rightarrow \sigma^*$, σ, π single excitations in HF, and the σ(HF) $\rightarrow$ $2p$, $3p$, $3d$, $4p$(Li), π(HF) $\rightarrow$ $2s$, $2p$, $3s$, $3p$, $3d$, $4s$, $4p$(Li), σ^2(HF) $\rightarrow$ $2s^1 2p^1$(Li), and π^2(HF) $\rightarrow$ $2s^1 2p^1$(Li) intersystem excitations, was defined for the $^2A''$ states. Thus, along with the

$$\tilde{\Phi}_n^{(1)} = \left|\{\text{core}\}(4a')^2(5a')^2(1a'')^2(na'')^1\right|, \tag{15}$$

$$\tilde{\Phi}_n^{(2)} = \left|\{\text{core}\}(4a')^1(5a')^2(1a'')^2(6a')^1(na'')^1\right|, \tag{16}$$

and

$$\tilde{\Phi}_n^{(3)} = \left|\{\text{core}\}(4a')^2(5a')^1(1a'')^2(6a')^1(na'')^1\right| \tag{17}$$

configurations, where $n = 2 - 7$, we included in the reference space the

$$\tilde{\Phi}_n^{(4)} = \left|\{\text{core}\}(4a')^2(5a')^2(1a'')^1(6a')^1(na')^1\right| \tag{18}$$

configurations with $n = 7 - 9$, and the

$$\tilde{\Phi}^{(5)} = \left|\{\text{core}\}(4a')^2(5a')^2(1a'')^1(6a')^2\right|, \tag{19}$$

$$\tilde{\Phi}^{(6)} = \left|\{\text{core}\}(4a')^2(1a'')^2(6a')^2(2a'')^1\right|, \tag{20}$$

and

$$\tilde{\Phi}^{(7)} = \left|\{\text{core}\}(5a')^2(1a'')^2(6a')^2(2a'')^1\right|, \tag{20}$$

configurations.

The above reference spaces do not represent complete model spaces. The fact that we did not use a complete active space approach, which would considerably increase the cost of our calculations, was compensated for by a careful choice of reference configurations. These reference configurations were selected in such a way that they rotate into one another when the nuclear geometry varies. The appropriateness of our selection of references can be best illustrated by the size of the sum of the squared magnitudes of the coefficients of the above reference CSFs in the final CI wave function expansions of the four lowest $^2A'$ and two lowest $^2A''$ states defining Strategy A, the two

lowest $^2A'$ states defining strategy B, and the lowest $^2A'$ state defining Strategy C (for the precise definitions of these strategies, see the next paragraph). For the majority of geometries considered in this study, these sums were greater than 0.95, and they were greater than 0.90 for all nuclear geometries and all computational strategies considered here.

As in our earlier study of the potential energy surfaces of the NaFH system,[34] the MRDCI calculations for LiFH were performed in three stages, with each successive stage employing a set of smaller selection thresholds T and a subset of geometries used in the earlier stage. Thus, the entire potential energy surfaces for the four lowest $^2A'$ and two lowest $^2A''$ states were first explored using the threshold values T = 4, 6, and 8 μE_h. This initial 6-root calculation is referred to as Strategy A. The exploratory calculations constituting Strategy A were followed by more accurate calculations for the $\tilde{X}\ ^2A'$ and $\tilde{A}\ ^2A'$ states, and this 2-root calculation is referred to as Strategy B. In these calculations, we used the smaller threshold values T = 1, 2, and 3 μE_h. This set of calculations focused on the regions of potential energy surfaces critical for the dynamics of the nonadiabatic dissociation of the excited LiFH system, including the geometries along the Li + HF → LiF + H reaction path, the regions of the van der Waals minima on the $\tilde{X}\ ^2A'$ and $\tilde{A}\ ^2A'$ potential energy surfaces, the saddle point region on the ground-state potential energy surface, and the region of the avoided crossing of the $\tilde{X}\ ^2A'$ and $\tilde{A}\ ^2A'$ states.

The final set of calculations, denoted as Strategy C, employed the smallest selection thresholds, namely, T = 0.15, 0.30, and 0.45 μE_h. In these most accurate calculations, performed only for the ground state, we focused on H–F distances not exceeding 2.6 a_0, i.e., on the shallow van der Waals minimum, the entire reactant valley, and the product valley up to the barrier for the Li + HF → LiF + H reaction. Strategy C was important for improving the description of the van der Waals well and the saddle point region on the ground-state potential energy surface, which have also been examined by one of us with highly accurate coupled-cluster calculations.[13] In fact, we used the

results of these coupled-cluster calculations to choose the optimum values of T for the MRDCI calculations defining Strategies B and C.

As pointed out in our earlier study of the NaFH system,[34] the use of very small thresholds T, such as those defining Strategy C, is essential to obtain the correct description of shallow minima on potential energy surfaces with the MRDCI method. For example, the estimated error of extrapolation to the $T = 0$ limit of the complete MRCISD problem characterizing Strategy C was 0.001–0.006 eV, which is a reasonable accuracy for the ground-state potential energy surface in that it is characterized by a van der Waals minimum located ~0.24 eV below the Li + HF asymptote. The other regions of the $\tilde{X}\ ^2A'$ and $\tilde{A}\ ^2A'$ potential energy surfaces are accurately described with Strategy B, which has estimated extrapolation errors of 0.01–0.03 eV for all nuclear geometries included in the calculations. The least expensive set of calculations, defining Strategy A, has extrapolation errors of 0.02–0.09 eV; this accuracy level was sufficient to provide information about the global topography of the potential energy surface of the four lowest $^2A'$ and two lowest $^2A''$ states, and information obtained in the 6-root Strategy A calculation was useful for choosing the functional form for our analytic fit of the potential energy surfaces of the $\tilde{X}\ ^2A'$ and $\tilde{A}\ ^2A'$ states described in Sections III and IV. The use of the above selection thresholds allowed us to substantially reduce the original dimension of the $^2A'$ MRCISD problem, from 23,616,292 CSFs for all single and double excitations to less than ~70,000 CSFs in the $T = 4, 6, 8\ \mu E_h$ case, to less than ~100,000 CSFs in the $T = 1, 2, 3\ \mu E_h$ case, and to less than ~200,000 CSFs in the $T = 0.15, 0.30, 0.45\ \mu E_h$ case. The use of the three-step approach (Strategies A–C) allowed us to reduce the cost of our calculations further, since we used more expensive Strategies B and C primarily in the regions important for the dynamics. The regions of the LiFH potential energy surfaces (for example, regions characterized by very high energies) which cannot be accessed during the nonadiabatic dissociation of the excited Li···FH complex do not have to be treated as accurately as regions critical for the dynamics of this process. The use of Strategies A–C and the use of the MRDCI scheme, which is based on selecting relatively small sets of CSFs out of large sets of CSFs corresponding to a complete MRCI

problem, allowed us to cut down the cost of our calculations so much that the otherwise expensive MRCI calculations could be performed on dense grids of nuclear geometries involving several thousands of points in a reasonable amount of time. The results of the MRDCI calculations for each of the three Strategies A–C for a wide range of nuclear geometries is available as supplementary information.[48] The *ab initio* energies are reported in the supplementary material relative to the zero of energy defined as the energy of the ground electronic state at r_{LiF} = 15.0 a_0, r_{HF} = 1.7325 a_0, and θ = 179.99°. The total absolute energies for the ground electronic state at this geometry are –107.803247, –107.804286, and –107.804580 E_h for Strategies A, B, and C, respectively.

The *ab initio* calculations were performed on different nuclear geometry grids for each set of calculations (i.e., for each Strategy A–C), and the grids are described in detail in the supporting information.[48] Briefly, the 3,380 Strategy A geometries were designed to be global and cover the range: r_{LiF} = 2.0 – 15 a_0, r_{HF} = 1.2 – 7.0 a_0, and θ = 45 – 179.99°, where r_{AB} is the A–B internuclear distance and θ is the Li–F–H bond angle. The 2,232 Strategy B geometries covered a more limited range: r_{LiF} = 2.0 – 15 a_0, r_{HF} = 1.4 – 3.0 a_0, and θ = 45 – 179.99°. The 1,362 Strategy C geometries covered the range: r_{LiF} = 2.5 – 15 a_0, r_{HF} = 1.4 – 2.6 a_0, and θ = 45 – 179.99°. Each of these grids was augmented by several additional calculations to improve the quality of the final fit.

The construction of the final quasidiabatic fit for the MRDCI potential energy surfaces of the $\tilde{X}\ ^2A'$ and $\tilde{A}\ ^2A'$ states, based on the sequence of three sets of MRDCI calculations described above (Strategies A–C), is discussed in Sec. III. In addition to using MRDCI to calculate the adiabatic potential energy surfaces of the LiFH system, the MRDCI method was also used to determine the asymptotic form of the off-diagonal matrix elements of the diabatic Hamiltonian. As explained in Section III, the diabatic coupling term U_{12} for the LiFH system is constructed using the following two pieces of information: the minimum energy gaps between the adiabatic potential energy surfaces of the $\tilde{X}\ ^2A'$ and $\tilde{A}\ ^2A'$ states, extracted from the MRDCI calculations for these states as

described above, and the magnitude of the coupling between the lowest two $^1\Sigma^+$ states of the LiF and LiH diatomic fragments.

It is much easier to calculate the diabatic coupling for a diatomic than for a triatomic system, and several methods for calculating a diabatic Hamiltonian for a diatomic molecule have been proposed.[38,49–54] In this work, we used the method proposed by Werner and Meyer,[49] in which information about the off-diagonal matrix element of the diabatic Hamiltonian is determined from the adiabatic states that are to be coupled and the transition dipole moments between them (in our case, the lowest two $^1\Sigma^+$ states of LiF and LiH). In order to be consistent, we used the MRDCI approach in these additional calculations. The basis sets for LiF and LiH were obtained using the basis sets for the Li, F, and H atoms employed in the calculations for the LiFH system. We performed two kinds of calculations. In the first set of calculations, we used three threshold values (0.2, 0.4, and 0.6 μE_h for LiF and 0.001, 0.002, and 0.003 μE_h for LiH) and extrapolated the resulting energies to the $T = 0$ limit, as we did in the calculations for LiFH. This gave us information about the entire ground- and excited-state potential energy curves of the LiF and LiH molecules (the $X\ ^1\Sigma^+$, $A\ ^1\Pi$, $B\ ^3\Pi$, $C\ ^3\Sigma^+$, and $D\ ^1\Sigma^+$ states of LiF and the $X\ ^1\Sigma^+$, $A\ ^3\Sigma^+$, $B\ ^1\Sigma^+$, $C\ ^3\Pi$, $D\ ^1\Pi$, $E\ ^3\Sigma^+$ states of LiH). Information about the ground and first-excited states was useful in designing the correct asymptotic form of our quasidiabatic fit in the LiF + H and LiH + F channels. The corresponding vertical excitation energies can be found in Tables 5 and 6.

In the second set of calculations, we used the nonextrapolated MRDCI energies for the lowest two $^1\Sigma^+$ states, obtained in the calculations with $T = 0.2\ \mu E_h$ for LiF and $T = 0.001\ \mu E_h$ for LiH, and the corresponding dipole moment functions, i.e., the adiabatic dipole moments in the lowest two $^1\Sigma^+$ states and the transition dipole moment between these states, to construct matrix elements U_{11}, U_{22}, and U_{12} of the diabatic Hamiltonians for LiF and LiH as functions of the internuclear separations. The relevant adiabatic energies and dipole moments were obtained on dense grids of points consisting of 45 Li–F distances, ranging between 1.7 and 31.0 a_0, for LiF, and 41 Li–H distances, ranging between 1.5 and 15.0 a_0, for LiH. The reference spaces included 96 references (128

CSFs) for the LiF molecule and 82 references (82 CSFs) for LiH. In order to improve the accuracy of our description of the U_{11}, U_{22}, and U_{12} diabatic potentials for LiF, for which the coupling is stronger, we uniformly shifted the ionic diabat U_{11} to reproduce the difference between the ionic and covalent diabats, $U_{11} - U_{22}$, at the Li–F separation of 31.0 a_0, that results from the classical Rittner model,[55] i.e.,

$$U_{11} - U_{22} = \mathrm{IP(Li)} - \mathrm{EA(F)} - 1/R_{\mathrm{LiF}} - \alpha/(2R_{\mathrm{LiF}}^4) \qquad (22)$$

where α equals the sum of the polarizabilities of Li^+ and F^- (we used the polarizability values reported in Refs. 56 and 57). The resulting diabatic potentials U_{11}, U_{22}, and U_{12} for LiF and the corresponding diabatic potentials for LiH were used to design the U_{12} coupling term of the LiFH system (see Sec. III). The high quality of the diabatic states of LiF, obtained in this work with the Werner-Meyer scheme[49] and by the subsequent shifting of the ionic diabat according to eq. (22) can be seen by analyzing the results listed in Table 7. The Li–F distance at which the U_{11} and U_{22} diabats cross (the crossing radius R_c), and the separation $\Delta E(R_c)$ between the adiabatic energies of the lowest two $^1\Sigma^+$ states of LiF, obtained by rediagonalizing the diabatic Hamiltonian at $R_{\mathrm{LiF}} = R_c$, compare very well with the empirical estimates of R_c and $\Delta E(R_c)$ provided in Ref. 50.

III. Fit of the Lowest Two Potential Energy Surfaces

Fitting the adiabatic *ab initio* energies obtained as described in Sec. II directly would involve fitting the complicated features of the avoided crossing, the saddle point and the ground-state van der Waals well to a single functional form. In addition, we would have to calculate the nonadiabatic vector coupling term

$$\mathbf{d}(\mathbf{q}) = \left\langle \tilde{X}\ ^2A' \middle| \nabla_{\mathbf{q}} \middle| \tilde{A}\ ^2A' \right\rangle, \qquad (23)$$

where $\mathbf{q}$ is the relevant set of nuclear coordinates, on the dense grid of nuclear geometries used in the calculations for the $\tilde{X}\ ^2A'$ and $\tilde{A}\ ^2A'$ states. This would considerably increase the cost and complexity of our calculations. Thus, instead of fitting the adiabatic

potential energy surfaces and nonadiabatic coupling term **d**, we fit the surfaces quasidiabatically.[35–44,58–60]

The quasidiabatic electronic states, which formally result from a 2 x 2 unitary transformation of the adiabatic states, are essentially the covalent and ionic states of a valence-bond model, and their energies are relatively smoothly varying functions of geometry. The quasidiabatic potential energy matrix is written as

$$\mathbf{U}(\mathbf{q}) = \begin{pmatrix} U_{11}(\mathbf{q}) & U_{12}(\mathbf{q}) \\ U_{12}(\mathbf{q}) & U_{22}(\mathbf{q}) \end{pmatrix}, \tag{24}$$

where U_{11} are U_{22} are the lower- and higher-energy diabatic surfaces, respectively, in the Li + HF asymptotic valley and the higher- and lower-energy diabatic surfaces, respectively, in the LiF + H valley (the quasidiabatic surfaces cross when all three atoms are interacting). The quasidiabatic surfaces are coupled by a single scalar coupling term U_{12}, which is a function of three internal coordinates of LiFH. By defining the set of coupled surfaces using the quasidiabatic surfaces as in eq. (24), we also define the adiabatic surfaces and their nonadiabatic coupling **d**. The adiabatic energies are obtained without approximation by diagonalizing eq. (24), i.e.,

$$V_{1(2)}(\mathbf{q}) = \tfrac{1}{2}\left[U_{11}(\mathbf{q}) + U_{22}(\mathbf{q})\right] \mp \tfrac{1}{2}\sqrt{\left[U_{22}(\mathbf{q}) - U_{11}(\mathbf{q})\right]^2 + 4U_{12}^2(\mathbf{q})}\,, \tag{25}$$

where V_1 and V_2 are the adiabatic $\tilde{X}\ ^2A'$ and $\tilde{A}\ ^2A'$ states, respectively. The nonadiabatic coupling **d** in eq. (23) may also be obtained without approximation from the quasidiabatic energies and their gradients.[61]

One disadvantage of using the quasidiabatic representation is that it is not unique. A strict diabatic representation would be one in which all of the components of the vector coupling **d** are zero,[51,54] but such a representation does not exist in general[41,42,58–60] (except for the trivial, nonphysical solution of a basis that is independent of nuclear geometry). Nevertheless, useful approximate diabatic representations (i.e., quasidiabatic representations that are expected to contain the essentially correct physics for most practical dynamics calculations even when the momentum coupling is neglected) may often be defined, either based on smoothness and the incorporation of the geometrical dependencies expected on the basis of an underlying valence bond picture of the

electronic structure[29–33,35–40] or based on more mathematical arguments.[41–44,62] In the present work we use the former approach.

As mentioned above, we fit the two lowest-energy adiabatic potential energy surfaces of LiFH to a 2 x 2 quasidiabatic potential energy matrix, eq. (24). The details of the functional form and parameters used in the 2 x 2 LiFH fit are presented in the supporting information.[48] Briefly, our first step towards obtaining an analytic global potential energy surface was to obtain one-dimensional analytic fits for the asymptotic potential energy curves for the diatomic potentials of HF and LiF, in each case with the third atom far away. (Note that the LiH diatomic is not accessible at energies for which the current fit was designed to be useful. We therefore did not include the accurate LiH curve explicitly in the present fit.) The HF curve used in fitting the Li + HF asymptotic potentials was based on the RKR experimental data presented in Ref. 63. The LiF curves for the two lowest states of LiF used to fit the LiF + H asymptotic potential, were based on the diatomic *ab initio* calculations for LiF discussed in Sec. II. Figures 1 and 2 show the fitted Li + HF and H + LiF curves, respectively. Also shown are the experimental and *ab initio* diatomic curves upon which the HF and LiF fits (with the third atom far away) were based, respectively, as well as the Strategy A data for these asymptotes (see Sec. II) upon which the global fit for LiFH is based. As seen from Figs. 1 and 2 and as discussed in Sec. II, the global data agrees well with the experimental and high-level *ab initio* data.

Also shown in Figs. 1 and 2 are the excited-state *ab initio* data and fits for HF and LiF, respectively, again with the third atom far away. For small r_{HF}, the excited-state fit for the HF curve is equal to the ground-state HF curve shifted to higher energy by the excitation energy of Li (1.848 eV). The full three-body fitting procedure is facilitated when both electronic states go to the same energy when all three atoms are fully separated, and therefore the excited-state HF asymptotic potential was cut off around $r_{HF} = 3.0\ a_0$. The HF asymptotic curves and the ground-state LiF asymptotic curves were not allowed to vary during the remainder of the fitting procedure. The excited-state LiF asymptotic curve is purely repulsive and was allowed to vary during the next step of the fitting procedure.

After determining the asymptotic H + LiF and Li + HF potentials, we developed highly-parameterized functional forms for the three-dimensional diabats and the diabatic coupling surface. These functional forms were modeled on our previous fits of the NaFH and NaH_2 systems,[28,33,34] with additional functionality added as demanded by the LiFH *ab initio* data. The U_{11} diabat is relatively featureless and contains only the van der Waals well and the Li(2*s*) + HF asymptote. We therefore used a simple sum of diatomic terms to describe U_{11}. The HF potential curve was taken as our fit to the accurate experimental[63] data as discussed above, and two parameterized repulsive curves were used to describe the LiF and LiH diatomic interactions. Flexibility was added to the HF curve in the interaction region. The U_{22} diabat is more complicated since it has two open arrangements, Li(2*p*) + HF and LiF + H, as well as a saddle point and a product van der Waals well. We used a highly parameterized generalized LEPS[64–67] function to describe the U_{22} surface. Considerable flexibility in the fit was obtained by using highly modified triplet functions as well as switching functions to add functionality to the singlet curves. See the supporting information[48] for details.

Proper treatment of long-range interactions[68,69] can have a significant impact on observables such as the reaction cross section, as discussed elsewhere.[33] Here we explicitly include the long-range dispersion and permanent multipole interactions in the U_{11} and U_{22} surfaces. (Note that here we may include the long-range interactions in the quasidiabatic states because the diabatic coupling is nonzero only in the strong interaction region. The quasidiabatic states are therefore equal to the adiabatic states in the regions where the long-range forces are important.) Dispersion and dipole-induced-dipole forces were included in the U_{11} surface for the Li(2*s*) – HF interaction and in the U_{22} surface for the Li(2*p*) – HF and H – LiF interactions. These interactions are asymptotic to $Q_{\mathrm{A,BC}}^{-6}$ for the interaction A – BC, where $Q_{\mathrm{A,BC}}$ is the distance from the separated atom A to the center of mass of the diatom BC. The Li(2*p*) atom has a permanent quadrupole moment, and the U_{22} surface also includes the quadrupole-quadrupole and dipole-quadrupole forces for the Li(2*p*) – HF interaction. The dipole-quadrupole and

quadrupole-quadrupole interactions are asymptotic to $Q_{\mathrm{Li,HF}}^{-4}$ and $Q_{\mathrm{Li,HF}}^{-5}$, respectively. See the supporting information[48] for further details of the long-range interactions.

The accuracy of the U_{12} surface is critical for obtaining the correct nonadiabatic dynamics, but the adiabatic *ab initio* energies alone do not provide any direct information about the strength of the coupling in the three-body interaction region. We used the following procedure to obtain a reasonable coupling surface. We selected a functional form for U_{12} that behaves asymptotically like the *ab initio* LiF and LiH diabatic coupling curves that we obtained as discussed in Sec. II. We assume that in the interaction region the diabatic coupling will behave similarly to the asymptotic coupling, but the magnitude may be different. The magnitude of the diabatic coupling in the interaction region was estimated from the adiabatic energies near the line of avoided crossing. As seen from eq. (25), when $U_{11} = U_{22}$, the diabatic coupling U_{12} is given by $(V_2 - V_1)/2$. We identified the approximate geometries of the diabatic crossing ($U_{11} = U_{22}$) by using the dense grid of *ab initio* data and locating the line of minimum adiabatic energy gaps at each Li–F–H bond angle. We then estimated the diabatic coupling along this line to be half the adiabatic energy gap and adjusted the functional form of the diabatic coupling to have, as well as possible, the estimated magnitude along the line of avoided crossing at each bond angle. Once the functional form for U_{12} was obtained, cutoff functions were added such that U_{12} vanishes in all asymptotes. This feature does not significantly affect the dynamics, but it greatly simplifies dynamics calculations.

The more than 80 adjustable parameters in the U_{11}, U_{22}, and U_{12} surfaces were optimized simultaneously during the coupled-state triatomic fitting procedure. We used a genetic algorithm[70] to simultaneously fit the parameters of all three surfaces by diagonalizing the quasidiabatic potential energy matrix to obtain the adiabatic energies V_1 and V_2. The parameters were optimized by minimizing the unfitness function f^{-1}, where

$$f^{-1} = \sum_{i=1}^{2} \sum_{j=1}^{N_i} w_{ij} \left| E_{ij} - V_i(\mathbf{R}_j) \right|, \tag{26}$$

N_i is the number of *ab initio* data points for surface i, $V_i(\mathbf{R}_j)$ is the value of adiabatic potential i for a given set of parameters at geometry $\mathbf{R}_j$, and E_{ij} is the *ab initio* energy of the i^{th} adiabatic surface at geometry $\mathbf{R}_j$. The weights w_{ij} were selected such that the more critical areas (the saddle point, the van der Waals well, the exciplex well, and the seam of avoided crossing) were weighted more heavily than less critical areas (e.g., the high-energy repulsive walls where two atoms are strongly repelling one another).

We determined the final values of the parameters in two stages. We first obtained the set of parameters which best fit the least accurate global Strategy A data. As mentioned in Section II, the Strategy A data is available over the largest range of geometries (3,380 data points). This stage also allowed us to add flexibility to our functional forms as needed. We further refined our fit by allowing subsets of the parameters to vary as we fit V_1 and V_2 to the more accurate Strategy B data (2,232 data points) for the V_2 surface and the Strategy C data (1,362 data points) for the V_1 surface. A comparison of the fitted values of V_1 and V_2 for a wide range of nuclear geometries is available as supporting information.[48]

The discussion so far has centered on our most accurate global fit which we will call surface fit J when we need to distinguish it from the preliminary fit of Ref. 26, which can be called fit H. In some cases one would like to perform dynamics calculations without the added complication of long-range forces (which require longer integration times or longer-ranged grids in dynamics calculations). We therefore also created another surface set, which can be called surface fit JS, that is almost as accurate as surface fit J in the regions where we have *ab initio* data, but has truncated long-range forces. This is fully described in the supporting information.[48] In the rest of the article, *all* discussion refers to surface fit J.

IV. Discussion of the LiFH Surfaces

IV.A. Two Lowest-Energy States

The mean unsigned error of the fit is tabulated as a function of energy in Table 8. For energies relative to the dynamics calculations of most interest to us (less than 2.5 eV)

the fit agrees with the *ab initio* data to within 0.06 eV (~1.4 kcal/mol) and is even more accurate for lower energies. This is a very good agreement, especially since the *ab initio* data varies over a wide range, as illustrated by the spread of the data, as measured by its unsigned deviation from its mean. The energy of the ground-state van der Waals well is extremely accurate and agrees with the *ab initio* data to within 0.01 eV (0.2 kcal/mol).

Figures 3 and 4 show contour plots of the LiFH ground-state surface at $\theta = 107^{o}$ (the angle of the minimum of the ground-state van der Waals complex) and 72.8^{o} (the angle of the ground-state saddle point), respectively, where θ is the Li–F–H bond angle. Figure 5 shows a contour plot of the LiFH first excited-state surface at $\theta = 122^{o}$ (the angle of the minimum energy of the exciplex well). The quasidiabatic states U_{11}, U_{22}, and U_{12} are shown in Fig. 6 for the 107^{o} bond angle. Figure 7 shows the adiabatic and diabatic energies along steepest-descent paths from the saddle point for the ground-state Li(2*s*) + HF → LiF + H reaction at a fixed Li–F–H bond angle of $\theta = 72.8^{o}$. Table 9 shows the geometries and the energies of the stationary points, as well as calculations in which the zero point energy was included by the Morse I approximation[71,72] using the POLYRATE software package.[73]

Table 10 compares the geometries and energies of stationary points of the fitted adiabatic potential surfaces to those for several other surfaces[4,5,8,11–13] that have appeared in the literature. The critical points of the previous ground-state surfaces agree reasonably well with the fit presented here, and the present fit has the additional advantage over all but one[8] of the previous fits that it also includes the first excited state and over all previous fits that it also includes the electronic state coupling. The excited-state properties of the current fit do not agree well with those reported for the ASP-ALPR fit,[8] as shown in Table 10. Specifically the Li–F–H bond angle of the minimum-energy geometry in the exciplex well for the current fit ($\theta = 122^{o}$) differs from the result reported by ASP-ALPR ($\theta = 180^{o}$), and the depth of the exciplex well with respect to the Li(2p) + HF asymptote also differs significantly; we report the an exciplex well depth of 0.68 eV, whereas the APS fit reports a well-depth of ~0.9 eV.

IV.B. Other Excited States

For completeness, we also include contour plots of the *ab initio* data for the second-excited ($\tilde{B}\ ^2A''$) and third-excited ($\tilde{C}\ ^2A'$) states as Figs. 8 and 9, respectively. Both figures show the *ab initio* data for $\theta = 110^o$. These two states are degenerate with the $\tilde{A}\ ^2A'$ state in the Li + HF limit (the $\tilde{A}\ ^2A'$, $\tilde{B}\ ^2A''$, and $\tilde{C}\ ^2A'$ states correspond to the three-fold degenerate $2p\ ^2P$ state of the Li atom in the Li + HF limit). To further illustrate the role that these states may play in the dynamics of electronically excited LiFH, Figs. 10 and 11 show cuts through the ground-state van der Waals well for $\theta = 110^o$ and fixed values of r_{HF} and r_{LiF}, respectively. The analytic fit for the ground-state and first-excited states are shown as solid lines and the *ab initio* data are connected with dashed lines for the excited-states that are not included in the analytic fit. The symbols represent the *ab initio* data.

V. Summary

We have presented the results of accurate high-level *ab initio* calculations for the first six states of the LiFH system at a large range of geometries. We have used these data to construct a highly accurate 2 x 2 quasidiabatic analytic fit to the first two adiabatic potential energy surfaces. The fit explicitly includes long-range interactions and the electronic state coupling. The geometries and energies of the stationary points (the ground-state reactant van der Waals well, the ground-state saddle point, the ground-state product van der Waals well, and the exciplex well) agree well with other (less complete) fits that have been presented in the literature. The surface set presented in this paper should be useful for dynamical modeling of the global electronically nonadiabatic dynamics in both reactive and nonreactive processes.

Acknowledgments

This work was supported in part by the National Science Foundation under grant no. CHE00-92019 and by the Michigan State University Intramural Research Grant Program. Mike Hack and Piotr Piecuch contributed to this chapter.

References

1 W. A. Lester, Jr. and M. Krauss, J. Chem. Phys. **52**, 4775 (1970).

2 G. G. Balint-Kurti and R. N. Yardley, Faraday Discuss. Chem. Soc. **62**, 77 (1977).

3 Y. Zeiri and M. Shapiro, Chem. Phys. **31**, 217 (1978); M. Shapiro and Y. Zeiri, J. Chem. Phys. **70**, 5264 (1979).

4 M. M. L. Chen and H. F. Schaefer III, J. Chem. Phys. **72**, 4376 (1980).

5 S. Carter and J. N. Murrell, Mol. Phys. **41**, 567 (1980).

6 A. Laganà and E. Garcia, Theochem **16**, 91 (1984); E. Garcia and A. Laganà, Mol. Phys. **52**, 1115 (1984); V. Aquilanti, A. Laganà, and R. D. Levine, Chem. Phys. Lett. **158**, 87 (1989); A. Laganà, G. O. d. Aspuru, and E. Garcia, J. Chem. Phys. **108**, 3886 (1998).

7 M. Paniagua and A. Aguado, Chem. Phys. **134**, 287 (1989); A. Aguado and M. Paniagua, J. Chem. Phys. **96**, 1265 (1992); C. Suárez, A. Aguado, and M. Paniagua, Chem. Phys. **178**, 357 (1993); C. Suárez, A. Aguado, C. Tablero, and M. Paniagua, Int. J. Quantum Chem. **52**, 935 (1994).

8 A. Aguado, C. Suárez, and M. Paniagua, Chem. Phys. **201**, 107 (1995); A. Aguado, M. Lara, M. Paniagua, and O. Roncero, J. Chem. Phys. **114**, 3440 (2001).

9 O. N. Ventura, Mol. Phys. **89**, 1851 (1996).

10 A. Laganà, O. Gervasi, and E. García, Chem. Phys. Lett. **143**, 174 (1988).

11 G. A. Parker, A. Laganà, S. Crocchianti, and R. T Pack, J. Chem. Phys. **102**, 1238 (1995).

12 A. Aguado, M. Paniagua, M. Lara, and O. Roncero, J. Chem. Phys. **106**, 1013 (1997), **107**, 10085 (1997).

13 R. Burcl, P. Piecuch, V. Špirko, and O. Bludský, Int. J. Quantum Chem. **80**, 916 (2000).

14 C. H. Becker, P. Casavecchia, P. W. Tiedeman, J. J. Valentini, and Y. T. Lee, J. Chem. Phys. **73**, 2833 (1980).

15 R. B. Walker, Y. Zeiri, and M. Shapiro, J. Chem. Phys. **74**, 1763 (1981).

16 J. M. Alvariño, M. L. Hernández, E. Garcia, and A. Laganà, J. Chem. Phys. **84**, 3059 (1986); A. Laganà, E. Garcia, and O. Gervasi, J. Chem. Phys. **89**, 7238 (1988); A. Laganà, X. Giménez, E. Garcia, and O. Gervasi, Chem. Phys. Lett. **176**, 280 (1991); A. Laganà, G. O. d. Aspuru, A. Aguilar, X. Giménez, and J. M. Lucas, J. Phys. Chem. **99**, 11696 (1995); J. M. Alvariño, V. Aquilanti, S. Cavalli, S. Crocchianti, A. Laganà, and T. Martinez, J. Chem. Phys. **107**, 3339 (1997); A. Laganà, A. Bologna, and S. Crocchianti, Phys. Chem. Chem. Phys. **2**, 535 (2000).

17 G. G. Balint-Kurti, F. Gögtas, S. P. Mort, A. R. Offer, A. Laganà, and O. Gervasi, J. Chem. Phys. **99**, 9567 (1993); F. Gögtas, G. G. Balint-Kurti, and A. R. Offer, J. Chem. Phys. **104**, 7927 (1996).

18 M. Hoffmeister, R. Schleysing, F. Steinkemeier, and H. J. Loesch, J. Chem. Phys. **90**, 3528 (1989); H. J. Loesch, E. Stenzel, and B. Wüstenbecker, J. Chem. Phys. **95**, 3841 (1991); H. J. Loesch and F. Steinkemeier, J. Chem. Phys. **98**, 9570 (1993), **99**, 9598 (1993); H. J. Loesch, A. Ramscheid, E. Stenzel, F. Steinkemeier, and B. Wuestenbecker, in *Physics of Electronic and Atomic Collisions*, edited by W. R. MacGilliuray, I. E. McCarthy, and M. C. Staudagi (Adam Hilyer, Bristol, 1992), p. 579.

19 M. Baer, H. J. Loesch, H.-J. Werner, and I. Last, Chem. Phys. Lett. **291**, 372 (1994); M. Baer, I. Last, and H. J. Loesch, J. Chem. Phys. **101**, 9648 (1994).

20 G. Villani and R. Wallace, Acta Chim. Hung. **131**, 167 (1994), ACH- Models Chem. **131**, 167 (1994).

21 W. Zhu, D. Wang, and J. Z. Zhang, Theor. Chem. Acc. **96** 31 (1997).

22 M. Paniagua, A. Aguado, M. Lara, and O. Roncero, J. Chem. Phys. **109**, 2971 (1998), **111**, 6712 (1999).

23 M. Lara, A. Aguado, O. Roncero, and M. Paniagua, J. Chem. Phys. **109**, 9391 (1998).

24 F. J. Aoiz, M. T. Martinez, M. Menéndez, V. S. Rábanos, and E. Verdasco, Chem. Phys. Lett. **299**, 25 (1999).

25 F. J. Aoiz, E. Verdasco, V. S. Rábanos, H. J. Loesch, M. Menéndez, and F. Steinkemeier, Phys. Chem. Chem. Phys. **2**, 541 (2000).

26 A. W. Jasper, M. D. Hack, A. Chakraborty, D. G. Truhlar, and P. Piecuch, J. Chem. Phys. **115**, 7945 (2001).

27 C. Sanz, O. Roncero, M. Paniagua, and A. Aguado, Chem. Phys. Lett. **351**, 295 (2002).

28 A. J. Hudson, H. B. Oh, J. C. Polanyi, and P. Piecuch, J. Chem. Phys. **113**, 9897 (2000). A. J. Hudson and J. C. Polanyi, personal communication.

29 J. C. Tully, J. Chem. Phys. **59**, 5122 (1993).

30 B. C. Garrett and D. G. Truhlar, *in Theory of Scattering: Papers in Honor of Henry Eyring* (*Theoretical Chemistry*, Vol. 6), edited by D. Henderson (Academic, New York, 1981), Part A, p. 216.

31 D. G. Truhlar, J. W. Duff, N. C. Blais, J. C. Tully, and B. C. Garrett, J. Chem. Phys. **77**, 764 (1982); N. C. Blais, D. G. Truhlar, and B. C. Garrett, J .Chem. Phys., **78**, 2956 (1983).

32 P. Halvick and D. G. Truhlar, J. Chem. Phys. **96**, 2895 (1992).

33 M. D. Hack and D. G. Truhlar, J. Chem. Phys. **110**, 4315 (1999).

34 M. S. Topaler, D. G. Truhlar, X. Y. Chang, P. Piecuch, and J. C. Polanyi, J. Chem. Phys. **108**, 5349 (1998); M. S. Topaler, D. G. Truhlar, X. Y. Chang, P. Piecuch, and J. C. Polanyi, J. Chem. Phys. **108**, 5378 (1998).

35 T. F. O'Malley, Adv. At. Mol. Phys. **7**, 223 (1971).

36 V. Sidis and H. Lefebvre-Brion, J. Phys. B **4**, 1040 (1971).

37 S. A. Evans, J. S. Cohen, and N. F. Lane, Phys. Rev. A **4**, 2235 (1971).

38 R. W. Numrich and D. G. Truhlar, J. Phys. Chem. **79**, 2745 (1975).

39 A. Macias and A. Riera, J. Phys. B **11**, L489 (1978).

40 V. Sidis, Adv. Chem. Phys. **82**, 73 (1992).

41 T. C. Thompson, D. G. Truhlar, and C. A. Mead, J. Chem. Phys. **82**, 2392 (1985).

42 T. Pacher, L. S. Cederbaum, and H. Köppel, Adv. Chem. Phys. **84**, 293 (1993).

43 V. M. García, M. Reguero, R. Caballol, and J. P. Malrieu, Chem. Phys. Lett. **281**, 161 (1997).

44 G. J. Atchity and K. Ruedenberg, Theor. Chem. Acc. **97**, 47 (1997).

45 R. J. Buenker and S. D. Peyerimhoff, Theor. Chim. Acta **35**, 33 (1974); **39**, 217 (1975); P. J. Bruna and S. D. Peyerimhoff, Adv. Chem. Phys. **67**, 1 (1987).

46 J. Paldus, in *New Horizons of Quantum Chemistry*, edited by P. O. Löwdin and B. Pullman (Reidel, Dordrecht, 1983), p. 31; R. J. Buenker and S. D. Peyerimhoff, *ibid*., p. 183; P. J. Bruna, S. D. Peyerimhoff, and R. J. Buenker, Chem. Phys. Lett. **72**, 278 (1980); K. Jankowski, L. Meissner, and J. Wasilewski, Int. J. Quantum Chem. **28**, 931 (1985).

47 R. Krishnan, J. S. Binkley, R. Seeger, and J. A. Pople, J. Chem. Phys. **72**, 650 (1980).

48 See EPAPS Document No. E-JCPSA6-116-312216 for supporting information including the nuclear geometry grids for the *ab initio* calculations, the functional forms and FORTRAN programs for the analytic LiFH potential energy matrices, and a selection of the *ab initio* and fitted energies. This document may be retrieved via the EPAPS homepage (http://www.aip.org/pubserv/epaps.html) or from ftp.aip.org in the directory /epaps/. See the EPAPS homepage for more information.

49 H.-J. Werner and W. Meyer, J. Chem. Phys. **74**, 5802 (1981).

50 R. Grice and D. R. Herschbach, Mol. Phys. **27**, 159 (1974).

51 F. T. Smith, Phys. Rev. **179**, 111 (1969).

52 S. A. Adelman and D. R. Herschbach, Mol. Phys. **27**, 159 (1974).

53 L. R. Kahn, P. J. Hay, and I. Shavitt, J. Chem. Phys. **61**, 3530 (1974).

54 M. Baer, Mol. Phys. **40**, 1011 (1980).

55 E. S. Rittner, J. Chem. Phys. **19**, 1030 (1951).

56 P. W. Fowler and P. A. Madden, Phys. Rev. B **29**, 1035 (1984).

57 S. A. Kucharski, Y. S. Lee, G. D. Purvis III, and R. J. Bartlett, Phys. Rev. A **29**, 1619 (1984).

58 A. D. McLachlan, Mol. Phys. **4**, 417 (1961).

59 C. A. Mead and D. G. Truhlar, J. Chem. Phys. **77**, 6090 (1982).

60 C. A. Mead, J. Chem. Phys. **78**, 807 (1983).

61 M. D. Hack, A. W. Jasper, Y. L. Volobuev, D. W. Schwenke, and D. G. Truhlar, J. Phys. Chem. A **103**, 6309 (1999).

62 H. Nakamura and D. G. Truhlar, J. Chem. Phys. **115**, 10353 (2001).

63 G. Di Lonardo and A. E. Douglas, Can. J. Phys. **51**, 434 (1973); J. A. Coxon, and P. G. Hajigeorgiou, J. Molec. Spec. **142**, 254 (1990).

64 S. Sato, J. Chem. Phys. **23**, 2465 (1955).

65 J. K. Cashion and D. R. Herschbach, J. Chem. Phys. **40**, 2358 (1964).

66 K. J. Laidler, and J. C. Polanyi, Prog. Reaction Kinetics **3**, 1 (1965).

67 P. J. Kuntz, E. M. Nemeth, J. C. Polanyi, S. D. Rosner, and C. E. Young, J. Chem. Phys. **44**, 1168 (1966).

68 J. O. Hirschfelder, C. F. Curtiss, and R. B. Bird, *Molecular Theory of Gases and Liquids*, corrected printing (John Wiley and Sons, New York, 1964).

69 G. C. Maitland, M. Rigby, E. B. Smith, and W. A. Wakeham, *Intermolecular Forces: Their Origin and Determination*, corrected printing (Clarendon Press, Oxford, 1987); P. Piecuch, in Molecules in Physics, Chemistry and Biology, edited by J. Maruani (Kluwer, Dordrecht, 1988), Vol. 2, p. 417.

70 Genetic algorithm calculations were carried out using the program FORTRAN GA, version 1.6.4 as described in D. L. Carroll, AIAA J. **34**, 338 (1996).

71 E. B. Wilson, J. C. Decius, and P. C. Cross, *Molecular Vibrations* (McGraw-Hill, New York, 1955).

72 A. D. Isaacson and D. G. Truhlar, J. Chem. Phys. **76**, 1380 (1982).

73 J. C. Corchado, Y.-Y. Chuang, P. L. Fast, J. Villà, W.-P. Hu, Y.-P. Liu, G. C. Lynch, K. A. Nguyen, C. F. Jackels, V. S. Melissas, B. J. Lynch, I. Rossi, E. L. Coitiño, A. Fernandez-Ramos, R. Steckler, B. C. Garrett, A. D. Isaacson, and D. G. Truhlar, POLYRATE-version 8.5.1, University of Minnesota, Minneapolis, 2000.

74 *CRC Handbook of Chemistry and Physics*, 77th ed., edited by D. R. Lide (Chemical Rubber, Boca Raton, 1996).

75 K. P. Huber and G. Herzberg, *Molecular Spectra and Molecular Structure*, Vol. 4, *Constants of Diatomic Molecules* (Van Nostrand Reinhold, New York, 1979).

76 M. Bettendorf, R. J. Buenker, S. D. Peyerimhoff, and J. Römelt, Z. Phys. A **304**, 125 (1982).

Table 1. Calculated (MRDCI) and experimental (Expt) excitation energies and ionization potentials (IP) of Li (in eV).

	MRDCI	Expt[a]
$2s\ ^2S \rightarrow 2p\ ^2P$	1.837	1.848
$2s\ ^2S \rightarrow 3s\ ^2S$	3.373	3.373
$2s\ ^2S \rightarrow 3p\ ^2P$	3.833	3.834
IP	5.372	5.392

[a]Reference 74.

Table 2. Calculated (MRDCI) and experimental (Expt) electron affinities of F and H (in eV).

	MRDCI	Expt[a]
F	3.31	3.40
H	0.74	0.75

[a]Reference 72.

Table 3. Ground-state properties of HF, LiF, and LiH. A comparison of the calculated (MRDCI) and experimental (Expt) data.

	r_e / Å[a]		ω_e / cm^{-1} [b]		D_0 / eV[c]		μ / D[d]		ΔE / eV[e]	
Diatom	MRDCI	Expt[f]	MRDCI	Expt[f]	MRDCI	Expt[f]	MRDCI	Expt[f,g]	MRDCI	Expt[h]
HF	0.9165	0.9168	4147.7	4138.3	5.68	5.87	1.819	1.826	0.00	0.00
LiF	1.5645	1.5639	903.7	910.3	5.67	5.91	6.358	6.325	0.21	0.17
LiH	1.5946	1.5957	1402.0	1405.7	2.44	2.43	5.851	5.882	3.37	3.60

[a]The equilibrium bond length.

[b]The harmonic vibrational frequency.

[c]The dissociation energy. The MRDCI value of D_0 was calculated from $D_e - \omega_e/2$, where D_e is a difference between the asymptotic (r = 7.5 a_0 for HF, r = 31 a_0 for LiF, and r = 15 a_0 for LiH) and equilibrium values of the MRDCI ground-state energies.

[d]The dipole moment.

[e]The difference between the energy of the diatom at its equilibrium bond length and the energy of the Li + HF asymptote at the HF equilibrium bond length.

[f]Reference 75.

[g]Average value for the ground vibrational state.

[h]Computed from D_0 and ω_e.

Table 4. Vertical excitation energies (in eV) from the $X\ ^1\Sigma^+$ state of HF at the experimental equilibrium distance $r_e = 0.917$ Å.[a]

State[b]	MRDCI[c]	MRDCI[d]
$^3\Pi$	10.060	10.06
$^1\Pi$	10.417	10.41
$^3\Sigma^+$	13.442	13.59

[a]Continuous absorption starting at 60600 cm^{-1} (7.51 eV) has been attributed to the $X\ ^1\Sigma^+ \rightarrow\ ^1\Pi$ transition (Ref. 75 and references therein).

[b]Lowest excited state for each symmetry.

[c]Present work, [5s4p3d2f/5s4p2d] basis set.

[d]Reference 76, [7s5p2d/3s1p] basis set.

Table 5. Vertical excitation energies (in eV) from the $X\ ^1\Sigma^+ = 1\ ^1\Sigma^+$ state of LiF at the experimental equilibrium distance $r_e = 1.564$ Å.[a]

State	MRDCI[b]
$1\ ^3\Pi$	6.58
$1\ ^1\Pi$	6.57
$1\ ^3\Sigma^+$	6.96
$2\ ^1\Sigma^+$	6.98

[a]Peaks in the electron energy loss spectrum are at 6.6, 8.7, 10.9, 62.0 eV (Ref. 75).

[b]Present work, [5s4p3d2f/5s4p3d2f] basis set.

Table 6. Vertical excitation energies (in eV) from the $X\ ^1\Sigma^+ = 1\ ^1\Sigma^+$ state of LiH at the experimental equilibrium distance r_e = 1.595 Å.

State	MRDCI[a]
$1\ ^3\Sigma^+$	3.27
$2\ ^1\Sigma^+$	3.62[b]
$1\ ^3\Pi$	4.25[c]
$1\ ^1\Pi$	4.26[d]

[a]Present work, [5s4p3d2f/5s4p2d] basis set.

[b]The T_e (minimum to minimum) excitation energy is 3.29 eV. The experimental value of T_e is 3.29 eV (Ref. 75).

[c]The lowest stable $^3\Pi$ state is located at ~1700 cm^{-1} or 0.21 eV below the lowest stable $^1\Pi$ state.

[d]The T_e (minimum to minimum) excitation energy is 4.32 eV. The experimental value of T_e is 4.33 eV (Ref. 75).

Table 7. The crossing radius R_c and the separation $\Delta E(R_c)$ between the two lowest adiabatic $^1\Sigma^+$ states of LiF at the Li–F separation equal to R_c.

	MRDCI[a]	Empirical[b]
R_c / a_0	13.98	13.72
$\Delta E(R_c)$, eV	0.024	0.021

[a]The nonextrapolated MRDCI calculation without the quasi-degenerate Davidson correction.[46] The crossing radius R_c was obtained by diabatizing the MRDCI adiabatic states using the method of Ref. 49. The separation $\Delta E(R_c)$ was obtained by adjusting the U_{11} (ionic) diabat at $R_{LiF} = 31$ a_0 to the classical Rittner potential [cf. eq. (22) and Ref. 55] and rediagonalizing the diabatic Hamiltonian to obtain adiabatic energies. The required values of the ionization potential of Li and electron affinity of F were taken from Ref. 74. The required values of the polarizabilities of Li^+ and F^- were taken from Refs. 56 and 57, respectively.

[b]Reference 50.

Table 8. Mean unsigned error (MUE) in eV of the fitted energies $V_i(\mathbf{R}_j)$ and mean unsigned deviation (MUD) in eV of the *ab initio* data E_{ij} from their mean value for several energy ranges.[a]

Surface	Energy range	N_{geom}	MUE	MUD	MUE / MUD
V_1	$E_{1i} < 2.5$ eV	1390	0.059	0.543	0.11
	$E_{1i} < 2.0$ eV	1323	0.055	0.488	0.11
	$E_{1i} < 1.0$ eV	886	0.039	0.275	0.14
	$E_{1i} < 0.0$ eV	98	0.017	0.060	0.29
V_2	$E_{2i} < 2.5$ eV	1037	0.063	0.294	0.21
	$E_{2i} < 2.0$ eV	640	0.044	0.188	0.24
	$E_{2i} < 1.8$ eV	436	0.042	0.138	0.31

[a]The mean errors were calculated with unit weight on every point. N_{geom} is the number of geometries for the state indicated that lie within the energy range given in each row.

Table 9. Geometries and energies of the adiabatic stationary points of LiFH as calculated from the global fit. All bond lengths are in bohrs, the Li–F–H angle θ is in degrees, and the energies are in eV.

Feature	r_{LiF}	r_{HF}	r_{LiH}	θ	V_1	V_1 + ZPE[a]	V_2	V_2 + ZPE[a]
Reactants	–	1.73	–	–	0.000	0.255	1.848	2.099
Reactant vdW well of V_1	3.56	1.76	4.42	107.	–0.241	0.033	1.244	–
Saddle point[b] of V_1	3.10	2.62	3.42	72.8	0.247	0.352	3.227	–
Product vdW well of V_1	2.98	3.90	3.94	68.4	0.150	0.242	5.567	–
Products	2.96	–	–	–	0.175	0.232	*c*	–
Exciplex of V_2	3.34	1.82	4.57	122.	–0.166	–	1.214	1.438

[a]The zero point energy (ZPE) was calculated by treating the normal modes as separable Morse I oscillators[71,72] using the POLYRATE v. 8.5.1 software package.[73] Zero point energy is included in one mode for reactants and products, in two modes for the saddle points, and in three modes for the local three-body minima.

[b]Imaginary frequency: $505i$ cm^{-1}.

[c]The product arrangement is not bound on the excited-state surface V_2.

Table 10. Comparisons of the geometries and energies of the stationary points on the adiabatic potential surfaces for several fitted LiFH potential energy surfaces.

	Present	CS[a]	CM[b]	ASP-ALPR[c]	PLCP[d]	APLR[e]	BPSB[f]
Reactants							
r_{HF} (a_0)	1.73	1.76	1.73	1.74	1.73	1.74	–
V_1 (eV)	0.0	0.0	0.0	0.0	0.0	0.0	–
V_2 (eV)	1.85	–	–	2.05	–	–	–
Van der Waals well							
r_{LiF} (a_0)	3.56	3.68	3.59	3.65	–	3.55	3.60
r_{HF} (a_0)	1.76	1.78	1.76	1.76	–	1.77	1.76
θ (deg)	107.	109.	114.	106.	–	107.	109.
V_1 (eV)	–0.24	–0.20	–0.26	–0.29	–0.30	–0.28	–0.25
Saddle point							
r_{LiF} (a_0)	3.10	3.21	3.12	3.20	–	3.20	3.14
r_{HF} (a_0)	2.62	2.44	2.48	2.46	–	2.46	2.42
θ (deg)	72.8	71.	74.	73.	74.	71.4	71.2
V_1 (eV)	0.25	0.43	0.34	0.25	0.18	0.23	0.25
Products							
r_{LiF} (a_0)	2.96	3.03	2.95	3.00	2.96	3.00	–
V_1 (eV)	0.18	0.13	0.17	0.10	0.15	0.08	–
Exciplex well							
r_{LiF} (a_0)	3.34	–	–	3.18	–	–	–
r_{HF} (a_0)	1.82	–	–	1.95	–	–	–
θ (deg)	122.	–	–	180.	–	–	–
V_2 (eV)	1.21	–	–	1.16	–	–	–

[a]Reference 4.
[b]Reference 5.
[c]Reference 8.
[d]Reference 11.
[e]Reference 12.
[f]Reference 13.

Figure captions

Figure 1. Asymptotic potential energy curves of LiFH in the Li + HF limit. The analytic fits used in the global fit are shown as solid lines, the solid circles represent the experimental data for HF from Ref. 61 used to obtain the ground-state fit, and the open symbols represent the Strategy A *ab initio* data for the ground state (triangles) and excited state (squares) of the LiFH system in the Li + HF limit.

Figure 2. Asymptotic potential energy curves of LiFH in the H + LiF limit. The analytic fits used in the global fit for LiFH are shown as solid lines, the solid circles represent the highly accurate MRDCI data for the ground-state of LiF used to obtain the ground-state fit, and the open symbols represent the Strategy A *ab initio* data for the ground state (triangles) and excited state (squares) of the LiFH system in the H + LiF limit.

Figure 3. Contour plot of the fitted ground-state adiabatic surface (V_1) at a Li–F–H bond angle of 107^o (the bond angle of the minimum energy of the van der Waals well). The contour spacing is 0.1 eV for energies less than 1.0 eV and 1.0 eV for energies above 1.0 eV. The contour corresponding to 0.0 eV is shown as a thick solid line. Note: the zero of energy for *all* contour plots in this paper is Li(2*s*) infinitely far from HF at its classical equilibrium separation.

Figure 4. Contour plot of the fitted ground-state adiabatic surface (V_1) at a Li–F–H bond angle of 72.8^o (the bond angle of the saddle point). The contour spacing is 0.1 eV for energies less than 1.0 eV and 1.0 eV for energies above 1.0 eV. The contour corresponding to 0.0 eV is shown as a thick solid line.

Figure 5. Contour plot of the fitted first excited-state adiabatic surface (V_2) at a Li–F–H bond angle of 122° (the bond angle of the minimum energy of the exciplex well). The contour spacing is 0.1 eV for energies less than 2.0 eV and 1.0 eV for energies above 2.0 eV. The contour corresponding to 1.9 eV is shown as a thick solid line.

Figure 6. Contour plots of the a) U_{11}, b) U_{22}, and c) U_{12} quasidiabatic surfaces at a Li–F–H bond angle of 107°. For panels a) and b), the contour spacing is 0.1 eV for energies less than 1.0 eV and 1.0 eV for energies above 1.0 eV. For panel c), the contours are labeled in eV.

Figure 7. Adiabatic (thick solid lines) and quasidiabatic (thin dashed lines) energies along the steepest descent path from the saddle point in unscaled rectilinear coordinates (r_{LiF} and r_{HF}) for the ground-state reaction Li($2s$) + HF → LiF + H at a fixed bond angle of $\theta = 72.8°$. The distance along the path is the reaction coordinate s.

Figure 8. Contour plot of the *ab initio* data for the second-excited state ($\tilde{B}\ ^2A''$) at a Li–F–H bond angle of 110°. The contour spacing is 0.1 eV for energies less than 2.0 eV and 1.0 eV for energies above 2.0 eV. The contour corresponding to 1.9 eV is shown as a thick solid line.

Figure 9. Contour plot of the *ab initio* data for the third-excited state ($\tilde{C}\ ^2A'$) at a Li–F–H bond angle of 110°. The contour spacing is 0.1 eV for energies less than 2.0 eV and 1.0 eV for energies greater than 2.0 eV. The contour corresponding to 1.9 eV is shown as a thick solid line.

Figure 10. Cut along r_{LiF} through the minimum of the ground-state van der Waals well at a fixed Li–F–H bond angle of 110° with r_{HF} fixed at 1.73 a_0. The analytic fits for the two lowest-energy states are shown as solid lines. The *ab initio* data are shown as symbols, where the circles represent the $\tilde{X}\ ^2A'$ state, triangles represent the $\tilde{A}\ ^2A'$ state, diamonds represent the $\tilde{B}\ ^2A''$ state, squares represent the $\tilde{C}\ ^2A'$ state, 'x' represent the $\tilde{D}\ ^2A$ state, and '+' represent the $\tilde{E}\ ^2A''$ state. The symbols are connected by dashed lines for the states not included in the analytic fits.

Figure 11. Cut along r_{HF} through the minimum of the ground-state van der Waals well at a fixed Li–F–H bond angle of 110° with r_{LiF} fixed at 2.96 a_0. The analytic fits for the two lowest-energy states are shown as solid lines. The *ab initio* data are shown as open symbols, where the circles represent the $\tilde{X}\ ^2A'$ state, triangles represent the $\tilde{A}\ ^2A'$ state, diamonds represent the $\tilde{B}\ ^2A''$ state, squares represent the $\tilde{C}\ ^2A'$ state, 'x' represent the $\tilde{D}\ ^2A$ state, and '+' represent the $\tilde{E}\ ^2A''$ state. The symbols are connected by dashed lines for the states not included in the analytic fits.

Figure 1

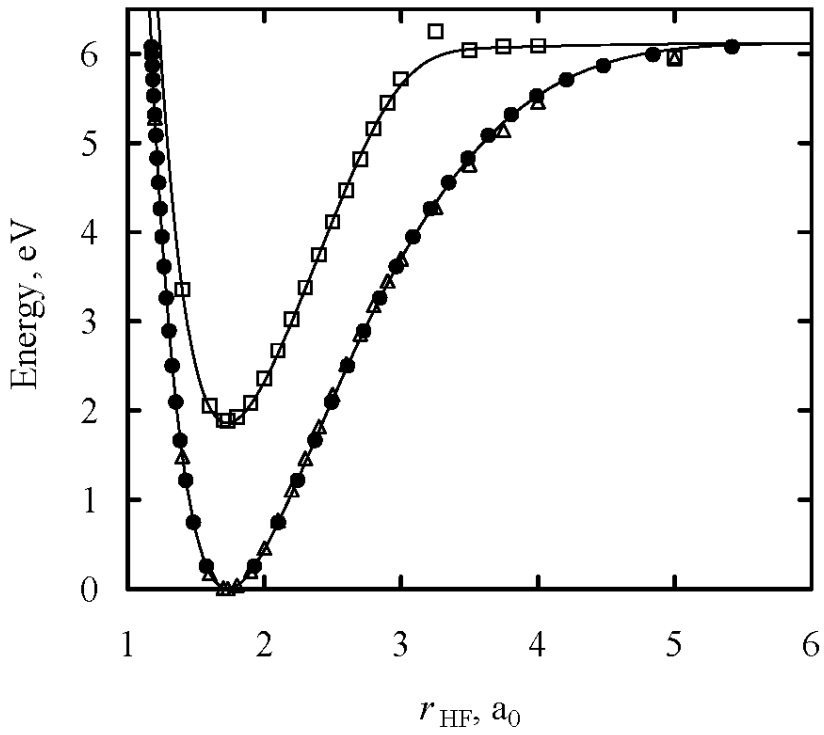

Figure 2

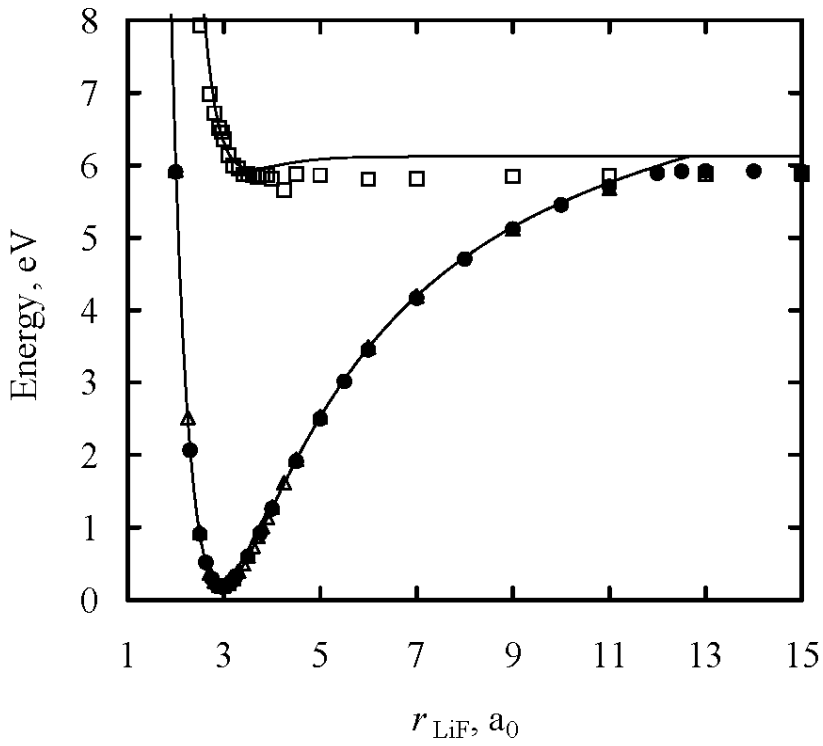

Figure 3

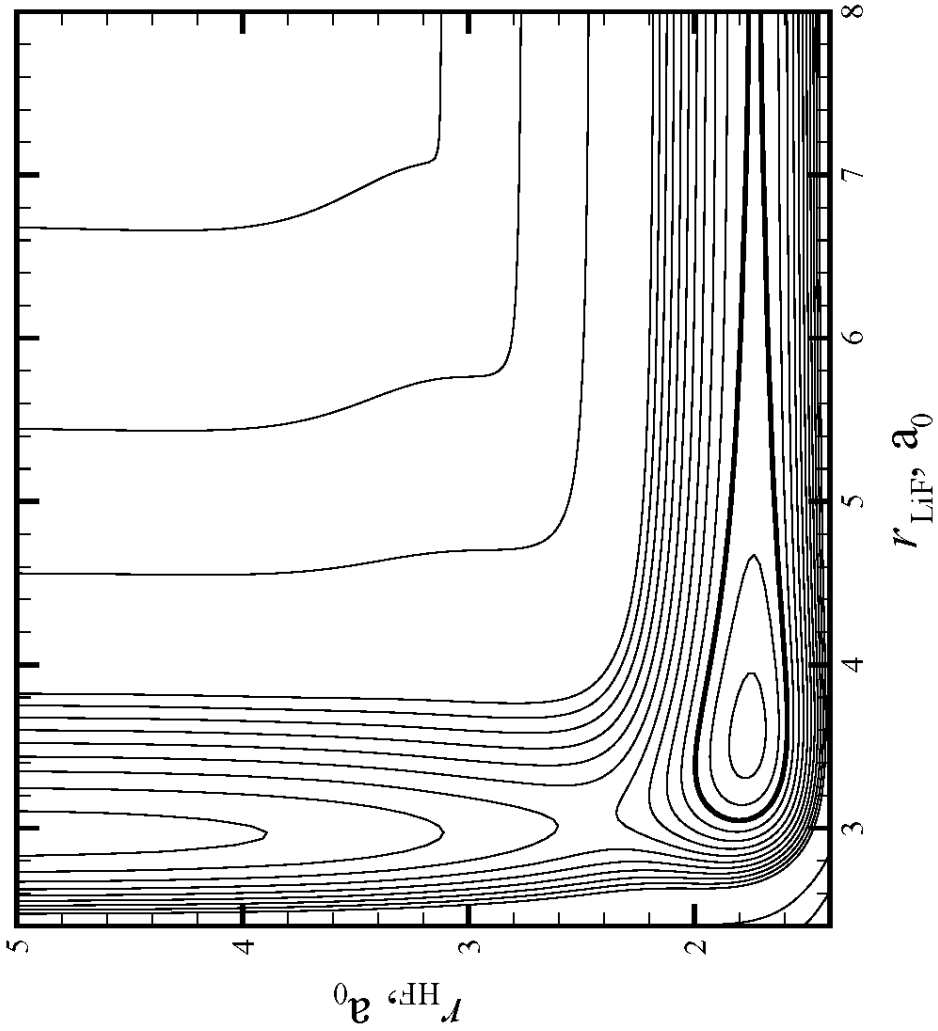

Figure 4

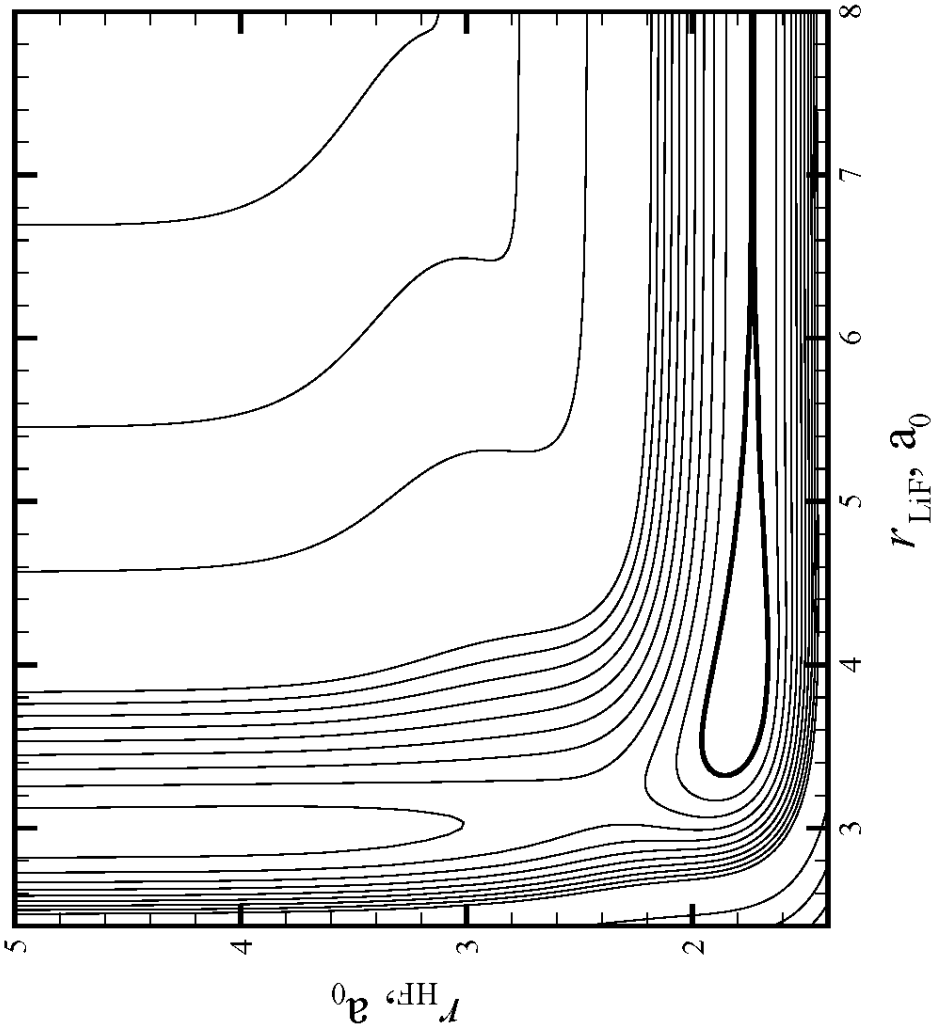

Figure 5

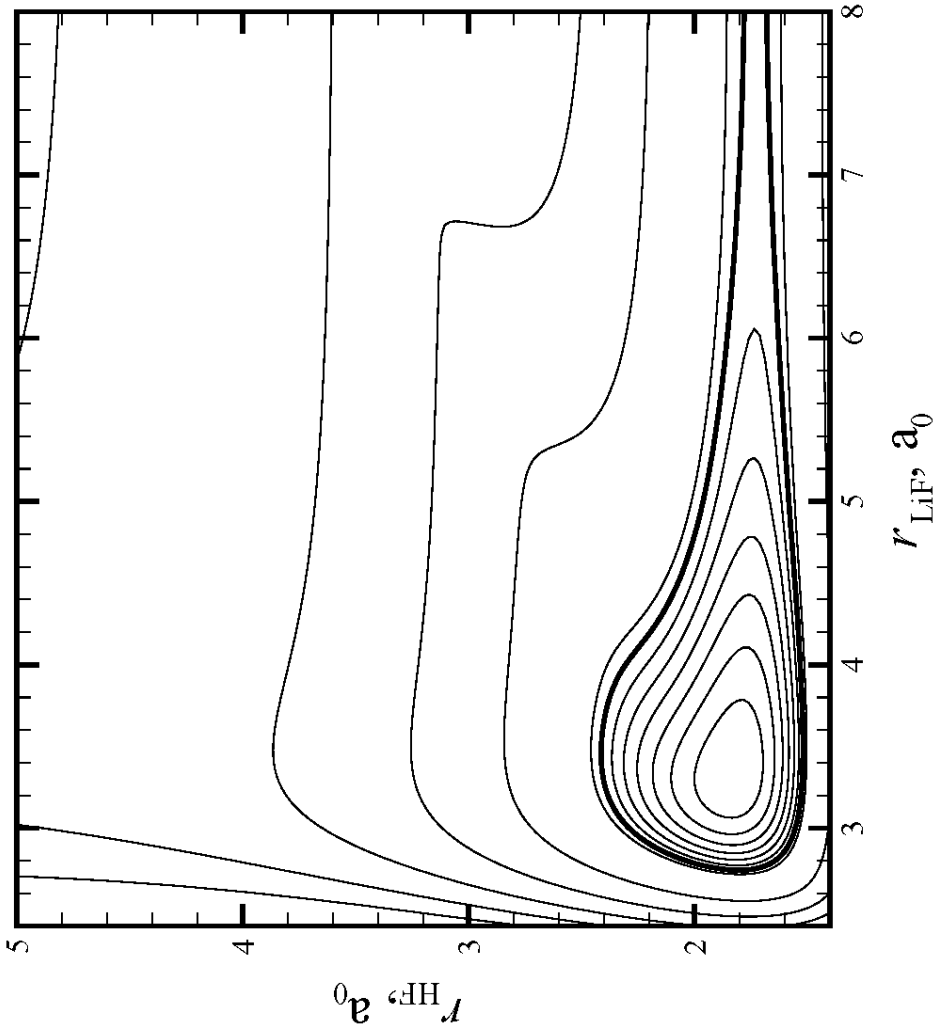

Figure 6

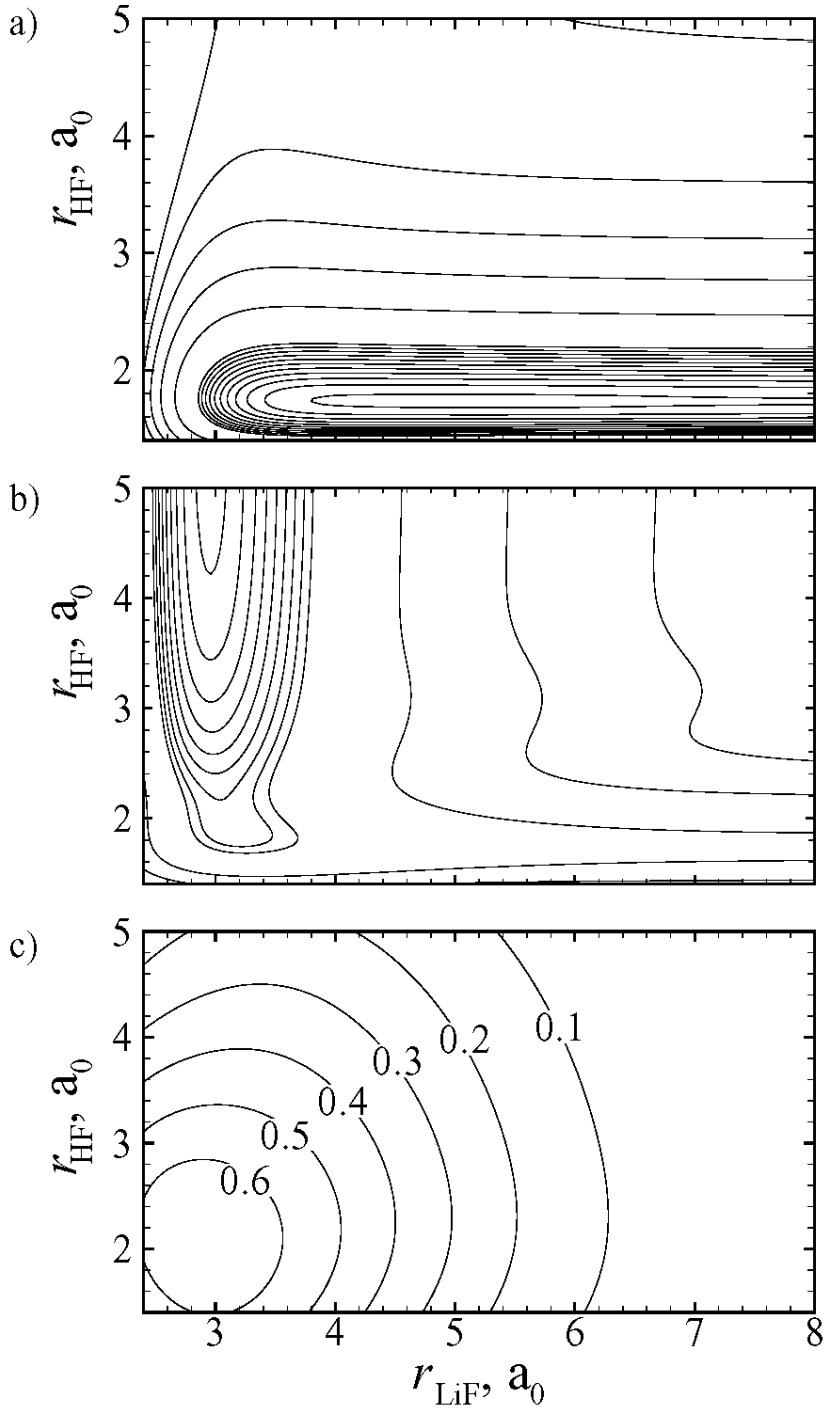

Figure 7

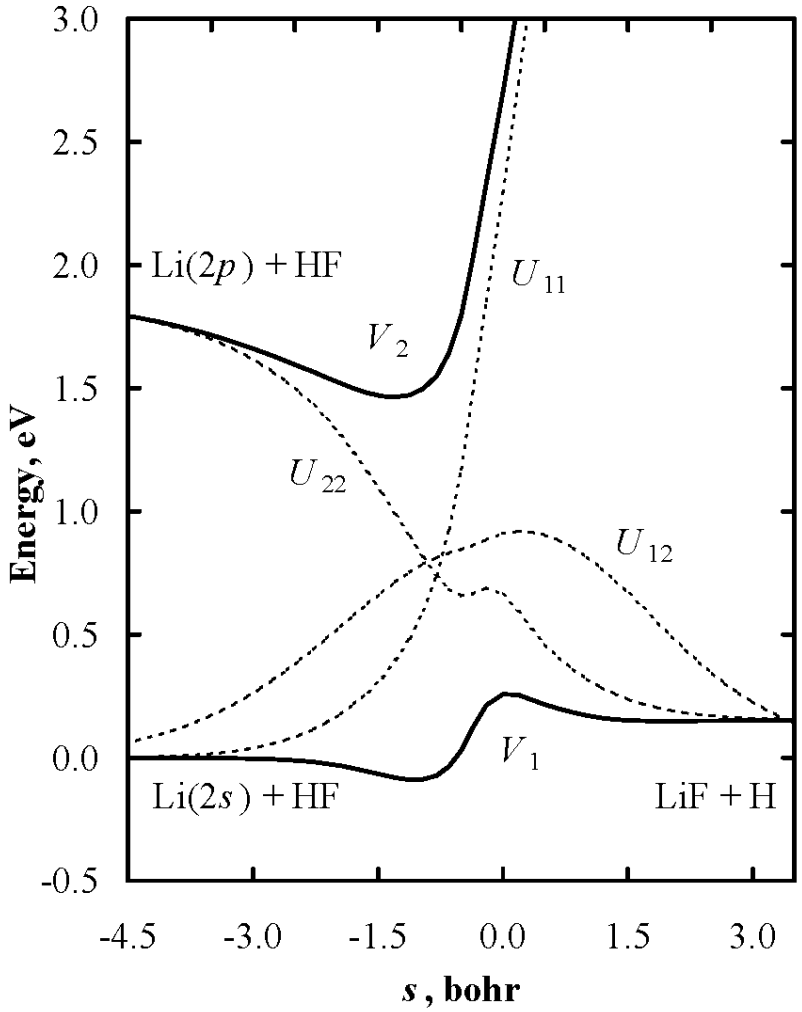
3.0
2.5
2.0
1.5
1.0
0.5
0.0
-0.5
Energy, eV
Li(2p) + HF
U_{11}
V_2
U_{22}
U_{12}
V_1
Li(2s) + HF
LiF + H
-4.5
-3.0
-1.5
0.0
1.5
3.0
s , bohr

Figure 8

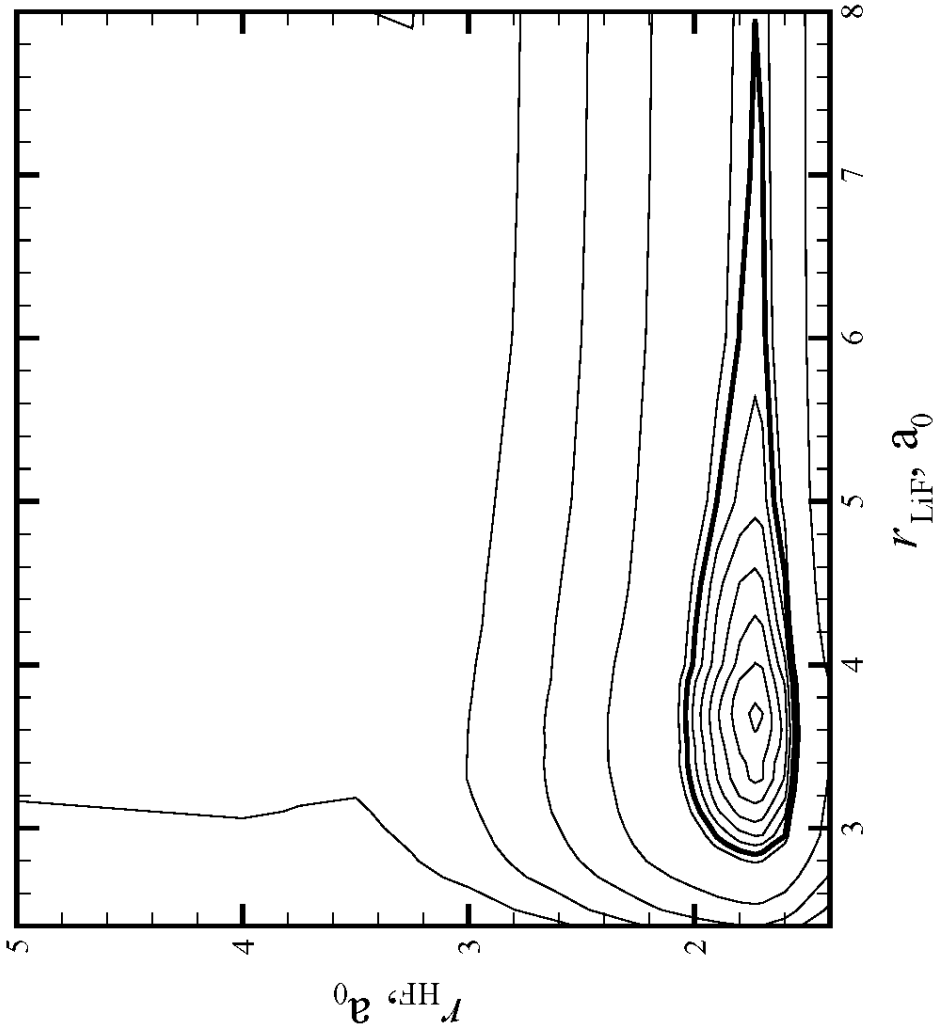

Figure 9

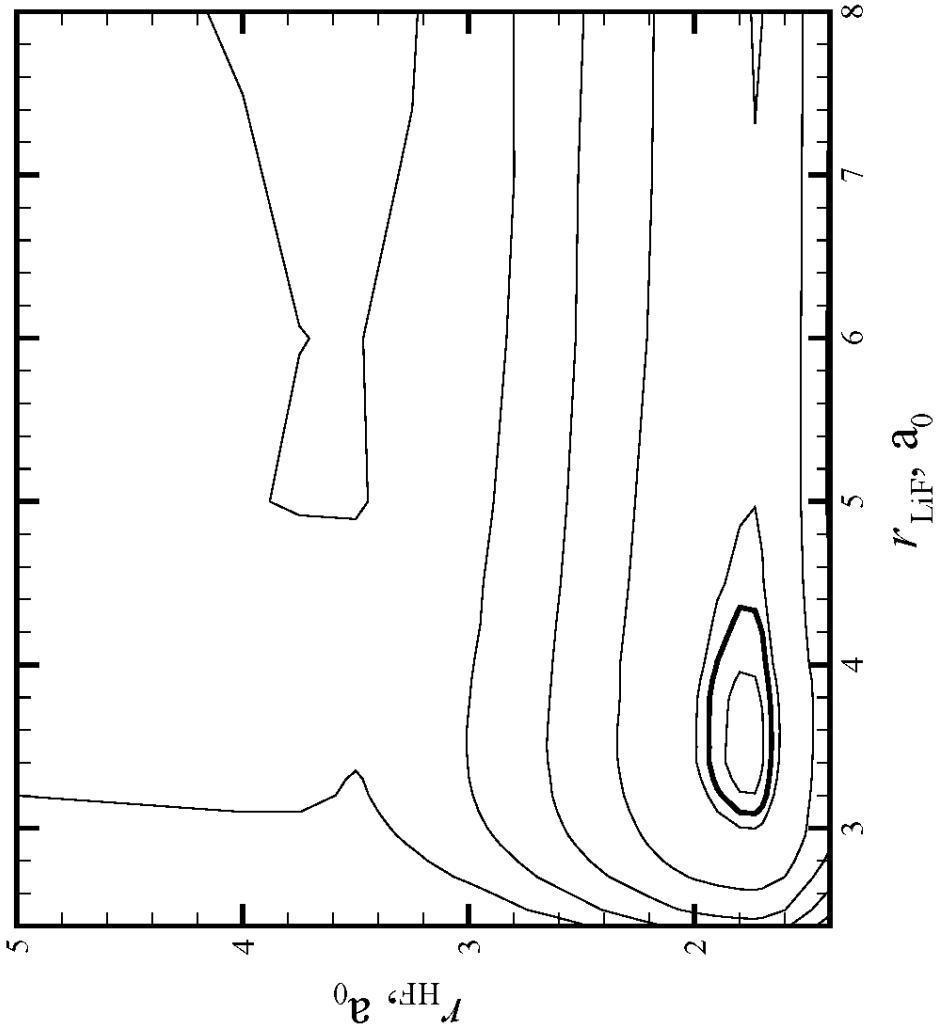

Figure 10

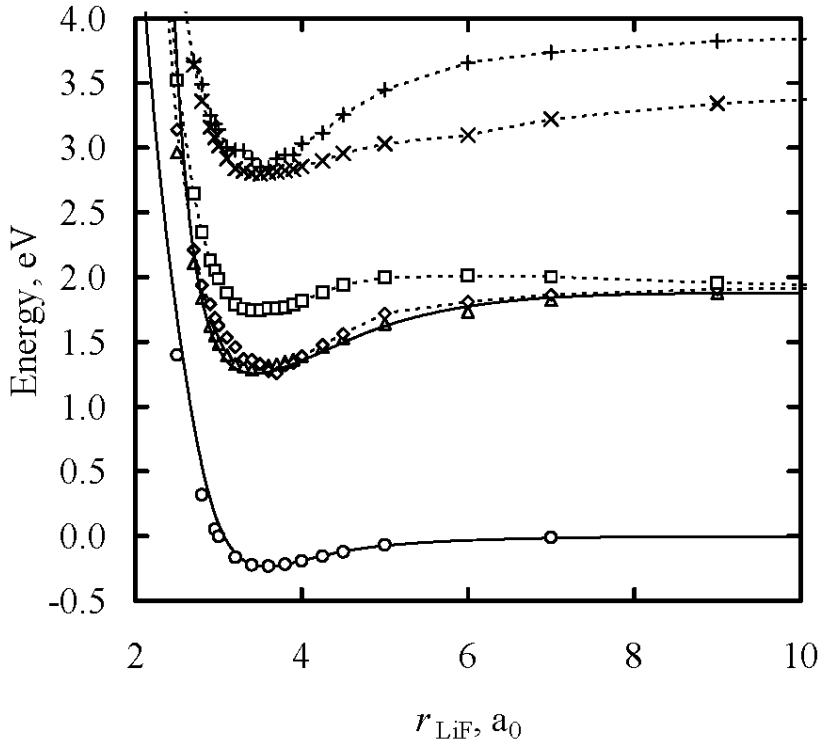

Figure 11

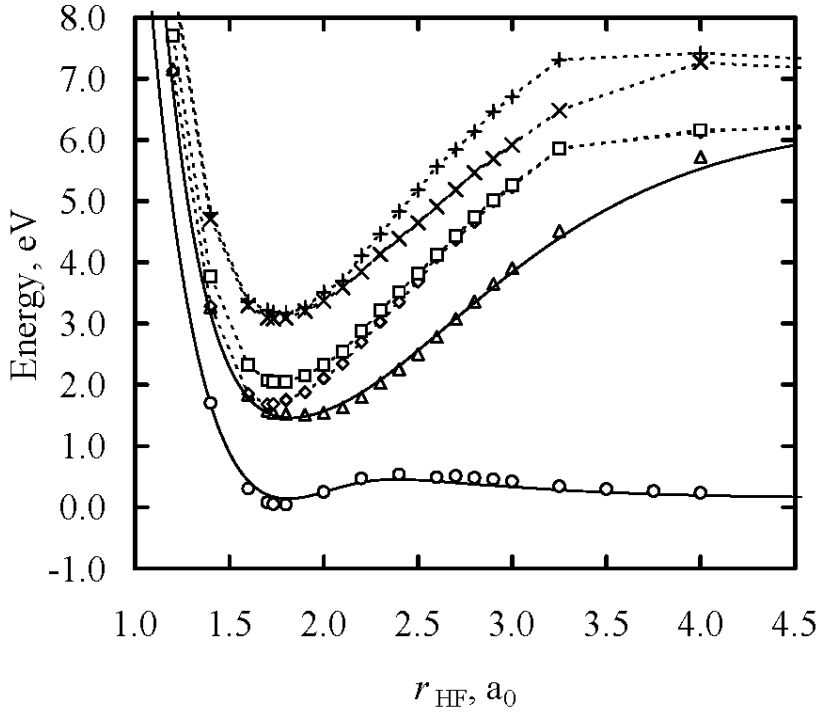

Supporting Information

S.1. Nuclear Geometry Grids for the *Ab Initio* Calculations

S.1.1. Strategy A Data

The 6-root MRDCI calculations employing the largest thresholds T, i.e., T = 4, 6, and 8 μE_h, (Strategy A) consisted of 3,380 geometries. In specifying grids we will use a shorthand notation that, for example, 2.5(0.1)2.8 denotes 2.5, 2.6, 2.7, and 2.8. The main grid included 27 Li–F distances: r_{LiF} = 2.0, 2.25, 2.5,2.7(0.1)2.9, 2.9553, 3.0(0.1)4.0, 4.25, 4.5, 5.0(1.0)7.0, and 9.0(2.0)15.0 a_0; 24 H–F distances: r_{HF} = 1.2(0.2)1.6, 1.7, 1.7325, 1.8(0.1)3.0, 3.25(0.25)4.0, 5.0, and 7.0 a_0; and five values of the Li–F–H angle: θ = 45, 70(20)110, and 179.99 degrees. Notice the presence of the equilibrium bond lengths for LiF (r_{LiF} = 2.9553 a_0) and HF (r_{HF} = 1.7325 a_0) among the values of r_{LiF} and r_{HF}, respectively. This grid of 3,240 points was augmented by calculations for θ = 0.01 degrees, r_{LiF} = 3.0(2.0)7.0, 11.0, and 15.0 a_0, and r_{HF} = 1.2, 1.4(0.1)1.8, and 2.0(0.2)2.4 a_0, and by calculations for r_{HF} = 3.8 a_0, r_{LiF} = 2.25, 2.5, 2.7(0.1)2.9, 2.9553, 3.0(0.1)4.0, 4.25, and 4.5 a_0, and θ = 45, 70(20)110, and 179.99 degrees.

S.1.2. Strategy B Data

For the 2-root MRDCI calculations employing the intermediate thresholds T, i.e., T = 1, 2, and 3 μE_h (Strategy B), the main grid consisted of 27 Li–F distances and five values of the Li–F–H angle identical to those described above, and of up to 18 H–F distances, covering the intervals 1.4–3.0 a_0 for θ = 45 degree, 1.4–2.7 a_0 for θ = 70, 90, and 110 degrees, and 1.4–2.5 a_0 for θ = 179.99 degrees. This grid of 2,052 geometries was augmented by two sets of extra calculations. In the first set of extra calculations, we added 45 points for θ = 0.01 degrees, using the following grid: r_{LiF} = 3.0(2.0)7.0, 11.0, and 15.0 a_0, and r_{HF} = 1.2, 1.4(0.1)1.8, and 2.0(0.2)2.4 a_0. In the second set of extra calculations, which played an important role in fine tuning the final fit, we added 135 nuclear geometries obtained by combining the 27 Li–F distances from the main grid with

the following values of r_{HF} and θ: r_{HF} = 2.7 a_0 and θ = 179.99 degrees, and r_{HF} = 3.0 a_0 and θ = 70, 90, 110, and 179.99 degrees. The total number of Strategy B geometries is 2,232, and these geometries form a subset of the Strategy A geometries.

S.1.3. Strategy C Data

Finally, the most accurate, 1-root calculations using the smallest selection thresholds T = 0.15, 0.30, and 0.45 μE_h (Strategy C) were performed on a grid of 15 Li–F distances: r_{LiF} = 2.5, 2.8, 2.9553, 3.0(0.2)4.0, 4.25, 4.5, 5.0, and 7.0(4.0)15.0 a_0, ten H–F distances: r_{HF} = 1.4, 1.6, 1.7, 1.7325, 1.8, 2.0, 2.1, and 2.2(0.2)2.6 a_0, and seven values of the Li–F–H angle: θ = 45, 70(20)150, and 179.99 degrees. This grid of 1,050 points was augmented by 24 extra points for θ = 0.01 degrees, r_{LiF} = 5.0 and 7.0(4.0)15.0 a_0, and r_{HF} = 1.5(0.1)1.8, 2.0, and 2.2 a_0 (to improve the description of the θ = 0 region) and by adding 11 values of θ for r_{LiF} = 3.6 a_0 and r_{HF} = 1.763 a_0, i.e., θ = 10(10)60, 80(30)140, 160, and 170 degrees, to improve the description of the θ-dependence. To further improve the description of the saddle point region and obtain a highly accurate description of the product channel (including the shallow minimum in the product valley and the LiF + H asymptote), we added 90 points corresponding to r_{HF} = 2.5, 2.9553, 3.2, 3.4, and 3.8 a_0, r_{HF} = 2.8, 3.0, 3.25, 3.5, 4.0, and 5.0 a_0, and θ = 45, 70, and 90 degrees, 140 points corresponding to r_{LiF} = 2.5, 2.9553, 3.2, 3.4, and 3.8 a_0, r_{HF} = 6.0, 7.0(2.0)15.0, and 20.0 a_0, and θ = 45, 70, 90, and 179.99 degrees, and 47 points corresponding to r_{HF} = 3.8 a_0, r_{LiF} = 2.25 – 5.0 a_0, and θ = 45, 70(20)110, and 179.99 degrees. The total number of points used in the MRDCI calculations for the ground state with Strategy C calculations was 1,362.

S.1.4. Additional Calculations

An additional 45 calculations were performed using the Strategy B thresholds (i.e., T = 1, 2, and 3 μE_h) for the six lowest-energy states of LiFH. The calculations were

performed along three one-dimensional cuts through the minimum of the ground state van der Waals well: q_{HF} = 1.76327 a_0, $Q_{Li,HF}$ = 2.5(0.2)3.3, 3.59757, 3.7, 4.0(0.5)5.0, 6.0, 8.0, 11.0, 15.0 a_0, and $\chi_{Li,HF}$ = 70.01 degrees; q_{HF} = 1.76327 a_0, $Q_{Li,HF}$ = 3.59757 a_0, and $\chi_{Li,HF}$ = 1, 10(10)60, 70.01, 80(10)170, 179 degrees; and q_{HF} = 1.3(0.1)1.7, 1.76327, 1.9(0.1)2.4, 2.7, 3.0 a_0, $Q_{Li,HF}$ = 3.59757 a_0, and $\chi_{Li,HF}$ = 70.01 degrees, where q_{HF} is the magnitude of the vector from H to F ($\mathbf{q}_{HF}$), $Q_{Li,HF}$ is the magnitude of the vector from Li to the center-of-mass of HF ($\mathbf{Q}_{Li,HF}$), and $\chi_{Li,HF}$ and is angle between $\mathbf{Q}_{Li,HF}$ and $\mathbf{q}_{HF}$.

S.2. Quasidiabatic Potential Energy Matrix for LiFH: Surface fit J

S.2.1. LiFH U_{11} Surface

The U_{11} potential energy surface explicitly contains long-range interactions in the Li(2*s*) + HF asymptote as a correction to the interaction potential

$$U_{11}(\mathbf{R}) = U_{11}^{I}(\mathbf{R}) + U_{11}^{LR}(\mathbf{R}), \tag{S-1}$$

where $\mathbf{R}$ = (r_{LiH}, r_{HF}, r_{LiF}), and r_{AB} is the A–B internuclear distance. The long-range forces U_{11}^{LR} are described in Sec. S.2.4. The interaction potential U_{11}^{I} contains only the Li + HF asymptote and the product van der Waals well. It is relatively simple and may be described by the sum of three diatomic terms,

$$U_{11}^{I}(\mathbf{R}) = S_{LiH}(\mathbf{R}) + S_{HF}(\mathbf{R}) + S_{LiF}(r_{LiF}) + D_{HF}^{e}, \tag{S-2}$$

where S_{AB} represents the AB diatomic interaction, and D_{HF}^{e} sets the zero of energy.

The LiH diatomic does not represent the isolated Li–H interaction. It represents Li–H interactions in the close presence of F and is purely repulsive,

$$S_{LiH}(\mathbf{R}) = S_{LiH}^{a}(r_{LiH}) + [S_{LiH}^{c}(r_{LiH}) - S_{LiH}^{a}(r_{LiH})]\Phi_{LiH}(\mathbf{R}), \tag{S-3}$$

$$S_{LiH}^{a}(r_{LiH}) = D_{LiH}^{a} \exp[-\beta_{LiH}^{a}(r_{LiH} - r_{LiH}^{0})], \tag{S-4}$$

$$S_{LiH}^{c}(r_{LiH}) = D_{LiH}^{c} \exp[-\beta_{LiH}^{c}(r_{LiH} - r_{LiH}^{0})], \tag{S-5}$$

where Φ_{LiH} is a switching function given by

$$\Phi_{\mathrm{LiH}}(\mathbf{R}) = \frac{1}{2} - \frac{1}{2}\tanh\left(\frac{r_{\mathrm{LiH}}^{\mathrm{x}}(\mathbf{R}) - \rho_{\mathrm{LiH}}}{\Delta_{\mathrm{LiH}}}\right), \tag{S-6}$$

$$r_{\mathrm{LiH}}^{\mathrm{x}} = r_{\mathrm{LiH}} - r_{\mathrm{LiF}} + \gamma_{\mathrm{LiH}} r_{\mathrm{HF}}. \tag{S-7}$$

The HF potential curve S_{HF} was fit to experimental Rydberg-Klein-Rees (RKR) data for the HF molecule.[2] The functional form is a Morse curve with a range parameter that depends on the HF bond length,

$$S_{\mathrm{HF}}^{\mathrm{e}}(r_{\mathrm{HF}}) = D_{\mathrm{HF}}^{\mathrm{e}} X_{\mathrm{HF}}^{\mathrm{e}}(r_{\mathrm{HF}})[X_{\mathrm{HF}}^{\mathrm{e}}(r_{\mathrm{HF}}) - 2], \tag{S-8}$$

where

$$X_{\mathrm{HF}}^{\mathrm{e}}(r_{\mathrm{HF}}) = \exp[-\beta_{\mathrm{HF}}^{\mathrm{e}}(r_{\mathrm{HF}})(r_{\mathrm{HF}} - r_{\mathrm{HF}}^{\mathrm{e}})] \tag{S-9}$$

and

$$\beta_{\mathrm{HF}}^{\mathrm{e}}(r_{\mathrm{HF}}) = b_{\mathrm{HF}}^{0} + b_{\mathrm{HF}}^{1}(r_{\mathrm{HF}} - r_{\mathrm{HF}}^{0}) + b_{\mathrm{HF}}^{2}(r_{\mathrm{HF}} - r_{\mathrm{HF}}^{0})^{2}. \tag{S-10}$$

Additional flexibility was added in the interaction region such that

$$S_{\mathrm{HF}}(\mathbf{R}) = S_{\mathrm{HF}}^{\mathrm{c}}(\mathbf{R}) + [S_{\mathrm{HF}}^{\mathrm{e}}(r_{\mathrm{HF}}) - S_{\mathrm{HF}}^{\mathrm{c}}(\mathbf{R})]\Phi_{\mathrm{HF}}(r_{\mathrm{LiF}}), \tag{S-11}$$

where

$$S_{\mathrm{HF}}^{\mathrm{c}}(\mathbf{R}) = D_{\mathrm{HF}}^{\mathrm{c}}(\mathbf{R}) X_{\mathrm{HF}}^{\mathrm{c}}(r_{\mathrm{HF}})[X_{\mathrm{HF}}^{\mathrm{c}}(r_{\mathrm{HF}}) - 2], \tag{S-12}$$

$$X_{\mathrm{HF}}^{\mathrm{c}}(r_{\mathrm{HF}}) = \exp[-\beta_{\mathrm{HF}}^{\mathrm{c}}(r_{\mathrm{HF}} - r_{\mathrm{HF}}^{\mathrm{c}})], \tag{S-13}$$

$$D_{\mathrm{HF}}^{\mathrm{c}}(\mathbf{R}) = D_{\mathrm{HF}}^{\mathrm{e}} - [D_{\mathrm{HF}}^{\mathrm{cc}} + \tfrac{1}{2} D_{\mathrm{HF}}^{\mathrm{chi}}(1 - \cos\chi_{\mathrm{Li,HF}})], \tag{S-14}$$

$$\Phi_{\mathrm{HF}}(r_{\mathrm{LiF}}) = \frac{1}{2} + \frac{1}{2}\tanh\left(\frac{r_{\mathrm{LiF}} - \rho_{\mathrm{HF}}}{\Delta_{\mathrm{HF}}}\right), \tag{S-15}$$

and $\chi_{\mathrm{Li,HF}}$ is the Jacobi angle, i.e., the angle between the vector from the Li atom to the center of mass of HF ($\mathbf{Q}_{\mathrm{Li,HF}}$) and the vector from H to F ($\mathbf{q}_{\mathrm{HF}}$). The Jacobi vector

$\mathbf{Q}_{\mathrm{Li,HF}}$ depends on the masses of the H and F nuclei, and these masses (along with the mass of Li as discussed below) are therefore parameters of the fit. The masses are taken as those of the most abundant isotopes and are listed in Table S-1.

The LiF diatomic $S_{\mathrm{LiF}}(r_{\mathrm{LiF}})$ is a shallow Morse curve,

$$S_{\mathrm{LiF}}(r_{\mathrm{LiF}}) = D_{\mathrm{LiF}} X_{\mathrm{LiF}}(r_{\mathrm{LiF}})[X_{\mathrm{LiF}}(r_{\mathrm{LiF}}) - 2], \tag{S-16}$$

$$X_{\mathrm{LiF}}(r_{\mathrm{LiF}}) = \exp[-\beta_{\mathrm{LiF}}(r_{\mathrm{LiF}} - r_{\mathrm{LiF}}^{0})]. \tag{S-17}$$

The values of the parameters used in the U_{11} potential matrix element are given in Table S-1.

S.2.2. LiFH U_{12} Coupling Surface

The diabatic scalar coupling U_{12} is described by

$$U_{12}(\mathbf{R}) = U_{12}^{0}(\mathbf{R})\Phi_{12}(r_{\mathrm{HF}}), \tag{S-18}$$

where $U_{12}^{0}(\mathbf{R})$ is a physically motivated functional form that is cut off for large values of r_{HF} where the excited-state potential energy surface becomes energetically inaccessible, i.e.,

$$\Phi_{12}(r_{\mathrm{HF}}) = \frac{1}{2} - \frac{1}{2}\tanh[(r_{\mathrm{HF}} - \rho_{12})/\Delta_{12}]. \tag{S-19}$$

Nonadiabatic transitions in this regions are unimportant and eliminating the off-diagonal coupling in these regions greatly reduces the expense of accurate quantum mechanical dynamics calculations.

As discussed in Secs. II and III of the main paper, we calculated the diabatic coupling for the isolated LiH and LiF diatoms. The coupling between the two states considered here vanishes for the isolated HF diatom. We therefore treat the diabatic coupling in the full system as arising from diatomic terms in the LiF and LiH bond distances,

$$U_{\mathrm{LiH}}(r_{\mathrm{LiH}}) = g_{\mathrm{LiH}}(r_{\mathrm{LiH}} / r_{\mathrm{LiH}}^0)^6 \exp[-6(r_{\mathrm{LiH}} / r_{\mathrm{LiH}}^0 - 1)], \tag{S-20}$$

$$U_{\mathrm{LiF}}(r_{\mathrm{LiF}}) = g_{\mathrm{LiF}}(r_{\mathrm{LiF}} / r_{\mathrm{LiF}}^0)^8 \exp[-8(r_{\mathrm{LiF}} / r_{\mathrm{LiF}}^0 - 1)]. \tag{S-21}$$

These are functions which are zero when the diatomic distances r_{LiX} (X = H, F) are zero, and increase in magnitude to a maximum of g_{LiX} at $r_{\mathrm{LiX}} = r_{\mathrm{LiX}}^0$ as r_{LiX} increases. For larger values of r_{LiX} the functions decrease in magnitude at a rate determined by exponential.

The magnitudes of isolated diatomic coupling terms are reduced by the approach of the remaining atom,

$$\begin{aligned} U_{12}^0(\mathbf{R}) = {} & U_{\mathrm{LiH}}(r_{\mathrm{LiH}})\Phi_{\mathrm{HF},1}(r_{\mathrm{HF}})\Phi_{\mathrm{LiF}}(r_{\mathrm{LiF}}) \\ & + U_{\mathrm{LiF}}(r_{\mathrm{LiF}})\Phi_{\mathrm{HF},2}(r_{\mathrm{HF}})\Phi_{\mathrm{LiH}}(r_{\mathrm{LiH}}). \end{aligned} \tag{S-22}$$

The functions $\Phi_{\mathrm{HF},1}$, Φ_{LiF}, $\Phi_{\mathrm{HF},2}$, and Φ_{LiH} are given by

$$\Phi_{\mathrm{HF},1}(r_{\mathrm{HF}}) = \frac{1}{2} + \frac{1}{2}\tanh\frac{r_{\mathrm{HF}} - \rho_{\mathrm{HF},1}}{\Delta_{\mathrm{HF},1}}, \tag{S-23}$$

$$\Phi_{\mathrm{LiF}}(r_{\mathrm{LiF}}) = \frac{1}{2} + \frac{1}{2}\tanh\frac{r_{\mathrm{LiF}} - \rho_{\mathrm{LiF}}}{\Delta_{\mathrm{LiF}}}, \tag{S-24}$$

$$\Phi_{\mathrm{HF},2}(r_{\mathrm{HF}}) = \frac{1}{2} + \frac{1}{2}\tanh\frac{r_{\mathrm{HF}} - \rho_{\mathrm{HF},2}}{\Delta_{\mathrm{HF},2}}, \tag{S-25}$$

$$\Phi_{\mathrm{LiH}}(r_{\mathrm{LiH}}) = \frac{1}{2} + \frac{1}{2}\tanh\frac{r_{\mathrm{LiH}} - \rho_{\mathrm{LiH}}}{\Delta_{\mathrm{LiH}}}. \tag{S-26}$$

The values of the parameters used in the U_{12} potential matrix element are given in Table S-2.

S.2.3. LiFH U_{22} Surface

The U_{22} potential energy surface explicitly contains long-range interactions in the Li(2*p*) + HF and LiF + H asymptotes as a correction to the interaction potential,

$$U_{22}(\mathbf{R}) = U_{22}^{\mathrm{I}}(\mathbf{R}) + U_{22}^{\mathrm{LR}}(\mathbf{R}). \tag{S-27}$$

The long-range forces U_{22}^{LR} are described in Sec. S.2.4. The interaction potential U_{22}^{I} is a modified[3] London-Eyring-Polanyi-Sato (LEPS)[4–6] form,

$$U_{22}^{\mathrm{I}}(\mathbf{R}) = J_{\mathrm{LiH}}(\mathbf{R}) + J_{\mathrm{HF}}(\mathbf{R}) + J_{\mathrm{LiF}}(\mathbf{R}) - \tfrac{1}{\sqrt{2}}\sqrt{W(\mathbf{R}) + Z(\mathbf{R})^2} + D_{\mathrm{HF}}^{\mathrm{e}}\,, \tag{S-28}$$

where

$$W(\mathbf{R}) = (K_{\mathrm{LiH}}(\mathbf{R}) - K_{\mathrm{HF}}(\mathbf{R}))^2 + (K_{\mathrm{HF}}(\mathbf{R}) - K_{\mathrm{LiF}}(\mathbf{R}))^2 + (K_{\mathrm{LiF}}(\mathbf{R}) - K_{\mathrm{LiH}}(\mathbf{R}))^2\,. \tag{S-29}$$

The functions J_α and K_α (α = LiH, HF, and LiF) are functions of diatomic singlet S_α and triplet T_α functions

$$J_\alpha(\mathbf{R}) = \frac{1}{2}(S_\alpha(\mathbf{R}) + T_\alpha(\mathbf{R}))\,, \tag{S-30}$$

$$K_\alpha(\mathbf{R}) = \frac{1}{2}(S_\alpha(\mathbf{R}) - T_\alpha(\mathbf{R}))\,. \tag{S-31}$$

The expression

$$Z(\mathbf{R}) = c_{2\mathrm{a}}\exp[-c_{2\mathrm{b}}W(\mathbf{R}) - c_{2\mathrm{c}}(r_{\mathrm{HF}} + r_{\mathrm{LiH}} + r_{\mathrm{LiF}})] \tag{S-32}$$

is a necessary to remove a cusp that would otherwise occur in eq. (28) when $W(\mathbf{R})$ goes to zero.

The LiH singlet curve is the sum of two repulsive curves, one of which is present only when the LiH diatom is interacting with F,

$$S_{\mathrm{LiH}}(\mathbf{R}) = S_{\mathrm{LiH}}^{\mathrm{a}}(r_{\mathrm{LiH}}) + S_{\mathrm{LiH}}^{\mathrm{c}}(r_{\mathrm{LiH}})\Phi_{\mathrm{LiH}}(\mathbf{R})\,, \tag{S-33}$$

$$S_{\mathrm{LiH}}^{\mathrm{a}}(r_{\mathrm{LiH}}) = D_{\mathrm{LiH}}^{\mathrm{a2}}X_{\mathrm{LiH}}^{\mathrm{a}}(r_{\mathrm{LiH}})^2 + D_{\mathrm{LiH}}^{\mathrm{a1}}X_{\mathrm{LiH}}^{\mathrm{a}}(r_{\mathrm{LiH}})\,, \tag{S-34}$$

$$X_{\mathrm{LiH}}^{\mathrm{a}}(r_{\mathrm{LiH}}) = \exp[-\beta_{\mathrm{LiH}}^{\mathrm{a}}(r_{\mathrm{LiH}} - r_{\mathrm{LiH}}^0)]\,, \tag{S-35}$$

$$S_{\mathrm{LiH}}^{\mathrm{c}}(r_{\mathrm{LiH}}) = D_{\mathrm{LiH}}^{\mathrm{c}}\exp[-\beta_{\mathrm{LiH}}^{\mathrm{c}}(r_{\mathrm{LiH}} - r_{\mathrm{LiH}}^0)]\,, \tag{S-36}$$

$$\Phi_{\mathrm{LiH}}(\mathbf{R}) = \frac{1}{2} - \frac{1}{2}\tanh\left(\frac{r^{\mathrm{x}}_{\mathrm{LiH}}(\mathbf{R}) - \rho_{\mathrm{LiH}}}{\Delta_{\mathrm{LiH}}}\right), \tag{S-37}$$

$$r^{\mathrm{x}}_{\mathrm{LiH}}(\mathrm{R}) = r_{\mathrm{LiH}} - r_{\mathrm{LiF}} + \gamma_{\mathrm{LiH}}\, r_{\mathrm{HF}}. \tag{S-38}$$

The LiH triplet is a modified anti-Morse curve,

$$T_{\mathrm{LiH}}(r_{\mathrm{LiH}}) = D^{\mathrm{t2}}_{\mathrm{LiH}} X^{\mathrm{t}}_{\mathrm{LiH}}(r_{\mathrm{LiH}})^2 + D^{\mathrm{t1}}_{\mathrm{LiH}} X^{\mathrm{t}}_{\mathrm{LiH}}(r_{\mathrm{LiH}}), \tag{S-39}$$

$$X^{\mathrm{t}}_{\mathrm{LiH}}(r_{\mathrm{LiH}}) = \exp[-\beta^{\mathrm{t}}_{\mathrm{LiH}}(r_{\mathrm{LiH}} - r^{\mathrm{t}}_{\mathrm{LiH}})]. \tag{S-40}$$

The asymptotic HF singlet is similar to the form used for the U_{11} potential matrix element but shifted upwards by the excitation energy of Li. The singlet is cut off such that the U_{11} and U_{22} surfaces are equal at large r_{HF},

$$S^{\mathrm{a}}_{\mathrm{HF}}(r_{\mathrm{HF}}) = S^{\mathrm{aa}}_{\mathrm{HF}}(r_{\mathrm{HF}}) + [S^{\mathrm{e}}_{\mathrm{HF}}(r_{\mathrm{HF}}) - S^{\mathrm{aa}}_{\mathrm{HF}}(r_{\mathrm{HF}})]\Phi^{\mathrm{a}}_{\mathrm{HF}}(r_{\mathrm{HF}}), \tag{S-41}$$

$$S^{\mathrm{e}}_{\mathrm{HF}}(r_{\mathrm{HF}}) = D^{\mathrm{e}}_{\mathrm{HF}} X^{\mathrm{e}}_{\mathrm{HF}}(r_{\mathrm{HF}})[X^{\mathrm{e}}_{\mathrm{HF}}(r_{\mathrm{HF}}) - 2] + E_{\mathrm{Li}(2p)}, \tag{S-42}$$

$$X^{\mathrm{e}}_{\mathrm{HF}}(r_{\mathrm{HF}}) = \exp[-\beta^{\mathrm{e}}_{\mathrm{HF}}(r_{\mathrm{HF}})(r_{\mathrm{HF}} - r^{\mathrm{e}}_{\mathrm{HF}})], \tag{S-43}$$

$$\beta^{\mathrm{e}}_{\mathrm{HF}}(r_{\mathrm{HF}}) = b^0_{\mathrm{HF}} + b^1_{\mathrm{HF}}(r_{\mathrm{HF}} - r^0_{\mathrm{HF}}) + b^2_{\mathrm{HF}}(r_{\mathrm{HF}} - r^0_{\mathrm{HF}})^2, \tag{S-44}$$

$$S^{\mathrm{aa}}_{\mathrm{HF}}(r_{\mathrm{HF}}) = D^{\mathrm{aa}}_{\mathrm{HF}} X^{\mathrm{aa}}_{\mathrm{HF}}(r_{\mathrm{HF}})[X^{\mathrm{aa}}_{\mathrm{HF}}(r_{\mathrm{HF}}) - 2], \tag{S-45}$$

$$X^{\mathrm{aa}}_{\mathrm{HF}}(r_{\mathrm{HF}}) = \exp[-\beta^{\mathrm{aa}}_{\mathrm{HF}}(r_{\mathrm{HF}})(r_{\mathrm{HF}} - r^{\mathrm{aa}}_{\mathrm{HF}})], \tag{S-46}$$

$$\Phi^{\mathrm{a}}_{\mathrm{HF}}(r_{\mathrm{HF}}) = \frac{1}{2} - \frac{1}{2}\tanh\left(\frac{r_{\mathrm{HF}} - \rho^{\mathrm{a}}_{\mathrm{HF}}}{\Delta^{\mathrm{a}}_{\mathrm{HF}}}\right). \tag{S-47}$$

Additional flexibility was added to the HF singlet in the interaction region

$$S_{\mathrm{HF}}(\mathbf{R}) = S^{\mathrm{c}}_{\mathrm{HF}}(\mathbf{R}) + [S^{\mathrm{a}}_{\mathrm{HF}}(r_{\mathrm{HF}}) - S^{\mathrm{c}}_{\mathrm{HF}}(\mathbf{R})]\Phi_{\mathrm{HF}}(r_{\mathrm{LiF}}), \tag{S-48}$$

where

$$S^{\mathrm{c}}_{\mathrm{HF}}(\mathbf{R}) = D^{\mathrm{c}}_{\mathrm{HF}}(\mathbf{R}) X^{\mathrm{e}}_{\mathrm{HF}}(r_{\mathrm{HF}})[X^{\mathrm{e}}_{\mathrm{HF}}(r_{\mathrm{HF}}) - 2]\Phi^{\mathrm{c}}_{\mathrm{HF}}(r_{\mathrm{HF}}) + E_{\mathrm{Li}(2p)}\,, \quad \text{(S-49)}$$

$$D^{\mathrm{c}}_{\mathrm{HF}}(\mathbf{R}) = D^{\mathrm{e}}_{\mathrm{HF}} - [D^{\mathrm{cc}}_{\mathrm{HF}} + \tfrac{1}{2} D^{\mathrm{chi}}_{\mathrm{HF}}(1 - \cos\theta_{\mathrm{LiFH}})]\,, \quad \text{(S-50)}$$

$$\Phi^{\mathrm{c}}_{\mathrm{HF}}(r_{\mathrm{HF}}) = \frac{1}{2} - \frac{1}{2}\tanh\left(\frac{r_{\mathrm{HF}} - \rho^{\mathrm{c}}_{\mathrm{HF}}}{\Delta^{\mathrm{c}}_{\mathrm{HF}}}\right), \quad \text{(S-51)}$$

$$\Phi_{\mathrm{HF}}(r_{\mathrm{LiF}}) = \frac{1}{2} + \frac{1}{2}\tanh\left(\frac{r_{\mathrm{LiF}} - \rho_{\mathrm{HF}}}{\Delta_{\mathrm{HF}}}\right), \quad \text{(S-52)}$$

and θ_{LiFH} is the Li–F–H bond angle.

The HF triplet contains angular dependence,

$$T_{\mathrm{HF}}(\mathbf{R}) = T^{0}_{\mathrm{HF}}(r_{\mathrm{HF}})\tfrac{1}{2}(1 + \cos\theta_{\mathrm{LiFH}}) + T^{180}_{\mathrm{HF}}(r_{\mathrm{HF}})\tfrac{1}{2}(1 - \cos\theta_{\mathrm{LiFH}})\,, \quad \text{(S-53)}$$

where

$$T^{0}_{\mathrm{HF}}(r_{\mathrm{HF}}) = D^{\mathrm{t2,0}}_{\mathrm{HF}} X^{\mathrm{t,0}}_{\mathrm{HF}}(r_{\mathrm{HF}})^2 + D^{\mathrm{t1,0}}_{\mathrm{HF}} X^{\mathrm{t,0}}_{\mathrm{HF}}(r_{\mathrm{HF}})\,, \quad \text{(S-54)}$$

$$T^{180}_{\mathrm{HF}}(r_{\mathrm{HF}}) = D^{\mathrm{t2,180}}_{\mathrm{HF}} X^{\mathrm{t,180}}_{\mathrm{HF}}(r_{\mathrm{HF}})^2 + D^{\mathrm{t1,180}}_{\mathrm{HF}} X^{\mathrm{t,180}}_{\mathrm{HF}}(r_{\mathrm{HF}})\,, \quad \text{(S-55)}$$

$$X^{\mathrm{t,0}}_{\mathrm{HF}}(r_{\mathrm{HF}}) = \exp[-\beta^{\mathrm{t,0}}_{\mathrm{HF}}(r_{\mathrm{HF}} - r^{\mathrm{t}}_{\mathrm{HF}})]\,, \quad \text{(S-56)}$$

$$X^{\mathrm{t,180}}_{\mathrm{HF}}(r_{\mathrm{HF}}) = \exp[-\beta^{\mathrm{t,180}}_{\mathrm{HF}}(r_{\mathrm{HF}} - r^{\mathrm{t}}_{\mathrm{HF}})]\,, \quad \text{(S-57)}$$

The LiF singlet curve is given by

$$S_{\mathrm{LiF}}(\mathbf{R}) = S^{\mathrm{c}}_{\mathrm{LiF}}(\mathbf{R}) + [S^{\mathrm{a}}_{\mathrm{LiF}}(\mathbf{R}) - S^{\mathrm{c}}_{\mathrm{LiF}}(\mathbf{R})]\Phi_{\mathrm{LiF}}(\mathbf{R})\,. \quad \text{(S-58)}$$

The asymptotic term is based on the RKR data of Ref. 7 and on the *ab initio* data presented in Sec. II of the main paper, and it is given by

$$S^{\mathrm{a}}_{\mathrm{LiF}}(\mathbf{R}) = \left[(D^{\mathrm{e}}_{\mathrm{LiF}} + E_{\mathrm{Li}(2p)}) X^{\mathrm{a}}_{\mathrm{LiF}}(\mathbf{R})[X^{\mathrm{a}}_{\mathrm{LiF}}(\mathbf{R}) - 2] + E_{\mathrm{Li}(2p)}\right] \Phi^{\mathrm{a}}_{\mathrm{LiF}}(\mathbf{R})\,, \quad \text{(S-59)}$$

where

$$X^{\mathrm{a}}_{\mathrm{LiF}}(\mathbf{R}) = \exp[-\beta^{\mathrm{a}}_{\mathrm{LiF}}(\mathbf{R})(r_{\mathrm{LiF}} - r^{\mathrm{e}}_{\mathrm{LiF}})]\,, \tag{S-60}$$

$$\Phi^{\mathrm{a}}_{\mathrm{LiF}}(\mathbf{R}) = \left(\frac{1}{2} - \frac{1}{2}\tanh\frac{r_{\mathrm{LiF}} - \rho^{\mathrm{a}}_{\mathrm{LiF}}}{\Delta^{\mathrm{a}}_{\mathrm{LiF}}}\right)\left[d^{\mathrm{aa}}_{\mathrm{LiF}} + (1 - d^{\mathrm{aa}}_{\mathrm{LiF}})\Phi^{\mathrm{aa}}_{\mathrm{LiF}}(r_{\mathrm{HF}})\right], \tag{S-61}$$

$$\Phi^{\mathrm{aa}}_{\mathrm{LiF}}(r_{\mathrm{HF}}) = \left(\frac{1}{2} + \frac{1}{2}\tanh\frac{r_{\mathrm{HF}} - \rho^{\mathrm{aa}}_{\mathrm{LiF}}}{\Delta^{\mathrm{aa}}_{\mathrm{LiF}}}\right), \tag{S-62}$$

$$\beta^{\mathrm{a}}_{\mathrm{LiF}}(\mathbf{R}) = \beta^{\mathrm{b}}_{\mathrm{LiF}}(\mathbf{R})\frac{\beta^{\mathrm{e}}_{\mathrm{LiF}}(r_{\mathrm{LiF}}) + \left(r_{\mathrm{LiF}}/\gamma_{\mathrm{LiF}}\right)^{n_{\mathrm{LiF}}}}{\beta^{\mathrm{b}}_{\mathrm{LiF}}(\mathbf{R}) + \left(r_{\mathrm{LiF}}/\gamma_{\mathrm{LiF}}\right)^{n_{\mathrm{LiF}}}}\,, \tag{S-63}$$

$$\beta^{\mathrm{b}}_{\mathrm{LiF}}(\mathbf{R}) = \beta^{\mathrm{e}}_{\mathrm{LiF}}(r_{\mathrm{LiF}}) + [\beta^{\mathrm{d}}_{\mathrm{LiF}} - \beta^{\mathrm{e}}_{\mathrm{LiF}}(r_{\mathrm{LiF}})]\Phi^{\mathrm{b}}_{\mathrm{LiF}}(\mathbf{R})\,, \tag{S-64}$$

$$\Phi^{\mathrm{b}}_{\mathrm{LiF}}(\mathbf{R}) = \left(\frac{1}{2} - \frac{1}{2}\tanh\frac{r_{\mathrm{HF}} - \rho^{\mathrm{b}}_{\mathrm{LiF}}}{\Delta^{\mathrm{b}}_{\mathrm{LiF}}}\right)\frac{1}{2}\left(1 + \cos\theta_{\mathrm{LiFH}}\right), \tag{S-65}$$

$$\beta^{\mathrm{e}}_{\mathrm{LiF}}(r_{\mathrm{LiF}}) = b^{\mathrm{e1}}_{\mathrm{LiF}} + \frac{b^{\mathrm{e2}}_{\mathrm{LiF}} r_{\mathrm{LiF}}}{\left(b^{\mathrm{e3}}_{\mathrm{LiF}} + b^{\mathrm{e4}}_{\mathrm{LiF}} r_{\mathrm{LiF}}\right)^2}\,. \tag{S-66}$$

The form of the LiF singlet in the presence of H is

$$S^{\mathrm{c}}_{\mathrm{LiF}}(\mathbf{R}) = [D^{\mathrm{c}}_{\mathrm{LiF}}(\mathbf{R}) + E_{\mathrm{Li}(2p)}]X^{\mathrm{c}}_{\mathrm{LiF}}(\mathbf{R})[X^{\mathrm{c}}_{\mathrm{LiF}}(\mathbf{R}) - 2], \tag{S-67}$$

$$D^{\mathrm{c}}_{\mathrm{LiF}}(\mathbf{R}) = D^{\mathrm{c},0}_{\mathrm{LiF}}\,\tfrac{1}{2}(1 + \cos\theta_{\mathrm{LiFH}}) + D^{\mathrm{c},180}_{\mathrm{LiF}}\,\tfrac{1}{2}(1 - \cos\theta_{\mathrm{LiFH}})\,, \tag{S-68}$$

$$X^{\mathrm{c}}_{\mathrm{LiF}}(\mathbf{R}) = \exp[-\beta^{\mathrm{c}}_{\mathrm{LiF}}(\mathbf{R})(r_{\mathrm{LiF}} - r^{\mathrm{e}}_{\mathrm{LiF}})]\,, \tag{S-69}$$

$$\beta^{\mathrm{c}}_{\mathrm{LiF}}(\mathbf{R}) = \beta^{\mathrm{c},0}_{\mathrm{LiF}}\,\tfrac{1}{2}(1 + \cos\theta_{\mathrm{LiFH}}) + \beta^{\mathrm{c},180}_{\mathrm{LiF}}\,\tfrac{1}{2}(1 - \cos\theta_{\mathrm{LiFH}})\,. \tag{S-70}$$

The asymptotic and close forms of the LiF singlet are joined together with a switching function that incorporates angular dependence

$$\Phi_{\mathrm{LiF}}(\mathbf{R}) = \frac{1}{2} - \frac{1}{2}\tanh\frac{\rho_{\mathrm{LiF}}(\mathbf{R})}{\Delta_{\mathrm{LiF}}(\mathbf{R})}, \tag{S-71}$$

$$\rho_{\mathrm{LiF}}(\mathbf{R}) = (r_{\mathrm{HF}}^{\mathrm{e}} - r_{\mathrm{HF}})\cos\phi_{\mathrm{LiF}}(\mathbf{R}) - (\rho_{\mathrm{LiF}}^{\mathrm{x}}(\mathbf{R}) - r_{\mathrm{LiF}})\sin\phi_{\mathrm{LiF}}(\mathbf{R}), \tag{S-72}$$

$$\rho_{\mathrm{LiF}}^{\mathrm{x}}(\mathbf{R}) = \rho_{\mathrm{LiF}}^{0} + (\rho_{\mathrm{LiF}}^{180} - \rho_{\mathrm{LiF}}^{0})\tfrac{1}{2}(1-\cos\theta_{\mathrm{LiFH}}), \tag{S-73}$$

$$\phi_{\mathrm{LiF}}(\mathbf{R}) = \phi_{\mathrm{LiF}}^{0} + (\phi_{\mathrm{LiF}}^{180} - \phi_{\mathrm{LiF}}^{0})\tfrac{1}{2}(1-\cos\theta_{\mathrm{LiFH}}), \tag{S-74}$$

$$\Delta_{\mathrm{LiF}}(\mathbf{R}) = \Delta_{\mathrm{LiF}}^{0} + (\Delta_{\mathrm{LiF}}^{180} - \Delta_{\mathrm{LiF}}^{0})\tfrac{1}{2}(1-\cos\theta_{\mathrm{LiFH}}). \tag{S-75}$$

The LiF triplet potential is a modified anti-Morse curve,

$$T_{\mathrm{LiF}}(\mathbf{R}) = T_{\mathrm{LiF}}^{0}(r_{\mathrm{LiF}})\tfrac{1}{2}(1+\cos\theta_{\mathrm{LiFH}}) + T_{\mathrm{LiF}}^{180}(r_{\mathrm{LiF}})\tfrac{1}{2}(1-\cos\theta_{\mathrm{LiFH}}), \tag{S-76}$$

$$T_{\mathrm{LiF}}^{0}(r_{\mathrm{LiF}}) = D_{\mathrm{LiF}}^{\mathrm{t2},0} X_{\mathrm{LiF}}^{\mathrm{t},0}(r_{\mathrm{LiF}})^2 + D_{\mathrm{LiF}}^{\mathrm{t1},0} X_{\mathrm{LiF}}^{\mathrm{t},0}(r_{\mathrm{LiF}}), \tag{S-77}$$

$$T_{\mathrm{LiF}}^{180}(r_{\mathrm{LiF}}) = D_{\mathrm{LiF}}^{\mathrm{t2},180} X_{\mathrm{LiF}}^{\mathrm{t},180}(r_{\mathrm{LiF}})^2 + D_{\mathrm{LiF}}^{\mathrm{t1},180} X_{\mathrm{LiF}}^{\mathrm{t},180}(r_{\mathrm{LiF}}), \tag{S-78}$$

$$X_{\mathrm{LiF}}^{\mathrm{t},0}(r_{\mathrm{LiF}}) = \exp[-\beta_{\mathrm{LiF}}^{\mathrm{t},0}(r_{\mathrm{LiF}} - r_{\mathrm{LiF}}^{\mathrm{e}})], \tag{S-79}$$

$$X_{\mathrm{LiF}}^{\mathrm{t},180}(r_{\mathrm{LiF}}) = \exp[-\beta_{\mathrm{LiF}}^{\mathrm{t},180}(r_{\mathrm{LiF}} - r_{\mathrm{LiF}}^{\mathrm{e}})], \tag{S-80}$$

The values of the parameters used in the U_{22} potential matrix element are given in Table S-3.

S.2.4. Long-Range Forces

Long-range interactions[8–10] were explicitly included in the U_{11} and U_{22} surfaces as shown in eqs. (1) and (27). The U_{11} surface contains the dipole-induced-dipole and dispersion interactions in the Li(2*s*) + HF arrangement,

$$U_{11}^{\mathrm{LR}}(\mathbf{R}) = U_{11,\mathrm{HF}}^{\mathrm{disp}}(\mathbf{R}) + U_{11,\mathrm{HF}}^{\mathrm{did}}(\mathbf{R}), \tag{S-81}$$

where the dispersion interactions are given by the London equation,[8,9]

$$U_{11,\mathrm{HF}}^{\mathrm{disp}}(\mathbf{R}) = -\frac{3}{2}\frac{I_{\mathrm{Li}(2s)} I_{\mathrm{HF}} \alpha_{\mathrm{Li}(2s)} \alpha_{\mathrm{HF}}(\mathbf{R})}{I_{\mathrm{Li}(2s)} + I_{\mathrm{HF}}} \frac{Q_{\mathrm{Li,HF}}}{Q_{\mathrm{Li,HF}}^7 + S_{11,\mathrm{HF}}^7} \times \Phi_{11,\mathrm{HF}}^{\mathrm{disp}}(\mathbf{R}) K_{11,\mathrm{HF}}(r_{\mathrm{HF}}), \quad \text{(S-82)}$$

where I_{A} is the ionization potential for species A, α_{A} is the polarizability of species A, $Q_{\mathrm{Li,HF}}$ is the magnitude of the translational Jacobi coordinate, i.e., $Q_{\mathrm{Li,HF}} = |\mathbf{Q}_{\mathrm{Li,HF}}|$, where $\mathbf{Q}_{\mathrm{Li,HF}}$ is the vector from Li to the center of mass of HF. The polarizability of HF includes angular dependence,

$$\alpha_{\mathrm{HF}}(\mathbf{R}) = \alpha_{\mathrm{HF}}^{\perp} \sin^2 \chi_{\mathrm{Li,HF}} + \alpha_{\mathrm{HF}}^{\parallel} \cos^2 \chi_{\mathrm{Li,HF}}, \quad \text{(S-83)}$$

where $\chi_{\mathrm{Li,HF}}$ is Jacobi angle, i.e., the angle between the translational Jacobi vector $\mathbf{Q}_{\mathrm{Li,HF}}$ and the diatomic Jacobi vector from H to F. The angular dependence is cut off in the interaction region,

$$\Phi_{11,\mathrm{HF}}^{\mathrm{disp}}(\mathbf{R}) = 1 + \left[\left(\tfrac{1}{3}\alpha_{\mathrm{HF}}^{\perp} + \tfrac{2}{3}\alpha_{\mathrm{HF}}^{\parallel}\right)/\alpha_{\mathrm{HF}}(\mathbf{R})\right] - 1\Big) \exp[-(Q_{\mathrm{Li,HF}}/S_{11,\mathrm{HF}})^4]. \quad \text{(S-84)}$$

The dipole-induced-dipole interaction is given by

$$U_{11,\mathrm{HF}}^{\mathrm{did}}(\mathbf{R}) = -\frac{1}{2}(3\cos^2 \chi_{\mathrm{Li,HF}} + 1)\alpha_{\mathrm{Li}(2s)} \mu_{\mathrm{HF}}(r_{\mathrm{HF}})^2 \frac{Q_{\mathrm{Li,HF}}}{Q_{\mathrm{Li,HF}}^7 + S_{11,\mathrm{HF}}^7} \times \Phi_{11,\mathrm{HF}}^{\mathrm{did}}(\mathbf{R}) K_{11,\mathrm{HF}}(r_{\mathrm{HF}}), \quad \text{(S-85)}$$

where the angular dependence is cut off in the interaction region,

$$\Phi_{11,\mathrm{HF}}^{\mathrm{did}}(\mathbf{R}) = 1 + \left[5/2(3\cos^2 \chi_{\mathrm{Li,HF}} + 1)\right] - 1\Big) \exp[-(Q_{\mathrm{Li,HF}}/S_{11,\mathrm{HF}})^4], \quad \text{(S-86)}$$

and the dipole moment of HF, μ_{HF}, is taken from Ref. 11. Both long-range interactions are cut off for large values of r_{HF},

$$K_{11,\mathrm{HF}}(r_{\mathrm{HF}}) = \frac{1}{2} - \frac{1}{2}\tanh[(r_{\mathrm{HF}} - r_{11,\mathrm{HF}}^0)/\Delta_{11,\mathrm{HF}}]. \quad \text{(S-87)}$$

The U_{22} surface contains the dipole-quadrupole, quadrupole-quadrupole, dipole-induced-dipole, and dispersion interactions in the Li(2*p*) + HF arrangement, and the dipole-induced-dipole and dispersion interactions in the LiF + H arrangement,

$$U_{22}^{\mathrm{LR}}(\mathbf{R}) = U_{22,\mathrm{HF}}^{\mathrm{dq}}(\mathbf{R}) + U_{22,\mathrm{HF}}^{\mathrm{qq}}(\mathbf{R}) + U_{22,\mathrm{HF}}^{\mathrm{disp}}(\mathbf{R}) + U_{22,\mathrm{HF}}^{\mathrm{did}}(\mathbf{R}) + U_{22,\mathrm{LiF}}^{\mathrm{disp}}(\mathbf{R}) + U_{22,\mathrm{LiF}}^{\mathrm{did}}(\mathbf{R}). \quad \text{(S-88)}$$

The dipole-quadrupole interaction is given by

$$U_{22,\mathrm{HF}}^{\mathrm{dq}}(\mathbf{R}) = \frac{3}{4}\mu_{\mathrm{HF}}(r_{\mathrm{HF}})\Theta_{\mathrm{Li}(2p)}\cos\chi_{\mathrm{Li,HF}}\frac{Q_{\mathrm{Li,HF}}}{Q_{\mathrm{Li,HF}}^5 + S_{22,\mathrm{HF}}^5} \times \Phi_{22,\mathrm{HF}}^{\mathrm{dq}}(\mathbf{R})K_{22,\mathrm{HF}}(r_{\mathrm{HF}}), \quad \text{(S-89)}$$

where Θ_{A} is the quadrupole moment of species A. The angular dependence of the dipole-quadrupole interaction is cut off in the interaction region,

$$\Phi_{22,\mathrm{HF}}^{\mathrm{dq}}(\mathbf{R}) = \exp[-(Q_{\mathrm{Li,HF}}/S_{22,\mathrm{HF}})^4]. \quad \text{(S-90)}$$

The quadrupole-quadrupole interaction is given by

$$U_{22,\mathrm{HF}}^{\mathrm{qq}}(\mathbf{R}) = \frac{3}{4}\Theta_{\mathrm{HF}}(r_{\mathrm{HF}})\Theta_{\mathrm{Li}(2p)}(3-7\cos^2\chi_{\mathrm{Li,HF}})\frac{Q_{\mathrm{Li,HF}}}{Q_{\mathrm{Li,HF}}^6 + S_{22,\mathrm{HF}}^6} \times \Phi_{22,\mathrm{HF}}^{\mathrm{qq}}(\mathbf{R})K_{22,\mathrm{HF}}(r_{\mathrm{HF}}), \quad \text{(S-91)}$$

where the quadrupole moment of HF is dependent on r_{HF} and is taken from Ref. 12. The angular dependence of the dipole-quadrupole interaction is cut off in the interaction region,

$$\Phi_{22,\mathrm{HF}}^{\mathrm{qq}}(\mathbf{R}) = 1 - [1/(6-14\cos^2\chi_{\mathrm{Li,HF}}) + 1]\exp[-(Q_{\mathrm{Li,HF}}/S_{22,\mathrm{HF}})^4]. \quad \text{(S-92)}$$

The dispersion interaction is given by the London equation,

$$U_{22,\mathrm{HF}}^{\mathrm{disp}}(\mathbf{R}) = -\frac{3}{2}\frac{I_{\mathrm{Li}(2p)}I_{\mathrm{HF}}\alpha_{\mathrm{Li}(2p)}(\mathbf{R})\alpha_{\mathrm{HF}}(\mathbf{R})}{I_{\mathrm{Li}(2p)} + I_{\mathrm{HF}}}\frac{Q_{\mathrm{Li,HF}}}{Q_{\mathrm{Li,HF}}^7 + S_{22,\mathrm{HF}}^7} \times \Phi_{22,\mathrm{HF}}^{\mathrm{disp}}(\mathbf{R})K_{22,\mathrm{HF}}(r_{\mathrm{HF}}), \quad \text{(S-93)}$$

The polarizability of Li(2*p*) includes angular dependence,

$$\alpha_{\mathrm{Li}(2p)}(\mathbf{R}) = \alpha_{\mathrm{Li}(2p)}^{\perp}\sin^2\chi_{\mathrm{Li,HF}} + \alpha_{\mathrm{Li}(2p)}^{\parallel}\cos^2\chi_{\mathrm{Li,HF}}. \quad \text{(S-94)}$$

The angular dependence is cut off in the interaction region,

$$\Phi^{\rm disp}_{22,\rm HF}(\mathbf{R}) = \left\{\left[\left[\tfrac{1}{3}\alpha^{\perp}_{\rm HF} + \tfrac{2}{3}\alpha^{\parallel}_{\rm HF}\right]\left[\tfrac{1}{3}\alpha^{\perp}_{\rm Li(2\it p)} + \tfrac{2}{3}\alpha^{\parallel}_{\rm Li(2\it p)}\right]/[\alpha_{\rm HF}(\mathbf{R})\alpha_{\rm Li(2\it p)}(\mathbf{R})]\right) - 1\right] \times \exp[-(Q_{\rm Li,HF}/S_{22,\rm HF})^4] + 1. \quad \text{(S-95)}$$

The dipole-induced-dipole interaction is given by

$$U^{\rm did}_{22,\rm HF}(\mathbf{R}) = -\frac{1}{2}(3\cos^2\chi_{\rm Li,HF} + 1)\alpha_{\rm Li(2\it p)}(\mathbf{R})\mu_{\rm HF}(r_{\rm HF})^2 \frac{Q_{\rm Li,HF}}{Q^7_{\rm Li,HF} + S^7_{22,\rm HF}} \times \Phi^{\rm did}_{22,\rm HF}(\mathbf{R})K_{22,\rm HF}(r_{\rm HF}), \quad \text{(S-96)}$$

where the angular dependence is cut off in the interaction region,

$$\Phi^{\rm did}_{22,\rm HF}(\mathbf{R}) = 1 + \left([5[\tfrac{1}{3}\alpha^{\perp}_{\rm Li(2\it p)} + \tfrac{2}{3}\alpha^{\parallel}_{\rm Li(2\it p)}]/[2\alpha_{\rm Li(2\it p)}(\mathbf{R})(3\cos^2\chi_{\rm Li,HF} + 1)]] - 1\right) \times \exp[-(Q_{\rm Li,HF}/S_{11,\rm HF})^4]. \quad \text{(S-97)}$$

The Li(2*p*) + HF long-range interactions are cut off for large values of $r_{\rm HF}$,

$$K_{22,\rm HF}(r_{\rm HF}) = \frac{1}{2} - \frac{1}{2}\tanh[(r_{\rm HF} - r^0_{22,\rm HF})/\Delta_{22,\rm HF}]. \quad \text{(S-98)}$$

The dispersion interaction in the LiF + H arrangement is given by the London equation,

$$U^{\rm disp}_{22,\rm LiF}(\mathbf{R}) = -\frac{3}{2}\frac{I_{\rm LiF}I_{\rm H}\alpha_{\rm LiF}\alpha_{\rm H}}{I_{\rm LiF} + I_{\rm H}}\frac{K_{22,\rm LiF}(r_{\rm LiF})}{Q^6_{\rm H,LiF} + S^6_{22,\rm LiF}}, \quad \text{(S-99)}$$

where $Q_{\rm H,LiF}$ is the magnitude of the translational Jacobi coordinate in the LiF + H arrangement, i.e., $Q_{\rm H,LiF}$ is the magnitude of the vector from H to the center of mass of LiF. The masses of Li and F are therefore parameters of the fit are given in Table S-1. The dipole-induced-dipole interaction is given by

$$U^{\rm did}_{22,\rm LiF}(\mathbf{R}) = -\frac{1}{2}\frac{(3\cos^2\chi_{\rm H,LiF} + 1)\alpha_{\rm H}\mu_{\rm LiF}(r_{\rm LiF})^2}{Q^6_{\rm H,LIF} + S^6_{22,\rm LiF}}\Phi^{\rm did}_{22,\rm LiF}(\mathbf{R})K_{22,\rm LiF}(r_{\rm LiF}), \quad \text{(S-100)}$$

where $\chi_{\rm H,LiF}$ is Jacobi angle in the LiF + H arrangement, i.e., the angle between the translational Jacobi vector $\mathbf{Q}_{\rm H,LiF}$ and the diatomic Jacobi vector from Li to F. The dipole moment of LiF is based on the data in Ref. 13 and is given by

$$\mu_{\mathrm{LiF}} = \mu_{\mathrm{LiF}}^{\mathrm{D}} \exp[-\mu_{\mathrm{LiF}}^{\alpha}(r_{\mathrm{LiF}} - \mu_{\mathrm{LiF}}^{r})^2], \tag{S-101}$$

$$\mu_{\mathrm{LiF}}^{\alpha}(r_{\mathrm{LiF}}) = \mu_{\mathrm{LiF}}^{\alpha 0} + \mu_{\mathrm{LiF}}^{\alpha 1} m_{\mathrm{LiF}}(r_{\mathrm{LiF}}) + \mu_{\mathrm{LiF}}^{\alpha 8} m_{\mathrm{LiF}}(r_{\mathrm{LiF}})^8, \tag{S-102}$$

$$m_{\mathrm{LiF}} = r_{\mathrm{LiF}} - m_{\mathrm{LiF}}^{0}. \tag{S-103}$$

The angular dependence is cut off in the interaction region,

$$\Phi_{22,\mathrm{LiF}}^{\mathrm{did}}(\mathbf{R}) = 1 + \left([5/(3\cos^2 \chi_{\mathrm{H,LiF}} + 1)] - 1\right)\exp[-(Q_{\mathrm{H,LiF}} / S_{22,\mathrm{LiF}})^4]. \tag{S-104}$$

The LiF + H long-range interactions are cut off for large values of r_{LiF},

$$K_{22,\mathrm{LiF}}(r_{\mathrm{LiHF}}) = \frac{1}{2} - \frac{1}{2}\tanh[(r_{\mathrm{LiF}} - r_{22,\mathrm{LiF}}^{0})/\Delta_{22,\mathrm{LiF}}]. \tag{S-105}$$

The parameters used for the long-range interactions are given in Table S-4.

S.3. Quasidiabatic Potential Energy Matrix for LiFH: Surface Fit JS

The surface fit described in Sec. S.2 (surface fit J) is our most accurate fit to the LiFH *ab initio* data. Surface fit J contains long-range interactions that are based on physically motivated functional forms and that depend on physical properties such as the polarizabilities and multipole moments of the H and Li atoms and of the HF and LiF molecules. We believe that surface fit J is extremely accurate; however, the presence of long-range forces may increase the computational effort required to obtain converged nuclear dynamics for both quantum mechanical and semiclassical simulations. We therefore present as a complement to surface fit J, surface fit JS, which features cut-off long-range forces. The long-range forces were cut off in such a way as to minimize the change to the interaction region, as discussed below. We also carefully cut off the diabatic coupling U_{12} in surface fit JS. The diabatic coupling is cut off in a region where the coupling is not expected to play a significant role in the dynamics, and this feature also decreases the difficulty of dynamics calculations.

The diagonal quasidiabatic matrix elements of surface fit JS (U_{11}^{JS} and U_{22}^{JS}) are identical to those of surface fit J, except that the long-range terms are cut off,

$$U_{ii}^{\mathrm{JS}}(\mathbf{R}) = U_{ii}^{\mathrm{I}}(\mathbf{R}) + U_{ii}^{\mathrm{JS}}(\mathbf{R}), \tag{S-106}$$

$$U_{11}^{\mathrm{JS}}(\mathbf{R}) = U_{11}^{\mathrm{LR}}(\mathbf{R})\Omega(Q_{\mathrm{Li,HF}}), \tag{S-107}$$

$$\begin{aligned} U_{22}^{\mathrm{JS}}(\mathbf{R}) = &\left[U_{22,\mathrm{HF}}^{\mathrm{dq}}(\mathbf{R}) + U_{22,\mathrm{HF}}^{\mathrm{qq}}(\mathbf{R}) + U_{22,\mathrm{HF}}^{\mathrm{disp}}(\mathbf{R}) + U_{22,\mathrm{HF}}^{\mathrm{did}}(\mathbf{R})\right]\ \Omega(Q_{\mathrm{Li,HF}}) \\ &+ \left[U_{22,\mathrm{LiF}}^{\mathrm{disp}}(\mathbf{R}) + U_{22,\mathrm{LiF}}^{\mathrm{did}}(\mathbf{R}).\right]\Omega(Q_{\mathrm{H,LiF}}), \end{aligned} \tag{S-108}$$

where i = 1 and 2, $Q_{\mathrm{A,BC}}$ is the magnitude of the translational Jacobi coordinate in the A + BC molecular arrangement, and the interaction potential $U_{ii}^{\mathrm{I}}(\mathbf{R})$ and the long-range forces are the same as those that were given for surface fit J in Sec. S.2. The cut off functions are

$$\Omega(Q_{\mathrm{A,BC}}) = \begin{cases} \exp[\Delta_\Omega /(Q_{\mathrm{A,BC}} - Q_\Omega)] & Q_{\mathrm{A,BC}} \le Q_\Omega \\ 0 & Q_{\mathrm{A,BC}} > Q_\Omega, \end{cases} \tag{S-109}$$

where "A,BC" is "Li,HF" or "H,LiF". Note that the cut off function in eq. (109) goes exactly to zero at Q_Ω and has an infinite number of continuous derivatives for all $Q_{\mathrm{A,BC}}$. The values for the cut off parameters are Q_Ω = 10.0 a_0 and Δ_Ω = 0.2 a_0. These values were optimized such that surface fit JS remained smooth and the mean unsigned errors calculated for surface fit JS were no more than 0.001 eV greater than those reported for surface fit J in Table 8 of the main paper.

The diabatic coupling (U_{12}^{JS}) was also cut off in surface fit JS,

$$U_{12}^{\mathrm{JS}}(\mathbf{R}) = U_{12}(\mathbf{R})\Xi(r_{\mathrm{HF}}), \tag{S-110}$$

where U_{12} is the diabatic coupling of surface fit J and is given in Sec. S.2, and

$$\Xi(r_{\mathrm{HF}}) = \frac{1}{2} - \frac{1}{2}\tanh[(r_{\mathrm{HF}} - r_\Xi)/\Delta_\Xi]. \tag{S-111}$$

The parameters for the cut off function are r_Ξ = 5.5 a_0 and Δ_Ξ = 0.2 a_0. This cut off function does not significantly effect the mean unsigned errors for surface fit JS.

References for the Supporting Information

1 POTLIB-online (http://comp.chem.umn.edu/potlib/) is a repository of potential energy routines and is the online version of POTLIB-2001. For a description of the POTLIB library, see R. J. Duchovic, Y. L. Volobuev, G. C. Lynch, D. G. Truhlar, T. C. Allison, A. F. Wagner, B. C. Garrett, and J. C. Corchado, Computer Physics Communications, **144**, 169 (2002).

2 G. Di Lonardo and A. E. Douglas, Can. J. Phys. **51**, 434 (1973); J. A. Coxon, and P. G. Hajigeorgiou, J. Molec. Spec. **142**, 254 (1990).

3 S. Sato, J. Chem. Phys. **23**, 2465 (1955).

4 J. K. Cashion and D. R. Herschbach, J. Chem. Phys. **40**, 2358 (1964).

5 K. J. Laidler, and J. C. Polanyi, Prog. Reaction Kinetics **3**, 1 (1965).

6 P. J. Kuntz, E. M. Nemeth, J. C. Polanyi, S. D. Rosner, and C. E. Young, J. Chem. Phys. **44**, 1168 (1966).

7 M. C. Douay, A. M. R. P. Bopegedera, C. R. Brazier, and P. F. Bernath, Chem. Phys. Lett. **148**, 1 (1988).

8 J. O. Hirschfelder, C. F. Curtiss, and R. B. Bird, *Molecular Theory of Gases and Liquids*, corrected printing (John Wiley and Sons, New York, 1964).

9 G. C. Maitland, M. Rigby, E. B. Smith, and W. A. Wakeham, *Intermolecular Forces: Their Origin and Determination*, corrected printing (Clarendon Press, Oxford, 1987); P. Piecuch, in Molecules in Physics, Chemistry and Biology, edited by J. Marioni (Kluwer, Dordrecht, 1988), Vol. 2, p. 417.

10 M. D. Hack and D. G. Truhlar, J. Chem. Phys. **110**, 4315 (1999).

11 P. Piecuch, V. Špirko, A. E. Kondo, and J. Paldus, Mol. Phys. **94**, 55 (1998).

12 V. Špirko, P. Piecuch, A. E. Kondo, and J. Paldus, J. Chem. Phys. **104**, 4716 (1996).

13 C. W. Bauschlicher Jr. and S. R. Langhoff, J. Chem. Phys. **89**, 4246 (1988).

14 *CRC Handbook of Chemistry and Physics*, 77th ed., edited by D. R. Lide (Chemical Rubber, Boca Raton, 1996).

15 M. Rérat, B. Bussery, and M. Frécon, J. Molec. Spec. **182**, 260 (1997).

16 C. Van Caillie and R. D. Amos, Chem. Phys. Lett. **328**, 446 (2000).

Table S-1. Values of the parameters used in the LiFH U_{11} potential energy function.

Parameter	Value	Parameter	Value
$D_{\mathrm{LiH}}^{\mathrm{a}}$	12.93744 eV	r_{HF}^{0}	2.1042 a_0
$D_{\mathrm{LiH}}^{\mathrm{c}}$	11.09130 eV	$r_{\mathrm{HF}}^{\mathrm{c}}$	1.6739 a_0
$\beta_{\mathrm{LiH}}^{\mathrm{a}}$	1.80587 a_0^{-1}	$\beta_{\mathrm{HF}}^{\mathrm{c}}$	0.74633 a_0^{-1}
$\beta_{\mathrm{LiH}}^{\mathrm{c}}$	1.21114 a_0^{-1}	$D_{\mathrm{HF}}^{\mathrm{cc}}$	0.86608 eV
r_{LiH}^{0}	1.34321 a_0	$D_{\mathrm{HF}}^{\mathrm{chi}}$	0.34457 eV
ρ_{LiH}	1.07143 a_0	ρ_{HF}	1.63 a_0
Δ_{LiH}	0.6 a_0	Δ_{HF}	2.9941 a_0
γ_{LiH}	0.4	D_{LiF}	0.17427 eV
$D_{\mathrm{HF}}^{\mathrm{e}}$	6.122 eV	β_{LiF}	1.49062 a_0^{-1}
$r_{\mathrm{HF}}^{\mathrm{e}}$	1.733 a_0	r_{LiF}^{0}	3.6 a_0
b_{HF}^{0}	1.1622 a_0^{-1}	m_{Li}	7.016003 amu[a]
b_{HF}^{1}	–0.025647 a_0^{-2}	m_{F}	18.998403 amu
b_{HF}^{2}	0.059062 a_0^{-3}	m_{H}	1.007825 amu

[a] 1 amu = 1822.887 m_e.

Table S-2. Values of the parameters used in the LiFH U_{12} potential energy function.

Parameter	Value	Parameter	Value
ρ_{12}	4.87097 a_0	$\rho_{HF,2}$	1.45161 a_0
Δ_{12}	2.0 a_0	$\Delta_{HF,1}$	1.75806 a_0
g_{LiH}	1.27742 eV	$\Delta_{HF,2}$	0.98387 a_0
g_{LiF}	0.48 eV	ρ_{LiF}	2.00098 a_0
r_{LiH}^0	3.00489 a_0	Δ_{LiF}	0.90626 a_0
r_{LiF}^0	3.49756 a_0	ρ_{LiH}	4.98436 a_0
$\rho_{HF,1}$	1.15484 a_0	Δ_{LiH}	2.08993 a_0

Table S-3. Values of the parameters used in the LiFH U_{22} potential energy function.

Parameter	Value	Parameter	Value
c_{2a}	3.5 eV	$D_{HF}^{t1,180}$	4.56304985 eV
c_{2b}	0.27362 eV^{-2}	$\beta_{HF}^{t,0}$	2.4105572 a_0^{-1}
c_{2c}	0.15 a_0^{-1}	$\beta_{HF}^{t,180}$	1.4046921 a_0^{-1}
D_{LiH}^{a2}	4.32258 eV	r_{HF}^{t}	1.61329423 a_0
D_{LiH}^{a1}	7.06452 eV	D_{LiF}^{e}	5.947 eV
β_{LiH}^{a}	1.36 a_0^{-1}	r_{LiF}^{e}	2.9553 a_0
D_{LiH}^{c}	14.74194 eV	ρ_{LiF}^{a}	13.0 a_0
β_{LiH}^{c}	0.90667 a_0^{-1}	Δ_{LiF}^{a}	0.5 a_0
r_{LiH}^{0}	1.2 a_0	d_{LiF}^{aa}	1.0243998
ρ_{LiH}	0.72 a_0	ρ_{LiF}^{aa}	3.340762 a_0
Δ_{LiH}	0.5 a_0	Δ_{LiF}^{aa}	0.56353861 a_0
γ_{LiH}	1.0	γ_{LiF}	4.6304985 $a_0^{1+1/n_{LiF}}$
D_{LiH}^{t2}	1.1935483 eV	n_{LiF}	8.0
D_{LiH}^{t1}	13.548387 eV	β_{LiF}^{d}	0.13225806 a_0^{-1}
β_{LiH}^{t}	2.41319648 a_0^{-1}	ρ_{LiF}^{b}	3.382209 a_0
r_{LiH}^{t}	1.203323 a_0	Δ_{LiF}^{b}	0.4947214 a_0^{-1}
D_{HF}^{e}	6.122 eV	b_{LiF}^{e1}	0.064076 a_0^{-1}

Table S-3(continued). Values of the parameters used in the LiFH U_{22} potential energy function.

Parameter	Value	Parameter	Value
$E_{\mathrm{Li}(2p)}$	1.848 eV	$b_{\mathrm{LiF}}^{\mathrm{e2}}$	103.57
$r_{\mathrm{HF}}^{\mathrm{e}}$	1.733 a_0	$b_{\mathrm{LiF}}^{\mathrm{e3}}$	4.6498 a_0^2
b_{HF}^{0}	1.1622 a_0^{-1}	$b_{\mathrm{LiF}}^{\mathrm{e4}}$	7.0489 a_0
b_{HF}^{1}	–0.025647 a_0^{-2}	$D_{\mathrm{LiF}}^{\mathrm{c},0}$	5.5904203 eV
b_{HF}^{2}	0.059062 a_0^{-3}	$D_{\mathrm{LiF}}^{\mathrm{c},180}$	2.352884 eV
r_{HF}^{0}	2.1042 a_0	$\beta_{\mathrm{LiF}}^{\mathrm{c},0}$	0.7795699 a_0^{-1}
$D_{\mathrm{HF}}^{\mathrm{aa}}$	2.3841642 eV	$\beta_{\mathrm{LiF}}^{\mathrm{c},180}$	0.8196480 a_0^{-1}
$\beta_{\mathrm{HF}}^{\mathrm{aa}}$	1.799609 a_0^{-1}	ρ_{LiF}^{0}	0.2017595 a_0
$r_{\mathrm{HF}}^{\mathrm{aa}}$	1.60215 a_0	$\rho_{\mathrm{LiF}}^{180}$	2.0 a_0
$\rho_{\mathrm{HF}}^{\mathrm{a}}$	3.0 a_0	ϕ_{LiF}^{0}	0.12463343 rad
$\Delta_{\mathrm{HF}}^{\mathrm{a}}$	0.5 a_0	$\phi_{\mathrm{LiF}}^{180}$	0.14907135 rad
$D_{\mathrm{HF}}^{\mathrm{cc}}$	0.72629521 eV	$\Delta_{\mathrm{LiF}}^{0}$	0.51710655 a_0^{-1}
$D_{\mathrm{HF}}^{\mathrm{chi}}$	0.0486803519 eV	$\Delta_{\mathrm{LiF}}^{180}$	0.43695014 a_0^{-1}
$\rho_{\mathrm{HF}}^{\mathrm{c}}$	2.2 a_0	$D_{\mathrm{LiF}}^{\mathrm{t2},0}$	–0.0552298 eV
$\Delta_{\mathrm{HF}}^{\mathrm{c}}$	0.5 a_0	$D_{\mathrm{LiF}}^{\mathrm{t1},0}$	1.8729228 eV
ρ_{HF}	1.00293 a_0	$D_{\mathrm{LiF}}^{\mathrm{t2},180}$	0.94662756 eV
Δ_{HF}	4.0899 a_0	$D_{\mathrm{LiF}}^{\mathrm{t1},180}$	0.2994134 eV
$D_{\mathrm{HF}}^{\mathrm{t2},0}$	1.4242424 eV	$\beta_{\mathrm{LiF}}^{\mathrm{t},0}$	0.9519061 a_0^{-1}
$D_{\mathrm{HF}}^{\mathrm{t1},0}$	14.203323 eV	$\beta_{\mathrm{LiF}}^{\mathrm{t},180}$	0.4531769 a_0^{-1}
$D_{\mathrm{HF}}^{\mathrm{t2},180}$	6.15835777 eV		

Table S-4. Values of the parameters used in the long-range interactions.

Parameter	Value	Parameter	Value
$I_{\mathrm{Li}(2s)}$	5.392 eV[a]	$\Delta_{22,\mathrm{HF}}$	2.0 a_0
I_{HF}	16.044 eV[a]	I_{LiF}	11.3 eV [a]
$\alpha_{\mathrm{Li}(2s)}$	165.0 a_0^3 [b]	I_{H}	13.598 eV [a]
$S_{11,\mathrm{HF}}$	6.0 a_0	α_{LiF}	72.9 a_0^3 [a]
$\alpha_{\mathrm{HF}}^{\perp}$	4.59 a_0^3 [c]	α_{H}	4.4997 a_0^3 [a]
$\alpha_{\mathrm{HF}}^{\parallel}$	5.10 a_0^3 [c]	$S_{22,\mathrm{LiF}}$	7.0 a_0
$r_{11,\mathrm{HF}}^{0}$	3.0 a_0	$\mu_{\mathrm{LiF}}^{\mathrm{D}}$	9.30039 e a_0
$\Delta_{11,\mathrm{HF}}$	2.0 a_0	μ_{LiF}^{r}	10.4994 a_0
$\Theta_{\mathrm{Li}(2p)}$	11.1 e a_0^2 [b]	$\mu_{\mathrm{LiF}}^{\alpha 0}$	0.02435 a_0^{-1}
$S_{22,\mathrm{HF}}$	6.0 a_0	$\mu_{\mathrm{LiF}}^{\alpha 1}$	0.015999 a_0^{-2}
$I_{\mathrm{Li}(2p)}$	3.544 eV[a]	$\mu_{\mathrm{LiF}}^{\alpha 8}$	9.9355 x 10^{-8} a_0^{-9}
$\alpha_{\mathrm{Li}(2p)}^{\perp}$	129.0 a_0^3 [b]	m_{LiF}^{0}	4.471959 a_0
$\alpha_{\mathrm{Li}(2p)}^{\parallel}$	131.0 a_0^3 [b]	$r_{22,\mathrm{LiF}}^{0}$	4.5 a_0
$r_{22,\mathrm{HF}}^{0}$	3.0 a_0	$\Delta_{22,\mathrm{LiF}}$	2.0 a_0

[a]Reference 14.

[b]Reference 15.

[c]Reference 16.

Chapter Six

6

Improved Treatment of Momentum at Classically Forbidden Electronic Transitions in Trajectory Surface Hopping Calculations

I. Introduction

Electronically nonadiabatic chemical dynamics (e.g., nonadiabatic charge transfer, ultraviolet photodissociation, chemiluminescence, etc.) is described by coupled potential energy surfaces, and the applicability of fully-converged quantum mechanical calculations is limited by computational considerations to systems with two atoms or three atoms and a few electronic states. It is desirable, therefore, to develop and validate the accuracy of approximate methods that may be applied to the large class of chemically interesting electronically nonadiabatic systems for which quantum mechanical calculations are not currently computationally feasible.

We have recently undertaken a program of developing realistic coupled potential energy surfaces for model three-atom reactive systems, performing fully three-dimensional accurate quantum calculations on the model systems, and systematically testing semiclassical methods against the accurate quantum calculations.[1–7] We have focused on semiclassical methods that are well defined so that they are systematically testable, computationally straightforward to implement, and readily applicable to large systems. Specifically, we have focused on methods that are based on what may be called the "trajectory ensemble" or TE approach,[8] where the nuclear wave packet is approximated as an ensemble of noninteracting classical trajectories.

Of course, classical trajectories do not exhibit quantum effects (such as transitions between electronic states, tunneling, etc.), and when these effects are important, they

must be explicitly added to the TE simulation. The key quantum effect for electronically nonadiabatic processes is the nonadiabatic transition itself, and a careful treatment of quantum transitions between electronic states is crucial in accurately modeling the dynamics of electronically nonadiabatic systems. The trajectory surface hopping[1–15] (TSH) approach starts from the TE formalism and includes nonadiabatic dynamics by allowing the trajectories in the ensemble to suddenly switch (i.e., to hop between) electronic states. The present paper is primarily concerned with the treatment of the nuclear momentum at so-called frustrated hopping points along the classical trajectory in the TSH method.

II. Theory

Briefly, the TSH method is implemented as follows. One first chooses an electronic representation with which to express the electronic energies and the electronic-state coupling. The potential energy surfaces for a nonadiabatic chemical system may be chosen either as the unique set of adiabatic potential energy surfaces, coupled by the nuclear momentum and nuclear kinetic energy operators and corresponding to electronic wave functions that are eigenfunctions of the electronic Hamiltonian, or as a nonunique set of diabatic potential energy surfaces, for which the nuclear momentum coupling and nuclear kinetic energy coupling is small compared to a scalar (potential energy) coupling introduced by the adiabatic-diabatic transformation. (Sometimes diabatic states are called "quasidiabatic" to emphasize that, in general, except for the trivial case of frozen electronic wave functions, a diabatic representation whose nuclear momentum couplings are exactly zero does not exist for real chemical systems.[8,16,17]) Quantum mechanically, diabatic representations and the adiabatic representations obtained by diagonalizing the potential energy result in identical dynamics. TSH simulations, however, are sensitive to the choice of electronic representation, and we have determined[5] that the best representation to use is the one with the least amount of nonadiabatic coupling as measured by the number of attempted surface hops. This best representation (called the Calaveras County or CC representation) may be estimated from a small batch of TSH trajectories run in both representations.

Once an electronic representation is chosen, each trajectory in the ensemble is assigned an initial electronic state that corresponds to the initial conditions of the simulation. For example, if the quenching of an excited electronic state is being modeled, all of the trajectories start in the excited electronic state. The initial coordinates and momenta of each trajectory are selected randomly from a quasiclassical distribution,[18] such that the initial ensemble of positions and momenta mimics the initial quantum mechanical wave packet. Each trajectory is then propagated classically (i.e., using Hamilton's equations of motion) under the influence of the potential energy surface that corresponds to the initial electronic state.

At arbitrarily small time intervals (such as the time step of the integrator), an electronic transition (or hopping) probability g_{ij} from the currently occupied electronic state *i* to some other target electronic state *j* is computed according to Tully's fewest-switches (TFS) algorithm.[12,15] The fewest-switches hopping probability is a function of the quantum mechanical electronic state populations, which are obtained by integrating the electronic Schrödinger equation along the classical trajectory. When this particular choice for the hopping probability is used, the TSH method is called the TFS method. A random number is generated and compared with g_{ij} to determine if a surface hop occurs. If a surface hop does not occur, the trajectory remains in the currently occupied electronic state. If a hop is called for, an electronic state change occurs, and the trajectory is propagated under the influence of the potential energy surface corresponding to the new electronic state.

Each trajectory in the ensemble may be thought of as an energy-conserving gas-phase event. When a surface hop occurs, the potential energy, in general, changes discontinuously, and the total energy of the system is conserved by adjusting the nuclear momentum. It has been suggested on the basis of semiclassical arguments[11,13] and confirmed with numerical tests against accurate quantum dynamics[1,2] that the best way to conserve energy is to adjust the nuclear momentum component in the direction of the hopping vector **h**, where **h** is a unit vector in the direction of the nuclear momentum coupling vector **d**. Whether or not a hop occurs, the trajectory is propagated forward one time step where another hopping decision is made, etc…, and the process is continued until the trajectory is deemed "finished" by some criterion (usually the separation of the products).

Occasionally, a surface hop to a higher-energy electronic state is called for at a point along the trajectory where the energy gap between the occupied and the target electronic states is greater than the kinetic energy associated with the momentum along **h**. When this occurs, the momentum cannot be adjusted along **h** in such a way as to conserve total energy, and these failed hopping attempts are called "frustrated" or "classically forbidden" surface hops.[6,7]

Previous treatments for frustrated hopping include ignoring the frustrated hop[14] or reflecting the nuclear momentum along **h** as though the trajectory hits a barrier as it tries to hop, and we will denote these two approaches with a '+' and a '–', respectively (e.g., the TFS+ and TFS– methods employ the same surface hopping algorithm, but differ in their treatment of frustrated hopping). In both cases, the trajectory continues without changing electronic states, which violates the self-consistency argument originally used to justify the TFS algorithm.[12] Numerical studies[6,7] of these methods have shown that the resulting electronic-state distribution of trajectories results in increased errors. (We note that Tully's original implementation of the TFS method was the TFS– method.[19] We also note that in some work both criteria have been used depending on other details of the frustrated hop,[3,10] or the momentum was changed along directions other than **h**,[3,4,6] but we have found[3,4,6] that such methods do not improve the accuracy compared to the simple + and – prescriptions.)

We have recently developed[7] a new implementation of the TSH method called the fewest switches with time uncertainty (FSTU) method which allows a trajectory that experiences a frustrated hop to hop nonlocally to a geometry along the trajectory where a hop is classically allowed so long as the nonlocal hopping point is within a time interval obtained from the time-energy Heisenberg uncertainty relations. (In other respects, the FSTU method is the same as the TFS algorithm.) By introducing nonlocal hopping, the FSTU method improves the electronic-state distribution of trajectories, and the FSTU method was found[7] to be more accurate than the TFS method. Although the FSTU method has less frustrated hopping than the TFS method, not all frustrated hops are removed, and therefore we have previously considered[7] two implementations of the FSTU method, namely FSTU+ and FSTU–.

From numerical studies,[6,7] we found that, in general, the TFS+ and FSTU+ methods are more accurate in predicting the average rotational and vibrational quantum numbers than are the TFS– and FSTU– methods, respectively, whereas the TFS– and FSTU– methods predict more accurate nonadiabatic transition probabilities and branching ratios. It is therefore reasonable to attempt to combine these two approaches. We note that a previous attempt[10] to combine the + and – approaches was unsuccessful

because it relied on a nonphysical criterion for discriminating between the + and – treatments. In particular, the criterion was based on the amount of energy in modes orthogonal to **h** at a frustrated hop.

A new physically-motivated prescription, called the ∇V prescription, is presented here that combines the desirable features of the + and – treatments in a more physically motivated fashion while retaining the simple implementation of the TSH method. Using the ∇V prescription, the dynamics at a frustrated hopping event is determined by allowing the trajectory to instantaneously feel the target electronic state. Specifically, when a frustrated hop is encountered, the following quantities are computed:

$$p_{\mathbf{h}} = \mathbf{p} \cdot \mathbf{h} \tag{1}$$

$$F_{\mathbf{h}} = -\nabla V_j \cdot \mathbf{h}\,, \tag{2}$$

where **p** is the nuclear momentum of the trajectory and ∇V_j is the gradient of the target electronic state j. Equations (1) and (2) are the projection of the nuclear momentum and the force of the target electronic state along the hopping vector **h**, respectively. If these two quantities have the same sign, the target electronic state can be thought of as instantaneously accelerating the trajectory along **h**, whereas if the two quantities have opposite signs, the target electronic state instantly retards the trajectory along **h**. We therefore use the following criterion for frustrated hopping

$$\text{If } p_{\mathbf{h}} F_{\mathbf{h}} \begin{cases} \geq 0 & \text{the + treatment is used} \\ < 0 & \text{the – treatment is used.} \end{cases} \tag{3}$$

The ∇V criterion has several desirable features: it contains both + and – treatments, it is simple to implement, it requires only information that is readily available in surface hopping computer codes, it is physical as it depends only on the components of the momentum along the hopping vector **h** to determine the nonadiabatic dynamics, and it incorporates a knowledge of the character of the excited surface to differentiate whether the + or – treatment is used.

III. Calculations

We tested the FSTU∇V, FSTU+, and FSTU– methods against accurate quantum mechanical results for a total of 21 test cases involving fully three-dimensional collisions of systems with realistic potential energy surfaces. Four parameterizations of the YRH system[6] with three different sets of initial conditions for the Y* + RH collision partners and three parameterizations of the MXH system[20] with three different sets of initial conditions for the M* + XH collision partners were included in the test set. In both cases, an asterisk denotes electronic excitation. Descriptions of the surfaces, the initial conditions, and the quantum mechanical calculations for the YRH and MXH surfaces have appeared previously.[6,20] The entire set of 21 test cases is qualitatively diverse and use of such a diverse set of test cases ensures against fortuitous agreement between the semiclassical and quantum mechanical results. The CC electronic representation was used for all of the semiclassical calculations.

Unsigned relative errors (UREs) were computed for eight observables: the reactive de-excitation probability P_R to produce R + YH or H + MX, the nonreactive de-excitation (quenching) probability P_Q to produce Y + RH or M + XH, the total de-excitation probability $P_N = P_R + P_Q$, the product branching fraction $F_R = P_R/P_N$, the averages (first moments) of the final reactive vibrational and rotational quantum numbers v' and j', and the averages (first moments) of the final quenching vibrational and rotational quantum numbers v'' and j''. Note that all reactive events are electronically nonadiabatic; electronically excited channels of R + YH or H + MX are not energetically accessible.

IV. Results and Discussion

For each of the eight observables, the UREs were averaged over all 12 YRH cases, all 9 MXH cases, and all 21 cases, and the resulting mean unsigned relative errors (MUREs) are summarized in Table 1. The average MURE for the four moments, the four probabilities, and all eight observables are also shown for each method in the last three columns of Table 1. The method with the lowest MURE is shown in bold for each case. Uncertainties in the MUREs were computed using the Monte Carlo uncertainties in

the calculated observables (these uncertainties result from finite sampling of initial collision variables such as vibrational phase and rotational orientation). If another method has an MURE that is statistically indistinguishable (within a 1σ range) from the method with the lowest MURE, that method is also listed in bold, and all bold entries are considered as "statistically significant winners". Table 1 shows that treatment of the nuclear momentum at frustrated hops has a significant effect on the reactive probability P_R and the product branching fraction F_R. For both the YRH and MXH systems, the FSTU∇V method is more accurate than the FSTU+ and FSTU– methods for P_R and F_R. For P_Q and P_N, all three methods are statistically indistinguishable for both the YRH and MXH cases. The three methods predict all four MXH moments and three of the four YRH moments equally well. In the case of the quenching vibrational moment, the FSTU+ and FSTU∇V methods are statistically preferred over the FSTU– method for the YRH system.

Table 1 contains highly averaged errors over observables with varying magnitudes. Table 2 shows the UREs on a case-by-case basis for P_N and F_R and supports the conclusion drawn from Table 1 that the FSTU∇V method is the best method for F_R. Specifically, the FSTU∇V method has the statistically-significant lowest URE for F_R for 14 of the 21 cases. We note that the trends in P_R are similar to the trends in F_R, and P_R is therefore not included in Table 2. Table 2 also reveals a trend in P_N that does not show up in the MUREs shown in Table 1. The FSTU∇V method has the statistically significant lowest URE for 19 of the 21 test cases for P_N. For the remaining two cases, the URE for all three methods is below 20%, where a 20% relative error may be considered satisfactory for semiclassical methods. We conclude therefore that the FSTU∇V method is better than the FSTU+ and FSTU– methods for P_N, P_R, and F_R.

In order to perform a case-by-case analysis on all eight of the observables without going into great detail, we have developed a scorecard method of evaluating the methods. In the scorecard method, for each of the eight observables a score of 1.0 is given to the statistically significant winning methods (as defined above), and a score of 0.0 is given to all other methods for that observable. The scores are then averaged over all 12 cases for

YRH and all 9 cases for MXH. An average score of 1.0 or 0.0 indicates that the method predicts the statistically-significant lowest unsigned error for all or none of the test cases, respectively. Table 3 shows these average scores for each observable. For each of the two kinds of systems (YRH and MXH), we averaged these average scores over all four probabilities, all four moments, and all eight observables, as shown in the last three columns of Table 3. Finally, we averaged over both kinds of systems, as shown in the last three rows. All averages are unweighted. Table 3 confirms the trends inferred from Tables 1 and 2, namely that the FSTU∇V method is greatly preferred over the other two methods in predicting probabilities (scoring 70% higher than the second-place method), that the FSTU+ method is preferred for predicting moments (scoring 22% higher than the second-place method), and that the FSTU∇V method is the best method overall (scoring 18% higher than the second-place method). Since there is no unique way to decide which method is "better" over a diverse test set, we believe that it is encouraging that the mean unsigned relative errors and the scorecard method lead to the same conclusions. Furthermore, it is pleasing that the prescription that has the best physical justification also turns out to be the prescription that performs the most accurately.

We note that the FSTU∇V results in Tables 1 and 2 support our previous observation[6] that the semiclassical trajectory approach is reasonably accurate for modeling the dynamics of systems with weakly coupled electronic states. The YRH systems feature highly classically forbidden electronic transitions (the quantum mechanical values of P_N range from 0.2 to 10^{-4}), and the overall MURE of the improved semiclassical method (FSTU∇V) for these systems is 39%. For the more strongly coupled MXH systems (with quantum mechanical P_N from 0.5 to 0.7), the overall MURE is 33%. Considering the probabilities only, the FSTU∇V method performs better for the small-probability YRH cases than for the MXH cases, with average MUREs for the probabilities of 38% and 48%, respectively.

We also tested the TFS+, TFS–, and TFS∇V methods and obtained similar trends with respect to the treatment of frustrated hopping (i.e., the TFS∇V method is more accurate than the TFS+ and TFS– methods). We have previously shown [7] that the FSTU method is, in general, more accurate than the TFS method, and the same trends

occur when both algorithms are implemented with the ∇V prescription, i.e., the FSTU∇V method has a smaller average error than the TFS∇V method. We also remind the reader that in previous papers[3,4,6] we have tested several other algorithms for treating surface hops, and this letter results from a distillation of those efforts in that the methods presented here are only the very best methods.

V. Concluding Remarks

The accuracy of semiclassical dynamics calculations using the trajectory surface hopping method for simulating non-Born-Oppenheimer processes is determined by the accuracy of the potential energy surfaces and the surface couplings, the selection of initial conditions, nonhopping trajectory propagation, the treatment of successful surface hops, and the treatment of frustrated hopping. We have shown in this work and previously[6,7] that frustrated hopping can be very important for realistic chemical systems, and allowing nonlocal hopping (as in the FSTU algorithm) and carefully treating frustrated hopping (as in the ∇V prescription) can have a significant quantitative effect on the overall semiclassical dynamics, and in some cases the treatment of frustrated surface hops is the dominant potential source of error. Semiclassical simulations of electronically nonadiabatic dynamics should therefore explicitly address the treatment of frustrated hopping, and based on the numerical studies presented here and elsewhere,[6,7] we recommend the FSTU∇V method as the most successfully validated option for trajectory surface hopping calculations.

Acknowledgements

This work was supported in part by the National Science Foundation under grant no. CHE00-92019.

References

1 M. S. Topaler, M. D. Hack, T. C. Allison, Y.-P. Liu, S. L. Mielke, D. W. Schwenke, and D. G. Truhlar, *J. Chem. Phys*. **106**, 8699 (1997).

2 M. S. Topaler, T. C. Allison, D. W. Schwenke, and D. G. Truhlar, *J. Chem. Phys*. **109**, 3321 (1998); **110**, 687(E) (1999); **113**, 3928(E) (2000).

3 M. D. Hack, A. W. Jasper, Y. L. Volobuev, D. W. Schwenke, and D. G. Truhlar, *J. Phys. Chem. A* **103**, 6309 (1999).

4 M. D. Hack, A. W. Jasper, Y. L. Volobuev, D. W. Schwenke, and D. G. Truhlar, *J. Phys. Chem. A* **104**, 217 (2000).

5 M. D. Hack and D. G. Truhlar, J. Phys. Chem. *A* **104**, 7917 (2000).

6 A. W. Jasper, M. D. Hack, and D. G. Truhlar, *J. Chem. Phys*. **115**, 1804 (2001).

7 A. W. Jasper, S. N. Stechmann, and D. G. Truhlar, *J. Chem. Phys*. **116**, 5424 (2002), **117**, 10427 (2002).

8 A. W. Jasper, B. K. Kendrick, C. A. Mead, and D. G. Truhlar, in Modern Trends in Chemical Reaction Dynamics*,* edited by X. Yang, K. Liu (World Scientific, Singapore, 2003), in press.

9 J. C. Tully and R. K. Preston, *J. Chem. Phys.* **55**, 562 (1971).

10 N. C. Blais and D. G. Truhlar, *J. Chem. Phys.* **79**, 1334 (1983).

11 M. F. Herman, *J. Chem. Phys.* **81**, 754 (1984).

12 J. C. Tully, *J. Chem. Phys.* **93**, 1061 (1990).

13 D. F. Coker, L. Xiao, *J. Chem. Phys.* **102**, 496 (1995).

14 U. Müller, G. Stock, *J. Chem. Phys.* **107**, 6230 (1997).

15 J. C. Tully, in Modern Methods for Multidimensional Dynamics Computations in Chemistry, edited by D. C. Thompson (World Scientific, Singapore, 1998), pp. 34, 72.

16 A. D. McLachlan, *Mol. Phys*. **4**, 417 (1961).

17 C. A. Mead and D. G. Truhlar, *J. Chem. Phys.* **77**, 6090 (1982).

18 D. G. Truhlar and J. T. Muckerman, in Atom-Molecule Collision Theory, edited by R. B. Bernstein (Plenum, New York, 1979), pp. 505–594.

19 See endnote 39 in S. Hammes-Schiffer and J. C. Tully, J. *Chem. Phys*. **101**, 4657 (1994).

20 Y. L. Volobuev, M. D. Hack, M. S. Topaler, and D. G. Truhlar, *J. Chem. Phys*. **112**, 9716 (2000).

Table 1. Mean unsigned relative errors (MUREs) for the 12 YRH cases, the 9 MXH cases, and all 21 cases.[a]

System	Method	P_R	$\langle v' \rangle$	$\langle j' \rangle$	P_Q	$\langle v'' \rangle$	$\langle j'' \rangle$	P_N	F_R	Moms[b]	Probs[c]	All[d]
YRH	FSTU+	1.25	**0.14**	**0.15**	**0.21**	**0.27**	**0.79**	**0.19**	1.12	**0.34**	0.69	0.51
	FSTU–	0.75	**0.20**	**0.14**	**0.22**	0.37	**0.88**	**0.18**	0.67	**0.40**	**0.46**	**0.43**
	FSTU∇*V*	**0.54**	**0.18**	**0.14**	**0.20**	**0.34**	**0.92**	**0.15**	**0.63**	**0.40**	**0.38**	**0.39**
MXH	FSTU+	1.09	**0.29**	**0.13**	**0.24**	**0.13**	**0.16**	**0.30**	0.66	**0.18**	0.58	0.38
	FSTU–	0.98	**0.27**	**0.13**	**0.23**	**0.14**	**0.16**	**0.29**	0.58	**0.17**	0.52	**0.35**
	FSTU∇*V*	**0.88**	**0.28**	**0.13**	**0.26**	**0.12**	**0.15**	**0.26**	**0.54**	**0.17**	**0.48**	**0.33**
Both[e]	FSTU+	1.18	**0.20**	**0.14**	**0.22**	**0.21**	**0.52**	**0.24**	0.92	**0.27**	0.64	0.46
	FSTU–	0.85	**0.23**	**0.13**	**0.23**	0.27	**0.57**	**0.23**	0.63	**0.30**	0.48	**0.39**
	FSTU∇*V*	**0.69**	**0.23**	**0.14**	**0.23**	**0.25**	**0.59**	**0.20**	**0.59**	**0.30**	**0.42**	**0.36**

[a]The methods with the statistically lowest MUREs for each observable are given in bold. See the text for more details.

[b]Average of the $\langle v' \rangle$, $\langle j' \rangle$, $\langle v'' \rangle$, and $\langle j'' \rangle$ MUREs.

[c]Average of the P_R, P_Q, P_N, and F_R MUREs.

[d]Average of all eight MUREs.

[e]MUREs averaged over all 21 test cases.

Table 2. Unsigned relative errors for the 12 YRH and 9 MXH cases.

System	Initial Conditions[a]	Parameter-ization[b]	P_N			F_R		
			FSTU+	FSTU–	FSTU∇V	FSTU+	FSTU–	FSTU∇V
YRH	(1.10, 0)	0.20	0.38	0.32	**0.14**	0.71	0.42	**0.10**
		0.10	**0.06**	**0.08**	0.17	0.57	0.30	**0.15**
		0.03	0.15	0.15	**0.05**	0.37	0.08	**0.07**
		0.01	**0.33**	**0.33**	**0.14**	**0.07**	**0.07**	**0.06**
	(1.10, 6)	0.20	**0.01**	0.09	**0.02**	0.54	**0.36**	0.60
		0.10	0.26	0.29	**0.24**	**0.66**	**0.67**	0.74
		0.03	**0.10**	**0.07**	**0.11**	**0.31**	0.39	0.46
		0.01	**0.11**	**0.07**	**0.13**	0.51	**0.40**	0.60
	(1.02, 0)	0.20	0.66	0.60	**0.45**	0.50	**0.00**	0.24
		0.10	**0.09**	0.13	0.18	3.58	2.37	**1.73**
		0.03	**0.05**	**0.03**	**0.05**	2.30	1.63	**1.18**
		0.01	**0.07**	**0.05**	**0.15**	3.26	**1.38**	1.57
Average of YRH cases			**0.19**	**0.18**	**0.15**	1.12	0.67	**0.63**
MXH	(1.10, 0)	SB	0.53	**0.44**	**0.43**	0.77	0.58	**0.48**
		SL	0.21	0.21	**0.18**	1.11	1.07	**1.00**
		WL	**0.35**	**0.34**	**0.31**	0.14	0.12	**0.08**
	(1.10, 1)	SB	0.19	**0.18**	**0.15**	1.45	0.99	**0.94**
		SL	0.18	0.19	**0.15**	1.46	1.42	**1.35**
		WL	**0.47**	**0.48**	**0.45**	0.19	0.17	**0.10**
	(1.10, 2)	SB	0.20	0.16	**0.12**	**0.23**	0.33	0.38
		SL	**0.40**	0.40	**0.37**	0.50	**0.45**	**0.43**
		WL	**0.19**	**0.19**	**0.18**	0.12	0.13	**0.08**
Average of MXH cases			**0.30**	**0.29**	**0.26**	0.66	0.58	**0.54**
Average of all 21 cases			**0.24**	**0.23**	**0.20**	0.92	0.63	**0.59**

[a]The initial conditions are denoted (E_{tot}/eV, j), where E_{tot} is the total energy in eV and j is the initial rotational state of the diatom. For more details see Refs. 6 and 20 for the YRH and MXH systems, respectively.

[b]See Refs. 6 and 20 for descriptions of the YRH and MXH parameterizations, respectively.

Table 3. Scorecard for the 12 YRH cases, the 9 MXH cases, and all 21 cases.[a]

System	Method	P_R	$<v'>$	$<j'>$	P_Q	$<v''>$	$<j''>$	P_N	F_R	Moms[b]	Probs[c]	All[d]
YRH	FSTU+	0.33	0.92	0.92	0.83	1.00	0.67	0.67	0.25	0.88	0.52	0.70
	FSTU–	0.58	0.58	0.83	0.67	0.25	0.67	0.50	0.50	0.58	0.56	0.57
	FSTU∇V	0.67	0.75	0.83	0.83	0.25	0.42	0.83	0.50	0.56	0.71	0.64
MXH	FSTU+	0.11	0.78	0.78	0.56	0.67	0.89	0.44	0.11	0.78	0.31	0.54
	FSTU–	0.00	1.00	0.78	0.78	0.56	0.78	0.56	0.11	0.78	0.36	0.57
	FSTU∇V	0.89	0.78	0.89	0.67	0.44	1.00	1.00	0.89	0.78	0.86	0.82
Both[e]	FSTU+	0.22	0.85	0.85	0.69	0.83	0.78	0.56	0.18	0.83	0.41	0.62
	FSTU–	0.29	0.79	0.81	0.72	0.40	0.72	0.53	0.31	0.68	0.46	0.57
	FSTU∇V	0.78	0.76	0.86	0.75	0.35	0.71	0.92	0.69	0.67	0.78	0.73

[a]See Sec. IV for a description of the scorecard method.

[b]Average of the $<v'>$, $<j'>$, $<v''>$, and $<j''>$ scores.

[c]Average of the P_R, P_Q, P_N, and F_R scores.

[d]Average of all eight scores.

[e]Average of the YRH and MXH scores.

Chapter Seven

7

Narrow Subthreshold Quantum Mechanical Resonances in the Li + HF ⟶ H + LiF Reaction

I. Introduction

The reaction Li + HF → H + LiF has become a prototype for both theoretical and experimental investigations of the dynamics of atom-diatom systems with three different atoms and the heavy-heavy-light mass combination. The ground-state potential energy surface has been calculated, and several analytic fits have been presented in the literature.[1–17] Various aspects of the dynamics of LiFH have been studied, including reactive collisions,[10,11,18–32] stereodynamics and vector correlations,[26,29,30,33–35] and photodissociation dynamics.[15,36–39] Experimentally observable quantities such as the differential and integral cross sections have also been discussed.[18,20,26,29,30]

A striking feature of the previously reported studies is the strong resonance structure.[10,11,19,21–25,28,32] It is well known that resonance structure in dynamical features may be associated with quasibound (i.e., metastable) states of the system. However, in all of the investigations carried out so far for the Li + HF reaction, the description of the resonance structure is phenomenological, and there is little quantitative characterization. In addition, research has been primarily focused on the scattering features, and there is no study of the intermediate metastable states of the Li···FH complexes, which are of fundamental interest. One objective in the present study is to identify the energies and lifetimes of the resonance states using fully converged quantum mechanical scattering calculations. The method employed is a time-independent, two-

arrangement Green's-function-based scattering approach, namely the outgoing scattering wave variational principle (OWVP).[40–43] The results are limited by the accuracy of the fitted multidimensional potential energy surface.

The present work is especially timely in light of the recent work of Bowman, Manolopoulos, and co-workers,[44,45] in which subthreshold resonances associated with the van der Waals wells of the HOCl system were identified in exact quantum mechanical scattering calculations and characterized using quasibound-state calculations. A similar analysis for the FH_2 system and its deuterated isotopes has demonstrated the existence of van der Waals well resonances.[46–48] In the present paper, we interpret observed resonances in the Li + HF reaction as due to metastable van der Waals complexes of the reactants, i.e., Li···FH van der Waals complexes.

This paper is organized as follows. Section II reviews the basic features of the ground-state potential energy surface for the reactive LiFH system. Section III contains a brief summary of the theory and methods that are used in the scattering and the bound- and quasibound-state calculations. In Sec. IV, we present state-to-state, initial-state-selected, and cumulative reaction probabilities for total angular momentum $J = 0$. The resonance energies and widths are obtained by fitting the energy dependence of the eigenphase sum to the multichannel Breit-Wigner formula. The product rotational state distributions resulting from the decay of two resonances are also presented. The resonance complexes are further characterized by assigning vibrational quantum numbers corresponding to quasi-bound states of the Li···FH van der Waals complex. Section V is a summary.

II. Ground-State Potential Energy Surface of the LiFH Complex

Details of the ground-state LiFH potential energy surface used here have been presented previously.[15] Briefly, potential energies for the two lowest-energy electronic surfaces were calculated at a high level of theory over a wide range of nuclear geometries. These adiabatic energies were fitted to analytic functional forms in the diabatic representation. The ground-state adiabatic potential energy surface used in the

present study is obtained by diagonalizing the fitted diabatic potential energy matrix. The surface fit used here has been labeled surface fit H in later work.[16]

The ground-state surface has two van der Waals wells: one in the entrance valley with a well depth of 0.21 eV with respect to the Li + HF asymptote at its equilibrium geometry, and the other in the product valley with a well depth of 0.043 eV with respect to the LiF + H asymptote at its equilibrium geometry. The surface also has two saddle points. The first saddle point is the transition state for the F transfer reaction and has a non-linear geometry and a potential barrier height of 0.35 eV with respect to the Li + HF asymptote at its equilibrium geometry. The second saddle point is the transition state for dissociation of the LiF···H complex and has a very small height of 0.014 eV with respect to the LiF + F asymptote at its equilibrium geometry and is located in the product valley. The overall reaction Li + HF → LiF + H is endoergic by 0.21 eV without including the zero-point energy of the reactants and products and by 0.015 eV when zero-point energy is included. The characteristic features of the stationary points of the ground-state LiFH surface are summarized in Table 1 and are shown schematically in Fig. 1. The zero-point energies in Table 1 are taken from Ref. 15 and were calculated using the Morse-I approximation[49,50] available in the POLYRATE[51] software package.

III. Theory

III.A. Quantum Mechanical Scattering Matrices

Quantum mechanical scattering matrix elements were obtained by solving the time-independent Schrödinger equation by the outgoing wave variational principle (OWVP).[40–43] In this method, the Schrödinger equation is solved by expanding the outgoing scattering waves in terms of internal-state channel functions for each asymptotic chemical arrangement. The solution to the Schrödinger equation can be written in integral form using the Lippmann-Schwinger formalism.[42,43,52,53] The first term in the solution is called the distorted wave and satisfies

$$\left(H_D^k - E\right)\Phi_{n_0}^{(+)k} = 0\,, \tag{1}$$

where H_D^k contains some of the channel-channel coupling, E is the total energy, k labels a chemical arrangement (k = 1 for the Li + HF arrangement and k = 2 for the H + LiF arrangement), n is the collection of quantum numbers describing the asymptotic state of the system (including the rotational, vibrational, and electronic states, and the chemical arrangement) and may be called an asymptotic channel, n_0 is the initial asymptotic channel, and $\Phi_{n_0}^{(+)k}$ is obtained by solving eq. (1) numerically using finite differences.[41,54] The difference between the full Hamiltonian for arrangement k and the distorted wave Hamiltonian H_D^k is the coupling potential V_C^k. The contribution to the scattering matrix from V_C^k is obtained variationally using a dynamically adapted basis set.[40–43]

Using this two-step scheme, the full scattering matrix is written as the sum of two terms,

$$S_{nn_0} = \delta_{kk_0}\,{}^0S_{nn_0}^k + \mathcal{S}_{nn_0}, \tag{2}$$

where the first term is the distorted wave Born approximation for the scattering matrix obtained using the distorted wave functions $\Phi_{n_0}^{(+)k}$, and the second term is the contribution from the coupling potential V_C^k. Two kinds of basis functions are employed in the present study: half-integrated Green's functions[54] (called type-g basis functions) and asymptotic eigenstate basis functions (called type-e basis functions). The type-g basis functions are used for energetically open channels, and type-e basis functions are used for energetically closed channels. See Refs. 40–43 for more details regarding our implementation of the OWVP scattering algorithm.

After the scattering matrix is calculated, the transition probabilities and cumulative reaction probabilities may be obtained according to their usual definitions.

III.B. Resonance Scattering

A resonance may be characterized in terms of its resonance energy E_α and total width Γ_α, where the index α labels the resonance. These observables may be correlated with the analytic properties of the scattering matrix such that the complex energies

$$z_\alpha = E_\alpha - \frac{i}{2}\Gamma_\alpha , \tag{3}$$

are the poles of the scattering matrix elements.[52,55]

In the neighborhood of an isolated narrow resonance (INR), the scattering matrix elements $S_{nn'}(E)$ can be separated into background (nonresonant) contributions $S^{\mathrm{b}}_{nn'}(E)$ and contributions from the resonance. This yields[52,55]

$$S_{nn'}(E) = S^{\mathrm{b}}_{nn'}(E) - i\frac{\gamma_{\alpha n}\gamma_{\alpha n'}}{E - z_\alpha}, \tag{4}$$

where $\gamma_{\alpha n}$ is the partial width amplitude for channel *n* and is related to the partial width by

$$\Gamma_{\alpha n} = \left|\gamma_{\alpha n}\right|^2 . \tag{5}$$

Each partial width is related to the lifetime $\tau_{\alpha n}$ for the unimolecular decay of resonance state α into a specific final channel *n*,

$$\tau_{\alpha n} = \hbar / \Gamma_{\alpha n} . \tag{6}$$

The sum over all of the partial widths for a given resonance α gives the total width of that resonance,

$$\Gamma_\alpha = \sum_n \Gamma_{\alpha n} , \tag{7}$$

and the total width is related to the lifetime of the resonance,

$$\tau_\alpha = \hbar / \Gamma_\alpha . \tag{8}$$

Using eqs. (3) and (4) and ignoring the background contribution, one can obtain the state-to-state or channel-to-channel transition probability in the neighborhood of resonance,

$$\left|S_{nn'}(E)\right|^2 = \frac{\Gamma_\alpha^2}{(E - E_\alpha)^2 + \Gamma_\alpha^2 / 4} P_{\alpha n} P_{\alpha n'}, \tag{9}$$

where

$$P_{\alpha n} = \Gamma_{\alpha n} / \Gamma_{\alpha} \tag{10}$$

is the branching ratio, i.e., the probability for entering the resonance state α from the initial channel n (or equivalently the probability of leaving the resonance state α into the final channel n).

In order to extract the resonance energy and resonance width, it is convenient to use the expression for the eigenphase sum $\Delta(E)$, which is defined by

$$\exp[2i\Delta(E)] = \det[S(E)]. \tag{11}$$

As the total energy E passes close to a resonance energy z_n, the eigenphase sum increases rapidly by approximately π. This behavior can be expressed analytically using the multi-channel Breit-Wigner formula,[56–58]

$$\Delta(E) = \Delta^{b}(E) + \arctan\left[\frac{\Gamma_{\alpha}}{2(E_{\alpha} - E)}\right] + m(E)\pi, \quad m = ...,-2,-1,0,1,2,..., \tag{12}$$

where $\Delta^{b}(E)$ is the nonresonant or background contribution. The term $m(E)\pi$ indicates that eq. (12) determines $\Delta(E)$ only within a factor of π, and for each value of E some integral multiple of π must be added to the eigenphase sum such that the eigenphase sum is a continuous function of E. The observables E_{α} and Γ_{α} may be extracted from $\Delta(E)$, by fitting the multi-channel Breit-Wigner formula, eq. (12), to the eigenphase sum data obtained from scattering calculations.[59–61]

Not all resonances are isolated and narrow. Overlapping resonances may occur and these resonance features involve strong interference effects and statistical behavior in contrast to the mode-specific behavior of the INRs.[62] The theoretical analysis of overlapping and broad resonances is much more complicated than the case of INRs and will not be considered here.

III.C. Bound and Quasibound States of the Reactant van der Waals well

The bound-state and quasibound-state energies and wave functions of the Li···FH van der Waals well were computed using the computer code ABCSPECTRA.[63] The bound-state and quasi-bound state wave functions were expanded in the basis Γ_β

$$\Psi_\alpha(\mathbf{R},\mathbf{r}) = \sum_\beta c_{\alpha\beta}\Gamma_\beta(\mathbf{R},\mathbf{r}), \tag{13}$$

where

$$\Gamma_\beta(\mathbf{R},\mathbf{r}) = \frac{1}{R}t_m(R)\frac{1}{r}\phi_{vj}(r)y_{jl}(\hat{\mathbf{R}},\hat{\mathbf{r}}), \tag{14}$$

$\mathbf{R} = R\hat{\mathbf{R}}$ is the mass-scaled translational Jacobi coordinate describing the Li to center-of-mass of HF motion, $\mathbf{r} = r\hat{\mathbf{r}}$ is the mass-scaled internal Jacobi coordinate describing the HF vibrational motion, α is a collection of quantum numbers and labels the bound or quasibound state, $c_{\alpha\beta}$ is an expansion coefficient, t_m is a Gaussian translational basis function, ϕ_{vj} is an asymptotic eigenstate rovibrational function of HF, and y_{jl} is an eigenfunction of the total angular momentum $J = 0$, the rotational state of HF j, and the orbital angular momentum of Li with respect to the center-of-mass of HF l. The basis function index β is the collection of the indices v, j, l, and m, where v is the vibrational quantum number of the isolated diatom, and m labels the translational basis functions.

The expansion coefficients in eq. (13) may be obtained by numerically computing the matrix elements

$$H_{\beta'\beta} = \langle\beta'|H|\beta\rangle \equiv \int \Gamma_{\beta'} H \Gamma_\beta d\mathbf{R}d\mathbf{r}, \tag{15}$$

$$S_{\beta'\beta} = \langle\beta' \mid \beta\rangle \equiv \int \Gamma_{\beta'}\Gamma_\beta d\mathbf{R}d\mathbf{r}, \tag{16}$$

where H is the full Hamiltonian and solving the generalized eigenvalue problem. Details of the bound-state calculations including the computational implementation and the numerical and basis set parameters are given in the appendix.

IV. Results and Discussion

IV.A. State-to-State, State-Selected, and Cumulative Reaction Probabilities

OWVP reactive scattering calculations were carried out at total energies ranging from 0.26 to 0.50 eV relative to the Li + HF asymptote at its equilibrium geometry using version 18.8 of the VP scattering code.[64] In order to resolve the resonance states, we used an energy grid of 0.0001 eV at low energies. Resonance widths usually increase with energy, and therefore we used a coarser grid of 0.00025 eV at high energies. Table 2 lists two sets of basis set and numerical parameters used for the scattering calculations at a total energy of 0.4 eV. The definitions of the parameters are given elsewhere.[42,43] At this energy, parameter set 1, for example, has a total of 511 asymptotic channels, of which 47 are open, and a total of 18 043 basis functions. The larger parameter set, parameter set 2, was used to check the convergence of the results with respect to variations in both the numerical and basis parameters. The state-to-state transition probabilities and eigenphase sums computed with parameter sets 1 and 2 differ from each other by no more than one percent.

Figure 2 shows the state-to-state reaction probability plotted as a function of energy for the process Li + HF($v = 0, j = 0$) $\longrightarrow$ H + LiF($v' = 0, j'$), where $j' = 0 - 5$. A strong resonance structure dominates the energy profiles, especially in the energy region associated with the Li···FH van der Waals well in Fig. 1. We note that even at resonance energies, the probability of reaction is small (less than 0.1), and therefore nonreactive collisions are the dominant process. This is not surprising due to the 0.35 eV barrier and 0.23 eV endoergicity of the reaction, as shown in Fig. 1.

Figure 3 presents the initial-state-selected reaction probability for the process Li + HF($v = 0, j$) $\longrightarrow$ H + LiF, where $j = 0 - 9$. We see that the major resonances displayed in the state-to-state reaction probabilities persist after summing over final states. Note the strong dependence of the state-to-state transition probabilities on the initial rotational state j of the HF diatom. Specifically, as j increases the background reaction probability increases and moves to higher energies. We also note that the resonances at low energies are mainly due to the contribution from the low-j channels, while for higher-energy

resonances, the contributions are primarily from the high-j channels even though the low-j channels are energetically accessible.

Figure 4(a) shows the cumulative reaction probability for the Li + HF ⟶ H + LiF reaction over the energy range 0.26–0.50 eV, where energy is given relative the Li + HF asymptote at its classical equilibrium geometry. The threshold for nonquantal passage over the barrier may be identified with the energy at which the background contribution first equals 0.5.[65–67] In Fig. 4(a) we see that this occurs at $E \approx 0.47$–0.49 eV, which is in reasonable agreements with the zero-point inclusive barrier height (0.45 eV) in Fig. 1 and Table 1. Figure 4(b) shows the cumulative reaction probability below the threshold. The reaction probability is almost zero except at several localized resonance energies, and even at resonance energies, the probability of reaction is small (much less than 0.5). As the energy increases above the effective threshold energy, the background reaction probability (which measures direct reaction) rises gradually. The transition probabilities, however, continue to exhibit sharp resonance features [see Fig. 4(c)]. The overall trend for both the background and resonance reaction probabilities is an increase with increasing energy.

IV.B. Resonance Energies and Total Widths

In order to characterize the resonance features, we computed the eigenphase sum Δ_j on a dense grid of energies (E_j, $j = 1 - N_E$) surrounding each resonance. The background contribution was expanded as a polynomial function of the total energy,

$$\Delta^{b}(E) = \sum_{l=0}^{N} a_l E^l \,, \tag{17}$$

and eq. (12) was fitted to the dense grid of eigenphase sums. To check the stabilization of the fitted E_α and Γ_α, we varied the order N of the polynomial in eq. (17) such that

$$\delta^2 = \frac{1}{N^E - N - 2} \sum_{j=1}^{N_E} [\Delta_j - \Delta(E_j)]^2 \,, \tag{18}$$

was minimized with respect to E_α, Γ_α, and a_l.

Table 3 presents the resonance energy and width for each of the resonances that was observed and characterized. Note that we observe both isolated narrow resonances and broad overlapping resonances. We calculate lifetimes [using eq. (8)] that range over approximately three orders of magnitude from 0.20 to 87 ps. This is not surprising since the decay rate often depends exponentially on the translational energy associated with the dissociation coordinate.[68–70] Even though not all of the resonances are INRs, the fits to the eigenphase sum are still relatively accurate. The root mean square error for each fit is smaller than 0.1 percent.

Figure 5 illustrates the energy dependence of the eigenphase sum in the region of an isolated narrow resonance with an energy of 0.274 eV, where the dots are the calculated results, the solid line is the fitted curve, and the straight line is the background contribution. As expected,[56–58] there is a rapid increase by π in the eigenphase sum around the resonance.

IV.C. Resonance Decay Product State Distributions

For an isolated narrow resonance, the partial widths $\Gamma_{\alpha n}$ [defined in eq. (5)] may be obtained from any column of the scattering matrix.[59–61] Specifically, the background contribution to each of the scattering matrix elements in eq. (4) is expressed as a polynomial of the total energy,

$$S^{\mathrm{b}}_{nn'}(E) = \sum_{l=0}^{N} A_{l,nn'} E^{l} \ . \tag{19}$$

Equation (4) may then be written

$$(E - z_{\alpha}) S_{nn'}(E) = \sum_{l=0}^{N+1} B_{l,nn'} E^{l} \ , \tag{20}$$

where

$$B_{0,nn'} = -z_{\alpha} A_{0,nn'} - i C_{\alpha nn'} \tag{21}$$

$$B_{l,nn'} = A_{l-1,nn'} - z_{\alpha} A_{l,nn'} \quad (l = 1, 2, ..., N) \tag{22}$$

$$B_{N+1,nn'} = A_{N,nn'} \tag{23}$$

and

$$C_{\alpha nn'} = \gamma_{\alpha n}\gamma_{\alpha n'}. \tag{24}$$

The partial width amplitudes $\gamma_{\alpha n}$ are related to $C_{\alpha nn'}$ by

$$\gamma_{\alpha n'} = \frac{C_{\alpha nn'}}{\sqrt{C_{\alpha nn}}}, \tag{25}$$

and $\Gamma_{\alpha n}$ may be calculated using eq. (5).

The quantities $\{B_{l,nn'}\}$ may be obtained by fitting eq. (20) to the calculated OWVP scattering matrix elements $S_{nn',j}$ and minimizing the quantity

$$\varepsilon_n^2 = \sum_{n'=1}^{N_o}\left\{\frac{\sum_{j=1}^{N_E}\left|S_{nn',j} - S_{nn'}(E_j)\right|^2}{N_E - N}\right\}^{1/2}, \tag{26}$$

where N_o is the number of open channels and N_E is the number of energies included in the fit. From $\{B_{l,nn'}\}$, we can calculate $\{A_{l,nn'}\}$ and $C_{\alpha nn'}$ from eqs. (21)–(23).

We present detailed results for two resonances, namely the E = 0.294 and 0.304 eV resonances, which have total reactive decay probabilities (calculated by summing the partial widths associated with reactive channels) of 0.03 and 0.53, respectively. At these energies, LiF is in its ground vibrational state, and the maximum rotational quantum number j that is energetically accessible is 18 and 20, respectively. From the partial widths and eq. (10), we computed the probability of decay into each rotational state, and the results are plotted in Fig. 6. The rotational state profiles do not differ significantly from the rotational state distributions resulting from direct scattering at nearby nonresonant energies. Considering that these calculated rotational state distributions are very sensitive to the anisotropy of PES, comparison of the calculated product state distributions to experiment would be a stringent test of theory, but no experimental result is currently available.

A more detailed study of the trends in the partial widths, although potentially illuminating as to the resonance decay mechanism, is not pursued in the present work.

IV.D. Bound and Quasibound States

In addition to their energies and widths, the resonance states of Li···FH identified in Secs. IV.A and IV.B can be approximately characterized by a set of three quantum numbers (when $J = 0$, as is the case throughout this paper). We note that for $J > 0$, a more sophisticated analysis is required than the simple one presented below.[71,72]

For resonances trapped in the reactant van der Waals well, one choice for the quantum numbers is (v, n, $j = l$), where v and j are the quantum numbers respectively describing the vibrational and rotational state of the tightly bound diatom HF, and n and l are quantum numbers describing the stretching motion and angular momentum of Li with respect to the center-of-mass of HF.[71–73] These quantum numbers are useful for interpreting the dynamics of the resonance when the Li atom is far from HF, i.e., when the interaction energy between Li with HF is small.

Alternatively, one may characterize the resonance states with a set of quantum numbers (ν_r, ν_R, ν_χ), where each quantum number represents the vibrational state of one of the normal modes of the system at its minimum energy geometry. The vibrational quantum numbers are listed in the order of decreasing frequencies, i.e., first the HF vibration mode ν_r, then the nonreactive dissociation mode ν_R, and finally the van der Waals bending mode ν_χ. This set of quantum numbers is useful for describing the dynamics of the resonance when Li is close to HF (i.e., when Li and HF are strongly interacting) and the system is in the deep reactant van der Waals well.

As the system dissociates nonreactively (i.e., to Li + HF) at a resonance energy, the more useful set of quantum numbers changes from the (ν_r, ν_R, ν_χ) set to the (v, n, $j = l$) set, and the two sets of quantum numbers may be correlated in this way. For example, ν_r is approximately equivalent to v, and increased excitation of the bending mode ν_χ is likely to result in increased excitation of j and l. Although both sets of quantum numbers represent idealized situations and are only zero-order approximations, the resonance states are localized over the deep Li···FH van der Waals well, and we expect the (ν_r, ν_R, ν_χ) scheme to be more useful in the present work.

In order to characterize the quasibound states by the (ν_r, ν_R, ν_χ) scheme for the Li···FH van der Waals complexes, we first computed the bound states of Li···FH. Details of the bound-state calculations are given in Sec. III.C and the Appendix. The Li···FH van der Waals well supports 25 bound states, as shown in Table 4. Excitation of the HF vibration requires ~0.5 eV of energy and therefore all of the bound states have $\nu_r = 0$. The bound-states were further characterized by computing the radial wave functions and counting nodes to obtain ν_R. The remaining quantum number ν_χ was assigned as required. Assignment by this method was straightforward, and the energy spacings of the bound states fit regular patterns, i.e., the progression of (0, 0, ν_χ) states is similar to the progression of (0, 1, ν_χ) states, etc. The assignments are shown on the left-hand side of Table 4.

The bound-state energy levels of the Li···FH van der Waals well have been studied previously.[14,17] Reference 17 compares the bound-state energies of potential surfaces obtained from fits to high-level *ab initio* data calculated at various levels of theory. The most accurate surface that was studied in Ref. 17 has a zero-point energy of 0.272 eV (relative to the bottom of the well), which agrees well with the value reported in the present work of 0.273 eV. The reported[17] values of the energies of the (0, 0, 1) and (0, 1, 0) states are 0.045 and 0.040 eV relative to the (0, 0, 0) state, respectively. We report values of 0.20 and 0.41 eV for the (0, 0, 1) and (0, 1, 0) states, respectively. Based upon our own bound-state calculations[74] of a previously published surface[14] and the current work, we believe that the (0, 0, 1) state is lower in energy than the (0, 1, 0) state, i.e., the (0, 0, 1) and (0, 1, 0) states in Ref. 14 (and possibly Ref. 17) are assigned incorrectly. We do not believe, however, that the surface used in the present work is quantitatively accurate in the van der Waals bend near the van der Waals well, i.e., the energy spacings of the energy levels with varying ν_χ quantum numbers are not quantitatively accurate. This defect has been corrected in surface fit J,[16] which has energies of 0.34 and 0.48 for the (0, 0, 1) and (0, 1, 0) states, respectively.[74] All of the results in the current paper were obtained using surface fit H,[15,16] and the results may therefore not provide quantitative comparison with experiment.

In principle, quasibound-states may also be obtained from the energy spectrum obtained by diagonalizing the Hamiltonian in a finite basis. In practice, however, the energies of these states are strongly dependent on the accidental closeness in energy to nearby continuum states. Furthermore, the nodal structure can become obscured as quasibound-state wave functions mix with nearby continuum or quasibound states. By inspection of the radial parts of the unbound wave functions, we were able to definitively determine the energy of and assign quantum numbers for all quasibound states with v_R = 0, 1, and 2, as well as one state with $v_R = 3$ on the energy range of the scattering calculations presented in Sec. IV.A. The quasibound states that we identified and assigned are given on the right-hand side of Table 4.

In order to obtain the full spectrum of quasibound states, we fit the bound-state and quasibound-state energies in Table 4 to the same kind of quantum number series[75] as used in conventional spectroscopy, taking the series to second order in the quantum numbers, i.e.,

$$\begin{aligned} E_{\rm fit}(v_R, v_\chi) = {} & \omega_R(v_R + \tfrac{1}{2}) + \omega_\chi(v_\chi + \tfrac{1}{2}) \\ & + x_R\omega_R(v_R + \tfrac{1}{2})^2 + x_\chi\omega_\chi(v_\chi + \tfrac{1}{2})^2 . \\ & + f_{R\chi}(v_R + \tfrac{1}{2})(v_\chi + \tfrac{1}{2}) + E_0 . \end{aligned} \tag{27}$$

The RMS error

$$\Delta \equiv \sqrt{\sum_{v_R, v_\chi} \left(E_{\rm fit}(v_R, v_\chi) - E_{v_R, v_\chi}\right)^2} , \tag{28}$$

was minimized with respect to ω_R, ω_χ, x_R, x_χ, $f_{R\chi}$, and E_0, where E_{v_R, v_χ} are the calculated bound-state and quasibound-state energies in Table 3, and the sum in eq. (28) runs over all observed states. The best-fit parameters for eq. (27) are given in Table 5, and the resulting fit has a RMS error of 0.006 eV. Using the fitted parameters, the full spectrum of quasibound states can be obtained, and the calculated E_{v_R, v_χ} (from Table 4) and fitted $E_{\rm fit}(v_R, v_\chi)$ quasibound-state energies are given in Table 6 for the energy range in Figures 2–4.

IV.E. Characterization of the observed resonances and decay mechanisms

The quantized energy of the saddle point for reaction is 0.45 eV including zero-point energy in the modes orthogonal to the reaction coordinate,[65] and this energy is within the energy range of total energies considered the present study (0.26 to 0.50 eV). It is possible that we may observe a "barrier passage" resonance corresponding to the decrease in the kinetic energy of the system as it passes over the transition state barrier.[58] Barrier passage resonances have short lifetimes (and therefore large widths), and we may associate such a resonance with a broad increase in the cumulative reaction probability between 0.45 and 0.50 eV; we will not analyze this further. The product van der Waals complex LiF···H is not bound when zero-point energy is included as shown in Fig. 1. We therefore consider all of the resonances in Table 3 to correspond to trapped-state resonances localized over the reactant van der Waals well.

The resonance energy widths vary over several orders of magnitude (from 8×10^{-6} to 3×10^{-3} eV), and trends in the widths may be explained by assigning (v_r, v_R, v_χ) quantum numbers to the resonances. Assignments were made using the estimated quasibound state energies in Table 6 as follows: Below the threshold energy (~0.35 eV) there is a one-to-one correspondence between the scattering resonance energies and the fitted quasibound-state energies if the quasibound states when the $v_R = 0$ and 1 are excluded. We conclude that quasibound states with $v_R = 0$ and 1 have widths too small (smaller than 10^{-6} eV) to observe in the scattering calculations presented here.

Above threshold, the nonresonant reaction probability increases, and the CRP energy profile becomes more complicated and contains several broad and overlapping features that are not characterized in Table 3. We assign the observed scattering resonances by again excluding the $v_R = 0$ and 1 quasibound states and based on closeness in energy to the computed quasibound states. There are several missing states, which may be explained as due to the complicated CRP structure above threshold. The missing states have radial dissociation quantum numbers with $v_R \leq 1$ or $v_R \geq 5$. We interpret this finding to indicate that the small-v_R quasibound states have energy widths too small to

observe and the high-v_R quasibound states resemble continuum states, have short lifetimes, and have broad, overlapping resonance features that are lost in the nonresonant reactive background probability.

The RMS error of the observed and fitted resonance energies is approximately equal to the RMS error of the bound-state energies (0.005 eV).

Figure 7 shows the energy width of the scattering resonance as a function of its assigned radial quantum number v_R. There is a strong exponential dependence of the resonance width on the dissociation energy as observed previously.[69] The trend persists over several orders of magnitude in the energy widths, and this strengthens our confidence in the accuracy of the quasibound-state quantum number assignments in Table 6. Although the trends in Table 6 are systematic, some irregularity persists, probably due to the precise but accidental positioning of each resonance energy with respect to asymptotic quantum states.

The scattering resonances undergo the following decay mechanism: At a quasibound-state resonance energy, the system is delayed (i.e., there in an increase in probability density) in the van der Waals well before the transition state barrier, resulting in enhanced tunneling to form the LiF product. The lifetime of the trapped state is determined by the overlap of the quasibound-state radial function with unbound continuum functions of the same translational energy. This overlap depends exponentially on the translational energy and therefore on the radial quantum number.

V. Summary

The Li + HF ⟶ H + LiF reaction has been investigated in detail using the OWVP full-dimensional time-independent quantum scattering approach to calculate scattering matrix elements, from which we calculated state-to-state, initial-state-specific, and cumulative reaction probabilities. The reaction probabilities are very well converged so that the resonance structure is not lost in the noise, indicating the robustness of the methods being used. All the dynamical features have been recovered, thereby permitting a precise description of resonance states. The scattering resonances were identified in terms of their complex resonance energies.

The Li + HF ⟶ H + LiF reaction exhibits a threshold near 0.35 eV, and below the threshold energy the reaction takes place via a mechanism of resonance tunneling, which results in several resonance spikes in the cumulative reaction probability. When the energy is above the threshold, the reaction is governed by both direct and resonance mechanisms. The resonance complexes populated by the collisions can decay nonreactively either by resonance tunneling through the centrifugal barrier in the entrance valley or by energy transfer from the bending mode to the nonreactive dissociation mode. The sum of the reactive and nonreactive rates of decay have been calculated from the fitted resonance widths, with lifetimes ranging from 0.20 to 87 ps.

For two resonances, the product LiF rotational state distributions that result from decay of the resonance complex have been calculated.

We have determined the resonance-state energies by both scattering and bound-state calculations, and quasibound-state vibrational quantum numbers have been assigned. Below threshold there is excellent agreement between the resonance and quasibound-state energies. Resonances corresponding to quasibound states with $v_R < 2$ are not observed in the scattering calculations. Above threshold, several resonances are observed that correspond to quasibound states with $2 \leq v_R \leq 4$. In both regimes, there is good exponential correlation between the energy width of the resonance and the radial quantum number v_R.

The present study is particularly intriguing in the context of identifying intrinsically quantum mechanical behavior in chemical reactions. Resonances that lead to sharp quantum mechanical spikes in the reaction probability at energies beneath the classical threshold are one of the most dramatic quantum effects that one can postulate.[45,66,76] The observation of long sequences of such resonances, both in the O + HCl reaction[45] and in the present study of Li + HF, provides a serious reminder of the necessity of checking classical models against quantum mechanical reality when interpreting chemical reactivity, especially are subthreshold energies.

In general, bimolecular chemical reactions feature van der Waals attractions on both sides of the transition state barrier, and these wells are often deep enough to support

bound states. The dramatically enhanced reactivity (i.e., the resonance in the reaction profile) at energies associated with van der Waals quasibound states that results from the localization of the wave function at the base of the barrier depends on several factors including the depth and shape of the well, the height and width of the barrier, the mass of the tunneling particles, etc. Recent experimental work on van der Waals complexes has included several examples of radical-molecule systems,[77–80] and it is not clear which of these might potentially show such behavior. The possibility of state-selected coherent reactivity at isolated narrow resonances raises new possibilities for exploiting quantum mechanical phenomena for control and technological advantage.

Acknowledgments

We are pleased to contribute to this paper to the Don Kouri Festschrift. His contributions to the quantum theory of chemical reactivity have been essential to modern progress. We thank Yuri Volobuev and Mike Hack for helpful discussions. This work was supported by the National Science Foundation, through Grant No. CHE-0092019. John Wei contributed to this chapter.

Appendix: Bound-State and Quasibound-State Calculations

The basis functions defined by eq. (14) and the matrix element evaluation strategies used to obtain the Hamiltonian matrix elements defined by eq. (15) have been presented in detail previously in the context of scattering calculations.[43] The application of these strategies to bound-state calculations (as implemented in the computer code ABCSPECTRA[63]) is straightforward. In this appendix, we briefly present some of the details of the bound-state calculations.

We restrict our attention to the case of zero total angular momentum ($J = 0$), and therefore $l = j$, in which case the elements of the overlap matrix in eq. (16) can be written

$$S_{\beta'\beta} = \delta_{v'v}\delta_{j'j}\int t_{m'}(R)t_m(R)dR\,, \tag{29}$$

where throughout this appendix $\beta = (v, j, l, m)$ and $\beta' = (v', j', l', m')$. The translational basis functions t_m are distributed Gaussian functions with evenly spaced centers

(R_m^T, where $m = 1, \ldots, n_{\text{trans}}$). The width parameter of the translational basis functions is determined by setting the overlap parameter c of Hamilton and Light.[81]

The Hamiltonian operator in eq. (15) can be written

$$H(\mathbf{R},\mathbf{r}) = -\frac{\hbar^2}{2\mu}\frac{1}{R}\frac{\partial^2}{\partial R^2}R + U^{\text{eff}}(\mathbf{R},\mathbf{r}) + \hat{\tau}(\mathbf{r}), \tag{30}$$

where

$$\mu = \left(\frac{m_{\text{Li}} m_{\text{H}} m_{\text{F}}}{m_{\text{Li}} + m_{\text{H}} + m_{\text{F}}}\right)^{1/2}, \tag{31}$$

$$U^{\text{eff}}(\mathbf{R},\mathbf{r}) = \frac{\hbar^2}{2\mu}\frac{\hat{l}^2}{R^2} + V^{\text{int}}(\mathbf{R},\mathbf{r}), \tag{32}$$

$$\hat{\tau}(\mathbf{r}) = -\frac{\hbar^2}{2\mu}\frac{1}{r}\frac{\partial^2}{\partial r^2}r + \frac{\hbar^2}{2\mu}\frac{\hat{j}^2}{r^2} + V^{\text{diat}}(r), \tag{33}$$

$$V(\mathbf{R},\mathbf{r}) = V^{\text{int}}(\mathbf{R},\mathbf{r}) + V^{\text{diat}}(r), \tag{34}$$

$$V^{\text{diat}}(r) = \lim_{R\to\infty} V(\mathbf{R},\mathbf{r}), \tag{35}$$

m_{A} is the mass of atom A, $\hat{l}$ is the orbital (Li to center-of-mass of HF) angular momentum operator, and $\hat{j}$ is the internal (for the HF diatom) angular momentum operator.

The matrix elements of the first term in eq. (30) can be written

$$\langle\beta'|-\frac{\hbar^2}{2\mu}\frac{1}{R}\frac{\partial^2}{\partial R^2}R|\beta\rangle = -\frac{\hbar^2}{2\mu}\delta_{v'v}\delta_{j'j}\int t_{m'}(R)\frac{\partial^2}{\partial R^2}t_m(R)dR, \tag{36}$$

and can be evaluated analytically. The matrix elements of the second term in eq. (30) are

$$\langle\beta'|U^{\text{eff}}(\mathbf{R},\mathbf{r})|\beta\rangle = \int_{R_{\min}}^{R_{\max}} t_{m'}(R)\left[\frac{\hbar^2}{2\mu}\frac{l(l+1)}{R^2}\delta_{v'v}\delta_{l'l} + V^{\text{int}}_{n'n}(R)\right]t_m(R)dR, \tag{37}$$

where $n = (v, j, l)$, $n' = (v', j', l')$,

$$V^{\text{int}}_{n'n}(R) = \int \phi_{v'j'}(r)\, y_{j'l'}(\hat{\mathbf{R}},\hat{\mathbf{r}}) V^{\text{int}}(\mathbf{R},\mathbf{r}) \phi_{vj}(r)\, y_{jl}(\hat{\mathbf{R}},\hat{\mathbf{r}}) d\hat{\mathbf{R}} d\mathbf{r}$$
$$= \sum_{i=1}^{N_{\text{QV}}} w^{i}_{n'n} \sum_{\lambda=0}^{\lambda_{\max}} v^{\text{int}}_{\lambda}(R, r_i) f^{\lambda}_{n'n} \tag{38}$$

$$v^{\text{int}}_{\lambda}(R,r) = \frac{2\lambda+1}{2} \int d(\cos\gamma) P_{\lambda}(\cos\gamma) V^{\text{int}}(R, r, \cos\gamma), \tag{39}$$

$$\cos\gamma = \hat{\mathbf{R}} \cdot \hat{\mathbf{r}}, \tag{40}$$

$P_\lambda(\cos\gamma)$ are the Legendre polynomials, and $f^{\lambda}_{n'n}$ are the $J = 0$ Percival-Seaton coefficients.[82,83] The radial integral in eq. (37) is handled by N_{rep} repetitions of N_{GL}-point Gauss-Legendre quadrature. Optimized vibrational quadrature with the Gauss ground-state option[84] is used to obtain the weights $w^{i}_{nn'}$ and nodes r_i in eq. (38). The angular integral in eq. (40) is carried out using N_{QA}-point Gauss-Legendre quadrature. Matrix elements of the third term in eq. (30) may be simplified because the functions ϕ_{vj} are eigenfunctions of $\hat{\tau}$, i.e.,

$$\langle \beta' | \hat{\tau} | \beta \rangle = S_{\beta'\beta} \varepsilon_{vj}, \tag{41}$$

where ε_{vj} is the diatomic energy of the state ϕ_{vj}.

The HF diatomic problem is solved in a harmonic oscillator basis $|h\rangle$, where $h = 0, \ldots, N_{\text{HO}} - 1$. The resulting matrix elements are evaluated by writing

$$\langle h' | H^{j}_{\text{diat}} | h \rangle = \delta_{h'h} \hbar\omega (h + \tfrac{1}{2}) + \langle h' | \frac{\hbar^2}{2\mu} \frac{j(j+1)}{r^2} + V_{\text{diat}}(r) - V_{\text{HO}}(r) | h \rangle \tag{42}$$

and using (N_{HO} + 14)-point Gauss-Hermite quadrature. The harmonic frequency ω is obtained from the second derivative of the HF asymptotic potential at its minimum-energy bond distance. This frequency is also used to determine the exponential parameter of the HO basis functions and the harmonic potential term V_{HO}. The resulting matrices (there is one matrix for each value of j) are diagonalized to obtain the required eigenenergies ε_{vj} and eigenfunctions ϕ_{vj}. All asymptotic eigenfunctions ϕ_{vj} with energies ε_{vj} less than E_{asym} (relative to the bottom of the asymptotic HF potential curve)

are included as basis functions, where E_{asym} is a parameter with respect to which the results are converged. The number of such asymptotic basis functions is n_{asym}.

Once the matrix elements for the Hamiltonian and overlap matrices were calculated, version 2.0 of the LAPACK linear algebra package[85] was used to solve the generalized eigenvalue equation

$$\underline{\underline{H}}\,\underline{c} = \underline{E}\,\underline{\underline{S}}\,\underline{c}\,, \tag{43}$$

where the underline and the double underline indicate vectors and matrices in the vibrational state space, respectively.

Two sets of numerical and basis set parameters are given in Table 7. The mass-scaled parameters R_{min} and R_{max} [of eq. (37)] and R_m^T are related to the distances S_{min}, S_{max}, and S_m^T by

$$S_{\text{min}} = R_{\text{min}} / M\,, \tag{44}$$

$$S_{\text{max}} = R_{\text{max}} / M\,, \tag{45}$$

$$\begin{aligned} S_m^T &= R_m^T / M \\ &= S_1^T + (m-1)\,\Delta\,, \end{aligned} \tag{46}$$

where

$$M = \left(\frac{m_{\text{Li}}(m_{\text{H}} + m_{\text{F}})^2}{m_{\text{H}} m_{\text{F}} (m_{\text{Li}} + m_{\text{H}} + m_{\text{F}})} \right)^{1/4}. \tag{47}$$

The total number of basis functions is $n_{\text{bas}} = n_{\text{asym}}\, n_{\text{trans}}$. The energies of the bound states computed using the two basis sets differ by less than 0.1%.

References

1 Y. Zeiri and M. Shapiro, *Chem. Phys.* **31**, 217 (1978).

2 M. M. L. Chen and H. F. Schaefer, *J. Chem. Phys.* **72**, 4376 (1980).

3 S. Carter and J. N. Murrell, *Mol. Phys.* **41**, 567 (1980).

4 A. Laganà, E. Garcia, *Theochem* **16**, 91 (1984).

5 E. Garcia and A. Laganà, *Mol. Phys.* **52**, 1115 (1984).

6 M. Paniagua and A. Aguado, *Chem. Phys.* **134**, 287 (1989).

7 P. Palmeiri and A. Laganà, *J. Chem. Phys.* **91**, 7303 (1989).

8 C. Suarez, A. Aguado, C. Tablero, and M. Paniagua, *Int. J. Quantum Chem.* **52**, 935 (1994).

9 A. Aguado, C. Suarez, and M. Paniagua, *Chem. Phys.* **201**, 107 (1995).

10 A. Aguado, M. Paniagua, M. Lara, and O. Roncero, *J. Chem. Phys.* **106**, 1013 (1997).

11 A. Aguado, M. Paniagua, M. Lara, O. Roncero, *J. Chem. Phys.* **107**, 10085 (1997).

12 A. Laganà, O. Gervasi, and E. Garcia, *Chem. Phys. Lett.* **143**, 174 (1998).

13 A. Laganà, G. O. d. Aspuru, and E. Garcia, *J. Chem. Phys.* **168**, 3886 (1998).

14 R. Burcl, P. Piecuch, V. Špirko, and O. Bludský, *Int. J. Quantum Chem.* **80**, 916 (2000).

15 A. W. Jasper, M. D. Hack, A. Chakraborty, D. G. Truhlar, and P. Piecuch, *J. Chem. Phys.* **115**, 7945 (2001).

16 A. W. Jasper, M. D. Hack, D. G. Truhlar, and P. Piecuch, *J. Chem. Phys.* **116**, 8353 (2002).

17 R. Burcl, P. Piecuch, V. Špirko, and O. Bludský, *Theochem* **591**, 151 (2002).

18 C. H. Becker, P. Casavecchia, P. W. Tiedermann, J. J. Valentini, and Y. T. Lee, *J. Chem. Phys.* **73**, 2833 (1980).

19 G. A. Parker, R. T Pack, and A. Laganà, *Chem. Phys. Lett.* **202**, 75 (1993).

20 M. Baer, I. Last, and H.-J. Loesch, *J. Chem. Phys.* **101**, 9648 (1994).

21 G. A. Parker, A. Laganà, S. Crocchianti, and R. T Pack, *J. Chem. Phys.* **102**, 1238 (1995).

22 F. Gogtas, G. G. Balint-Kurti, and A. Offer, R. *J. Chem. Phys.* **104**, 7927 (1996).

23 W. Zhu, D. Wang, and J. Z. H. Zhang, *Theor. Chem. Acc.* **96**, 31 (1997).

24 M. Lara, A. Aguado, O. Roncero, and M. Paniagua, *J. Chem. Phys.* **109**, 9391 (1998).

25 S. C. Althorpe, D. J. Kouri, and D. K. Hoffman, *J. Phys. Chem. A* **102**, 9494 (1998).

26 F. J. Aoiz, M. T. Martinez, and M. Menéndez, V. Sáez Rábanos, E. Verdasco, *Chem. Phys. Lett.* **299**, 25 (1999).

27 A. Laganà, A. Bolloni, S. Crocchianti, and G. A. Parker, *Chem. Phys. Lett.* **324**, 466 (2000).

28 M. Lara, A. Aguado, M. Paniagua, and O. Roncero, *J. Chem. Phys.* **113**, 1781 (2000).

29 F. J. Aoiz, E. Verdasco, V. Sáez Rábanos, H. T., Loesch, M. Menéndez, and F. Stienkemeier, *Phys. Chem. Chem. Phys.* **2**, 541 (2000).

30 F. J. Aoiz, M. T. Martinez, and V. Sáez Rábanos, *J. Chem. Phys.* **114**, 8880 (2001).

31 A. Laganà and S. Crocchianti, *J. Phys. Chem. A* **105**, 2361 (2001).

32 A. Laganà, A. Bolloni, and S. Crocchianti, *Phys. Chem. Chem. Phys.* **2**, 535 (2002).

33 J. M. Alvarino, V. Aquilanti, S. Cavalli, S. Crocchianti, A. Laganà, and M. T. Martinez, *J. Chem. Phys.* **107**, 3339 (1997).

34 J. M. Alvarino, V. Aquilanti, S. Cavalli, S. Crocchianti, A. Laganà, and M. T. Martinez, *J. Phys. Chem. A* **102**, 9638 (1998).

35 Stereochemistry and Control in Molecular Reaction Dynamics, *Faraday Discuss.* **113** (1999).

36 M. Paniagua, A. Aguado, M. Lara, O. and Roncero, *J. Chem. Phys.* **109**, 2971 (1998).

37 M. Paniagua, A. Aguado, M. Lara, O. and Roncero, *J. Chem. Phys.* **111**, 6712 (1999).

38 A. J. Hudson, H. B. Oh, J. C. Polanyi, and P. Piecuch, *J. Chem. Phys.* **113**, 9897 (2000).

39 A. Aguado, M. Lara, M. Paniagua, and O. Roncero, *J. Chem. Phys.* **114**, 3440 (2001).

40 Y. Sun, D. J. Kouri, D. G. Truhlar, and D. W. Schwenke, *Phys. Rev. A* **41**, 4857 (1990).

41 D. W. Schwenke, S. L. Mielke, and D. G. Truhlar, *Theor. Chim. Acta* **79**, 241 (1991).

42 G. J. Tawa, S. L. Mielke, D. G. Truhlar, and D. W. Schwenke, *J. Chem. Phys.* **100**, 5751 (1994).

43 G. J. Tawa, S. L. Mielke, and D. G. Truhlar, D. W. Schwenke, in *Advances in Molecular Vibrations and Collision Dynamics: Quantum Reactive Scattering*, edited by J. M. Bowman (JAI, Greenwich, CT, 1994) Vol. 2B, pp. 45–116.

44 S. Zou, S. Skokov, and J. M. Bowman, *Chem. Phys. Lett.* **339**, 290 (2001).

45 T. Xie, D. Wang, J. M. Bowman, and D. E. Manolopoulos, *J. Chem. Phys.* **116**, 7461 (2002).

46 T. Takayanagi and Y. Kurosaki, *Chem. Phys. Lett.* **286**, 35 (1998).

47 T. Takayanagi and Y. Kurosaki, *J. Chem. Phys.* **109**, 8929 (1998).

48 T. Takayanagi and Y. Kurosaki, *Phys. Chem. Chem. Phys.* **1**, 1099 (1999).

49 B. C. Garrett and D. G. Truhlar, *J. Phys. Chem.* **83**, 1079 (1979).

50 A. D. Isaacson and D. G. Truhlar, *J. Chem. Phys.* **76**, 1380 (1982).

51 J. C. Corchado, Y.-Y. Chuang, P. L. Fast, J. Villá, W.-P. Hu, Y.-P. Liu, G. Lynch, K. A. Nguyen, C. F. Jackels, M. Z. Gu, I. Rossi, E. L. Coitiño, S. Clayton, V. S. Melissas, R. Steckler, B. C. Garrett, A. D. Isaacson, and D. G. Truhlar, POLYRATE, version 8.5.1, University of Minnesota, Minneapolis, 2000.

52 R. G. Newton, *Scattering Theory of Waves and Particles*, 2nd ed Springer-Verlag, New York, 1982.

53 D. J. Kouri, Y. Sun, R. C. Mowrey, J. Z. H. Zhang, D. G. Truhlar, K. Huag, and D. W. Schwenke, in *Mathematical Frontiers in Computational Chemical Physics*, edited by D. G. Truhlar (Springer-Verlag, New York, 1988), p. 207.

54 D. W. Schwenke, K. Haug, M. Zhao, D. G. Truhlar, Y. Sun, J. Z. H. Zhang, and D. J. Kouri, *J. Phys. Chem.* **92**, 3202 (1998).

55 J. R. Taylor, *Scattering Theory* Wiley, New York, 1972, pp. 238–244.

56 R. K. Nesbet, *Adv. At. Mol. Phys.* **13**, 315 (1997).

57 A. U. Hazi, *Phys. Rev. A* **19**, 920 (1979).

58 R. S. Friedman and D. G. Truhlar, in *Multiparticle Quantum Scattering with Applications to Nuclear, Atomic, and Molecular Physics*, edited by D. G. Truhlar and B. Simon (Springer-Verlag, New York, 1997), pp. 243-281.

59 D. W. Schwenke and D. G. Truhlar, *J. Chem. Phys.* **87**, 1095 (1987).

60 S. L. Mielke, G. J. Tawa, and D. G. Truhlar, *Int. J. Quantum Chem.: Quantum Chem. Symp.* **27**, 621 (1993).

61 M. D. Hack, A. W. Jasper, Y. L. Volobuev, and D. G. Truhlar, *J. Phys. Chem. A* **103**, 6309 (1999).

62 S. A. Reid and H. Reisler, *Annu. Rev. Phys. Chem.* **47**, 495 (1996).

63 A. W. Jasper, D. W. Schwenke, and D. G. Truhlar, ABCSPECTRA, version 1.0 University of Minnesota, Minneapolis, 2003.

64 D. W. Schwenke, Y. L. Volobuev, S. L. Mielke, G. J. Tawa, D. C. Chatfield, Y. Sun, K. Haug, T. C. Allison, R. S. Friedman, M. Zhao, P. Halvick, M. D. Hack, and D. G. Truhlar, VP, version 18.8 University of Minnesota, Minneapolis, 1999.

65 B. C. Garrett, D. G. Truhlar, R. S. Grev, and A. W. Magnuson, *J. Phys. Chem.* **84**, 1730 (1980).

66 B. C. Garrett, D. G. Truhlar, R. S. Grev, G. C. Schatz, and R. B. Walker, *J. Phys. Chem.* **85**, 3806 (1981).

67 D. C. Chatfield, R. S. Friedman, D. G. Truhlar, B. C. Garrett, and D. W. Schwenke, *J. Am. Chem. Soc.* **113**, 486 (1991).

68 J. A. Beswick, and J. Jortner, *Chem. Phys. Lett.* **49**, 13 (1977).

69 G. E. Ewing, *J. Chem. Phys.* **71**, 3143 (1979).

70 G. E. Ewing, *Faraday Discuss. Chem. Soc.* **73**, 325 (1982).

71 S. Bratož and M. L. Martin, *J. Chem. Phys.* **42**, 1051 (1965).

72 J. M. Hutson, *Adv. Mol. Vibrat. Collision Dyn.* **1A**, 1 (1991).

73 J. M. Hutson, *J. Chem. Phys.* **89**, 4550 (1988).

74 A. W. Jasper and D. G. Truhlar, unpublished results, 2003.

75 G. Herzberg, *Molecular Spectra and Molecular Structure. II. Infrared and Raman Spectra of Polyatomic Molecules* D. Van Nostrand, Princeton, 1945.

76 M. S. Child, *Mol. Phys.* **12**, 401 (1967).

77 Y. Chen and M. C. Heaven, *J. Chem. Phys.* **109**, 5171 (1998).

78 Y. Chen and M. C. Heaven, *J. Chem. Phys.* **112**, 7416 (2000).

79 M. I. Lester, B. V. Pond, M. D. Marshall, D. T. Anderson, L. B. Harding, and A. F. Wagner, *Faraday Discuss.* **118**, 373 (2001).

80 B. V. Pond and M. I. Lester, *J. Chem. Phys.* **118**, 2223 (2003).

81 I. P. Hamilton and J. C. Light, *J. Chem. Phys.* **84**, 306 (1985).

82 I. C. Percival and M. J. Seaton, *Proc. Cambridge Phil. Soc.* **53**, 654, (1957).

83 A. M. Arthurs and A. Dalgarno, *Proc. R. Soc. London A* **256**, 540 (1960).

84 D. W. Schwenke and D. G. Truhlar, *Computer Phys. Commun.* **34**, 57 (1984).

85 E. Anderson, Z. Bai, C. Bishof, S. Blackford, J. Demmel, J. Dongarra, J. Du Croz, A. Greenbaum, S. Hammerling, A. McKenney, and D. Sorensen, *LAPACK Users' Guide* SIAM, Philadelphia, PA, 1999. The LAPACK library of routines may be found at http://www.netlib.org/lapack.

Table 1. Geometries and energies of the stationary points for the ground-state potential energy surface of the Li + HF ⟶ H + LiF reaction. Distances are in bohr, angles are in degrees, and energies are in eV.

Stationary Point		Geometry				Energy		
		R_{HF}[b]	R_{LiF}	R_{LiH}	θ_{LiFH}[c]	V	ZPE	V + ZPE
Reactant	(A)[d]	1.733	–	–	–	0.000	0.255	0.255
Reactant well	(B)	1.750	3.563	4.483	110.	–0.211	0.281	0.070
First saddle point	(C)	2.422	3.151	3.379	73.3	0.352	0.098	0.451
Product well	(D)	3.316	2.997	3.592	69.2	0.171	0.136	0.306
Second saddle point	(E)	4.506	2.957	5.294	87.8	0.227	0.062	0.290
Product	(F)	–	2.953	–	–	0.213	0.056	0.270

[a]The zero point energies (ZPE) were calculated using the Morse I approximation[46,47] with the POLYRATE software package.[48]

[b]R_{AB} is the internuclear distance between atoms A and B.

[c]θ_{LiFH} is the Li–F–H bond angle.

[d]The letters A–F correspond to the features labeled in Fig. 1.

Table 2. Basis set parameters and numerical parameters for the outgoing scattering wave calculation for the total energy 0.4 eV. Atomic units are used.

Basis set parameters	Set 1	Set 2	Basis set parameters	Set 1	Set 2
$j_{\max}(k=1,v=0)$	26	28	$j_{\max}(k=2,v=3)$	56	62
$j_{\max}(k=1,v=1)$	22	24	$j_{\max}(k=2,v=4)$	50	56
$j_{\max}(k=1,v=2)$	17	19	$j_{\max}(k=2,v=5)$	43	50
$j_{\max}(k=1,v=3)$	10	12	$j_{\max}(k=2,v=6)$	35	43
$j_{\max}(k=1,v=4)$		4	$j_{\max}(k=2,v=7)$	24	35
$N(\mathrm{HO})\ (k=1)$	80	80	$j_{\max}(k=2,v=8)$	14	24
$m^{\mathrm{g}}\ (k=1)$	37	39	$j_{\max}(k=2,v=9)$		2
$m^{\mathrm{e}}\ (k=1)$	37	39	$N(\mathrm{HO})\ (k=2)$	80	80
$S_l^G\ (k=1)$	1.80	1.50	$m^{\mathrm{g}}\ (k=2)$	35	37
$S_u^G\ (k=1)$	7.20	7.58	$m^{\mathrm{e}}\ (k=2)$	35	37
$\Delta^S\ (k=1)$	0.15	0.16	$S_l^G\ (k=2)$	1.80	1.50
$w^S\ (k=1)$	0.75	0.80	$S_u^G\ (k=2)$	6.56	6.90
$j_{\max}(k=2,v=0)$	72	76	$\Delta^S\ (k=2)$	0.14	0.15
$j_{\max}(k=2,v=1)$	67	72	$w^S\ (k=2)$	0.75	0.80
$j_{\max}(k=2,v=2)$	62	67			
Numerical parameters	Set 1	Set 2	Numerical parameters	Set 1	Set 2
$N^{\mathrm{QV}}(k=1)$	20	25	$\varepsilon_{\mathrm{rad}}$	7	9
$N^{\mathrm{QA}}(k=1)$	75	80	ε_B	10	12
$N_e^{\mathrm{QA}}(k=1)$	0	0	ε_W	10	12
$S_l^{\mathrm{QR}}(k=1)$	1.5	1.3	$S_0^{\mathrm{F}}(k=1)$	1.0	0.8
$S_u^{\mathrm{QR}}(k=1)$	15	17	$S_{N(F)+1}^{\mathrm{QV}}(k=1)$	20	22
$N^{\mathrm{QGL}}(k=1)$	100	100	$N^{\mathrm{FD}}(k=1)$	13	13
$N^{\mathrm{QS}}(k=1)$	7	7	$N(F)(k=1)$	730	733
$N^{\mathrm{QV}}(k=2)$	20	25	$N^{\mathrm{SD}}(k=1)$	30	33
$N^{\mathrm{QA}}(k=2)$	75	80	$f^{SD}(k=1)$	0.9	0.9
$N_e^{\mathrm{QA}}(k=2)$	75	80	$S_0^{\mathrm{F}}(k=2)$	1.0	0.8
$S_l^{\mathrm{QR}}(k=2)$	1.0	0.8	$S_{N(F)+1}^{\mathrm{QV}}(k=2)$	25	27
$S_u^{\mathrm{QR}}(k=2)$	15	17	$N^{\mathrm{FD}}(k=2)$	11	11
$N^{\mathrm{QGL}}(k=2)$	120	120	$N(F)(k=2)$	870	873
$N^{\mathrm{QS}}(k=2)$	7	7	$N^{\mathrm{SD}}(k=2)$	30	33
ε_χ	10	12	$f^{SD}(k=2)$	0.9	0.9
ε_t	50	55			

Table 3. Energies, widths, and lifetimes for several observed resonances.

α	E_α (eV)	Γ_α (eV)	τ_α (ps)
1	0.274	7.81×10^{-5}	8.43
2	0.278	1.40×10^{-3}	0.470
3	0.285	2.81×10^{-3}	0.234
4	0.287	1.48×10^{-3}	0.445
5	0.294	1.68×10^{-5}	39.2
6	0.298	1.04×10^{-3}	0.633
7	0.304	7.91×10^{-4}	0.832
8	0.313	3.25×10^{-3}	0.203
9	0.319	7.68×10^{-6}	86.7
10	0.322	6.61×10^{-4}	0.996
11	0.327	9.63×10^{-4}	0.683
12	0.349	5.59×10^{-4}	1.18
13	0.354	2.34×10^{-4}	2.81
14	0.381	6.83×10^{-4}	0.964
15	0.387	1.99×10^{-5}	33.1
16	0.418	2.57×10^{-4}	2.56
17	0.439	3.05×10^{-4}	2.16
18	0.460	5.30×10^{-5}	12.4
19	0.485	3.92×10^{-4}	1.68

Table 4. Bound and quasibound states of the Li···FH van der Waals well.

Bound States			Quasibound States		
v_R	v_χ	E_{v_R,v_χ} (eV)	v_R	v_χ	E_{v_R,v_χ} (eV)
0	0	0.062	0	5	0.266
0	1	0.082	2	4	0.279
1	0	0.103	1	5	0.301
0	2	0.112	0	6	0.330
1	1	0.123	2	5	0.334
2	0	0.139	3	5	0.355
1	2	0.148	1	6	0.363
0	3	0.156	2	6	0.389
2	1	0.162	0	7	0.401
3	0	0.170	1	7	0.430
2	2	0.181	2	7	0.450
3	1	0.190	0	8	0.475
4	0	0.197	1	8	0.499
1	3	0.200			
0	4	0.209			
4	1	0.210			
3	2	0.218			
5	0	0.222			
2	3	0.232			
5	1	0.233			
6	0	0.238			
4	2	0.245			
1	4	0.247			
7	0	0.248			
6	1	0.253			

Table 5. Li···FH van der Waals well bound-state and quasibound-state fitted energy parameters.

Parameter	Value
ω_R	4.506 x 10^{-2} eV
ω_χ	1.100 x 10^{-2} eV
x_R	–2.378 x 10^{-2}
x_χ	4.539 x 10^{-3}
$f_{R\chi}$	–5.311 x 10^{-4} eV
E_0	3.794 x 10^{-2} eV

Table 6. Fitted and calculated Li···FH quasibound-state energies and assigned resonance energies and widths.

v_R	v_χ	$E_{\rm fit}(v_R, v_\chi)$ (eV)	E_{v_R, v_χ} (eV)	E_α (eV)	Γ_α (eV)
4	3	0.278		0.274	7.81×10^{-5}
6	2	0.278		0.278	1.40×10^{-3}
7	2	0.288		0.285	2.81×10^{-3}
1	5	0.294	0.301		
8	2	0.294		0.287	1.48×10^{-3}
5	3	0.298		0.298	1.04×10^{-3}
3	4	0.300		0.294	1.68×10^{-5}
6	3	0.312		0.304	7.91×10^{-4}
0	6	0.321	0.330		
7	3	0.322		0.313	3.25×10^{-3}
4	4	0.323		0.327	9.63×10^{-4}
2	5	0.326	0.334	0.319	7.68×10^{-6}
8	3	0.327		0.322	6.61×10^{-4}
5	4	0.342		0.354	2.34×10^{-4}
3	5	0.354	0.355	0.349	5.59×10^{-4}
6	4	0.356			
1	6	0.358	0.363		
7	4	0.366			
8	4	0.370			
4	5	0.377		0.381	6.83×10^{-4}
2	6	0.390	0.389	0.387	1.99×10^{-5}
5	5	0.396			
0	7	0.396	0.401		
6	5	0.409			
3	6	0.418		0.418	2.57×10^{-4}
7	5	0.418			
8	5	0.422			
1	7	0.432	0.430		
4	6	0.440		0.439	3.05×10^{-4}
5	6	0.458			
2	7	0.464	0.450	0.460	5.30×10^{-5}
6	6	0.471			
0	8	0.479	0.475		
7	6	0.479			
8	6	0.483			
3	7	0.490		0.485	3.92×10^{-4}

Table 7. LiFH bound-state and quasibound-state basis set and numerical parameters.

Parameter[a]	Set 1	Set 2
N_{HO}	20	25
N_{QV}	20	25
N_{QA}	50	60
N_{rep}	40	55
N_{GL}	7	7
S_{min} (a_0)	0.5	0.2
S_{max} (a_0)	12	14
E_{asym} (eV)	2.8	3.0
S_1^T (a_0)	2.73	2.23
$S_{n_{\mathrm{trans}}}^T$ (a_0)	9.77	10.33
Δ (a_0)	0.11	0.10
c	0.9	0.8
n_{asym}	132	161
n_{trans}	64	81
n_{bas}	8448	13041

[a]See the Appendix for definitions of the parameters.

Figure Captions

Figure 1. Relative energies of stationary points of Li + HF ⟶ H + LiF reaction on the electronic ground-state potential energy surface. The features labeled A–F are described in Table 1 and correspond to: (A) reactants, (B) the reactant van der Waals well, i.e., Li···FH, (C) the saddle point, (D) the product van der Waals well, i.e., LiF···H, (E) the product saddle point, and (F) products. The lower potential scheme is zero-point exclusive, and the upper potential scheme is zero-point inclusive. The zero-point energy that is included is from one mode at A and F, from two modes at C and E, and from three modes at B and D.

Figure 2. State-to-state reaction probabilities as a function of the total energy for the reaction Li + HF($v = 0, j = 0$) ⟶ H + LiF ($v' = 0, j'$): (a) $j' = 0$, (b) $j' = 1$, (c) $j' = 2$, (d) $j' = 3$, (e) $j' = 4$, and (f) $j' = 5$.

Figure 3. Initial-state-selected reaction probability for the vibrational ground state ($v = 0$) and different rotational states, i.e., the probability of the reaction Li + HF($v = 0$, j) ⟶ H + LiF(all v', all j'), as a function of the total energy: (a) $j = 0, 1, 2, 3$, (b) $j = 3, 4, 5, 6$, and (c) $j = 6, 7, 8, 9$.

Figure 4. Cumulative reaction probability, i.e., the probability of the reaction Li + HF(all v, all j) ⟶ H + LiF(all v', all j'), as a function of the total energy for the energy range: (a) 0.25–0.50 eV, (b) 0.25–0.36 eV, (c) 0.34–0.50 eV.

Figure 5. Eigenphase sum as a function of the total energy for the Li + HF ⟶ H + LiF reaction at energies near the resonance state energy with $E_\alpha = 0.274$ eV. The dots are from the OWVP calculations (smoothed by adding integral multiples of π). The solid line is from the multichannel Breit-Wigner formula. The straight line is the fitted background contribution.

Figure 6. Product rotational state distributions of LiF for the decay of the resonance state with the resonance energy: (a) 0.294 eV, (b) 0.304 eV.

Figure 7. Resonance widths as a function of the translational quantum number. Note that the ordinate scale is logarithmic.

Figure 1

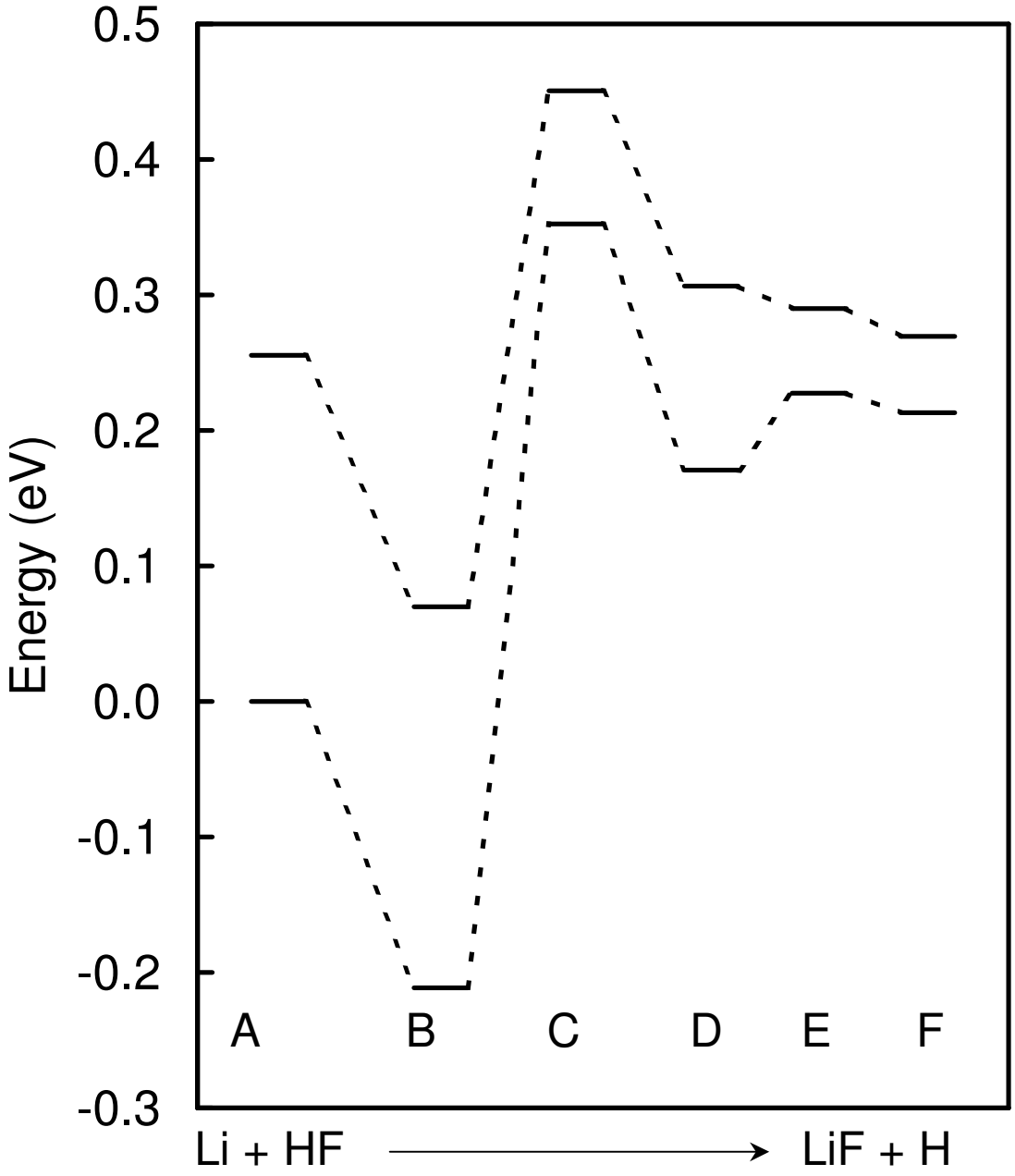

Figure 2(a)

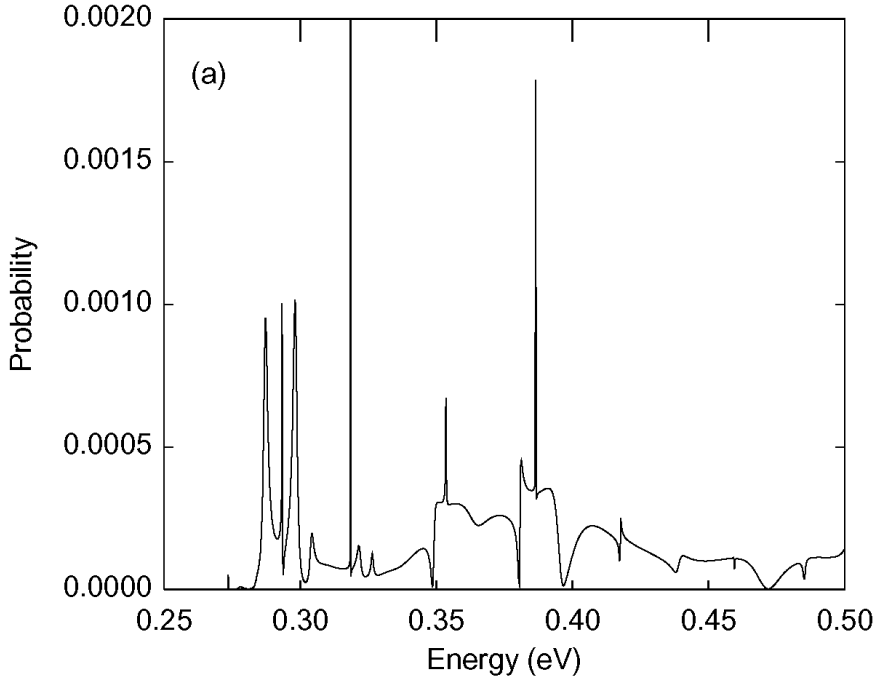
(a)
Probability
0.0020
0.0015
0.0010
0.0005
0.0000
0.25
0.30
0.35
0.40
0.45
0.50
Energy (eV)

Figure 2(b)

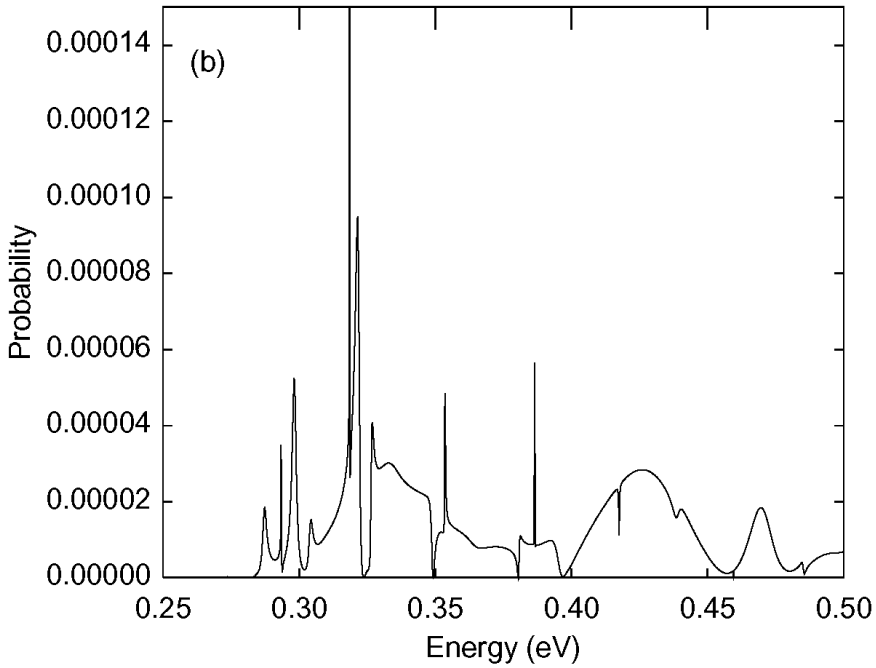
(b)
Probability
0.00014
0.00012
0.00010
0.00008
0.00006
0.00004
0.00002
0.00000
0.25
0.30
0.35
0.40
0.45
0.50
Energy (eV)

Figure 2(c)

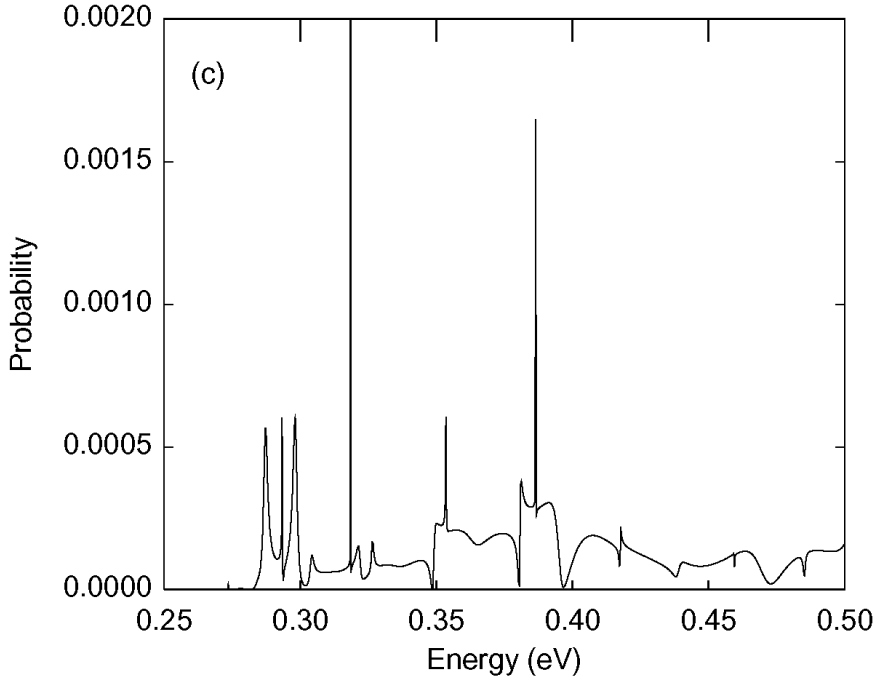
(c)
0.0020
0.0015
0.0010
0.0005
0.0000
Probability
0.25
0.30
0.35
0.40
0.45
0.50
Energy (eV)

Figure 2(d)

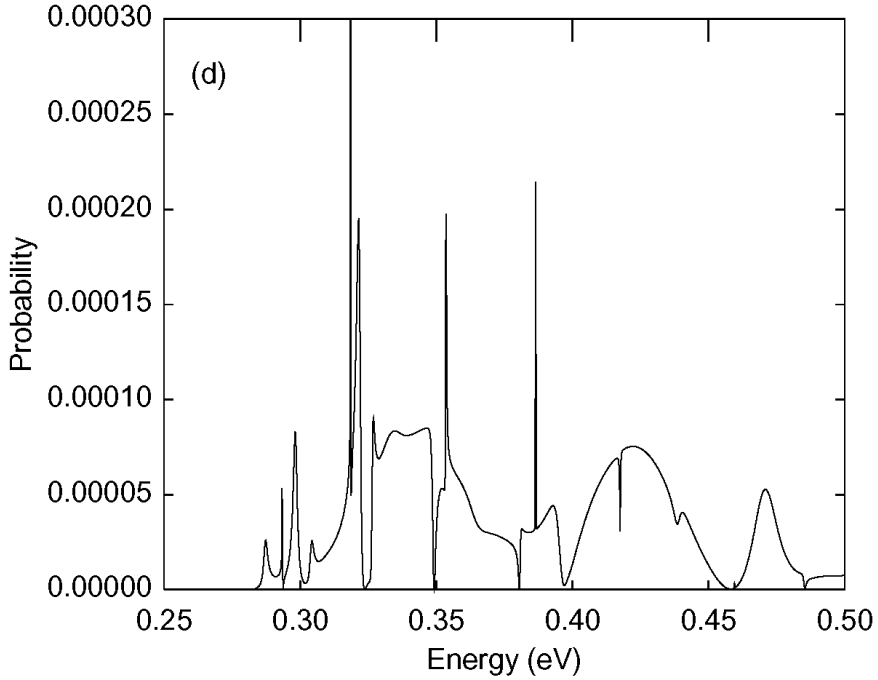
(d)
Probability
0.00030
0.00025
0.00020
0.00015
0.00010
0.00005
0.00000
0.25
0.30
0.35
0.40
0.45
0.50
Energy (eV)

Figure 2(e)

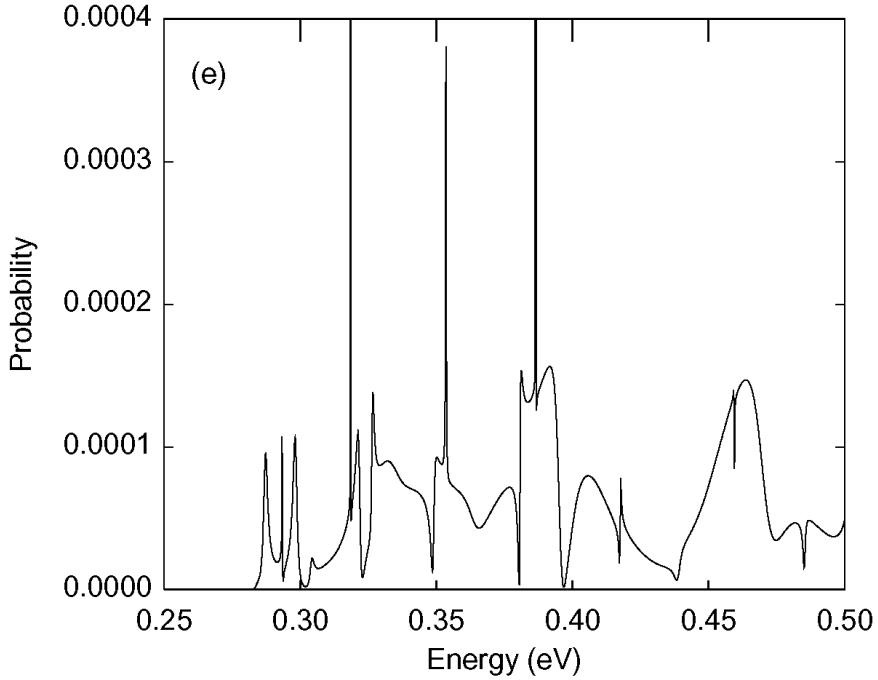
(e)
0.0004
0.0003
0.0002
0.0001
0.0000
Probability
0.25
0.30
0.35
0.40
0.45
0.50
Energy (eV)

Figure 2(f)

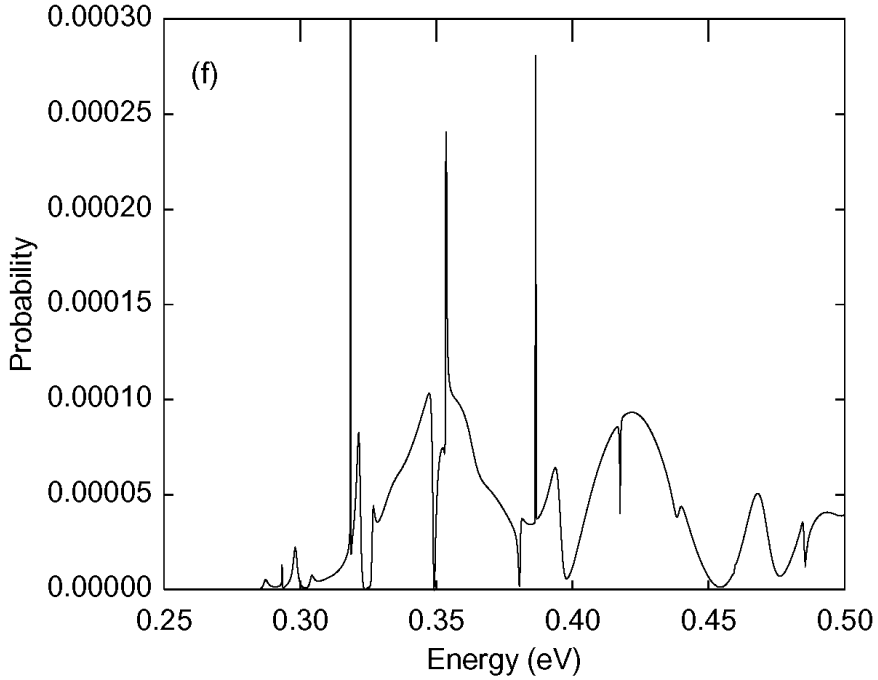
(f)
Probability
0.00030
0.00025
0.00020
0.00015
0.00010
0.00005
0.00000
0.25
0.30
0.35
0.40
0.45
0.50
Energy (eV)

Figure 3(a)

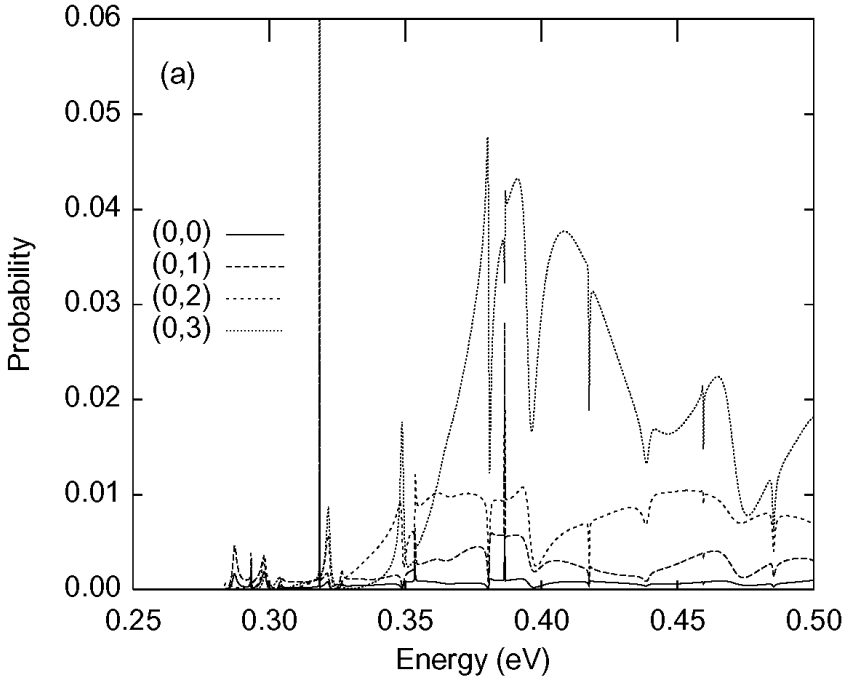
(a)
(0,0)
(0,1)
(0,2)
(0,3)
Probability
Energy (eV)
0.00
0.01
0.02
0.03
0.04
0.05
0.06
0.25
0.30
0.35
0.40
0.45
0.50

Figure 3(b)

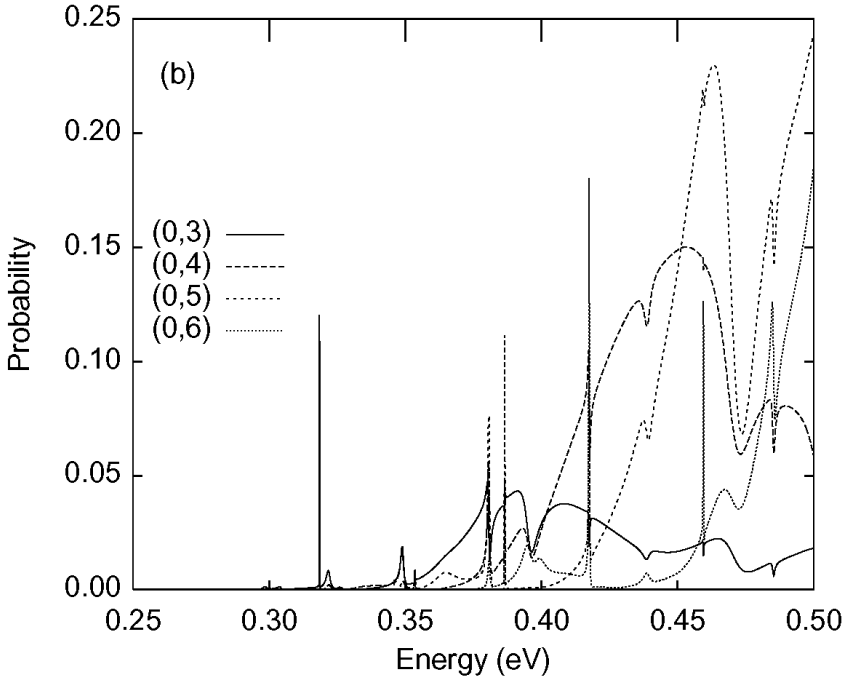
(b)
(0,3)
(0,4)
(0,5)
(0,6)
Probability
Energy (eV)
0.25
0.20
0.15
0.10
0.05
0.00
0.25
0.30
0.35
0.40
0.45
0.50

Figure 3(c)

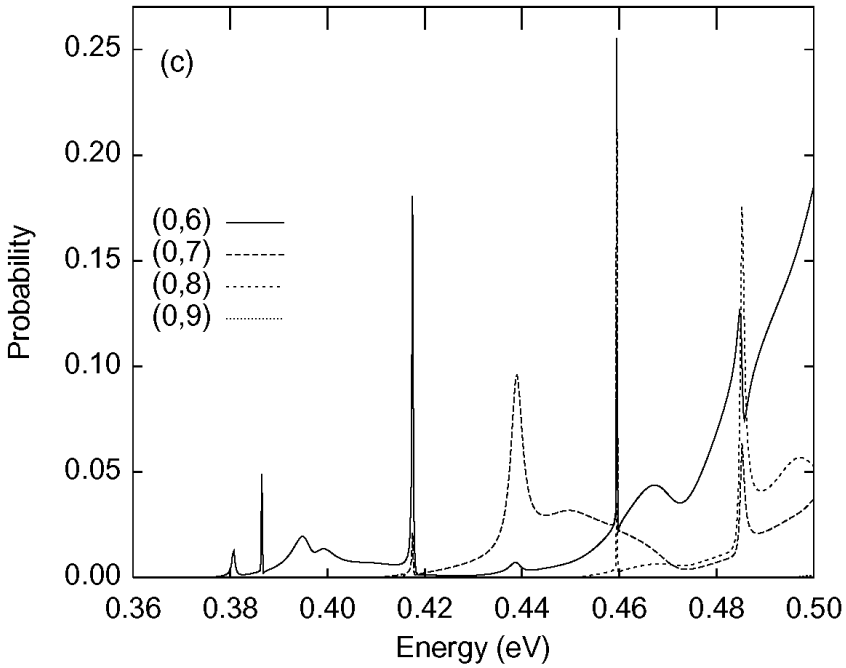
(c)
(0,6)
(0,7)
(0,8)
(0,9)
Probability
Energy (eV)
0.00
0.05
0.10
0.15
0.20
0.25
0.36
0.38
0.40
0.42
0.44
0.46
0.48
0.50

Figure 4(a)

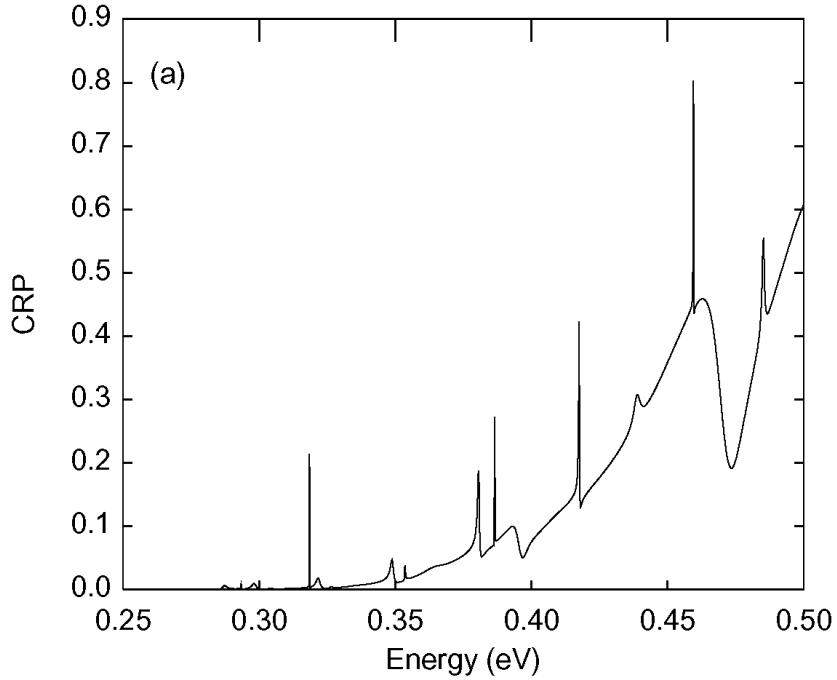
(a)
CRP
Energy (eV)
0.0
0.1
0.2
0.3
0.4
0.5
0.6
0.7
0.8
0.9
0.25
0.30
0.35
0.40
0.45
0.50

Figure 4(b)

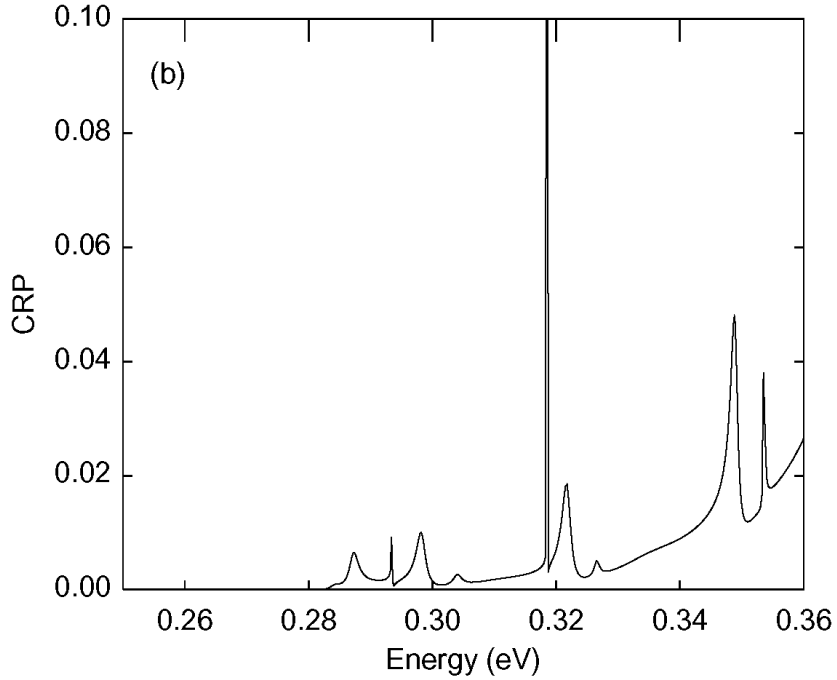

Figure 5

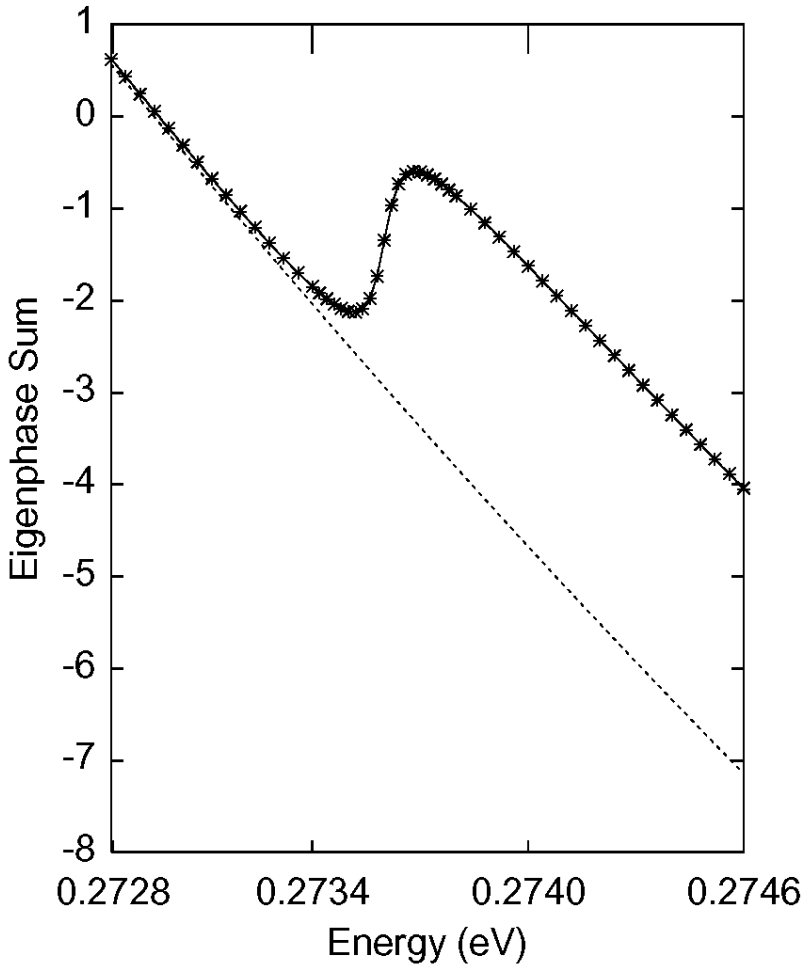
1
0
-1
-2
-3
-4
-5
-6
-7
-8
Eigenphase Sum
0.2728
0.2734
0.2740
0.2746
Energy (eV)

Figure 6(a)

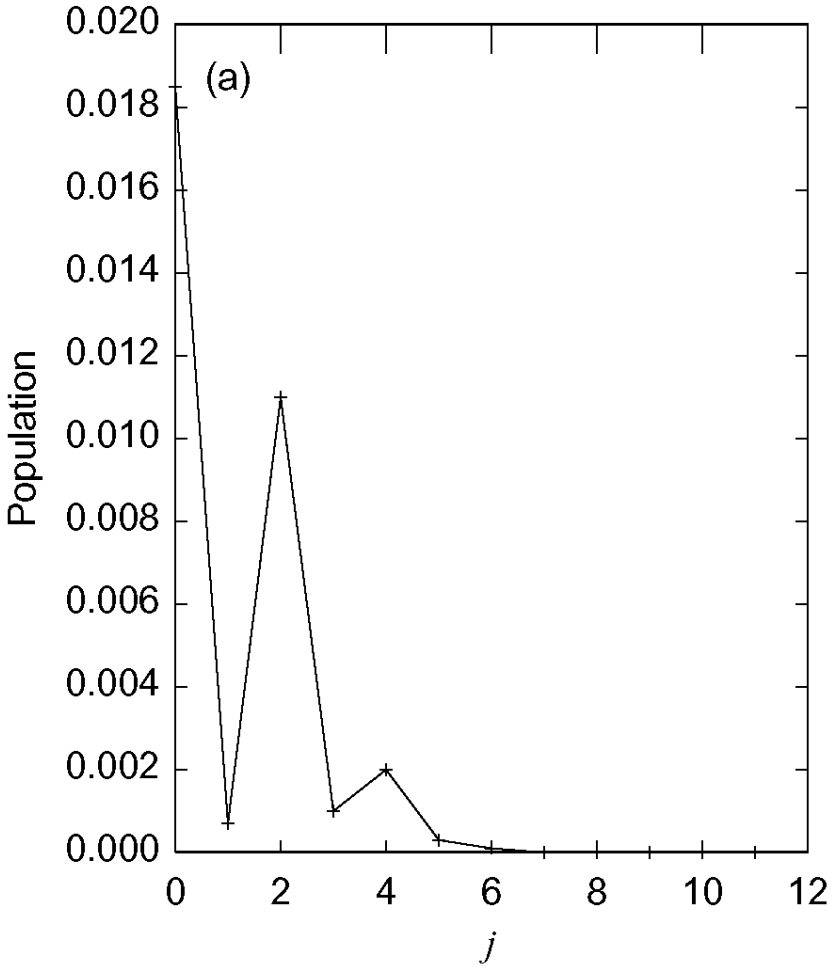
(a)
Population
0.020
0.018
0.016
0.014
0.012
0.010
0.008
0.006
0.004
0.002
0.000
0
2
4
6
8
10
12
j

Figure 6(b)

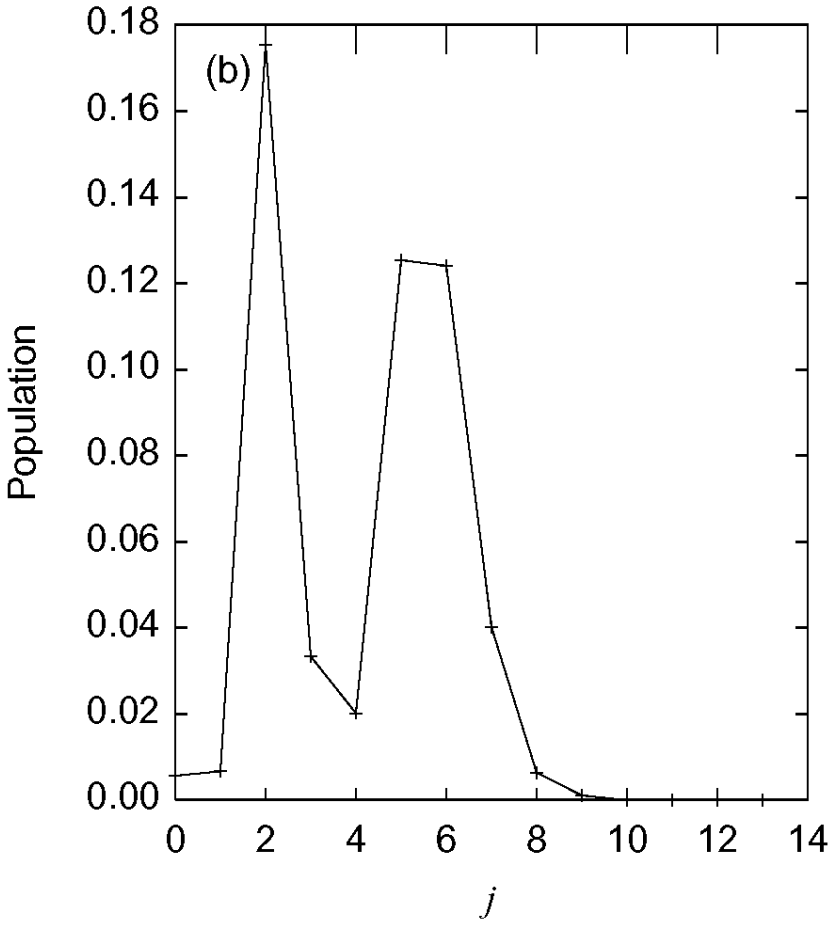
(b)
Population
0.18
0.16
0.14
0.12
0.10
0.08
0.06
0.04
0.02
0.00
0
2
4
6
8
10
12
14
j

Figure 7